



HAL
open science

Towards Patient-Based Fluid-Structure Interaction Simulation of the Mitral Valve

Nariman Khaledian

► **To cite this version:**

Nariman Khaledian. Towards Patient-Based Fluid-Structure Interaction Simulation of the Mitral Valve. Computer Science [cs]. Université de Lorraine, 2024. English. NNT: 2024LORR0037 . tel-04685470

HAL Id: tel-04685470

<https://hal.univ-lorraine.fr/tel-04685470v1>

Submitted on 3 Sep 2024

HAL is a multi-disciplinary open access archive for the deposit and dissemination of scientific research documents, whether they are published or not. The documents may come from teaching and research institutions in France or abroad, or from public or private research centers.

L'archive ouverte pluridisciplinaire **HAL**, est destinée au dépôt et à la diffusion de documents scientifiques de niveau recherche, publiés ou non, émanant des établissements d'enseignement et de recherche français ou étrangers, des laboratoires publics ou privés.



**UNIVERSITÉ
DE LORRAINE**

**BIBLIOTHÈQUES
UNIVERSITAIRES**

AVERTISSEMENT

Ce document est le fruit d'un long travail approuvé par le jury de soutenance et mis à disposition de l'ensemble de la communauté universitaire élargie.

Il est soumis à la propriété intellectuelle de l'auteur. Ceci implique une obligation de citation et de référencement lors de l'utilisation de ce document.

D'autre part, toute contrefaçon, plagiat, reproduction illicite encourt une poursuite pénale.

Contact bibliothèque : ddoc-theses-contact@univ-lorraine.fr
(Cette adresse ne permet pas de contacter les auteurs)

LIENS

Code de la Propriété Intellectuelle. articles L 122. 4

Code de la Propriété Intellectuelle. articles L 335.2- L 335.10

http://www.cfcopies.com/V2/leg/leg_droi.php

<http://www.culture.gouv.fr/culture/infos-pratiques/droits/protection.htm>

Towards Patient-Based Fluid-Structure Interaction Simulation of the Mitral Valve

THÈSE

présentée et soutenue publiquement le 12 Juin 2024

pour l'obtention du

Doctorat de l'Université de Lorraine
(mention informatique)

par

Nariman KHALEDIAN

Composition du jury

Président : Sylvain Lefevre, Directeur de recherche Inria, Nancy

Rapporteurs : Christian Duriez, Directeur de recherche Inria, Lille
Yohan Payan, Directeur de recherche CNRS, Grenoble

Examineurs : Hao Gao, Senior Lecturer, School of Mathematics and Statistics, University of Glasgow
Sylvain Lefevre, Directeur de recherche Inria, Nancy

Encadrants : Marie-Odile Berger, Directrice de Recherche Inria
Pierre-Frédéric Villard, Maître de Conférences, Université de Lorraine

Mis en page avec la classe thesul.

Remerciements

I want to thank my family who were by my side supporting me from the first day of school to the end of my PhD. I never felt alone with their unconditional support. They showed me the way, helping me find the right path in life.

I want to thank my colleagues Romain, Karim, Youssef, Daryna, Yasmine, Dr Vincent, Matthieu, Nicolas, and Hugo, who helped me to integrate more easily in France and have a pleasant working environment. I want to thank my friends in Nancy, Lea, Lisou, Selma, Aurore, (les fourmis), Aurelien, Melanie, Pauline, and Emile for all the amazing moments we shared together during the past years.

Finally, I want to thank Dr. Hammer and Dr. Perrine for their expertise and outstanding input during my PhD. I also thank my supervisors for hiring me and allowing me to work on this project. Moreover, I thank the members of the jury and rapporteurs for putting the time and effort into reading this manuscript and evaluating my thesis. Also, other members of the TANGRAM team and everyone in Nancy whom I encountered during the past three years. It was an amazing journey.

Contents

Acronyms	xv
Introduction	1
1 Clinical context	1
1.1 Mitral valve anatomy	1
1.2 Healthy and pathological mitral valve	2
1.3 Surgical intervention	4
2 Numerical simulation	6
2.1 Applications	6
2.2 Patient-specific model	7
3 Challenges in mitral valve simulation	10
3.1 Objective	10
3.2 Limitations	11
4 Contributions	13
4.1 Convergence	13
4.2 Contact measurement	14
4.3 Moving toward a patient-specific model	14
4.4 Influence of geometry and fluid volume	15
4.5 Robustness and flexibility of the model	15
1 Fluid-Structure Interaction Techniques for Modeling Mitral Valve Behavior	17
1.1 State of the art on fluid-structure interaction	17
1.1.1 Mitral valve simulation	17
1.1.2 Mesh representation	18
1.1.3 Method comparison	19
1.2 Immersed boundary method	22
1.2.1 Equation of state	22
1.2.2 Eulerian formulation	23

1.2.3	Structure formulation	25
1.2.4	Interaction	26
1.2.5	The choice of solver	27
1.3	Contact	28
1.3.1	Challenges in self-contact between mitral valve leaflets	28
1.3.2	Master-slave contact model	29
1.4	Conclusion	30
2	Data	33
2.1	Generic mitral valve	33
2.1.1	Using generic geometry in the mitral valve simulation	33
2.1.2	Characteristics of the generic mitral valve	34
2.1.3	Discretized domain	34
2.2	Image-based mitral valve	36
2.2.1	Using image-based geometry in the mitral valve simulation	36
2.2.2	Obtaining the image-based geometry	37
2.2.3	Smoothness of the leaflets in the segmentation process	39
2.2.4	Discretized domain	41
2.2.5	Limitations	41
2.3	Conclusion	42
3	Proposition of the Fluid-Structure Interaction Model	45
3.1	Fluid domain	45
3.1.1	Left ventricle in the mitral valve fluid-structure interaction studies	45
3.1.2	Tubular left ventricle	46
3.2	Fluid-structure interaction setup	47
3.2.1	Mitral valve inside a fitted tube	47
3.2.2	Mitral valve inside a large cylinder	47
3.3	Model configuration	48
3.3.1	Modeling self-contact of mitral valve leaflets	49
3.3.2	Annulus ring	54
3.3.3	Leaflets	55
3.3.4	Chordae	56
3.3.5	Blood	57
3.3.6	Assembly of the numerical domains	58
3.4	Conclusion	59

4	Capturing Contact in Fluid-Structure Interaction Simulation of Generic Mitral Valve	61
4.1	Replicating pathologies	61
4.2	Simulation setup	63
4.2.1	Isotropic constitutive model	63
4.2.2	Mesh independence study	64
4.2.3	Membrane blood leakage	65
4.3	Results and discussion	66
4.3.1	Deformed shape	67
4.3.2	Stress map	68
4.3.3	Streamlines	68
4.3.4	Cross-section	70
4.3.5	Flow rate	71
4.3.6	Contact map	72
4.4	Conclusion	74
5	Investigating the Influence of Anisotropy and Geometry	77
5.1	Material models	78
5.1.1	Anisotropic constitutive models	78
5.1.2	Planar biaxial tensile test	81
5.1.3	Fitting experimental data on the generalized Fung constitutive model	83
5.1.4	Obtaining the material parameters for the Holzapfel-Gasser-Ogden constitutive model	86
5.1.5	Isotropic model	90
5.2	Image-based geometry and case setup	92
5.3	Results and discussion	92
5.3.1	Influence of anisotropy	93
5.3.2	Influence of geometry and fluid volume	97
5.4	Conclusion	103
6	Microstructure of the Leaflets	107
6.1	Fiber models	107
6.1.1	Measurement-based and representation simplification	109
6.1.2	Fiber map based on physical computation	110
6.1.3	Expert observation and physiological traits	111
6.1.4	Random fiber model	114
6.2	Results and discussion	115

6.2.1	Closed state	115
6.2.2	Contact	115
6.2.3	Chordae forces	116
6.3	Conclusion	117
Conclusion		121
1	Contributions	121
1.1	Exploring various numerical frameworks for fluid-structure interaction simulation of mitral valve dynamic closure	121
1.2	Replicating mitral valve behavior in healthy and pathological cases	121
1.3	Investigating the influence of material model and case setup on both generic and image-based mitral valve geometries	122
1.4	Microstructure of the leaflet tissue	122
2	Future works	122
2.1	Evaluating the simulation results	122
2.2	Real-time simulation with application to the surgery room	123
2.3	Work toward more accurate material model	123
List of publications		125
A Résumé Étendu en Français		127
A.1	Exploration de divers cadres numériques pour la simulation d'interaction fluide-structure de la fermeture dynamique de la valve mitrale	128
A.2	Mesure du contact	129
A.3	Vers un modèle spécifique au patient	129
A.4	Influence de la géométrie et du volume de fluide	130
A.5	Investigation de différents modèles de matériaux	131
A.6	Travaux futurs	131
A.6.1	Évaluation des résultats de la simulation	131
A.6.2	Simulation en temps réel avec application à la salle d'opération	132
A.6.3	Vers un modèle de matériau plus précis	132
A.7	Structure de la thèse	133
Bibliography		135

List of Figures

1	(<i>a.</i>) Longitudinal ¹ , and (<i>b.</i>) transversal ² cross-section of heart.	1
2	(<i>a.</i>) MV anatomy ¹ (<i>b.</i>) flattened view of the dissected MV. The black line shows the approximate location of the annulus surrounding the MV [GQF ⁺ 17]	2
3	Ventricular pressure during the cardiac cycle [ANAW22]	2
4	(<i>a.</i>) Illustration of the MV cross-section in the closed state showing the concept of bulging and coaptation area. The red line represents the cross-section of the annulus plane. (<i>b.</i>) A healthy MV leaflet in the peak-systole forms a saddle-shaped [HGG05].	3
5	(<i>a.</i>) Cross section showing MV regurgitation caused by ruptured chordae [AMP17] (<i>b.</i>) Comparing the orifice of healthy MV with inflated MV with stenosis ¹ (<i>c.</i>) Illustration of MV with annulus calcification ²	4
6	(<i>a.</i>) Edge-to-edge repair [FMB08], (<i>b.</i>) Mitraclip installed on the catheter (left) and mounted on the MV (right) ¹ , (<i>c.</i>) Annuloplasty ring mounted on the MV [RZG ⁺ 17].	5
7	(<i>a.</i>) Widening the MV orifice: a deflated balloon is inserted in the MV with a catheter (left), then the balloon is inflated (right) ¹ . (<i>b.</i>) Top view of a prosthetic MV with two semi-circles as leaflets [SB09].	6
8	The process of obtaining MV geometry from medical imaging for FSI simulation [TJE ⁺ 16].	8
9	(<i>a.</i>) Transparent view of the case setup including both the fluid and structure domains, and (<i>b.</i>) cross-section of the structure domain with uniformly distributed force (arrows), replacing the fluid domain. The solid blue line illustrates the open state of the leaflets, while the dashed line signifies their anticipated closed state.	9
1.1	Left: cross-section of a simple fluid wave, middle: mesh-based numerical domain, right: particle-based numerical domain ¹	18
1.2	(<i>a.</i>) Lagrangian mesh, (<i>b.</i>) Eulerian mesh [SDKT23]	19
1.3	Cross-section of a ALE (<i>a.</i>) and IB (<i>b.</i>) mesh representation of MV leaflet inside fluid control volume	19
1.4	In ALE approach, when deformation occurs, depending on the severity of the distortion, the numerical domain is re-meshed [AABS21].	20

1.5	(<i>a.</i>) Cross-section of two leaflets (shown in black) and the porous medium in between shown as a gray region [BRI ⁺ 16]. (<i>b.</i>) Cross-section of two leaflets shown in green having actual contact in IB mesh representation. (<i>c.</i>) Cross-section of MV leaflets with spurious flow (the colors show the fluid velocity) [KMP19].	21
1.6	Distribution of volume fraction in an Eulerian domain with square control volume [LJ18].	24
1.7	The flux of fluid material is calculated in two steps. The Eulerian domain remains fixed at the end of each cycle. [Skr12]	24
1.8	Result of FSI simulation from [CWG ⁺ 19], showing flow rate through cardiac cycle. Once the valve is at peak systole, the flow rate drop to zero while orifice holes are visible in the peak systole.	29
1.9	(<i>a.</i>) Illustration of a discretized domain of master and slave surfaces [Man12]. (<i>b.</i>) Slave node penetrating the master surface.	30
2.1	Orthographic views of the generic MV used for our simulation purposes. (<i>a.</i>) Top, (<i>b.</i>) 3D, (<i>c.</i>) front, (<i>d.</i>) and right side view [Ham11].	35
2.2	The process of creating the generic valve. (<i>a.</i>) The intersection between the cone and the cylinder creates the annulus ring. (<i>b.</i>) The leaflets are extracted from the body of the cone after its intersection with four semi-cylinders.	35
2.3	(<i>a.</i>) The discretized numerical domain of the MV geometry, (<i>b.</i>) C3D10, (<i>c.</i>) and C3D4 tetrahedral element ¹	36
2.4	CT scan images of porcine heart MV in the (<i>a.</i>) open and (<i>b.</i>) closed state [Ham11]. (<i>c.</i>) The extracted geometry after segmentation with the chordae structure (shown in red) and the leaflets (shown in green) in the open state.	38
2.5	Three image-based MV geometry manually segmented in the opened state [Ham11]: P-1 (<i>a.</i>), P-2 (<i>b.</i>), and P-3 (<i>c.</i>)	39
2.6	(<i>a.</i>) An image-based geometry segmented in the closed state [Pan21]. (<i>b.</i>) P-4: Opening the segmented geometry with fluid passing from the left atrium to the left ventricle.	40
2.7	Image-based P-1 valve before (<i>a.</i>) and after (<i>b.</i>) applying the smoothing filter.	41
3.1	A simplified illustration showing the LV geometry extracted from medical images (<i>a.</i>), simplified ventricle shape, or U-shape (<i>b.</i>), and two different representations of the tubular volume (<i>c.</i>) and (<i>d.</i>). During the closure, fluid inlets are in green, and fluid outlets are in red.	46
3.2	Case set-up showing the P-1 image-based (left) and generic (right) MV mounted in a generalized and elliptic base fitted tube.	48
3.3	Case setup for (<i>a.</i>) fitted tube, and (<i>b.</i>) large cylinder. Orange: valve, red: chordae, blue: additional geometry to obstruct the flow, and light green: pinned annulus region.	48
3.4	Simplified trajectory of a hypothetical slave node in contact interacting with multiple facets and able to separate from the master surface [Man12].	50
3.5	2D illustration of a hypothetical bin in a global search [Man12].	50

3.6	Local search finding the newly tracked master surface node as the slave surface is displaced [Man12].	51
3.7	Numerical representation of two surface in contact [RMK14].	52
3.8	(a.) Hard contact force overclosure. As the distance between the slave node and the master surface reaches zero, any possible contact force will be applied on the node to keep it clear from penetrating the surface. (b.) Penalty constraint enforcement with exponential formulation [Man12].	53
3.9	Sphere of influence for chordae endpoints: The chordae are depicted in red, while the connections between the chordae endpoint and the leaflet nodes are illustrated in yellow. The dark lines represent a transparent view of the tetrahedral elements.	57
3.10	(a.) FSI discretized domain in case of generic MV. For better visibility, only the cross-section of the fluid domain is shown. (b.) Cross-section of the blood volume fraction: The blue region shows the presence of blood in fluid elements and the red region is considered as void.	58
4.1	(a.) Cross-section view of the MV showing the approximate position of each chordae category [CAF10]. (b.) Different chordae categories are shown on dissected MV [TBP ⁺ 17].	62
4.2	Removed chordae highlighted in red in case of (a.) regurgitation, and (b.) prolapse.	62
4.3	Experimental measurements of the MV posterior leaflet from [MNY95] and mechanical response of the third-order Ogden material model with the fitted parameters.	64
4.4	Blood leakage after closure in four different mesh resolutions.	66
4.5	Closed state of the generic MV in case of (a.) no chordae attached, (b.) leakage, (c.) bulging, and (d.) healthy.	67
4.6	Stress distribution of leaflets with (a.) leakage, (b.) bulging, and (c.) perfect closure.	68
4.7	Stress pattern and magnitude reported in the literature: [CMMS20] (a.) and [CWG ⁺ 19] (b.).	69
4.8	(a.) illustrates the volume of fluid in the open state, and (b) depicts the volume of fluid when the MV is closed. Blue regions indicate the areas occupied by fluid, whereas red regions represent areas that are void of fluid.	69
4.9	Streamlines over MV with (a.) no chordae attached, (b.) leakage, (c.) bulging, and (d.) healthy.	70
4.10	Mid-leaflet cross-section of MV in case of leakage (blue), bulging (green), and healthy (red).	71
4.11	Flow rate in case of leakage (blue), bulging (green), and healthy (red).	72
4.12	Obtaining contact map: (a.) One of the leaflets in contact, (b.) cloud of points in contact, and (c.) projection on a cylinder.	73
4.13	Obtaining contact map: (a.) Flat representation of the cloud of points in contact, (b.) flat representation of the leaflets with triangular mesh, and (c.) final result of contact map (for the case of healthy MV).	74
4.14	Contact map: Healthy (a.), leakage (b.), and bulging (c.).	75

5.1	Planar annulus surface: a flat plane with a minimum distance to the nodes on the annulus ring (a.). Fibers specified parallel to the circumferential direction of the MV leaflet. For better visualization, only the anterior leaflet is shown (b.).	82
5.2	Biaxial tensile test: (a.) specimen preparation, (b.) test setup, and (c.) data analysis.	83
5.3	Mechanical response of the heart myocardium tissue: (a.) Stress-strain data in 1 : 1 and 1 : 3 measurement protocol, (b.) Shear tension in 1 : 3 measurement protocol [Sac99].	85
5.4	Illustration of the grid search, show the isocontour of residuals for C_{10} and K_1 by fixing the K_2 and κ	89
5.5	Flowchart showing the process of obtaining the material parameters in MCalibration.	90
5.6	The result of the inverse finite element analysis procedure: Showing the mechanical response of the HGO model with the optimized parameters (dashed lines) compared to the input data (solid lines) [JLK ⁺ 18b].	91
5.7	Comparison of the HGO mechanical response in case of $\kappa = 1/3$, which results in planar isotropic characteristics, against the stress-strain data (solid lines) reported in [JLK ⁺ 18b].	91
5.8	P-1 (a.), P-2 (b.), and P-4 (c.) inside a large tube. Orange: valve, red: chordae, blue: additional geometry to obstruct the flow, and light green: pinned annulus region. (d.) shows the P-1 inside a fitted tube.	93
5.9	Top row: bulging on the generic valve with (a.) isotropic and (b.) anisotropic constitutive model. Bottom row: bulging on the image-based valve with (a.) isotropic and (b.) anisotropic constitutive model.	94
5.10	Chordae force distribution on ex-vivo data from [PIMW ⁺ 20] (a.), simulation with isotropic (b.), and anisotropic (c.) constitutive model.	95
5.11	Contact map with isotropic (a.) and anisotropic constitutive model (b.).	96
5.12	Cumulative distribution function (CDF) of the contact pressure in both isotropic and anisotropic constitutive models.	97
5.13	Flow rate in both isotropic and anisotropic constitutive models.	98
5.14	Bulging on the (a.) P-1 with fitted tube and anisotropic model and (b.) smoothed P-1 with the fitted tube and anisotropic model.	99
5.15	Contact maps for the P-1 valve with the fitted tube setup and anisotropic model (a.), the smoothed P-1 valve with the fitted tube setup and anisotropic model (b.), and the smoothed P-1 valve with the large cylinder setup and anisotropic model (c.).	100
5.16	Cumulative distribution function (CDF) of the contact pressure with anisotropic model.	101
5.17	Flow rate shown for P-1 in the fitted tube, smoothed P-1 in the fitted tube, smoothed P-1 in the large cylinder. All cases are with the anisotropic model.	101
5.18	Top view of the stress distribution in case of P-1 with fitted-tube and anisotropic model (a.) and P-1 with large cylinder and anisotropic model (b.).	102
5.19	Bulging on the (a.) smoothed P-1 with the fitted tube and anisotropic model, (b.) and smoothed P-1 with the large cylinder and anisotropic model.	102

5.20	Top view of the stress distribution: (a.) in case of P-2 with the fitted tube and anisotropic model, (b.) in case of P-3 with the fitted tube and anisotropic model, and (b.) in case of P-4 with the fitted tube and anisotropic model.	103
5.21	Top view of the stress distribution: (a.) in case of P-2 with large cylinder and anisotropic model, and (b.) in case of P-4 with large cylinder and anisotropic model.	104
5.22	Bulging on the (a.) P-2 with the large cylinder and anisotropic model, and (b.) P-4 with large cylinder and anisotropic model.	104
6.1	The anisotropy rate changes depending on the region where the specimen is obtained. Data reported in [LRJ ⁺ 19].	108
6.2	Left: MV anterior leaflet. Middle: the small-angle light scattering data. Right: magnified view of the fiber orientations near the chordae insertion point [PSL ⁺ 10].	109
6.3	Map of fibers for MV anterior leaflet obtained based on PLD data [CKC ⁺ 91]. . .	110
6.4	Fiber map based on maximum principal stress direction (a.), affine model (b.), and the chordae structure (c.).	112
6.5	An example of expert observation of MV leaflet tissue. A hypothesis is that the presence of fibers within the leaflet tissue can be detected through the crease lines that these bundles of fibers leave on the tissue surface.	113
6.6	Expert-based fibers: Fibers following the trail defined based on numerous observations of MV leaflet microstructure.	113
6.7	Distribution of the logarithmic strain over the leaflet tissue at the peak systole in case of fiber models based on: Parallel to the annulus (a), expert-based (b), random distribution (c), stress-based (d), affine model (e), and chordae-based (f).	116
6.8	Bulging volume at the peak systole in case of fiber models based on: Parallel to the annulus (a), expert-based (b), random distribution (c), stress-based (d), affine model (e), and chordae-based (f). The red region shows the bulging volume where the valve stretches over the annulus surface.	117
6.9	Contact map showing the coaptation area and the contact pressure in case of fiber models based on: Parallel to the annulus (a), expert-based (b), random distribution (c), stress-based (d), affine model (e), and chordae-based (f).	118
6.10	Cumulative distribution function (CDF) of the contact pressure in various fiber models.	118
6.11	The chordae force during the dynamic closure of the MV in case of fiber models based on: Parallel to the annulus (a), expert-based (b), random distribution (c), stress-based (d), affine model (e), and chordae-based (f).. The figure at the bottom shows the ex vivo measurement of the chordae force during the cardiac cycle reported in [PIMW ⁺ 20].	119

List of Figures

List of Tables

2.1	Summary of the data we used for our study of MV simulation.	40
3.1	Influence of distortion control on MV leaflet node displacement with two different distortion thresholds.	56
4.1	Material parameters for the 3rd-order Ogden hyperelastic material model, derived from experimental data reported in [MNY95].	64
4.2	Comparison of stress and strain between leaflet mesh with $20k$ and $80k$ elements.	65
4.3	Average blood leakage in four different fluid mesh sizes.	66
5.1	Upper and lower bounds and an example of initial value for the direct optimization of the strain energy function.	89
5.2	Material parameters for the HGO model, derived from experimental data reported in [JLK ⁺ 18b].	90
5.3	Material parameters for the 3rd-order Ogden hyperelastic material model, derived from experimental data reported in [JLK ⁺ 18b].	92
5.4	Number of elements used in the simulation of P-2 and P-4 with the case setup of large cylinder.	103

Acronyms

- ALE** Arbitrary Lagrangian-Eulerian. 18
- CT** Computed Tomography. 8
- FSI** Fluid-Structure Interaction. 8
- HGO** Holzapfel-Gasser-Ogden. 77
- IB** Immersed Boundary. 17
- LV** Left Ventricle. 1
- MV** Mitral Valve. 1
- SPH** Smoothed-Particle Hydrodynamics. 18

Introduction

1 Clinical context

In this section, we will explore the Mitral valve (MV) anatomy, its intricate functioning in both healthy and pathological conditions, and surgical treatments commonly available for addressing MV pathologies.

1.1 Mitral valve anatomy

The MV is one of the four valves of the heart located between the left atrium and the left ventricle (LV), as illustrated in Fig.1. It comprises two primary leaflets, the anterior and posterior leaflets, which are encompassed by the annulus ring. Additionally, the surface of the leaflet tissue and its free edge is connected to the papillary muscle at the base of the left ventricle (LV) through a set of chordae structures. These chordae tendineae act as a tether, holding the MV leaflets in place during the cardiac cycle, and preventing them from inverting into the left atrium. A sketch of MV anatomy is shown in Fig.2.a and a flattened view of dissected MV is shown in Fig.2.b.

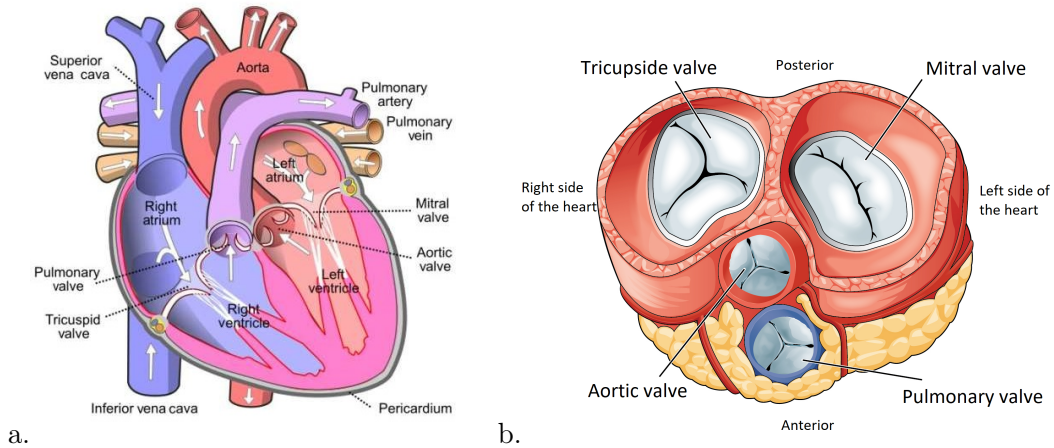


Figure 1: (a.) Longitudinal¹, and (b.) transversal² cross-section of heart.

The MV opens and closes in response to changes in ventricular pressure throughout the cardiac cycle (see Fig.3). The pressure difference within the cardiac cycle arises from the dynamic changes in ventricle volume as the heart muscles contract and expand. During the diastolic

¹[https://commons.wikimedia.org/wiki/File:Diagram_of_the_human_heart_\(cropped\).svg](https://commons.wikimedia.org/wiki/File:Diagram_of_the_human_heart_(cropped).svg)

²https://commons.wikimedia.org/wiki/File:2011_Heart_Valves_es.png

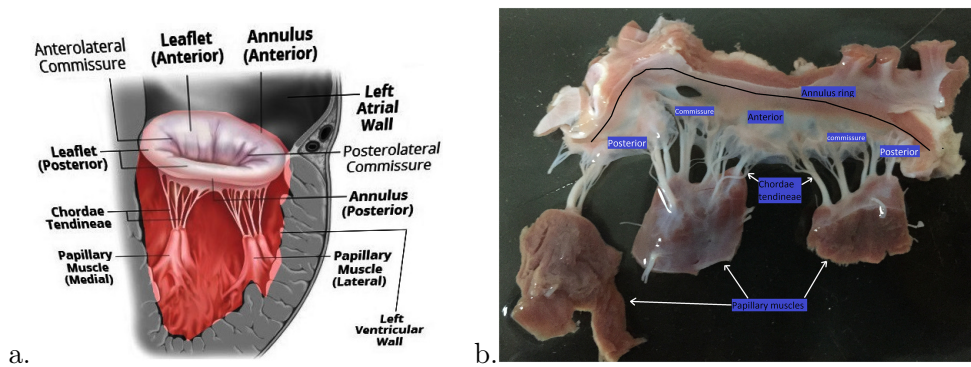


Figure 2: (a.) MV anatomy¹ (b.) flattened view of the dissected MV. The black line shows the approximate location of the annulus surrounding the MV [GQF⁺17]

phase, MV is opened, which allows the oxygenated blood from the lungs to enter the LV and fill it with blood. In the systolic phase, the heart muscles contract, and the blood is pressurized and propelled out of the ventricle from the aortic valve. This mechanism effectively employs the MV, akin to a parachute, to ensure that oxygenated blood does not flow back into the lungs.

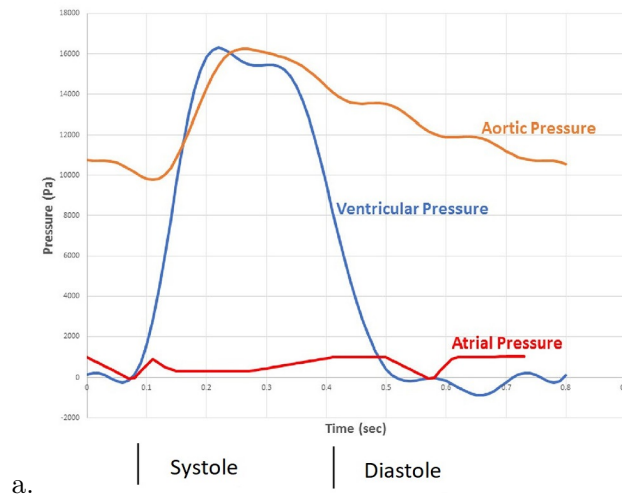


Figure 3: Ventricular pressure during the cardiac cycle [ANAW22]

1.2 Healthy and pathological mitral valve

Healthy mitral valve function

The main purpose of the MV is to provide a one-way passage for the blood in an efficient way. A healthy MV should function as described below [CAF10]:

- Closure with no leakage: Proper sealing of the MV during peak systole is essential to prevent the backflow of blood into the lungs, ensuring efficiency in the cardiac cycle and preventing problems such as shortness of breath in patients.

¹<https://www.ncbi.nlm.nih.gov/books/NBK549884/figure/article-37651.image.f2/>

- **Leaflet elasticity:** Various factors, including aging, smoking, and calcification (the accumulation of calcium from the bloodstream on the leaflets through time), influence the elasticity of the MV leaflets [PS14]. It is crucial for the leaflets to maintain sufficient elasticity to ensure unimpeded blood flow, without the movement of the leaflets acting as a barrier.
- **Proper coaptation length:** In the peak systole, the area where the two leaflets meet is considered as the coaptation area which is shown in Fig.4.a. The shape and size of this area play an important role in determining the quality of MV closure. Coaptation length is the term used to describe the length of the cross-section of the coaptation area. The coaptation length can be observed in medical imaging and used to assess and ensure the appropriate sealing of the MV. Based on the experimental data reported in [GDD⁺10], in the case of healthy MV functioning, depending on the cross-section of the measurement, the coaptation length can reach up to 5mm.
- **Closed state:** According to Hayek et al. [HGG05], during peak systole, a healthy MV assumes a saddle-shaped position (see Fig.4.b). This positioning results in the leaflets being situated below the annulus surface. By adopting this configuration, the unnecessary loads and strain on the leaflets are reduced, allowing the MV to function efficiently. When the leaflets overpass the annulus ring, the volume above creates a bulging volume which is a sign of a diseased valve (see Fig.4.a).

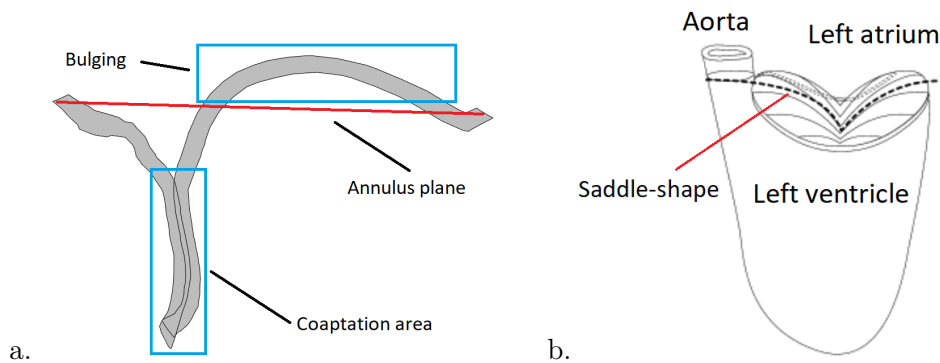


Figure 4: (a.) Illustration of the MV cross-section in the closed state showing the concept of bulging and coaptation area. The red line represents the cross-section of the annulus plane. (b.) A healthy MV leaflet in the peak-systole forms a saddle-shaped [HGG05].

Mitral valve dynamic dysfunction

Similar to other biological tissues and organs in the body, the MV is also susceptible to pathologies. In this context, the pathologies that are specifically associated with the dynamic dysfunction of the MV are presented as follows:

Mitral valve regurgitation: Multiple factors, including defects in the chordae structure or dilated annulus ring, can influence the MV closure. As a consequence, regurgitation occurs, characterized by incomplete sealing and the presence of orifice holes at the peak systole. MV

regurgitation is the second most common heart disease worldwide that undergoes surgical treatment. To gain a deeper understanding of this pathology, it is crucial to examine the dynamics of leaflet collision and identify the factors that impact the contact between the leaflets. Exploring the mechanisms behind how the two leaflets interact with each other provides valuable insights into a better understanding of MV regurgitation. An illustration of MV regurgitation caused by ruptured chordae is shown in Fig.5.a.

Mitral valve prolapse: MV prolapse is characterized by the abnormal positioning of one or both leaflets during the peak systole, resulting in the bulging of the leaflets into the left atrium or an uneven coaptation between the leaflets. Measuring the MV bulging volume is a qualitative measurement that can show the amount of prolapse in the MV. In Fig.4.a, leaflet bulging above the annulus plane accounts for MV prolapse. As the issue with the coaptation area worsens, the orifice holes appear, leading to the occurrence of blood leakage. In such cases, this condition is classified as MV regurgitation.

Mitral valve stenosis: MV stenosis is a group of abnormalities (fibrous thickening, calcific deposits) in the MV anatomy [WHF94], mostly caused by inflammatory conditions, the valve opening is narrowed, restricting blood flow from the left atrium to the LV. In Fig.5.b an example of MV with stenosis compared to a healthy MV is shown.

Mitral annulus calcification: Mitral annulus calcification is a chronic process in which calcium in the bloodstream is sedimented and build up on the valve's annulus, which can cause the MV to become rigid and interfere with its function (see Fig.5.c). In some cases, Mitral annulus calcification can lead to MV regurgitation or MV stenosis.

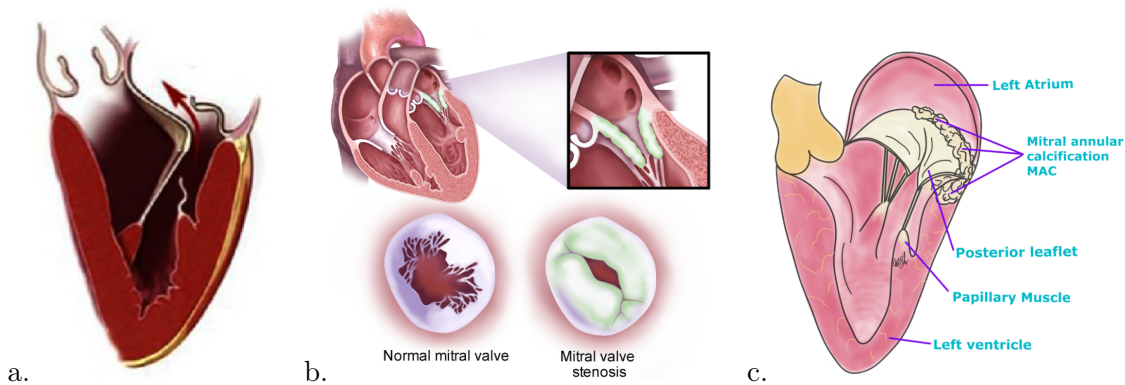


Figure 5: (a.) Cross section showing MV regurgitation caused by ruptured chordae [AMP17] (b.) Comparing the orifice of healthy MV with inflated MV with stenosis¹ (c.) Illustration of MV with annulus calcification².

1.3 Surgical intervention

Surgical intervention offers a viable solution for addressing the aforementioned pathologies. In this context, we will explore the most common treatments available for addressing MV dynamic dysfunctions.

¹https://medmovie.com/library_id/3255/topic/ahaw_0164i/

²<https://www.mitraltherapies.com/mac>

To restore proper valve function, address MV bulging, and achieve a sealed closure during the peak systole, surgical techniques involve reshaping and repairing the MV by manipulating specific parts of its geometry. This may include removing or stitching certain parts of the leaflets to obtain the desired geometry, as well as reshaping the chordae structure and annulus ring by incorporating additional components [CAF10]. Depending on the severity of the pathology, MV replacement is also practiced. To gain a better understanding of the available surgical interventions, here, the most common approaches are mentioned.

Edge-to-edge repair

In this approach, two leaflets are stitched together in a single point to restore the proper function of the MV (see Fig.6.a). Surgeons commonly adopt this approach when conventional reparative techniques, such as valve resection (trimming damaged portions of the MV), patching the leaflets, and resuturing torn edges, are unlikely to result in positive outcomes. A specific form of edge-to-edge repair involves the utilization of a small metal clip called MitraClip to connect two leaflets (see Fig.6.b). The MitraClip is deployed on the MV through a minimally invasive procedure using a catheter inserted through a small incision.

Annuloplasty

Another method for repairing the MV involves manipulating the shape of the annulus ring through the use of rigid or flexible rings. These rings are placed around the annulus to resize the MV, aiming to restore its normal geometry and function. In Fig.6.c, annuloplasty ring mounted on MV is shown.

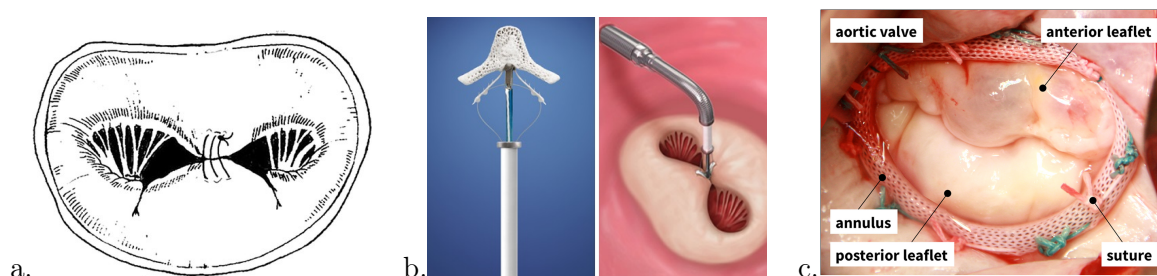


Figure 6: (a.) Edge-to-edge repair [FMB08], (b.) Mitraclip installed on the catheter (left) and mounted on the MV (right)¹, (c.) Annuloplasty ring mounted on the MV [RZG⁺17].

Balloon valvuloplasty

In cases of MV stenosis, a minimally invasive procedure called balloon valvuloplasty is performed to widen the narrowed MV orifice. This procedure involves inserting a deflated balloon into the MV area using a catheter and then inflating it to treat the narrow opening. Once the MV is appropriately stretched, the balloon is carefully extracted, completing the procedure (see Fig.7.a). This catheter-based approach offers a less invasive alternative, and the patient benefits from quicker recovery and reduced postoperative complications.

¹<https://www.ottawaheart.ca/fr/document/mitraclip-guide-%C3%A0-lintention-des-patients>

Mitral valve replacement

In severe cases, the MV can be replaced with a mechanical prosthetic valve or a biological valve. The prosthetic valve is usually made of metal or ceramic. The prosthetic valve usually consists of two semi-circles that are able to rotate or three leaflets that open and close in response to the pressure difference during the cardiac cycle. An example of mechanical prosthetic MV is shown in Fig.7.b. The artificial nature of the implemented valve necessitates the patient's use of anticoagulation medication to prevent strokes caused by blood clot obstruction. On the other hand, the biological valve is made from animal or human tissue are less prone to blood clots. However, the lifespan of the biological valve is shorter than the one made from a prosthetic.

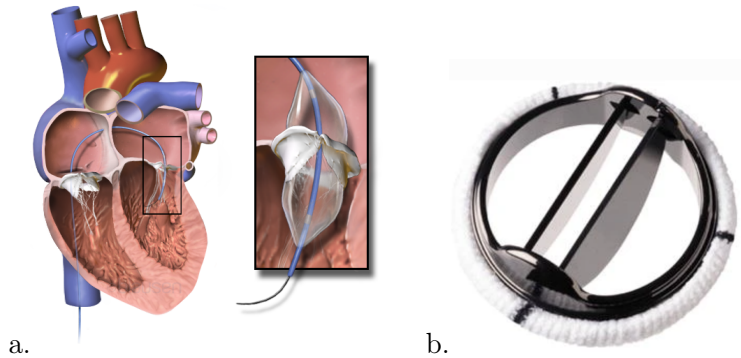


Figure 7: (a.) Widening the MV orifice: a deflated balloon is inserted in the MV with a catheter (left), then the balloon is inflated (right)¹. (b.) Top view of a prosthetic MV with two semi-circles as leaflets [SB09].

In the following section, the possibility of employing numerical simulation as a tool that can potentially improve the outcome of the MV treatments is discussed.

2 Numerical simulation

Decisions concerning modifications to the MV structure rely on the expertise of medical professionals, while the overall success of the procedure is significantly influenced by their experience. One approach to improve the overall surgical outcome is employing computational tools to simulate the MV behavior. Based on input data from medical imaging and experimental tests on biological tissues, these computational tools can anticipate the expected outcome of the procedure and provide valuable information that can be utilized in different ways to support medical professionals and enhance the chances of a successful outcome.

2.1 Applications

Numerical tools can help in a number of ways, from scientific understanding to clinical planning. In order to have a model that can be used for the operating room, computation time compatible with the clinical gesture is required. Numerical simulations are time-consuming and usually, reducing the computation time comes with simplifications such as not considering the influence

¹https://commons.wikimedia.org/wiki/File:Blausen_0889_MitralValvuloplasty.png

of blood motion in the simulation and reducing the accuracy of the results [LDSB10, TBP⁺17]. Some studies are focused on using fast computing numerical approaches, such as excluding the effects of fluid motion in simulations, with the goal of reducing their computation cost and employing them in the operating room [HPH11, VHP⁺18].

In the literature, various studies [LDSB10, RFS⁺13, CWG⁺19, BRI⁺16, FQG⁺18, LDSB10, RFS⁺13, KMP19] aim to understand the behavior of biological tissues under various conditions by using simplified setup and geometries. The insights derived from the simulation results are primarily utilized for educational purposes and to enhance scientific comprehension. For example, in [XJW⁺21], they used generic geometry, a simplified representation that captures the main features and characteristics of MV without detailing individual-specific variations, to observe how replacing the MV with bioprostheses influences the overall ventricular hemodynamics. The purpose of the study was to provide more understanding of cardiac mechanics by using numerical simulation. In [MVV19], the focus was on investigating the impact of MV stenosis on ventricular flow alteration. Specifically, the research examines four different stages of MV stenosis severity to assess their influence on ventricular flow patterns.

In the case of surgical planning, numerical simulation can be used to replicate the MV behavior in various conditions, or predict the outcome of the surgery in different scenarios and choose the most suitable approach [Ham11, MCM⁺17, CMM⁺18, BGG⁺19, TBE⁺16, CMMS20, SOV⁺15, MGG⁺13]. The level of details included in these studies are relatively higher than the fast simulations intended for real-time application, and the computation time is in the scale of hours. In [DYS⁺19], the impact of various variables, including the number of implemented MitraClip devices and their positioning, on tricuspid valve regurgitation, is investigated. Additionally, the study explores how these variables affect the distribution of force exerted on the valve leaflets. The performance of novel designs for artificial parts to be implemented in the heart can also be predicted with the help of numerical simulation. In [BCL⁺15], they employ computational modeling to evaluate the performance of their recently developed annuloplasty ring. The authors emphasize that their approach enables the possibility of testing various innovative annuloplasty rings, thereby enhancing surgical outcomes through preoperative optimization.

Generic geometries are practical tools for scientific understanding, however, the diverse geometry and material characteristics observed in each patient necessitate the use of a model that can effectively handle diverse input data and accurately replicate the specific behavior of each patient. In the following, such models are described more in detail.

2.2 Patient-specific model

A patient-specific model refers to a numerical simulation that is based on individual patient data and is capable of realistically capturing the MV behavior. Such a model aims to replicate the unique characteristics and mechanics of the MV for a specific patient. A functional patient-specific model should be able to accept any image-based geometry. While many studies in the literature utilize patient data and incorporate the necessary physical aspects for realistic MV simulations, these studies are only demonstrated on one single input data and do not show the adaptability aspect of the patient-specific model. Examples of such studies are [TBP⁺17, TBE⁺16, TJE⁺16] by Toma et al, or [FQG⁺18, FGG⁺19, FGQ⁺21] by Feng et al.

The patient-specific model will provide valuable information that can be directly utilized for

surgical planning. The primary goal is to obtain an accurate simulation that can be done for any patient geometry and material. Then, simulation results can give insights into the overall dynamic behavior of the MV during the closure. The numerical simulation for the patient-specific model is acquired through the following procedure:

Obtaining the patient data

Acquiring the required input data is the initial stage of numerical simulation. This data encompasses the geometry, physiological boundary conditions, initial state, and material data. The MV geometry, consisting of the leaflets and chordae structure, is acquired using medical imaging techniques. Ultrasound imaging and magnetic resonance imaging (also known as MRI) enable the observation of MV in motion [SMC⁺11, GFQ⁺17, BGG⁺19, MGG⁺13, DVD⁺12], while computed tomography (CT) scan and micro CT scan allow for static visualization of the MV [CMMS20, TJE⁺16, TBP⁺17, RT23, OÖB⁺21].

For studies primarily seeking a scientific understanding, the simulation often relies on a simplified or generic MV geometry as in [LDSB10, GMQ⁺14, KMP19, AEHE19, AAAB⁺22, ESH14, LDZSB11, WS13]. Conversely, when the focus of the study shifts toward surgical planning and patient-specific models, researchers tend to utilize image-based simulations [KSE⁺23, BVG⁺23, MCM⁺17, FQG⁺18, TBP⁺17, BGG⁺19, CMMS20]. For example, in [TJE⁺16], they utilized CT scan imaging to examine a porcine MV in an in vitro setting. Following this, they performed segmentation and image processing, which allowed them to extract the MV geometry as a solid mesh. They used this geometry to implement in their fluid-structure interaction FSI model. By conducting FSI simulations, they conducted the FSI simulation to measure the chordae forces during the cardiac cycle. Fig.8 illustrates the process of obtaining geometry from medical imaging.

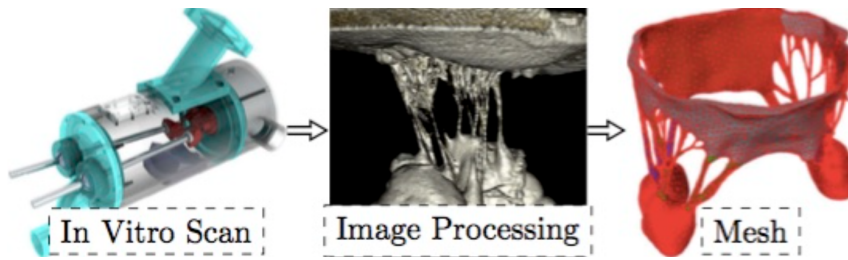


Figure 8: The process of obtaining MV geometry from medical imaging for FSI simulation [TJE⁺16].

The initial state and boundary conditions for the case setup are derived from physiological measurements of the heart available in the literature. These measures are usually constant across all the patients and the values are taken from the measurements reported in the literature. For example, the time-varying transvalvular pressure (see Fig.3), obtained from actual measurements of the human heart, can be incorporated into the MV simulation as mentioned in [Lev13]. Additionally, crucial data related to the material characteristics of the MV tissue is necessary for the simulation. This includes essential information on the mechanical response of the chordae and leaflets, such as stress-strain measurements [JLK⁺18a, PSSH10, PS14, JLK⁺18b], and the mi-

crostructure of the leaflet [DCBB08, Lau12, DCBB08, LZL⁺15]. Furthermore, it is important to define blood characteristics, such as fluid viscosity and density, before initiating the simulation. However, the information regarding the blood characteristics is mostly uniform across various patients, and utilizing the reported data in the literature can be sufficient.

Simulation

The dynamic motion of the MV involves two distinct physical states: the fluid phase represented by blood flow and the solid phase represented by the chordae and leaflets. For example, a cross-section of both these domains in a scenario where MV leaflets and chordae structure are mounted in a tube filled with blood is shown in Fig.9.a. The red lines show the streamlines of the blood flow passing over the leaflets. The principles of fluid dynamics are applied to model the dynamic motion of the blood flow, while structural analysis techniques are utilized to model the motion of the MV itself.

The dynamic motion of the MV is complex and no analytical solution is available, instead, a numerical simulation is performed. The type of numerical simulation influences the accuracy of the results, limits the possibility of obtaining certain information from the simulation outcome, and influences the computation time. In some studies like [Ham11, VHP⁺18, WS13, PSSH10, PVHB19], the fluid motion is simplified as a uniformly distributed force on MV leaflets, and only the solid phase is involved in the model which is simulated with the principles of structural analysis. The numerical domain in this case involves only the MV structure as shown in Fig.9.b. The studies based on structural analysis rely on fast computation time to focus on providing a tool that can be used in close to real-time. Since the speed is achieved by omitting the fluid domain in the simulation, the accuracy of the results is influenced and the ability to obtain certain outcomes such as blood flow rate is restricted.

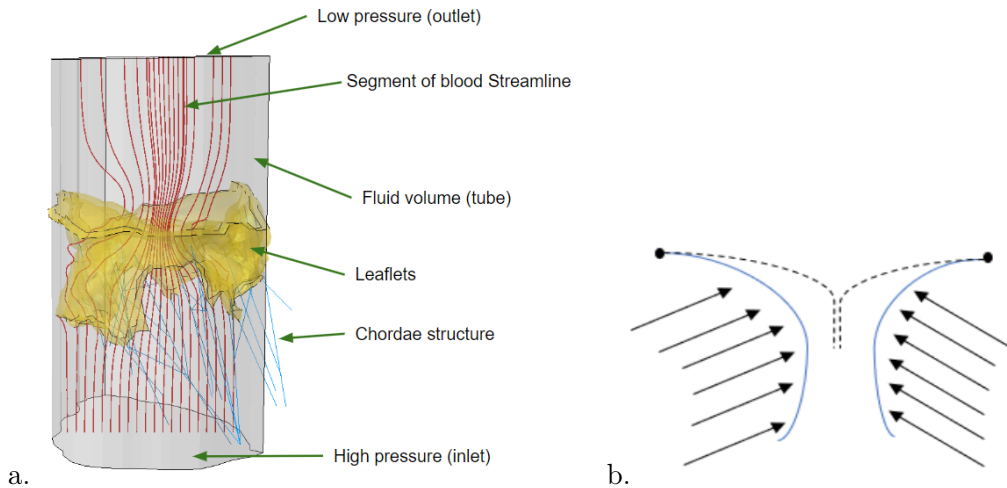


Figure 9: (a.) Transparent view of the case setup including both the fluid and structure domains, and (b.) cross-section of the structure domain with uniformly distributed force (arrows), replacing the fluid domain. The solid blue line illustrates the open state of the leaflets, while the dashed line signifies their anticipated closed state.

The fluid motion exerts complex force distribution on the leaflets and it is necessary to include the fluid motion in the simulation to have an accurate MV dynamic closure. Notably, studies by [LDSB10] and [TBP⁺17] have specifically compared MV behavior results from structural analysis to those from FSI simulations. Their findings suggest that including the influence of the fluid as FSI simulation is important in accurately capturing the dynamic motion of the MV. The FSI model used for MV simulation must adequately manage the MV complex motion, large deformation, and self-contact between leaflets.

Extracting results

After the simulation, basic information such as the MV deformation, stress, and strain distribution over the leaflets are available to analyze. To extract more valuable information tailored specifically for analyzing MV dynamic motion, the simulation data needs further post-processing. Various useful information can be extracted from the simulation results including, stress and strain distribution over the leaflets, tension forces acting on each chordae attachment (which eventually lead to identifying the tethering or slacking chordae), and the flow rate passing through the MV orifice during the MV closure. We also presented a novel method for evaluating MV closure quality, the contact map. This metric measures bulging volume, contact pressure, and coaptation area during peak systole. These additional metrics serve as valuable tools for comparing the functioning of the healthy MV in its normal physiological state.

3 Challenges in mitral valve simulation

In this section, we explore some of the main limitations and challenges in MV simulation.

3.1 Objective

The primary objective of MV simulation is to develop a practical tool that can be applied in a clinical setting. The majority of MV studies in existing literature typically focus on establishing patient-specific models, replicating pathologies, or addressing technical aspects within the numerical approach used for the MV simulation. In the following, the current challenges of these studies are mentioned.

Patient-specific model

Several studies have attempted to incorporate MV geometry from medical imaging to numerical simulation [TEBI⁺20, CMMS20, RT23, TBP⁺17]. In [DKS18], they developed a pipeline from micro CT to structural analysis to investigate the fully loaded and unloaded state of the MV. Their approach is capable of successfully extracting the fine geometric details of the MV, but their approach relies on a simplified structural model and does not account for fluid motion, thereby limiting its application as a patient-specific model. Another study [BGG⁺19], demonstrates a workflow that integrates FSI into their patient-specific model. The approach involves extracting patient data using cardiac magnetic resonance imaging and ultrasound and conducting FSI simulations. While this model successfully replicated the case of MV regurgitation based on the patient data, it also has certain limitations. These include the use of a simplified linear

elastic material model for the leaflets, a generic chordae structure, and a high computation time requirement.

Replicating pathologies

The FSI simulation of chordae rupture is presented in [TBP⁺17]. They used micro CT imaging to extract the accurate chordae structure for the first time. The influence of chordae rupture is also studied in [CMM⁺18]. They adopt a more complex image-based LV, resulting in a simulation setup that closely resembles the conditions of the human heart. However, this increased complexity also poses challenges. Specifically, when trying to integrate data from different patients into the model, difficulties arise in implementing and capturing the intricate geometry of both the LV and the MV. One instance of this complexity is seen in the LV shape, which undergoes significant changes throughout the cardiac cycle. To effectively integrate image-based MV and LV into the FSI simulation, it is essential to extract both the MV geometry (including segmentation of leaflet and chordae structure) and the temporal data of the LV from the same patient, which needs a great effort to obtain.

It should be noted that both studies highlight the computational expense associated with their numerical models. In [AAAB⁺22], the MV dynamic motion in the case of healthy and prolapsed leaflets is simulated. While the FSI simulation results presented in this study include deformable LV geometry and detailed blood flow patterns, it is important to note that the numerical models used lack the ability to provide detailed information regarding some crucial characteristics of MV dynamic closure. Factors such as coaptation area, contact force, and the assurance of proper valve sealing are not adequately addressed in their model.

Technical aspects of mitral valve modeling

Some studies focused on investigating the influence of different approaches to modeling MV behavior. The aim is to improve some aspects of the numerical simulation that can be beneficial for studying MV behavior in future works. In [WS13], the influence of using an image-based chordae structure compared to a generic one is investigated. Other studies such as [BRI⁺16, LDSB10, TBP⁺17], are more focused on comparing the accuracy and performance of different numerical techniques in the simulation of MV. In the next section, we offer a more in-depth discussion of the technical challenges and limitations inherent in MV simulations.

3.2 Limitations

A patient-specific model should be practical, meaning capable of handling diverse input data with inherent challenges like noise and segmentation errors, while also having the ability to simulate realistic behavior. Although researchers in the field are actively pursuing this goal [LSP⁺23, BGG⁺19, WS13], a model with these capabilities is currently lacking in the existing literature. Here, we will briefly examine the key limitations of the numerical simulation of MV, shedding light on the need for an advanced patient-specific model.

Data acquisition

Due to the thin tissue and dynamic structure of MV, acquiring precise temporal data poses a challenge, and extracting geometric information from medical imaging data is complex. Observing the MV in motion through manual segmentation of images from ultrasound or magnetic resonance imaging is somewhat less complicated than obtaining the chordae structure. This is because the resolution often is not high enough to fully capture the intricate details of the chordae [GFQ⁺17]. Obtaining a precise image of chordae structure is important because a slight change in the chordae structure can significantly influence the MV dynamic closure as discussed in [PVH⁺21a, CMM⁺18, CMMS20, TBP⁺17]. Micro CT imaging enables the acquisition of high-resolution images of the MV, where the chordae structure is visible. However, the process is tedious and time-consuming, rendering it impractical for imaging in an in-vivo setup involving a beating heart and rapidly moving structures of the MV. Studies based on ultrasound employ diverse methods to model the chordae structure. For example, some studies adopt a generic chordae structure [MGG⁺13], while others reconstruct it through statistical analysis of chordae insertion points, as seen in [LSP⁺23] utilizing a Chordae insertion density map. Furthermore, certain studies derive the chordae structure by directly observing chordae insertion points [BGG⁺19]. While these efforts are a step forward, the geometries they utilize are not precisely patient-specific.

The MV leaflet consists of an intricate tissue structure strengthened by a complex network of collagen fibers, with multiple chordae insertion points distributed across its surface. Therefore, each specimen has its own unique material characteristics. One of the limitations in MV simulation is obtaining the proper material data, interpretation of the data, and its implementation in the numerical model. In [WS13], they compared the simulation outcome in the case of using various material characteristics. They realized that the material data could have a significant influence on the simulation outcome. The material model, which is the numerical interpretation of how the tissue behaves in various conditions, can also influence the simulation outcome. The influence of using different material models on the MV simulation is extensively discussed in [RFS⁺13, CWG⁺19]. However, having the complex anisotropy direction defined for a specific patient is still an open problem.

Another factor that influences the MV simulation is the leaflet collagen fiber distribution. Each MV leaflet has its own microstructure and obtaining it is a challenging task. In [CKC⁺91], they extracted a map of the leaflet's collagen fiber architecture with the small-angle light scattering (also known as SALS) technique. The outcome of this study is used for modeling the microstructure of the leaflets in MV simulations. Since it is not possible to analyze the patient tissue microstructure in vivo, it is important to explore other ways to infer the map of fibers. Several studies [CKC⁺91, KMP19] attempted to present a general fiber model for simulation purposes, but further attempts can be made to reach its full potential, a microstructure model that is largely independent of experimental measurements while resulting in a most physiologically coherent simulation. In conclusion, the difficulties in obtaining the material data and geometry of the MV, also implementing these data into the numerical model is one of the limitations of MV numerical simulation.

Contact model and mesh representation

In MV simulation, having a mesh representation that captures the self-contact of the leaflets is crucial. This enables the model to replicate the sealed closure of the leaflets. To analyze the MV function in healthy and pathological states, the numerical model needs to be able to capture the detailed contact between the MV leaflets. MV leaflet coaptation area and contact between the leaflets are important topics that are not extensively studied in the literature on the MV numerical simulation.

Computation time and simulation outcomes are influenced by the employed mesh representation. In [CMM⁺18], the utilization of a particle-based approach to replace the fluid mesh resulted in a lengthy simulation duration of five days. Also, in [DYM⁺21], with the impressive computational power of 30 cores and 240 GB of main memory the simulation still took six hours to compute. In [GFQ⁺17] by using different mesh representations, the simulation took 10 days to compute. In addition, the convergence of the simulation is another factor influenced by the mesh representation. The large deformation of the leaflets can cause distortion in the fluid numerical domain which makes it difficult for the simulation to converge.

Evaluation of the simulation outcome

Due to technical challenges in measuring the in vivo behavior of the MV, it is difficult to quantitatively evaluate the simulation outcome. Several studies attempted to compare their simulation outcome with the measurements based on medical imaging. The comparison is mostly qualitative. For example in [MGG⁺13] curvature, patterns, and position of the MV final state in the peak systole are qualitatively compared to the magnetic resonance imaging data. In [MCM⁺17], the blood velocity in the simulation outcome is compared with the echocardiography data. Therefore, techniques to quantitatively evaluate the simulation and metrics to compare the simulation outcome with the expected physiological behavior of the MV are missing in the state of the art.

4 Contributions

In this thesis, we tackle some of the important challenges in the MV simulation mentioned earlier. FSI simulations of the MV involve several physical domains with large deformation of the structure, raising convergence and stability issues. We identified and analyzed methods that fit the best to this problem. A model representing detailed self-contact between MV leaflets is vital; we highlighted and employed essential approaches for this representation. By integrating image-based MV geometry, we improved our model for potential clinical use. Additionally, we investigated the impact of foundational MV simulation aspects, including material models, case setup, and geometry. In the following, a summary of these contributions is categorized and presented.

4.1 Convergence

In chapter 1, a thorough exploration of various approaches and mesh representations to model MV behavior is presented. For simulating the MV dynamic closure, we employed the immersed

boundary approach introduced in [Pes72]. Based on the immersed boundary approach, we simulated the dynamic closure of MV in both healthy and pathological cases. Our findings are published in the IJCARS (International Journal of Computer Assisted Radiology and Surgery) as a journal paper [KVB22].

The immersed boundary is a mathematical and computational framework for simulating FSI problems where an elastic structure is immersed in a viscous and incompressible fluid, allowing for two-way interaction between the fluid and the structure. Incorporating such mesh representation in our model enhances the convergence properties of MV simulation by reducing the complexities associated with mesh deformation in FSI simulation. In our model, the fluid mesh remains intact despite the significant deformation of the leaflet, thereby minimizing the requirement for re-meshing techniques and eliminating factors that hinder simulation convergence. Additional factors that impact convergence include mesh control and boundary conditions, particularly how chordae attachment and annulus boundary conditions are defined. The self-contact between the leaflets during the closure involves arbitrary-like interaction between a large number of nodes and having an efficient contact model to handle this complex interaction influences the convergence of the simulation. This thesis precisely presents how the contact has been modeled for a robust and fast computation.

4.2 Contact measurement

One of our contributions is our detailed description of how to model self-contact between the leaflets during the dynamic closure of the MV in an efficient way (see chapter 4). A benefit of our FSI model based on the immersed boundary mesh representation is its compatibility with capturing actual contact. We included both normal and frictional contact between the leaflets in our model and there is the possibility of analyzing the sealed closure of the MV, contact map, and coaptation area in detail. In the literature, no study on FSI simulation of MV provided detailed information regarding the coaptation area, contact force, and sealed closure. Previously, experimental works measure the coaptation area [GDD⁺10, YWK⁺09] or contact force [GBL⁺20, GBC⁺20] during the MV closure, and our contact map is the first numerical tool that can predict if the valve is closing properly with the information related to the coaptation area. Detailed information on how we obtained the contact map is presented in chapter 4.

4.3 Moving toward a patient-specific model

One of our contributions was to compare different material models on image-based and generic MV geometries. We also provided detailed information on the challenges in the implementation of material models and image-based MV geometries. Initially, we implemented a generic geometry and a simplified material model described in chapter 4, which considers the stress-strain response of the MV leaflets to be homogenous. We then moved toward having a patient-specific model by implementing image-based geometry and a more complex material model in chapter 5. The majority of the studies in the literature use simplified geometry of the MV [BGG⁺19, MGG⁺13, GFQ⁺17]. The first step was to implement geometries with accurate chordae structure and leaflets segmented from micro CT images in our FSI model. Despite difficulties raised by using complex and non-smooth geometry with irregularities in the topology of the geometry, our model

is capable of accepting image-based geometries and simulating MV dynamic closure with patient-specific geometries.

In regards to the material model, experimental measurements indicate that the MV leaflets exhibit non-isotropic (anisotropic) behavior, displaying varying stress-strain responses along different directions [JLK⁺18b]. In order to accurately capture the material characteristics, we have incorporated an anisotropic constitutive model into our material representation which better reflects the actual material properties. Another difficulty related to the material model is obtaining the material parameters by fitting experimental data into the equations of the constitutive model. We shed light on the difficulties and challenges in this task and managed to obtain the necessary coefficients through an optimization process. We published our findings on the influence of material model on image-based and generic MV in FIMH (Functional Imaging and Modeling of the Heart) as an international conference paper [KVH⁺23].

4.4 Influence of geometry and fluid volume

In the literature of FSI simulation of MV, a simplified LV is often represented by a fitted tube in computational simulations [DYS⁺19, TBP⁺17, OÖB⁺21]. We have expanded upon this approach by investigating how the size of this tube and the placement of the MV inside this volume influence the simulation outcome. Such exploration allows us to discern the effect that varying the representation of blood volume has on the results.

Moreover, the segmented geometry of the MV is often characterized by irregularities on its surface. These irregularities, including minor inaccuracies introduced during the segmentation process, can potentially affect the simulation outcome. To understand this, we utilized Laplacian filtering to reduce the roughness of the segmented leaflet. This approach allowed us to preserve the overall geometry while minimizing surface irregularities.

Therefore, we studied the influence of the MV geometry and fluid volume on the simulation outcomes (see chapter 5). We believe that this approach helps in generating a more reliable simulation of the MV.

4.5 Robustness and flexibility of the model

By modifying the chordae structure, we managed to replicate the pathologies of MV such as prolapse and regurgitation. Therefore, the FSI model is capable of performing in various scenarios. An essential aspect of a patient-specific model is its versatility, ensuring it is not exclusively designed for a particular set of input data. The model must possess the capability to converge and accurately simulate patient data encompassing diverse geometries. Most of the studies in the literature are based on a single MV geometry data. For our studies, we had five MV geometries available and with the same case setup, we managed to run the simulation on the four different image-based geometries and one generic valve which shows the flexibility of our model. We presented the simulation results of two of these image-based geometry in chapter 5.

Structure of the thesis

After completing this introductory chapter, this thesis is divided into several chapters, each exploring a different aspect of the mitral valve (MV) simulation. In chapter 1, "Fluid-structure interaction techniques for modeling mitral valve behavior", we explore the state of the art in the simulation of MV with fluid-structure interaction (FSI) and how contact between the leaflets is modeled in such studies. We then present the details of the geometrical data we used to represent the MV in our simulations in chapter 2, "Data". In this chapter, we will discuss how the geometry of the generic and image-based MV is obtained.

In chapter 3, "Proposition of the fluid-structure interaction mode", we explore the basic understanding of the immersed boundary (IB) method and implementation of boundary conditions and model configuration necessary for simulating the dynamic closure of MV. We also delineate the details of the contact model we used for capturing the self-contact between the leaflets. Following that, we highlight the information related to the challenges, necessary modifications, and various case setups in the FSI simulation of MV.

Afterward, first, we discuss the initial results obtained from the generic model in chapter 4, "Capturing contact in fluid-structure interaction simulation of generic mitral valve", by replicating MV dynamic closure in healthy and pathological cases. In chapter 5, "Investigating the Influence of Anisotropy and Geometry", we strive toward implementing patient-specific geometry and investigating the more complex constitutive models in our simulations. In this chapter, we explore the effects of incorporating anisotropy in the leaflet mechanical response, exploring different constitutive models, and the process of optimization and obtaining coefficients. We also compare the simulation results in different fluid volume and the smoothness of the image-based geometry. This chapter will conclude with a discussion of the results.

Chapter, 6, "Microstructure of the leaflets", will provide a brief introduction to the microstructure of the leaflet, insight into different fiber models, and lead toward more advanced rule-based models. The chapter finishes with a discussion of the results.

Finally, the thesis concludes by summarizing all findings and laying out potential avenues for future research.

Chapter 1

Fluid-Structure Interaction Techniques for Modeling Mitral Valve Behavior

In this chapter, we explore the methodologies used for simulating mitral valve (MV) dynamic closure with a fluid-structure interaction (FSI) approach. In the first section, we provide an overview of the current state of the art of the FSI approaches and offer insight into the most popular models used in the field. We then present the foundational framework of the FSI model employed for our simulations. This approach, known as the immersed boundary (IB) method, is discussed in depth, with a detailed breakdown of its characteristics and advantages. Following that, we discuss the challenges in capturing contact in MV dynamic closure for the case when the fluid physical response is included in the simulation.

1.1 State of the art on fluid-structure interaction

Understanding the numerical solution to the FSI problems requires basic knowledge of computational fluid dynamics (CFD), finite element analysis, and how the interaction between both domains is managed. The numerical scheme needs to be capable of incorporating several physical models in a harmonic and efficient way. In the following, we will explore different ways the FSI simulation is done, and explain the challenges, drawbacks, and advantages of each method for mitral valve (MV) simulation. The final goal is to identify which approach will give us the opportunity to extract the important information from the MV simulation and allow us to move toward having a patient-based simulation.

1.1.1 Mitral valve simulation

To model the impact of blood flow and the MV structure, the problem is formulated as an (FSI) problem, integrating principles from both fluid dynamics and solid mechanics. The development and integration of FSI models have been an ongoing focus in the numerical simulation of MV. One of the early fluid-structure interaction models for MV was presented by Einstein et al. [EKR⁺05a, KEC07], paving the way for future research in this area [TBP⁺17, CWG⁺19, CMM⁺18, KMP19, AEHE19, KSE⁺23, AAAB⁺22, MCM⁺17, DYS⁺19].

The choice of FSI formulation is important and it determines the capabilities and limitations

of the simulation and influences the type of information that can be extracted from the final results [BRI⁺16]. In a majority of the FSI simulations of MV behavior, the MV and blood are defined as two separate domains, and their interaction is effectively handled through the mesh representation. Here, the focus will be on studies where fluid and structure are separate domains. For a detailed exploration of all existing methods, we encourage the readers to see the review papers [GQF⁺17, ANAW22].

Three main categories of formulation frequently used in the literature are based on arbitrary Lagrangian-Eulerian (ALE) [AAAB⁺22, ESH14, LDSB10, XJW⁺21, KFN17, RT23, AEHE19], IB [FGG⁺19, CVM⁺19, DP15, CZW⁺23, CWG⁺19, KMP19, CZCP19, GFQ⁺17], and smoothed-particle hydrodynamics (SPH) [CMM⁺18, MCM⁺17, TBP⁺17, BGG⁺19, DYM⁺21, OÖB⁺21]. The SPH is particle-based, whereas the ALE and IB approaches are mesh-based. The difference lies in the fluid numerical domain. In the particle-based model, the fluid domain consists of numerous particles that move freely within a control volume [AGS07]. On the other hand, in ALE and IB methods, the fluid domain is represented by a discretized mesh [GQF⁺17]. To have a more clear view, Fig.1.1 shows a cross-section of a fluid wave, and its numerical domains in mesh-based and particle-based representation.

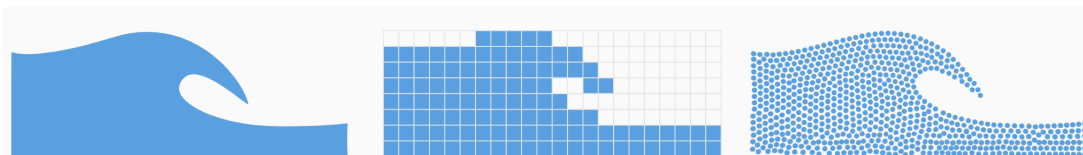


Figure 1.1: Left: cross-section of a simple fluid wave, middle: mesh-based numerical domain, right: particle-based numerical domain¹.

1.1.2 Mesh representation

The MV structure is represented by Lagrangian mesh, while the mesh-based fluid numerical domain can be represented by Eulerian mesh (in studies utilizing IB), Lagrangian mesh (in studies based on SPH), or a mix between the two (in studies based on ALE). Fig.1.2.a and Fig.1.2.b illustrate the Lagrangian mesh and Eulerian mesh respectively. In both figures, the initial shape of the material is defined as a circle. Within the Lagrangian domain, as the material undergoes deformation, the Lagrangian mesh distorts and conforms to the deformation of the material. In the Eulerian domain, a square region is discretized and considered as a control volume. The Eulerian numerical domain consists of two regions: one where the material exists, shown in gray, and the remaining area which is considered void. The material deformation is described as a mass flux through the fixed discretized mesh. [QHG11].

In the IB method, the structure is immersed inside the fluid numerical domain with Eulerian mesh. The key advantage of this approach is that the deformation of the structure does not cause distortion in the fluid mesh [GQF⁺17, ANAW22, BRI⁺16]. The influence of the structure movement on the fluid domain is introduced by adding a body force to the fluid equation. more information about the details of IB formulation is discussed in the next section.

¹<https://www.dive-solutions.de/blog/sph-basics>

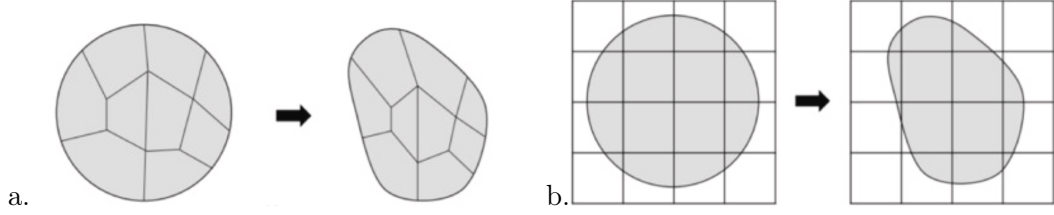


Figure 1.2: (a.) Lagrangian mesh, (b.) Eulerian mesh [SDKT23]

On the other hand, the ALE takes a different approach. Instead of immersing the structure inside the fluid domain, the fluid domain shares boundary walls with the structure. As a result, when the structure deforms and moves, its boundary with the fluid domain also moves, leading to distortion in the fluid mesh [DGH82]. Therefore, the fluid domain in the ALE approach is a mix between Eulerian and Lagrangian mesh definitions. Fig.1.3 illustrates the difference between mesh representation in ALE and IB.

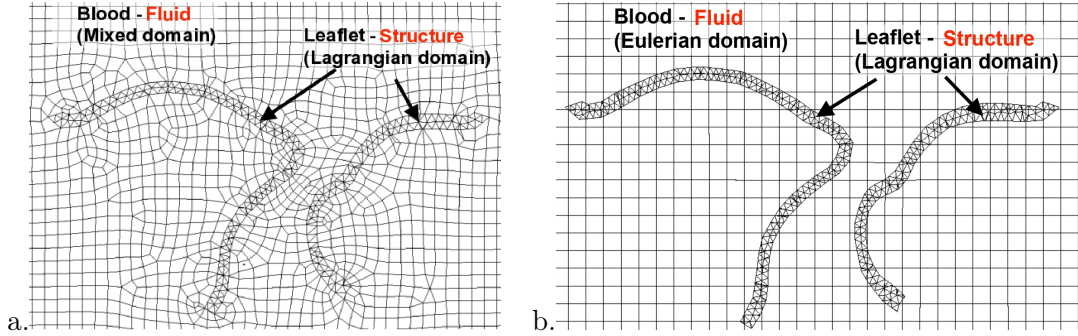


Figure 1.3: Cross-section of a ALE (a.) and IB (b.) mesh representation of MV leaflet inside fluid control volume

1.1.3 Method comparison

All FSI approaches mentioned are used in the literature to simulate MV behavior. However, proper choice of FSI formulation can eliminate some of the challenges mentioned in the introduction section including convergence issues, capturing contact, sealed closure, robustness, and versatility of the model. In the following, we go through each FSI formulation and discuss their pros and cons for MV simulation.

Smoothed-particle hydrodynamics

Many researchers utilize SPH for FSI simulation [AGS07]. SPH is available in some of the powerful commercial solvers such as LS-DYNA [Dev92] and Abaqus [Man12] which adds to its popularity among researchers and engineers. Similar to IB, by using SPH, it is possible to capture the detailed contact between the leaflets of the MV [BGG⁺19]. The main downside of using SPH is the high computation cost due to its particle-based nature [CMM⁺18, DYM⁺21, TCAA⁺21]. Other challenges in using SPH are low accuracy within high-order approximation schemes [TCAA⁺21], and limitation of the method in capturing details of the flow and turbulence near the surface

walls [BGG⁺19, NRRS19, SOLT16]. Near-wall turbulence often involves very small-scale flow structures, and capturing these details can require a prohibitive number of particles. In addition, SPH is an inherently viscous method, which means it tends to over-dampen small-scale turbulent flows. This makes it difficult to accurately capture turbulent behavior, especially near walls where viscous effects are important. There are a number of methods that can be used to improve the accuracy of SPH simulations in these regions. Using higher particle resolution will allow the particles to resolve the smaller-scale turbulent structures, but it will also increase the computational cost of the simulation.

Arbitrary Lagrangian-Eulerian

The ALE approach, first described in [DGH82], is also a widely used approach in the literature of MV FSI simulation. The boundary between the fluid domain and the structure is explicitly defined which is known as body-fitted mesh. Therefore, the surface of MV leaflets is laid over the external walls of the fluid control volume (see Fig.1.3.a). This creates a situation in which the information about the location of the structure is accurately delivered to the fluid equations. Furthermore, the no-slip boundary condition, when the fluid sticks to the structure surface (hence the term "no-slip"), is correctly applied in the ALE approach. This situation enhances the convenience and accuracy when calculating the turbulent behavior of blood.

The ALE approach provides an accurate representation of the flow, but this approach is not without some drawbacks. The primary challenge lies in the need for re-meshing techniques when MV leaflets undergo deformation during closure [SB09, ANAW22]. If the deformation leads to distortion that exceeds a predefined threshold, the distorted region is then subject to re-meshing. In the case of MV simulation, the MV closure is a rapid and large deformation which re-meshing in this situation makes the convergence of the simulation difficult to obtain [BRI⁺16, SB09, GQF⁺17]. Re-meshing techniques usually add extra load to the computation process and increase the simulation time. Fig.1.4 illustrates an example of ALE domain during the re-meshing process [AABS21].

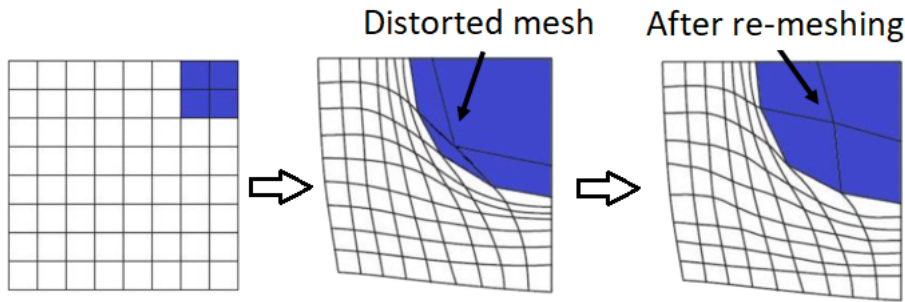


Figure 1.4: In ALE approach, when deformation occurs, depending on the severity of the distortion, the numerical domain is re-meshed [AABS21].

Another critical issue is related to the self-contact between MV leaflets during simulation progression. As the simulation progresses, anterior and posterior leaflets get closer to each other, and eventually, the MV closes. In ALE, this results in the fluid elements between the leaflets getting crushed, causing the element size to become zero or negative, which leads to the

divergence of the simulation. This issue is addressed in the literature by defining a minimum distance threshold between leaflet walls [BRI⁺16]. Upon reaching this threshold, the walls can no longer approach each other. To block the flow and seal the closure, they compensate by considering the fluid domain cells in between the leaflets as a porous medium, which is a sponge-like region to absorb the momentum of the flow. Fig.1.5 illustrates this concept, showing a cross-section of two leaflets about to make contact with a porous medium in between [BRI⁺16].

During our research, we attempted to incorporate porous medium with ALE approach in Ansys Fluent solver [Mat22]. However, due to the complexity of the model, the simulation did not reach convergence. Moreover, this solution will not allow for extracting detailed information regarding the leaflet self-contact and coaptation area.

Immersed boundary

Instead of using a body-fitted mesh, immersing the structure inside the fluid domain significantly reduces the complexity of the interaction between the fluid and structure domains and reduces the computation cost, making the IB method highly efficient and scalable.

With the ability to capture the interaction between the fluid and the structure without requiring the grid to conform to the structure, the IB method is especially well-suited for MV dynamic motion where the leaflets largely deform over time. In addition, the leaflets can be involved in self-contact without distorting the fluid domain, which makes IB an excellent tool for capturing detailed contact between the leaflets, where other methods like ALE struggle (see Fig.1.5.a in ALE and Fig.1.5.b in IB) as described in [BRI⁺16].

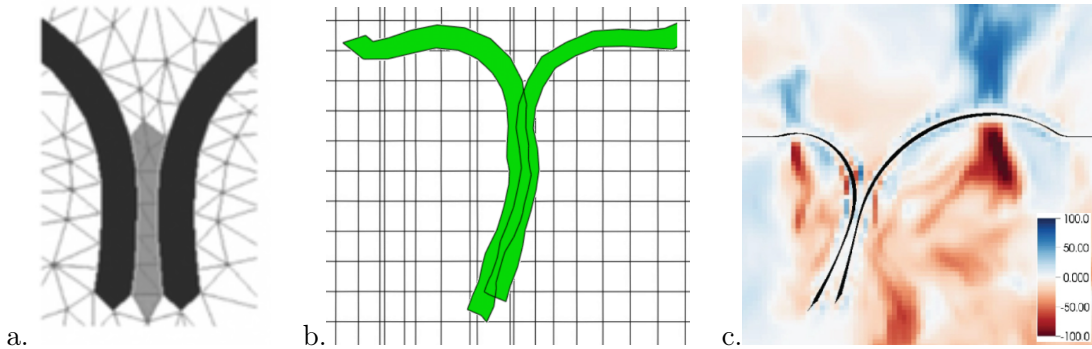


Figure 1.5: (a.) Cross-section of two leaflets (shown in black) and the porous medium in between shown as a gray region [BRI⁺16]. (b.) Cross-section of two leaflets shown in green having actual contact in IB mesh representation. (c.) Cross-section of MV leaflets with spurious flow (the colors show the fluid velocity) [KMP19].

One of the concerns in using IB is the leakage of fluid through the Lagrangian structure, which is more known as spurious flow. In a situation where the structure is thin and the pressure field inside the Eulerian domain is discontinuous, the IB is prone to this issue. Figure 1.5.c illustrates an example of this situation. It is important to note that, in this example, a thin two-dimensional membrane is used as the structure, resulting in a significant amount of leakage. One approach to mitigating this issue is to increase the thickness of the structure, as suggested in [KMP19]. Another solution is to further reduce the size of the Eulerian mesh [BRI⁺16] to

reach acceptable results. In our simulations, we employed the IB formulation and took special care to address the problem of spurious flow in the IB. This was achieved by reducing the size of the Eulerian mesh until mesh independence was satisfied in the simulation results. Therefore, the leakage due to the grid size does not affect the dynamic closure of the MV. In the following section, the FSI simulation of MV with IB formulation is described in detail.

1.2 Immersed boundary method

The IB was first developed by Peskin to simulate the flow around MV [Pes72]. In IB, no clear border between the fluid and the structure domain exists. Instead, materials described in the Eulerian framework (blood) engage with elements defined in the Lagrangian framework by adding a force field to the fluid equations. The force field is calculated based on the positions of the structure. This specific type of interaction is embedded in coupled Eulerian-Lagrangian (also known as CEL) [Skr12, BO04]. The coupled Eulerian-Lagrangian is an implementation of the IB and finite element methods in a single solver. In [BO04], they used coupled Eulerian-Lagrangian formulation to facilitate the contact behavior in machining industrial parts. The coupled Eulerian-Lagrangian is already implemented in Abaqus explicit solver [Man12]. We utilized this commercial solver for our simulations. The following section provides a detailed presentation of the governing equations associated with the coupled Eulerian-Lagrangian method.

1.2.1 Equation of state

In the fluid domain, several variables, including pressure (P), volume (V), density (ρ), and velocity (u) are unknown. These variables are solved based on several equations, including the conservation of mass, conservation of momentum, viscosity equation, and equation of state. To solve the fluid motion equation, several assumptions are needed. For example, we considered the blood to be Newtonian, meaning that in the viscosity equation, the relation between the shear tension and local strain rate is linear. We also considered the fluid to be incompressible and isothermal, which means that with the change in the pressure and temperature, the volume of fluid stays constant. These assumptions are introduced to the solver while solving the equation of state. In the following, we will first describe how the equation of state, which defines the compressibility rate in the fluid, is introduced to the Abaqus explicit solver, and in the following section, the equations of conservation of mass and momentum are described.

Blood is an incompressible fluid, meaning that the influence of pressure on the volume, and consequently density, is close to zero and negligible. To simulate the behavior of the blood, it is necessary to define the relation between the applied pressure and its density by the equation of state. There are several equations of state that model the relation between pressure, volume, and temperature in a closed system. For blood, we used an equation of state as Mie-Gruneisen [Heu12], which states that pressure is a linear function of internal energy. This equation is described as follows:

$$P = P_H \left(1 - \frac{\Gamma_0 \eta}{2}\right) + \Gamma_0 \rho_0 E_m. \quad (1.1)$$

The Hugoniot pressure, denoted as P_H , is the pressure that a fluid medium experiences when

a shock wave passes through it. It is calculated as a function of density (ρ) which is extracted by conducting experimental measurements. Γ_0 is material constant, ρ_0 is reference density (density of the fluid under atmospheric pressure), and $\eta = 1 - \rho_0/\rho$ known as nominal volumetric compressive strain. In our case, we used a U_s-U_p Hugoniot form as $P_H = \rho_0 c_0^2 \eta / (1 - c_1 \eta)^2$. In this equation, c_0 and c_1 are constants that establish the relationship between the shock velocity (U_s) and particle velocity (U_p) inside the fluid. This relationship is explicitly given by $U_s = c_0 + c_1 U_p$. To satisfy the incompressibility condition of the blood, we used the values mentioned in [ASFB14] where the relation between pressure and density is modeled with Mie-Gruneisen equation of state for simulation of a solid sphere entering incompressible liquid. In the Abaqus explicit solver, we defined c_0 , c_1 , and Γ_0 respectively as 1450m/s , 0 , and 0 .

1.2.2 Eulerian formulation

Based on the conservation laws, the summation of measurable entities is constant over the control volume of the Eulerian domain. Meaning, the integral of mass, momentum, and energy passing through the borders of the control volume remains constant. The governing equations of the Eulerian domain are the same as the ones for incompressible and viscous fluid flow which is written as:

$$\frac{\partial \rho}{\partial t} + \nabla \cdot (\rho \mathbf{u}(\mathbf{x}, t)) = 0, \quad (1.2)$$

and

$$\frac{\partial \rho \mathbf{u}(\mathbf{x}, t)}{\partial t} + \nabla \cdot (\rho \mathbf{u}(\mathbf{x}, t) \otimes \mathbf{u}(\mathbf{x}, t)) = \nabla \cdot \sigma + \rho f(\mathbf{x}, t). \quad (1.3)$$

Here, $\mathbf{u}(\mathbf{x}, t)$ is the Eulerian velocity field, and $\mathbf{x} = (x, y, z) \in \Omega$ is the Cartesian coordinates of the fixed fluid control volume in which $\Omega \in \mathbb{R}^3$ is the physical domain. ρ , σ , and $f(\mathbf{x}, t)$ respectively denote fluid density, Cauchy stress, and body forces. For conciseness, only the equations for the conservation of mass (1.2), and momentum (1.3) are presented, and the equation describing the conservation of energy is not mentioned. These equations are also known as Navier-Stokes equations, which are solved numerically within the control volume that represents the fluid domain. For mathematical convenience and being able to introduce the influence of the forces exported from the Lagrangian domain to the Eulerian domain, conservation equations can be divided into two parts:

$$\frac{\partial \varphi}{\partial t} = S, \quad (1.4)$$

and

$$\frac{\partial \varphi}{\partial t} + \nabla \cdot (\Phi) = 0. \quad (1.5)$$

φ is the arbitrary solution variable (which can take velocity, pressure, etc.), Φ is a flux function, and S represents source terms. In a physical sense, the first equation is interpreted as the influence of external forces on the system, and the second equation deals with the convection terms. In the Eulerian domain, the control volume in 3D space is discretized by a fixed mesh. The presence of fluid in each cell of the control volume is described by a value between zero and

one. For example, Fig.1.6 shows fluid as a gray circle in the center of a square shape control volume. Cells that are fully occupied by fluid is given the value of one, the borders are between zero and one, and the empty cells are considered as zero.

0.0	0.0	0.0	0.0	0.0	0.0
0.0	0.32	0.91	0.91	0.32	0.0
0.0	0.91	1.0	1.0	0.91	0.0
0.0	0.91	1.0	1.0	0.91	0.0
0.0	0.32	0.91	0.91	0.32	0.0
0.0	0.0	0.0	0.0	0.0	0.0

Figure 1.6: Distribution of volume fraction in an Eulerian domain with square control volume [LJ18].

Equation 1.4 and 1.5 are discretized separately and solved consecutively in a Lagrangian step (eq.1.4) and an Eulerian step (eq.1.5). A visual illustration of these two steps is shown in Fig.1.7.

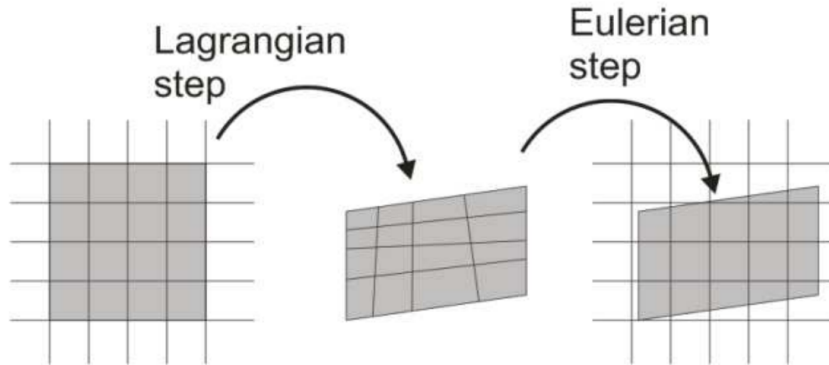


Figure 1.7: The flux of fluid material is calculated in two steps. The Eulerian domain remains fixed at the end of each cycle. [Skr12]

The control volume is considered a flexible object for the Lagrangian step. The initial conditions and applied forces from the structure (MV in our case) will deform the control volume and updated values are calculated by solving the eq.1.4 numerically. When dealing with rapid deformations in a system, the behavior can change significantly over a very short period of time. In such cases, an explicit approach is more appropriate. Explicit methods directly compute the state of the system at the next time step based on the known state at the current time step, without the need to solve complex equations. Therefore, an explicit approach can capture rapid changes more accurately by using small time step sizes. The implicit formulation, despite allowing for larger time steps, is not preferable because the extra computational effort required to solve the nonlinear equations outweighs the benefits of the larger time steps. Therefore, the explicit approach is more appropriate and the equation 1.3 is discretized and solved explicitly

[BO04].

In the Lagrangian step, the nodal displacement (x_s), velocity (v_s), and acceleration (a_s) are calculated using the Abaqus explicit solver. This solver discretizes and numerically solves the governing equations for the equation of motion:

$$\mathbf{M}a_s + \mathbf{F}^{int} = \mathbf{F}^{ext}. \quad (1.6)$$

\mathbf{M} and a_s represent the diagonal mass matrix and nodal acceleration, while \mathbf{F}^{int} and \mathbf{F}^{ext} denote the internal and external force vectors, respectively. By using central difference, acceleration, velocity, and the position of the Lagrangian step are derived from the explicit formulation as:

$$a_s^n = \mathbf{M}^{-1}(\mathbf{F}^{ext} - \mathbf{F}^{int}), \quad (1.7)$$

$$v_s^{n+1/2} = v_s^{n-1/2} + \Delta t a_s^n, \quad (1.8)$$

and

$$x_s^{n+1} = x_s^n + \Delta t v_s^{n+1/2}. \quad (1.9)$$

In the Eulerian step, the virtual displacement is governed by the equation of virtual work, derived from Equation 1.3. The virtual work derived from eq.1.3 is formulated as:

$$\int_{\mathbf{v}} \rho \mathbf{a} \cdot \delta \mathbf{v}(\mathbf{x}, t) d\mathbf{u}(\mathbf{x}, t) + \int_{\mathbf{v}} \sigma : \delta \epsilon d\mathbf{u}(\mathbf{x}, t) = \int_{\mathbf{s}} \mathbf{t} \cdot \delta \mathbf{v}(\mathbf{x}, t) ds + \int_{\mathbf{v}} \rho f(\mathbf{x}, t) \cdot \delta \mathbf{v}(\mathbf{x}, t) d\mathbf{u}(\mathbf{x}, t). \quad (1.10)$$

Here, $\delta \mathbf{v}(\mathbf{x}, t)$, $\delta \epsilon$, a , and \mathbf{t} are respectively the virtual displacement, virtual strain, spacial acceleration, and traction. Once the virtual work is calculated, the virtually displaced grid is repositioned back into the initially discretized control volume. However, the displaced fluid will remain in its position, and only the volume fraction of the control volume will be updated. During the process, the time step size is restricted such that no material is able to traverse more than a single element in any given step.

1.2.3 Structure formulation

The geometry in the Lagrangian domain is discretized with a set of polyhedron elements (in our case, tetrahedron) which deforms as the applied forces change the shape of the structure. More information regarding the discretized domain is mentioned in chapter 2. Since the MV closure is a rapid movement, the dynamic equation of motion, with the inertia terms included, is considered for the discretized domain of the MV structure:

$$\mathbf{M} \frac{\partial^2 \mathbf{X}(\mathbf{s}, t)}{\partial t^2} + \mathbf{C} \frac{\partial \mathbf{X}(\mathbf{s}, t)}{\partial t} + f_{int} + f_{cnt} + f_{bc} + f_{ext} = \mathbf{R}(\mathbf{X}(\mathbf{s}, t)). \quad (1.11)$$

Here, \mathbf{M} and \mathbf{C} are mass and damping at each node, obtained by the lumped method, in which the properties of each element are equally distributed on the nodes of that specific element. $\mathbf{R}(\mathbf{X}(\mathbf{s}, t))$ is the residual function that needs to be reduced to zero [Bor13]. In this equation,

four forces of f_{int} , f_{cnt} , f_{bc} , and f_{ext} influence the dynamic motion of the MV. f_{int} is the internal forces on the Lagrangian nodes. This force is calculated based on the local components of the stress tensor. Constitutive law based on the strain energy function is used to model the stress response of the MV tissue. These constitutive models consider the non-linear response of the MV leaflet tissue as hyperelastic material by including exponential terms in the strain energy function. More details regarding the material response of the MV tissue are discussed in chapter 4 and chapter 5.

In our study, we used several types of stress and strain for different purposes such as obtaining the material model and representing the simulation results. For example, to obtain the mechanical response of the MV leaflets, we used the concepts of strain (the ratio of deformation to the original length), and principal stretch ratio (λ). The relationship between stretch and strain is represented by the equation $\lambda = 1 + E$. Strain is a dimensionless quantity denoting the deformation a material undergoes when exposed to stress. It is the ratio of the deformation $d\delta$ to the original length (d), expressed as $E = \delta d/d$.

We also used true strain and Von Mises stress to show the stress distribution over the leaflets. The concept of true strain, also referred to as logarithmic strain, is mathematically defined by the equation $\epsilon_t = \ln(1 + \epsilon_e)$. In this equation, ϵ_e represents the engineering strain, which is commonly the value reported in experimental measurements. The von Mises stress is a scalar quantity that represents the six independent components of stress in a three-dimensional state into a single value. This unified metric serves as a reliable indicator for assessing the level of stress experienced by a material specimen. These concepts are used in the following chapters as we describe the material model and simulation results.

In Equation 1.11, f_{cnt} refers to the contact forces exerted on each node that is involved in the self-contact of the MV leaflets. The next section of the current chapter is dedicated to the technical details of the self-contact model. The force f_{bc} is applied to Lagrangian nodes subject to various boundary conditions that restrict their movement. For instance, the annulus nodes have constraints on their displacement in 3D space. Finally, the force f_{ext} is calculated based on the pressure force and viscous forces exerted on each element node from the fluid domain as:

$$f_{ext} = - \int p n dA + \int \tau \cdot n dA. \quad (1.12)$$

p is the fluid pressure applied on the Lagrangian element node in the direction of normal (n) to the surface area differential dA . τ denotes the shear stress tensor from the viscous fluid applied on the Lagrangian node. p and τ are extracted by projecting the force from the immersed boundary nodes in the direction of normal, and perpendicular to the structure surface respectively [Bor13].

1.2.4 Interaction

In equation 1.3, $f(\mathbf{x}, t)$ is a body force that accounts for the presence of the structure. The forcing term is computed using interpolation and integration techniques that map the Lagrangian grid onto the Eulerian grid:

$$f(\mathbf{x}, t) = \int_{\Gamma} \mathbf{F}(\mathbf{s}, t) \delta(\mathbf{x} - \mathbf{X}(\mathbf{s}, t)) ds. \quad (1.13)$$

Here, $\mathbf{s} = (x, y) \in \Gamma$ is the Lagrangian material coordinates on the structure, which $\Gamma \in \mathbb{R}^2$ is the curvilinear coordinate for the Lagrangian domain. $\mathbf{X}(\mathbf{s}, t) \in \Omega$ is the physical position vector of the structure at time t . $\mathbf{F}(\mathbf{s}, t)$ denotes the elastic force density generated by the deformation of the structure. The $\delta(\mathbf{x} - \mathbf{X}(\mathbf{s}, t))$ is the Dirac delta function, which couples the Lagrangian and Eulerian domains together [Pes02]. To pose the no-slip boundary condition, the motion of the boundary is assumed to follow the local fluid velocity. Therefore, by matching both velocities, we have:

$$\frac{\partial \mathbf{X}(\mathbf{s}, t)}{\partial t} = \mathbf{u}(\mathbf{X}, t) = \int_{\Omega} \mathbf{u}(\mathbf{x}, t) \delta(\mathbf{x} - \mathbf{X}(\mathbf{s}, t)) d\mathbf{x}. \quad (1.14)$$

Equation 1.13 and 1.14 describe how the fluid and the structure communicate with each other. With the help of the Delta function, only the Eulerian elements that are occupied by the structure nodes will be considered in equation 1.14, and the rest of the Eulerian control volume will be ignored. At these elements, when the structure moves, the deformation of the structure pushes the fluid present in the surrounding elements. Likewise, the momentum of the fluid in these elements exerts forces on the structure points and moves the structure with the same local fluid velocity. The volume fraction shown in Fig.1.6 keeps track of Eulerian elements that contain the fluid material. It is described as:

$$\sigma^{n+1} = \sigma_m^{n+1} V_m^f. \quad (1.15)$$

Here, $n + 1$ denotes the value in the next iteration, and m denotes the value of the material, i.e. blood. The mean stress in each Eulerian element (σ^{n+1}) is obtained from the material stress (σ_m^{n+1}), where the value of the volume fraction (V_m^f) is non-zero. The interaction between the fluid and the structure nodes is imposed by penalty formulation due to its simplicity and robustness [BO04]. The penalty method essentially involves introducing springs at the material interface points, in order to resist penetration. The depth of the penetration can be updated incrementally, or the total depth at the end of each step is used for the penalty formulation. The first approach gives smoothly applied force but the depth of the penetration needs to be stored which needs more space. Once the contact force, f^c , from the penalty formulation is calculated, it will be added to the virtual work in equation 1.10. As a result, a virtual displacement resulting from the interaction of fluid with structure $\delta \mathbf{v}^c$ will be added to the equation of virtual work. This yields:

$$\int_{\mathbf{v}} \rho \mathbf{a} \cdot \delta \mathbf{v}(\mathbf{x}, t) d\mathbf{u}(\mathbf{x}, t) + \int_{\mathbf{v}} \sigma : \delta \epsilon d\mathbf{u}(\mathbf{x}, t) = \int_{\mathbf{s}} \mathbf{t} \cdot \delta \mathbf{v}(\mathbf{x}, t) ds + \int_{\mathbf{v}} \rho f(\mathbf{x}, t) \cdot \delta \mathbf{v}(\mathbf{x}, t) d\mathbf{u}(\mathbf{x}, t) + \int_{\mathbf{s}} f^c \cdot \delta \mathbf{v}^c ds. \quad (1.16)$$

1.2.5 The choice of solver

For numerical simulation, a variety of open-source (for example OpenFOAM¹) and commercial solvers (such as Ansys², COMSOL³, and Abaqus⁴) are accessible. There are several open-source

¹<https://www.openfoam.com/>

²<https://www.ansys.com/>

³<https://www.comsol.com/>

⁴<https://www.3ds.com/products-services/simulia/products/abaqus/>

platforms that already implemented immersed boundary methods for solving fluid problems. For example, the open-source IBAMR platform⁵, Conjugate Heat Transfer in SIMSCALE⁶ for heat exchange with IB, and implementation of IB with the help of FEniCS computing platform as described in [BLZ⁺21]. Among the commercial solvers, to the best of our knowledge, Abaqus Explicit is the only commercial solver offering simulation based on IB. The MV simulation is complex and needs several models to capture the realistic behavior of the valve closure, for example, a complex hyperelastic material model, large deformation of the leaflets, complex geometry from medical imaging, interaction between the fluid and structure, and contact between the structure walls. Even though there are open-source platforms available for IB, we used the commercial Abaqus explicit solver, because it is versatile, and many of the functionalities for simulating complex multiphysics problems, such as MV closure, are already implemented.

After exploring the IB formulation, in the following section, we will discuss the details related to the self-contact between the MV leaflets in the FSI simulation.

1.3 Contact

Self-contact between the leaflets is one of the aspects of the MV FSI simulation that is not extensively described in the literature. A model that can capture detailed contact between the leaflets allows for obtaining detailed information about various pathologies of MV, including blood leakage. This motivated us to put our attention on investigating the appropriate contact models that are suited to MV and allow proper simulation in typical clinical cases with a specific focus on a sealed closure. In this section, some of the challenges in modeling the self-contact of the MV leaflets are discussed, and common approaches used in the literature to model contact in MV simulation are mentioned.

1.3.1 Challenges in self-contact between mitral valve leaflets

Self-contact of the MV is a complex problem and needs an efficient numerical approach for modeling contact. The main attributes of capturing contact that impact the computation cost and convergence of the model can be categorized as follows:

- The Lagrangian domain of the leaflet structure comprises thousands of element nodes. At the initial state of the simulation, the MV is open, and the leaflet nodes are far from each other. This makes the contact problem more challenging and computationally intensive, as all element nodes can potentially engage in the self-contact model.
- In self-contact of the leaflets, the leaflet walls should apply equal forces on each other and both sides of the contact should be treated equally in the formulation.
- The contact model, needs to incorporate both normal contact and frictional contact between the leaflets.

⁵<https://ibamr.github.io/>

⁶<https://www.simscale.com/docs/analysis-types/conjugate-heat-transfer-ibm/>

In addition, capturing contact in MV dynamic closure, with the FSI context, sometimes produces closure with orifice holes and gives rise to instabilities or divergence. For example, in studies [GMQ⁺14, CWG⁺19, TBP⁺17, FQG⁺18, LDSB10, BGG⁺19], zero flow rate is obtained at peak systole despite holes in the MV. An example of such cases is shown in Fig.1.8, where the flow rate passing through the MV reaches zero while orifice holes are visible in the closed state. Therefore, in modeling contact between MV leaflets, a sealed closure with no orifice hole should be obtained in the healthy MV closure.

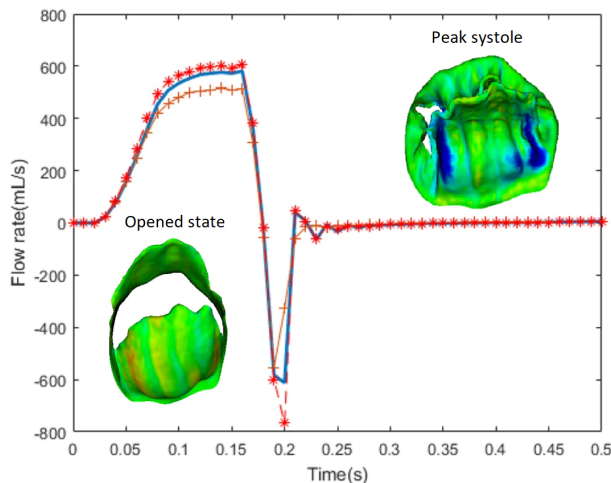


Figure 1.8: Result of FSI simulation from [CWG⁺19], showing flow rate through cardiac cycle. Once the valve is at peak systole, the flow rate drops to zero while orifice holes are visible in the peak systole.

1.3.2 Master-slave contact model

Modeling contact between two arbitrary surfaces has been studied in the literature [HPH11, RMK14, AGPT09, PMFC01]. The most common approach used to model the contact between two surfaces numerically is the master-slave contact model [PMFC01, SMB11]. The master-slave concept was adopted in various fields, including control systems, robotics, and computational mechanics, to describe interactions where one body has a dominant influence over another. For modeling contact in structural analysis, the master-slave formulation was initially presented in [HGB85].

The master-slave approach is the interaction between two or more surfaces in which one surface, the "master," controls or influences the behavior of the other surface, the "slave." The master surface is responsible for enforcing the contact constraints, while the slave surface is allowed to deform freely. The selection of which surface is the master and which is the slave can be based on material properties, geometrical complexity, or other considerations. The contact surfaces are typically discretized into a mesh of nodes. The nodes on the master surface are called master nodes, and the nodes on the slave surface are called slave nodes. Fig.1.9.a shows the discretized domain of both surfaces in the proximity of each other.

For each slave node, the closest distance to the master surface is constantly calculated (see

Fig.1.9.a). As both surfaces get in contact, the slave nodes are allowed to penetrate the master surface. Depending on the depth of the penetration (see Fig.1.9.b), if the penetration rate is greater than zero, a counter force is applied on the slave node, normal to the direction of the master surface, to push away from the master surface [SMB11].

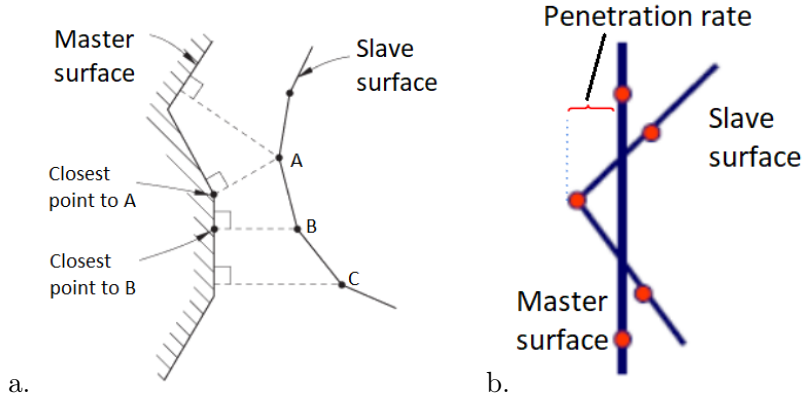


Figure 1.9: (a.) Illustration of a discretized domain of master and slave surfaces [Man12]. (b.) Slave node penetrating the master surface.

Contact models such as the master-slave model do not consider the contact surfaces to play the same role, resulting in contact forces that are not equally distributed on both sides of the contact. In addition, considering the challenges in capturing contact between the MV leaflets, there is a need for a contact model specifically suitable for capturing the complex collision of MV leaflet surfaces. This model should efficiently manage the inclusion of thousands of contact pairs concurrently, anticipate the collision between two arbitrary facets in advance, and be capable of simulating a sealed closure with no orifice hole in the healthy MV. In the current studies on FSI simulation of MV, there is limited information discussed regarding the strategies they employed for capturing contact between the MV leaflets in the MV simulation, therefore, we decided to discuss the implementation of the self-contact model we used in our simulation in more depth which is presented in chapter 3.

1.4 Conclusion

In this chapter, we investigated various fluid-structure interaction (FSI) methodologies for simulating the dynamic closure of the mitral valve (MV). The primary focus is on FSI models that can accurately capture the interactions between leaflets, a critical element for simulating a sealed MV that prevents blood leakage—indicative of a healthy valve. We focused on three major FSI methodologies available in the literature: smoothed-particle hydrodynamics (SPH), arbitrary Lagrangian-Eulerian (ALE), and the immersed boundary (IB) method.

Based on our observation, we realized that both SPH and the IB method are effective in capturing the self-contact between MV leaflets as well as large deformations. However, due to the elevated computational cost and the particle-based fluid description associated with SPH, the IB method was selected for our simulations. Despite its limitations, such as the potential for blood leakage through the tissue membrane, the IB method emerged as the most suitable for

simulating MV dynamic closure.

Following that, we presented detailed information regarding the IB formulation. The immersed boundary (IB) method offers an advanced computational framework that is highly practical in the simulation of FSI, especially in simulating the MV dynamic closure. This method addresses many of the conventional challenges associated with fluid mesh distortion, large displacement, computation cost, and convergence issues by using a fluid domain with a fixed mesh and allowing the structure to immerse inside this domain.

The key advantage of the IB method lies in its ability to couple the momentum equations of fluid flow with the kinematic and dynamic equations of the solid structure. This is particularly valuable when modeling the large deformation of the MV leaflets during the dynamics closure of the valve, ensuring efficiency and robustness in simulating such behavior. However, there are some limitations to this approach as well.

Finally, we discussed the challenges in modeling self-contact between the MV leaflets and explored technical aspects of the master-slave formulation. This formulation is necessary for modeling self-contact between the MV leaflets. Self-contact is a complex behavior occurrence during the valve's closure, and failing to accurately represent it can lead to inconsistent results and numerical instability. In Chapter 4, we outline the numerical methods we used to model the self-contact between the MV leaflets.

Chapter 2

Data

To harness the full potential of mitral valve (MV) computational models and avoid misinterpretation of the outcome, it is crucial to grasp the underlying data used in these models. In this chapter, the details of the generic and image-based MV geometry are presented.

MV geometry can be represented either as generic, capturing the essence of a typical MV, or in more complex forms, derived directly from medical imaging. Depending on the purpose of the study, the geometry used in the literature is generic [KMP19], parameterized [PHS09], or image-based [RFS⁺13]. In our study, we implemented generic and image-based geometries in our fluid-structure interaction (FSI) model. The image-based geometry is extracted from a 3D micro computed tomography (microCT) scan of an explanted porcine heart. The image-based porcine valve closes naturally ex-vivo without orifice holes. For the generic geometry case, the chordae structure is optimal such as the valve closes. In this chapter, we discuss the details of both geometries.

2.1 Generic mitral valve

2.1.1 Using generic geometry in the mitral valve simulation

One of the primary reasons for adopting simplified or generic geometry is that the generic representation facilitates applicability in various scenarios. It reduces the complexities introduced to the simulation by having simplified surfaces, symmetric shapes, and more uniform borders. Generic MV geometry is suitable for scientific understanding, helping with the identification of fundamental MV behavior traits [KMP19, AAAB⁺22, AEHE19, ESH14]. But, the use of generic geometry can be attributed to other reasons as well.

As generic MV does not consist of highly detailed and multifaceted surfaces, the simplified shape of the valve can prevent some numerical instabilities that can be raised by the irregular leaflet surface and complex annulus shape. In addition, it is relatively less challenging to implement generic MV in the simulation setup. Realistic geometries can introduce complexities in applying appropriate boundary conditions. Simplified models can sometimes provide clearer and more controlled environments to apply specific boundary conditions. Initially, as we created our FSI model to simulate the MV dynamic closure, using generic geometry helped us identify some numerical issues more easily and create the simulation setup faster.

Modifying the generic geometry is also more convenient in studies that investigate the influence of various factors on MV behavior. Therefore, researchers might lean towards the generic MV when conducting parameter studies [KMP19, MVV19, LDSB10]. In this instance, generic MV can be used to discern the impact of various factors such as material properties [KMP19] or numerical method [LDSB10] without distraction if behavioral changes are predominantly attributed to the controlled parameter, rather than the complexities of geometry.

Another use of such geometry lies in the fact that there can be a lack of detailed data, or difficulties related to obtaining useful data. Obtaining real geometries can pose challenges. Even if advanced imaging methods required to visualize the structure of the mitral valve (MV), like magnetic resonance imaging (MRI), computed tomography (CT) scan, and microCT scans are common, extracting the valve components from the medical imaging is challenging. In our study, we implemented both generic and image-based geometries for different purposes. In the following, the details of obtaining the generic MV we used in our simulation and details of its geometrical characteristics are discussed.

2.1.2 Characteristics of the generic mitral valve

The generic geometry we used was designed by one of the collaborators of this study, Dr. Peter E. Hammer, as a part of his PhD work [Ham11], and we utilized this geometry for our simulation purposes. Fig.2.1 shows the orthographic views of the generic valve. It consists of two main leaflets, anterior and posterior, two commissures, and a set of chordae structures. The annulus ring follows a hyperbolic paraboloid curvature (potato chips), which is shown in red, and the chordae structure is initiated from two papillary muscles, shown in green nodes in Fig.2.1.b.

The length and width of the annulus ring are 3.5cm and 2.8cm respectively. The leaflets have a uniform thickness of 0.1cm , which is in accordance with other numerical studies of MV [MGG⁺13]. The potato chips curve of the annulus ring is created by dividing a cylinder and a cone geometry as shown in yellow in Fig.2.2.a. The leaflets are generated by dividing four hollow semi-cylinders from the original cone. For better visualization, only one of the semi-cylinders is shown in Fig.2.2.b. By changing the size of the cylinders and the intersection positions, different valve and leaflet sizes can be made.

2.1.3 Discretized domain

The leaflet of the generic MV geometry we used consists of smaller facets, which preserve the curvature of the geometry (see Fig.2.1). The generic MV geometry is discretized and represented by C3D10, a 10-node tetrahedral element. An example of the generic MV discretized mesh is shown in Fig.2.3.a. The main difference between the C3D10 and C3D4 elements is the order of interpolation. The C3D10 element uses quadratic interpolation, which means that it can represent curved surfaces more accurately than the C3D4 element, which uses linear interpolation. This makes the C3D10 element a better choice for modeling structures with curved surfaces, such as MV geometry. An illustration of C3D10 and C3D4 are shown in Fig.2.3.b and Fig.2.3.c respectively.

¹https://web.mit.edu/calculix_v2.7/CalculiX/ccx_2.7/doc/ccx/node33.html

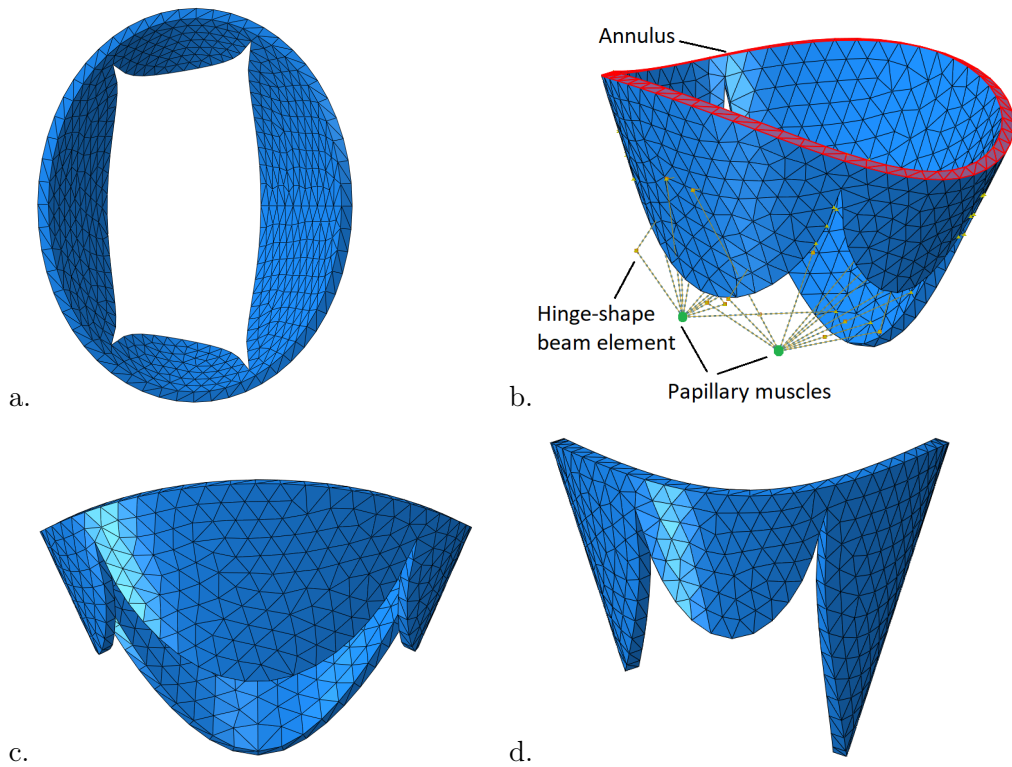


Figure 2.1: Orthographic views of the generic MV used for our simulation purposes. (a.) Top, (b.) 3D, (c.) front, (d.) and right side view [Ham11].

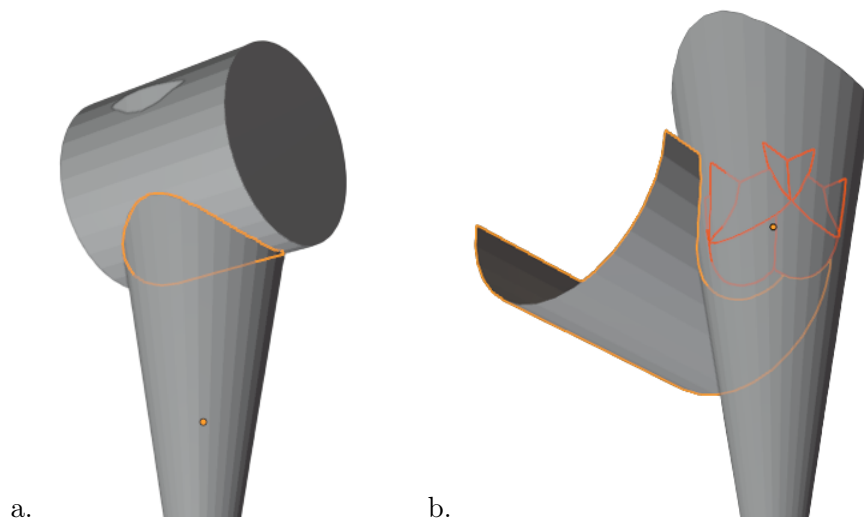


Figure 2.2: The process of creating the generic valve. (a.) The intersection between the cone and the cylinder creates the annulus ring. (b.) The leaflets are extracted from the body of the cone after its intersection with four semi-cylinders.

The C3D10 element has four integration points, while the C3D4 element has only one. This means that the C3D10 element can more accurately integrate the strain energy over the element, which can lead to a more accurate solution. However, the C3D10 element is more complex

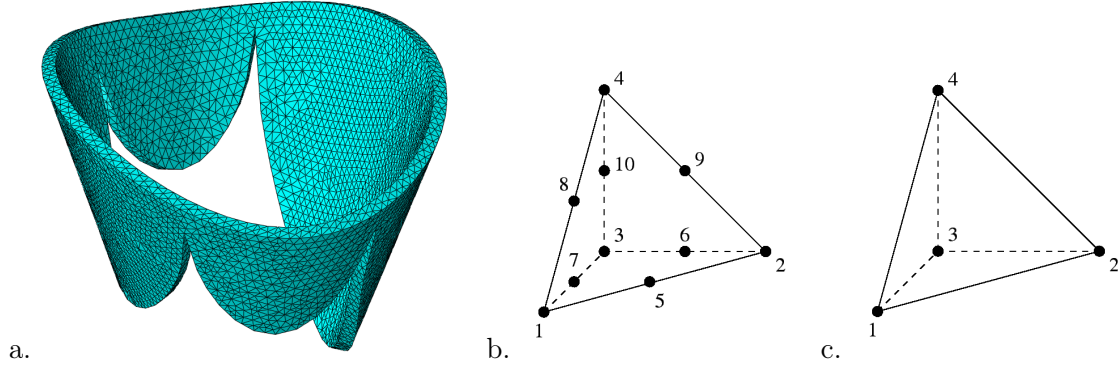


Figure 2.3: (a.) The discretized numerical domain of the MV geometry, (b.) C3D10, (c.) and C3D4 tetrahedral element¹.

than the C3D4 element, which might introduce some difficulties related to the convergence in problems involved with complex contact and deformation. In addition, this type of element needs more nodes to define which requires more computational resources to solve. In conclusion, the C3D4 element is often used for most structures, while the C3D10 element is used when a precise representation of the curvatures, also a more accurate distribution of stress and strain, is required.

The chordae structure is inspired by the actual heart anatomy where they initiate from two papillary muscles (shown as two green nodes fixed in the 3D space in Fig.2.1.b) and stretch to the leaflet surface. The chordae structure was fine-tuned for sealed closure of the MV in the healthy case. This was obtained by adding additional chordae or modifying the position of their attachment points on the leaflet surface. In the numerical framework, each chordae is represented using a two-node beam element, a specific type of finite element that simulates the linkage between two nodes in a three-dimensional space as a beam. These elements can withstand both compressive and tensile forces, following the linear Hookean law with a constitutive model based on experimental data [MES⁺11]. Given that the chordae within the heart function solely as tension cables, additional nodes are defined between the chordae endpoints. This configuration ensures that the beams assume a hinge-like shape, preventing them from experiencing compression and allowing them to operate exclusively in tension (see Fig.2.1.b).

In our study, we used the generic valve to capture contact in FSI simulation of MV (see chapter 4) and investigate the influence of anisotropy in MV dynamic behavior in chapter 5.

2.2 Image-based mitral valve

2.2.1 Using image-based geometry in the mitral valve simulation

While generic MV provides valuable insights regarding scientific understanding, capturing the intricacies of individual valves and the associated variations demands a more precise approach. Generic valves might introduce assumptions or simplifications that don't necessarily align with real-world anatomical variations. For instance, in the generic valve, the annulus ring is defined as a potato chip. Moreover, the chordae structure originated solely from two distinct nodes, intended

to represent the papillary muscles. However, in actual anatomical structures, the morphology of the annulus ring can be more complex, and the initiation of the chordae structure can be a cloud of points in the numerical domain. The heart valve behaves differently under different physiological and pathological conditions. Therefore, oversimplification of mentioned characteristics can lead to unrealistic results. Such details, the nuances of the leaflets and chordae structure, are crucial for personalized or patient-specific models. Utilizing geometry derived from medical imaging can enhance accuracy; however, working with patient-specific data may prove to be intractable or yield results that are less robust compared to those obtained with generic models.

The objective of integrating image-based geometry into the FSI simulation is to investigate patient-specific cases to achieve better predictive accuracy for outcomes such as valve closure, the likelihood of regurgitation, or the potential for valve-related complications. This is especially crucial when considering interventions like valve replacements or repairs, where understanding the post-operative valve behavior can guide optimal treatment strategies. Since the complete chordae network is not visible under clinical imaging modalities, many works use generic evenly distributed chordae tendinae [GFQ⁺17], adapt existing data to a specific patient [BGG⁺19], or use ex-vivo setup to obtain clean and high-resolution subject-specific MV imaging [TBE⁺16]. Most of the time, the annulus is approximated with a circular or elliptic shape, or cubic Hermitian splines [RFS⁺13] though its real shape is much more complex [PVH⁺21a, TEBI⁺20]. Only a small number of papers address MV simulation with leaflet and chordae geometry based on medical imaging as [FQG⁺18] who investigate how chordae structure impacts the MV dynamics and [RT23] in the context of prolapsus study. In our study, the geometry of both leaflet and chordae structures are obtained from medical imaging data.

2.2.2 Obtaining the image-based geometry

Here, we discuss the details of obtaining the image-based geometry extracted from a CT scan for our simulation purposes. A detailed discussion on various approaches to acquiring MV geometry from medical imaging is presented in [Pan21]. To the best of our knowledge, no publicly shared image-based geometry of the MV exists within the research community. For our study, we utilized image-based geometries that were previously obtained by other members of the CURATIVE associate team¹ in [Ham11, Pan21]. In terms of the extraction process, the geometry dataset we utilized can be classified into two specific categories: those segmented in the open state, as detailed in [Ham11], and those segmented in the closed state, as outlined in [Pan21]. In the following, we discuss more on the specifics of both datasets.

Segmentation in the opened state

Initially, the images of porcine heart valves in ex-vivo are obtained by using high-resolution computed tomography (MicroCAT, Siemens, Munich, Germany). During the imaging, the valve was pressurized by inserting an air pump through the aorta with regulated pressure similar to the physiological condition of the ventricular. All the porcine valves used for the imaging close naturally ex-vivo without orifice holes. The valve was scanned in both open and closed state which are shown in Fig.2.4.

¹<https://team.inria.fr/curative/team-members/>

The segmentation of both leaflet tissue and the chordae structure in this case was done manually by Dr. Peter E. Hammer, a member of the CURATIVE associate team¹. First, the open state of the image from the CT scan data is segmented to obtain the leaflet geometry. The advantage of segmenting the leaflets in their open state is that the leaflets are not under mechanical stress, thus they are not stretched. However, this approach presents a limitation: segmentation may become subjective when the leaflets come into contact with the ventricle wall, thereby making it difficult to differentiate between the leaflet tissue and the ventricle wall. In addition, as the chordae are not under tension in the opened state, the chordae structure is not clearly visible for the segmentation. Instead, the chordae structure is extracted by manual segmentation of the MV image in the closed state. Later, the chordae structure is reconstructed in the open state based on their attachment points on the leaflets [Ham11]. The top view of the image-based MV geometry in the open state with the chordae structure extracted is shown in Fig.2.4.c. In this category of dataset, three MV geometry was available. The 3D view of these three image-based MV geometry is shown in Fig.2.5a, Fig.2.5b, and Fig.2.5c. During this thesis, most of our analysis with the image-based geometry is done by using the P-1 valve.

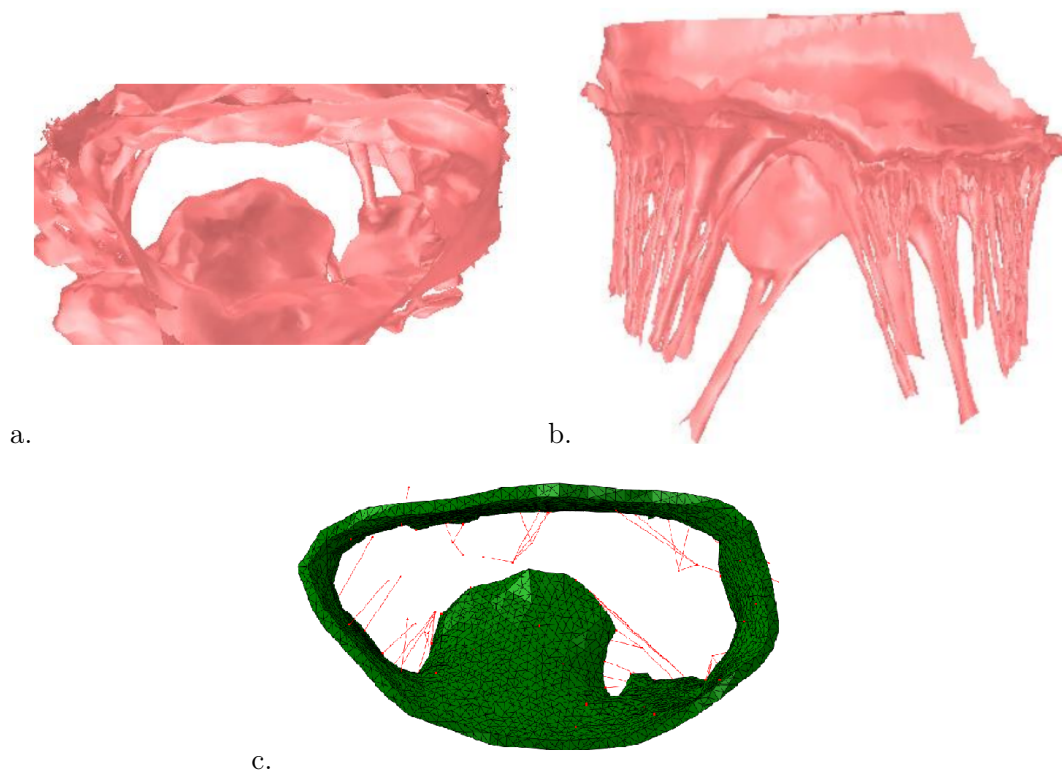


Figure 2.4: CT scan images of porcine heart MV in the (a.) open and (b.) closed state [Ham11]. (c.) The extracted geometry after segmentation with the chordae structure (shown in red) and the leaflets (shown in green) in the open state.

¹<https://team.inria.fr/curative/team-members/>

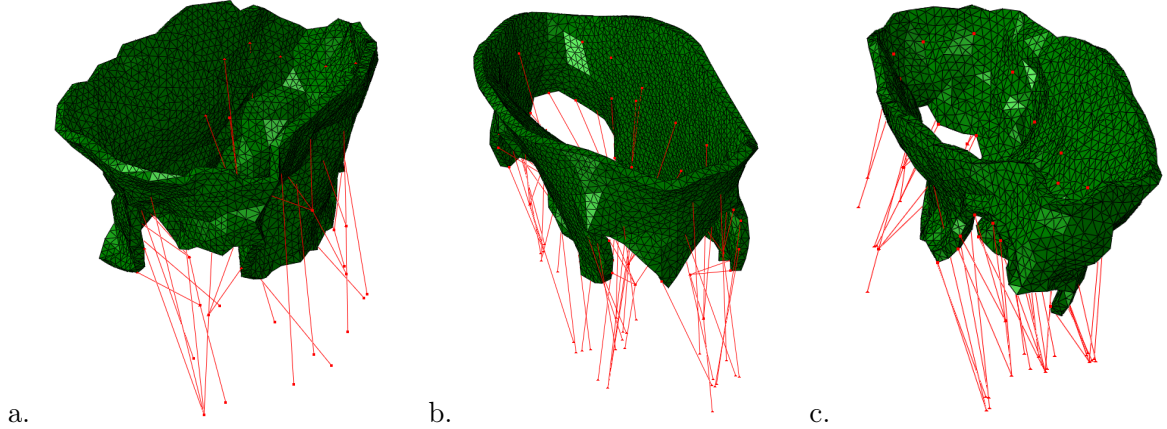


Figure 2.5: Three image-based MV geometry manually segmented in the opened state [Ham11]: P-1 (a.), P-2 (b.), and P-3 (c.)

Segmentation in the closed state

The second category of dataset, which contains only one MV geometry is based on a study done in [Pan21] to extract the MV chordae architecture with a fully automatic pipeline. In this research, high-resolution microCT (X-TEK HMXST225) was utilized to acquire MV images. Subsequently, the leaflet in its closed state was manually segmented. The chordae structure was then automatically segmented using a fully automated pipeline described in their work.

In the closed state of the MV, both the leaflet surface and chordae structure are under tension. This offers optimal visibility for exploring the chordae structure but influences the accuracy of the segmented leaflet. It is crucial to note that as the images are captured in their closed state, the leaflets are already subject to physiological stress and are in a stretched configuration. When we incorporate this extracted geometry into our simulation, initially, the leaflet is not under any external stress but the valve is in its stretched form as per the CT images. Consequently, the introduction of physiological stress during the simulation leads to further stretching of the leaflet. This is one of the limitations of the dataset we used and it presents a challenge for directly comparing the ground truth data from the CT scans with our simulation results, as the two scenarios do not perfectly align in terms of mechanical loading conditions on the valve.

The final result of the segmented MV in the closed state is shown in Fig.2.6.a. In our study, we start our simulation from the open state and simulate the dynamic closure of the MV. To obtain the opened state, we put the leaflet in a tube and passed a blood flow from the top surface of the leaflet (atrium surface) to penetrate the leaflet and open the valve. This process was done by conducting a fluid-structure interaction (FSI) simulation. The opened state of the valve is shown in Fig.2.6b. A summary of the data we used for our simulation is shown in table 2.1.

2.2.3 Smoothness of the leaflets in the segmentation process

Obtaining accurate leaflet geometry and chordae structure is a challenging task. While medical imaging can provide the MV geometry, it is difficult to observe the chordae structure or extract

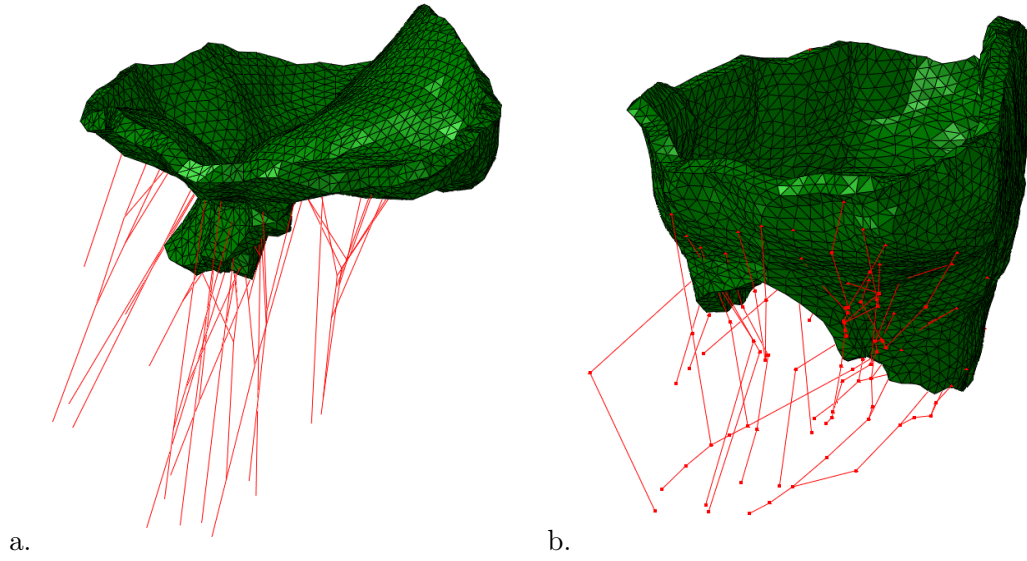


Figure 2.6: (a.) An image-based geometry segmented in the closed state [Pan21]. (b.) P-4: Opening the segmented geometry with fluid passing from the left atrium to the left ventricle.

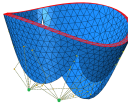
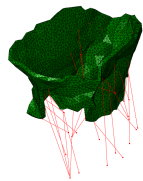
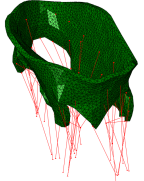
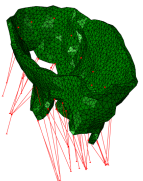
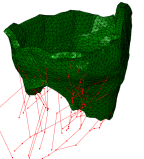
Data	Generic valve	P-1	P-2	P-3	P-4
Origin:	geometry-based	image-based	image-based	image-based	image-based
Acquisition state:		open state	open state	open state	close state
Chordae extraction:		manual	manual	manual	automatic
Mesh size:	20k	30k	30k	26k	38k
Image:					

Table 2.1: Summary of the data we used for our study of MV simulation.

the leaflet geometry with high accuracy [PVH⁺21b]. In the literature, several studies attempted to make the segmentation process automatic or semi-automatic. For example, in [CMB⁺21], they attempted to use artificial intelligence to automatically extract the MV geometry, or in [PVH⁺21b], a fully automatic pipeline for extracting the MV chordae structure is proposed. The final geometry resulting from the segmentation process is prone to error. In [CMB⁺21], they used mean absolute surface distance (MASD) to evaluate the segmentation outcome with the ground-truth measurements. We noticed that the mesh irregularities from the segmentation process are at the origin of the convergence difficulties adding complexities to the simulation. In addition, the roughness of segmented valves may impair the quality of the closure. We thus decided to investigate how smoothing impacts the simulation results. For this purpose, Laplacian

filtering is used to reduce the roughness of the leaflet surface in P-1 while preserving the whole geometry [Sor05]. Fig.2.7 shows the P-1 before and after applying the filter. The average absolute distance of each node in the smoothed valve, to the one in P-1 is 0.145mm . In both cases, 1mm uniform thickness is specified for the MV leaflet. In chapter 5, we compared the valve closure in both the original P-1 and the smoothed case to investigate the impact of smoothness on MV closure.

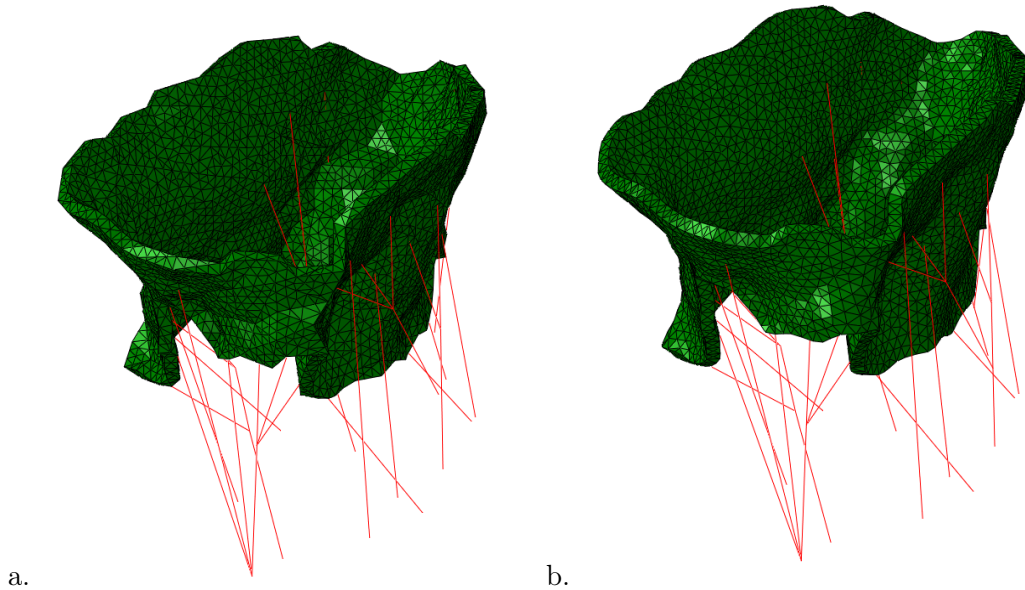


Figure 2.7: Image-based P-1 valve before (a.) and after (b.) applying the smoothing filter.

2.2.4 Discretized domain

The leaflet geometry consists of smaller faces. In contrary to the generic valve, using the C3D10 element resulted in element skewing under applied forces, and eventually diverging the computation. Therefore, the quadratic nature of C3D10 makes it not suitable when element nodes on complex surfaces are included in a contact model. This issue is alleviated by using a simpler C3D4 element (see Fig.2.3.c) which is more robust for surfaces that undergo complex contact behavior. The chordae structure is represented by a linear elastic two-node beam element with an articulated mechanism, similar to the hinge-shape beam element mentioned in the section of the generic valve (see Fig.2.1.b), to avoid compression load in the chordae.

2.2.5 Limitations

Acquisition

The utilization of high-resolution imaging, such as CT scans, poses a risk to human subjects, thereby necessitating the reliance on animal models, mainly porcine valves, for numerical studies on MV due to their physiological similarity to human valves [Pan21]. Therefore, high-resolution data is possible to obtain ex vivo. The geometries employed in our simulations were derived

exclusively from ex vivo measurements, which constrains the applicability of our results to in vivo scenarios. In the open-state segmentation process, the leaflets are connected to the LV wall [Ham11]. Distinguishing between the leaflet surface and the LV wall can be challenging, leading to potential errors in measurements. In the case of closed-state, our dataset was obtained based on automatic extraction of chordae structure explained in [Pan21]. In the CT images, the structure of the chordae is not clearly visible near its attachment point to the leaflet. As a result, during automatic extraction, the chordae are accurately identified only up to a point near the leaflets. Subsequently, the chordae are artificially extended to reach the leaflet surface. This approach may introduce segmentation errors in the chordae structure close to the leaflet surface.

Evaluation

In the dataset obtained from the open state, the annulus ring is not fixed, therefore the annulus shape changes between the peak systole and peak diastole. On the contrary, in our simulation, we assumed a fixed annulus ring, which does not accurately reflect the actual physiological changes in the MV throughout the cardiac cycle [CAF10]. This assumption of a fixed annulus ring limits the validity of comparisons between our simulated outcomes and ground truth data. In the dataset derived from the closed-state condition, the ex vivo setup features a fixed annulus ring. As a result, the annulus ring remains constant between peak systole and peak diastole. However, in the closed state, the leaflets are already under tension. In our simulations, where the valve remains closed, this tension in the leaflet tissue is further increased. Consequently, this limits the ability to make accurate comparisons between the MV behavior in the simulation results at the peak systole, and the ground truth data.

Therefore, in our study, only global behavior of the MV dynamic motion is evaluated. We compared the valve behavior with some expected physiological aspects of the MV, such as by measuring the leaflet bulging volume and observing the coaptation between the leaflets during the self-contact between the leaflets. Furthermore, to evaluate the dynamic closure of the MV, we do not have any intermediate data to compare our valve motion between the opened and closed states. Instead, we compared our simulation outcomes with alternative measurements available in the literature, for instance, the in vitro chordae force as reported in [JSH⁺03].

2.3 Conclusion

In this chapter, the basic information regarding the MV geometrical data, characteristics, and its acquisition is presented. We explored both generic and image-based MV geometries, emphasizing the importance of each.

We have detailed the acquisition processes for both generic and image-based geometries. It is important to note certain limitations in image-based geometries, such as the subjective segmentation of leaflets in the open state and the stretched tissue of the leaflet in the closed state. In total, we described one generic and four image-based geometries for our simulation purposes. In chapter 4, we utilized the generic valve to simulate the MV dynamic closure in healthy and pathological cases. Subsequently, we used the generic valve and P-1 image-based valve in chapter 5, to investigate the influence of material model and geometrical characteristics.

Furthermore, in chapter 5, we employed the P-2, P-3, and P-4 image-based geometries to show the scalability of the FSI model.

Chapter 3

Proposition of the Fluid-Structure Interaction Model

The fluid-structure interaction (FSI) formulation based on the immersed boundary (IB) mesh representation is already available in the Abaqus explicit solver [Man12]. Once the geometry is obtained, we implement these geometries in the FSI solver with a set of boundary conditions. In this chapter, the detailed setup for the FSI simulation of the mitral valve (MV) is presented.

In this chapter, we first explore the specifics of incorporating the MV geometry into the FSI case setup. We also discuss various approaches to define the numerical domain of the left ventricle (LV). This section presents the case setup necessary for implementing the FSI simulation of MV inside the Abaqus explicit solver. Following that, we provide detailed descriptions of the model configuration and the parameters involved, which include the details necessary to have a proper contact model to capture the self-contact between the MV leaflets, boundary conditions, and simulation settings used in the FSI model.

This chapter serves as a bridge, connecting the theoretical foundation of the MV FSI simulation with the practical applications that follow. It lays down the basic understanding of the implementation and model configuration used for the subsequent chapters, where the MV behavior in various cases is investigated and simulation results will be unveiled and discussed.

3.1 Fluid domain

3.1.1 Left ventricle in the mitral valve fluid-structure interaction studies

With respect to the information provided regarding the FSI numerical domain in the previous chapter, the MV geometry is introduced to the FSI setup as a Lagrangian mesh. The MV mesh is then immersed inside an Eulerian domain representing the blood inside the LV. For an accurate simulation of the MV dynamic closure, it is essential to model the fluid effects on the leaflets [LDSB10] and the surrounding anatomic structures: annulus, chordae, papillary muscle, and ventricle. In the literature on MV FSI simulation, the representation of the LV shape can be classified into three distinct categories (Fig.3.1). In the first category, the MV is mounted inside the LV geometry extracted from medical imaging (Fig.3.1.a). Typically, for the closure of the valve during the cardiac cycle, no pressure inlet is defined in this setup, and

the pressure is built up by squeezing the ventricle geometry which leads to the valve closure as explained in [CMMS20, GFQ⁺17, BGG⁺19]. In the second approach (Fig.3.1.b), a U-shaped geometry, which is a simplified version of the LV is utilized, as demonstrated in studies such as [AEHE19, LDZSB11]. During the closure of the valve, the fluid enters from the left side of the domain and passes through the MV. In the final approach, the MV is placed inside a tubular geometry [TEBI⁺20, OÖB⁺21, TBP⁺17]. Depending on the placement of the annulus ring, a tube can be fitted on the annulus ring as in [DYS⁺19] (Fig.3.1.d), or housing is used to seal the area between the annulus ring and the cylinder walls as in [TEBI⁺20, OÖB⁺21, TBP⁺17] (Fig.3.1.c).

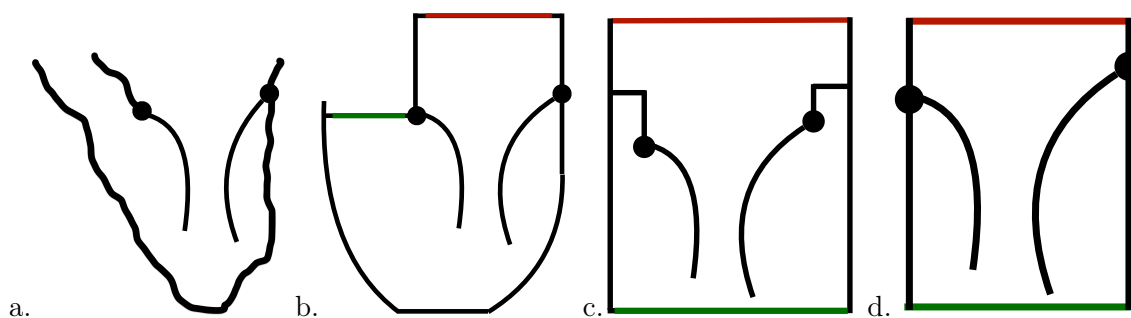


Figure 3.1: A simplified illustration showing the LV geometry extracted from medical images (a.), simplified ventricle shape, or U-shape (b.), and two different representations of the tubular volume (c.) and (d.). During the closure, fluid inlets are in green, and fluid outlets are in red.

3.1.2 Tubular left ventricle

MV behavior with image-based LV has already been investigated in studies such as [GFQ⁺17, CMMS20, MCM⁺17, BGG⁺19, AEHE19]. However, the practicality of implementing such geometries for patient-specific models needs further investigation. In one study in particular, [LDSB10], they conducted a comparison between a U-shape and a tubular ventricle. The results showed that although the stress pattern on the leaflet was similar in both cases, the magnitude and closed state differed. The FSI approach used in this study was based on the ALE method, which due to the limitation of the method in capturing contact between the leaflets, the quality of the closure and the coaptation area could not be investigated.

The image-based LV is a highly irregular and asymmetric structure and it varies for each case. The implementation of such geometry requires accurate knowledge of the LV motion from temporal data extracted from medical imaging. This information is necessary to define the LV displacement as a boundary condition during the simulation to build up the proper physiological pressure that closes the MV. Most of the time, such data is not available, or easy to obtain accurately. In addition, validation of results based on such data is not straightforward. On the other hand, with a simplified LV geometry, validation experiments can be designed more easily in a controlled lab setting. Therefore, a simpler tubular representation of LV is preferred in the literature for investigating the MV behavior as in [DYS⁺19, TEBI⁺20, OÖB⁺21]. In our simulations, we also used a simpler tubular representation of LV and put our focus on understanding and investigating other aspects of MV behavior. Such aspects, which are

mentioned in the next chapters, are investigating the coaptation and closure of the MV in healthy and pathological cases and the influence of the material characteristics on MV behavior.

In the case of the tubular volume, one advantage of using a fitted tube compared to the larger cylinder is the computation time. The size of the fluid domain in FSI simulation affects computation time, and using a fitted tube can have a noticeable impact on this aspect. In addition, using a large cylinder with housing compared to a fitted tube might lead to a more accurate representation of the force distribution on the leaflet, taking into account the impact of other organs and the blood motion pushing the MV inward during the closure. Therefore, in our simulations, we considered both fitted tube and large cylinder as a representation of LV. Details regarding the effect of using both LV are further discussed in the next chapters.

3.2 Fluid-structure interaction setup

In our simulations, we used two FSI setups. In the first setup, the MV is mounted inside a tube fitted on the annulus ring. In the second, the MV is situated within a cylinder whose diameter exceeds that of the annulus ring. In the following, both cases are described in detail.

3.2.1 Mitral valve inside a fitted tube

The MV is immersed inside a tubular blood domain representing the LV geometry, with chordae endpoints connected to a fixed node located on a papillary muscle and to the leaflet surfaces. The annulus nodes are fixed to the ventricular wall. Fig.3.2 shows the FSI case setup for generic and image-based MV mounted inside a fitted tube. One of the differences between the generic MV case setup and the image-based setup is that the annulus shape in the image-based setup is more complex than the generic one, which influences the shape of the tubular LV. The tube in the generic valve is relatively simple with an elliptic base, but the one in the image-based valve has a more complex shape. The tube base needs to be the shape of the annulus ring to prevent blood from passing over the annulus. The tube direction is normal to the annulus plane and is determined based on a principal component analysis on the vertices of the annulus ring.

3.2.2 Mitral valve inside a large cylinder

The LV representation with a fitted tube can help with sealing the streamline in the case of image-based valves whose annulus is generally not planar and with arbitrary shape. However, with a fitted tube, a difficulty is that image-based acquired leaflets may be partly outside the tube. The other issue is that the fitted tube imperfectly reflects the fact that the valve is immersed in a large volume of blood in the ventricle. We thus also consider implementing a large cylinder as LV in our case setup. A large cylinder needs an additional geometry to obstruct the flow between the annulus ring and the cylinder walls and define it as an elastic material with a high Young's modulus. The expected outcome from using a large cylinder and a seal would be a more accurate representation of the force exerted on the MV leaflets during closure by other organs, as it captures the effect of flow pushing the leaflets from the sides. In the next chapters, the MV behavior in a fitted tube and large cylinder is compared. Fig.3.3 displays the cross-section view of the implementation of P-1 image-based valve in both a fitted tube and a larger cylinder.

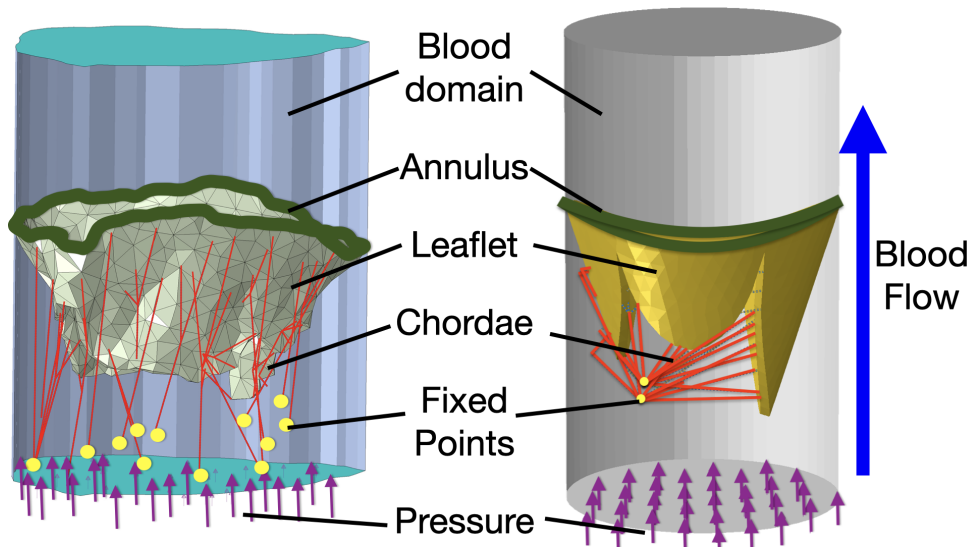


Figure 3.2: Case set-up showing the P-1 image-based (left) and generic (right) MV mounted in a generalized and elliptic base fitted tube.

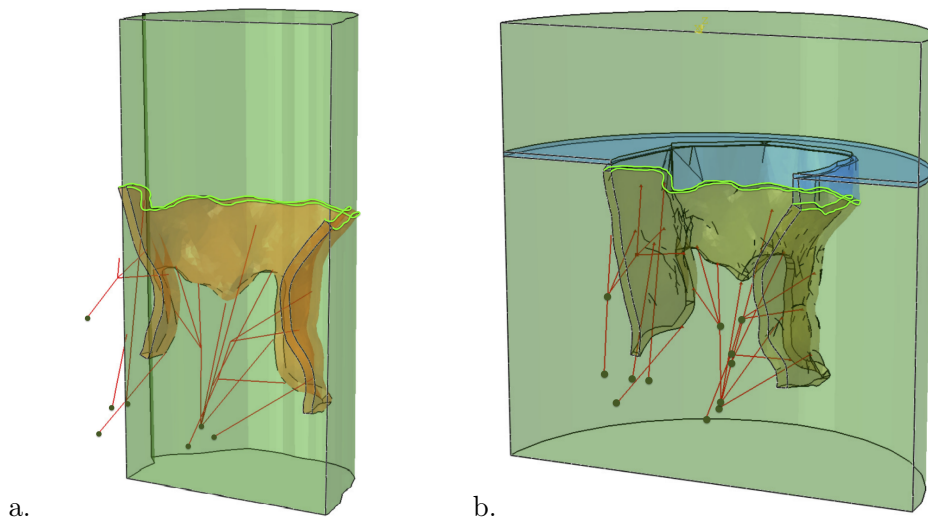


Figure 3.3: Case setup for (a.) fitted tube, and (b.) large cylinder. Orange: valve, red: chordae, blue: additional geometry to obstruct the flow, and light green: pinned annulus region.

3.3 Model configuration

In the FSI simulation setup, several components, including the annulus ring, leaflets, chordae structure, and ventricles are involved. We will finish this chapter by exploring the details of the initial and boundary conditions assigned to these parts and the numerical aspects that facilitate the convergence of our simulations.

3.3.1 Modeling self-contact of mitral valve leaflets

Here, we outline the details of the self-contact model employed for our simulations. Each subsection provides technical aspects and information essential for ensuring an efficient and robust model. This information is important for convergence in the simulation of self-contact between the MV leaflets.

Balanced master-slave contact model

The contact between the two surfaces of the MV leaflet should exert equal and opposite forces on each other. In the master-slave formulation, the contact forces are only applied to the slave nodes. For our simulations, we used a balanced master-slave formulation [Man12]. The balanced master-slave model fundamentally enhances the master-slave approach by essentially applying it twice, inverting the roles of the surfaces on the second iteration. Initially, one surface assumes the role of the master while the other serves as the slave. Afterward, their roles are switched in the subsequent iteration, making the former slave the new master and vice versa. After both iterations are complete, the contact forces computed from each application are averaged. This method not only ensures symmetry and balance in the contact formulation but also aims to improve the accuracy and stability of the contact interactions by taking into account the characteristics and responses of both surfaces.

Relative motion of the surfaces in contact

In our simulation, the nodes involved in the contact model are allowed to move and rotate freely in the 3D space. This means that the contact pairs are allowed to separate after getting in contact or slide over each other. This will increase the computation cost, as each time the slave nodes can change the master facet that they are registered to in the contact model. However, this is important to consider, as the surfaces in self-contact of the MV leaflets have many folds and complex geometrical shapes as curtains, and slide on each other in an arbitrary manner. Fig.3.4 shows an example of this free movement. The dotted line shows the arbitrary path of the slave node S through time. Once the contact pair between the slave node and the master facet is defined in the initial state, the contact model allows the slave node to change the master facet depending on its proximity to the facets on the master surface. This behavior is known as finite sliding motion [Man12]. In other simpler contact forms, once the closest master facet is defined, the slave node is only interacting with the tangent plane of that specific facet. These simple contact models are faster to compute but they are not able to capture the complex contact behavior of the thousands of nodes involved in the self-contact of the MV leaflets.

Search for contact pairs

When modeling contact in a large numerical domain, thousands of nodes can arbitrarily get involved in the contact model. Therefore, it is necessary to determine potential contact pairs, essentially, figuring out which points on one surface might come into contact with another surface. To manage this effectively, we used a contact model that employs global and local search algorithms for contact.

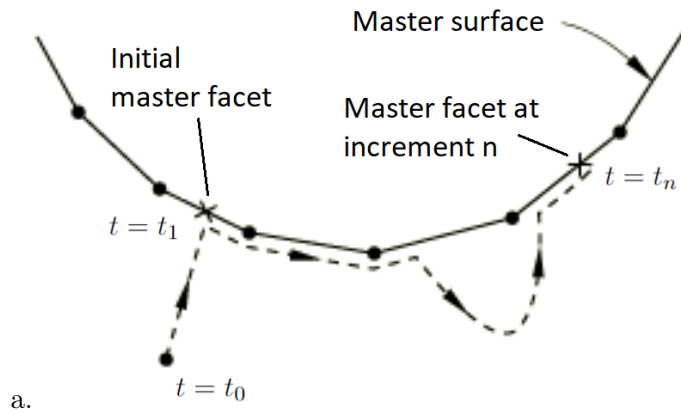


Figure 3.4: Simplified trajectory of a hypothetical slave node in contact interacting with multiple facets and able to separate from the master surface [Man12].

A global search is a procedure used to determine the closest master surface facet for each slave node in a given contact pair. If the minimum distance is detected, the slave node is considered to be in "potential contact" with the master surface. The global search is computationally intensive, as it requires checking all slave nodes against the master surface. Therefore, a bucket sorting algorithm is used to minimize the computational expense of these searches. The global search is performed by first dividing the master surface into a number of bins. Each bin contains a set of facets that are close together in space. The global search then proceeds by looping through each slave node and computing the distance from the node to all of the facets in the same bin as the node. Due to the large number of nodes and high computation cost, by default, the global search is performed every 100 increments [Man12]. However, problems involving self-contact are more complex and need more frequent global search. Therefore, in our self-contact model for MV leaflets, the global search is performed every four increments. Fig.3.5 shows the global search in one single bin. After measuring the distance between the node S to all the facets in that bin, the closest facet is identified. The node A , which is the nearest node to the S on this facet, is considered the tracked master surface node.

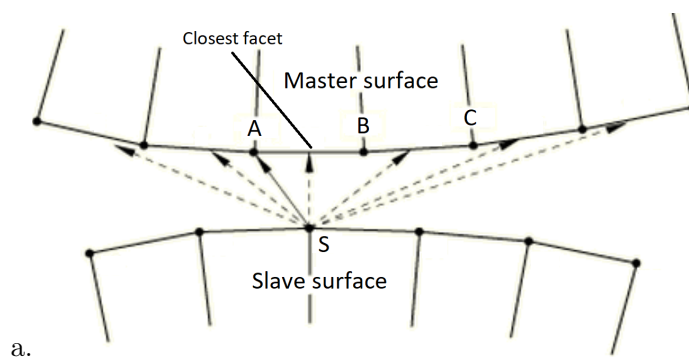


Figure 3.5: 2D illustration of a hypothetical bin in a global search [Man12].

Once the closest facet to the slave node is identified, a local search is activated. A local search is a procedure that is used to keep track of the closest master surface facet for each slave

node and update the closest master surface if necessary. The local search is performed every increment by default, and it only considers the slave nodes that are close to the master surface. This search is computationally cheaper than the global search since it only focuses on previously identified potential contact pairs. In the local search, the distance between the slave node (S) and each neighboring facet of the tracked master surface node is measured. As the simulation progresses, the slave surface is displaced. Once the closest facet to the slave node is updated, the closest master node on that facet to the slave node is identified. This node will be the new tracked master surface node. To show this procedure in an example, Fig.3.6 illustrates one iteration of local search. Initially, node A is the tracked master surface node. As the slave surface is displaced, node C , which has a smaller distance to S compared to node A , will become the newly tracked master surface node.

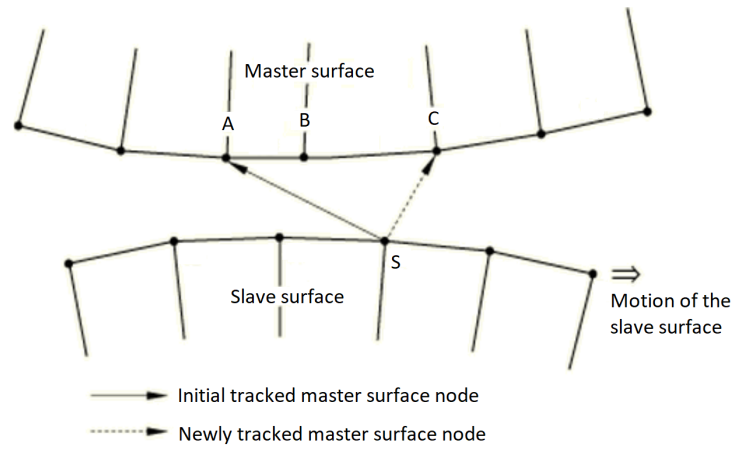


Figure 3.6: Local search finding the newly tracked master surface node as the slave surface is displaced [Man12].

Normal and frictional contact

Surfaces in contact transmit normal and shear forces across their interface. In our model, contrary to some existing works that used friction-less contact models [HPH11, AGPT09], both perpendicular and frictional contacts between leaflets are considered. Fig.3.7 shows the discretized surfaces in contact when a slave node, S , penetrates the master surface with the penetration rate of g_n in the direction n normal to the master surface.

The normal contact force applied on the slave node (S) depends on the penetration rate (g_n) and the penalty term (\mathbf{K}_n) as:

$$f_n = \mathbf{K}_n(g_n). \quad (3.1)$$

\mathbf{K}_n can be a real number, tabular, linear function, or exponential function of the distance between the slave node and the master surface. It is defined based on the constraint enforcement which will be discussed in the next section. The frictional contact is basically the contact force applied on the slave node S , in the tangential direction of the master surface. This force is calculated by the Coulomb's friction model:

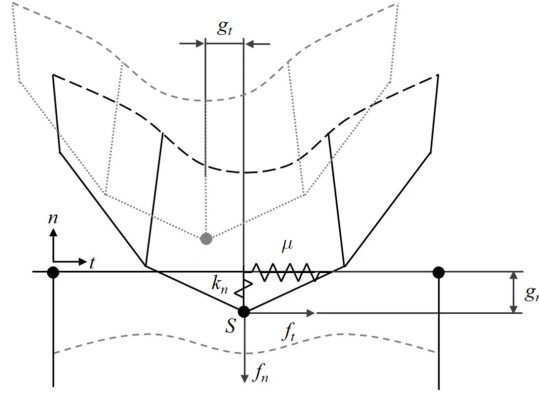


Figure 3.7: Numerical representation of two surface in contact [RMK14].

$$f_t = -sgn(g_t)\mu f_n, \quad (3.2)$$

where $sgn(g_t)$ is the sign function of the lateral displacement of the slave node (g_t) described as:

$$sgn(g_t) = \begin{cases} 1, & \text{if } g_t > 0 \\ 0, & \text{if } g_t = 0 \\ -1, & \text{if } g_t < 0. \end{cases} \quad (3.3)$$

μ , the friction coefficient, is a number between zero and one that determines the roughness of the surfaces. According to this model, the amount of frictional contact depends on the normal contact force and the friction coefficient [RMK14].

Constraint enforcement

The contact force introduces a significant amount of force on a single node in the whole structure's numerical domain. Implementing the contact force abruptly is known as hard contact. By using this approach, when the distance between the slave node and the master surface reaches zero, a significant contact force is suddenly exerted on the node to prevent its penetration into the surface. Hard contact reduces the penetration in contact, but in most cases that involving complex contact behavior, it can lead to numerical instability and divergence in the whole system. Fig.3.8.a shows the relationship between the contact force and the penetration rate in case of hard contact.

Another way to address force overclosure is soft contact. Once the contact forces are calculated, they will be introduced to the system gradually. In most complex contact situations, soft contact is necessary for the convergence of the simulation. The soft contact is implemented by two approaches, the method using a penalty function and the method employing Lagrange multipliers [SMB11].

The Lagrange multipliers method introduces auxiliary variables (the Lagrange multipliers) to enforce non-penetration constraints between contacting bodies. When a slave node exceeds a given penetration tolerance into the master surface, the contact pressure is adjusted. Iterations

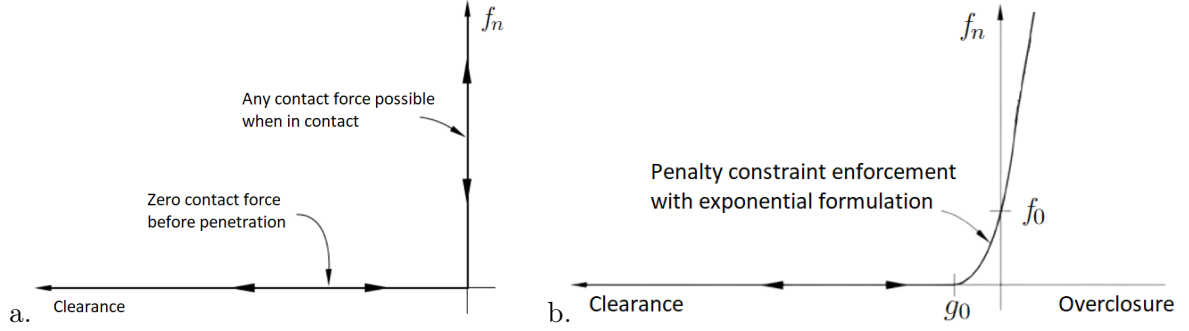


Figure 3.8: (a.) Hard contact force overclosure. As the distance between the slave node and the master surface reaches zero, any possible contact force will be applied on the node to keep it clear from penetrating the surface. (b.) Penalty constraint enforcement with exponential formulation [Man12].

are then performed until convergence is reached. This adjustment and iterative process continue until the penetration falls below the set tolerance. This method ensures that two bodies in contact neither penetrate each other nor pull apart when they should be in contact. By solving for these multipliers along with the original system equations, the contact constraints are precisely maintained, providing an exact solution to the contact problem. Even though the promise of a precise solution for contact and no penetration seems appealing, the implementation of contact constraint based on the Lagrange multiplier is too complex for self-contact between MV leaflets and the simulation based on this approach diverges.

A more suitable approach to our problem is using penalty-based constraint enforcement. As shown in Fig.3.8.b, the contact force in the penalty approach follows an exponential rate depending on the clearance, a distance between the slave node to the master surface. According to this approach, as the clearance reaches a certain distance (g_0), the contact force becomes non-zero. f_0 is the contact force applied on the node when it touches the slave surface. This exponential function is mentioned in equation 3.1. In our simulation, we set g_0 to be zero. Therefore, f_0 will consequently be zero and the contact force will be active from the moment when the slave node penetrates the master surface. As the depth of penetration increases, the contact force applied to the slave nodes escalates at an exponential rate to counter the intrusion. Simultaneously, an equivalent force is exerted on the master surface at the point of penetration. This approach will result in a model that allows for penetration but reduces the numerical instabilities caused by the abrupt change in the force distribution on the nodes.

Self-contact loop

The contact model we used for our simulation is an efficient computational approach, which is designed to calculate the intricate interaction between the MV leaflets. This process is guided toward reducing computational issues and computational costs, while most importantly, ensuring convergence of the simulation process. Based on the information provided, the systematic progression of the self-contact model we used can be described as follows.

- **General search:** The algorithm initiates by conducting the general search. The purpose

is to identify potential contact pairs. This step is vital to preemptively identify nodes that might come into contact during the simulation, ensuring efficient computational resource utilization.

- **Local search:** Once potential contact pairs are identified, a local search is executed to frequently track these contact pairs. This will increase the model's efficiency by focusing on imminent or active contact areas.
- **Identifying penetration and calculating normal contact:** By monitoring the potential contact pairs, the penetration rate is measured. Afterward, the normal contact force is calculated by utilizing the penalty approach. The penalty function has an important influence on determining the extent of penetration by generating an appropriate normal force in response.
- **Frictional contact:** Frictional force is calculated based on the relative motion between the contact pairs. The Coulomb's friction model is used for this computation, a standard method that offers both accuracy and computational efficiency.
- **Balanced master-slave:** Applying the aforementioned steps twice, by changing the role of the master and slave surfaces in the second time. Then, averaging the calculated forces based on the balanced master-slave approach. This step provides a symmetric and stable representation of contact forces in self-contact between the MV leaflets.
- **Integration into the finite element model:** The contact forces, encompassing both normal and frictional contributions, are integrated into the finite element model. Consequently, the trajectory of the nodes in contact is predicted. The final contact force, the combination of both normal and frictional contact force, will be implemented in equation 1.11 as the f_{cnt} term.

In the default setting of the Abaqus explicit solver, a general contact algorithm is employed. This algorithm detects any element in contact and exerts a normal contact force to prevent penetration. However, based on our observation, utilizing the general contact algorithm for MV leaflets does not yield precise results. This is due to the fact that the general contact algorithm prevents surfaces from colliding (keeping a small gap between the surfaces in contact) and it considers all the elements on the leaflet to be involved in the contact model, which is not necessary. Additionally, it does not consider frictional contact. In our specific setup, we first excluded the leaflet elements in the general contact algorithm. We then selected the elements on the atrium surface of the leaflets and established a self-contact set. Within this set, we specified all the requisite settings outlined in this chapter, including the specifications related to global and local search, the penalty method, as well as frictional and normal contact. Consequently, the leaflet surfaces are allowed to collide as they would naturally, with no gap between the contact surfaces.

3.3.2 Annulus ring

In Fig.3.3, the annulus is positioned in between the two light green straps. We noticed that by applying the pinned boundary condition (meaning the displacement of nodes is restricted, but

it can rotate freely about any axis) on all the nodes on the annulus ring, including the nodes in between the two straps, the annulus becomes over-constrained. In this case, perturbations on the leaflets, as small vibrations, were observed in the leaflet movement, which is caused by a numerical instability. Therefore, to address the issue of over-constrained nodes, we applied the pinned boundary condition solely to the nodes on the two light green straps, restricting their displacement, while allowing the nodes in between to be free. In the case of the large cylinder, the nodes on the upper surface of the seal part (shown in blue in Fig.3.3.b) are also fixed to resist the forces from the blood momentum.

3.3.3 Leaflets

For the leaflets, in both generic and image-based MV, a uniform thickness of $1mm$ is specified. However, our model is not restricted to only uniform thickness. We used uniform thickness because from the CT scan, the position of the top surface of the leaflet (atrial surface) is known, but the lower surface is a mixture of leaflet tissue and chordae bundles. For the self-contact between the leaflets, the simulation with the image-based valve diverges when both sides of the leaflet are involved in the contact model. In image-based MV geometry, the angle between the leaflet facets is relatively sharper compared to the generic valve. This makes contact behavior more complex by assuming that neighboring facets are constantly going to be engaged in contact. Therefore, only the nodes that are situated on the atrial surface are included in the contact model. In both generic and image-based valves, a friction coefficient of 0.2 is used [XJN⁺12] to model the shear contact between the leaflets.

Large deformation of MV during the MV closure eventually leads to distortion in some of the tetrahedron elements used for the discretized numerical domain of the leaflets. This may potentially lead to negative element volumes, where node alignments in the element may exhibit skewness or asymmetric deformation. Divergence issues in large deformation simulations can be fixed with techniques such as smoothing, re-meshing, and element distortion control. We thus used a penalty-based element distortion approach to make large deformations possible. In this technique, elements are monitored for distortion. The effect of the penalty-based element distortion depends on the threshold specified for identifying the elements as distorted. Once the strain in a specific element reaches a certain percentage of nominal strain, for example, a rectangular element under uniaxial compression undergoes 95 percent of nominal strain, deformation constraints are applied to this element. To have more stability in the system, once the element distortion is activated for a specific element, the stiffness of that element is increased based on a penalty technique.

Based on our observations, element distortion control only involves a small number of elements (less than 1% percent) during the MV closure, where some elements are compressed in between the wrinkles of the leaflet. To evaluate the influence of distortion control on the accuracy of the results, we compare the displacement in the results of the simulation with the thresholds of 10 and 30 percent for the element distortion (see table.3.1). Considering the small difference in the displacement of the leaflet nodes, the effect of distortion control used in the FSI simulation of MV is negligible. The threshold can be further reduced below 10 percent, however, it does not guarantee the convergence of the simulation. We noticed that with the threshold set at 10 percent, the element distortion does not lead to divergence of the simulation. Therefore,

distortion control, in combination with a fine mesh resolution, prevents elements from becoming non-convex and generating negative element volumes, which is the cause for the majority of convergence issues in large deformation simulations.

Element distortion threshold (of principal strain)	Displacement
10 % :	1.434×10^{-2}
30 % :	1.428×10^{-2}
Difference :	0.4 %

Table 3.1: Influence of distortion control on MV leaflet node displacement with two different distortion thresholds.

3.3.4 Chordae

The chordae structure is basically a set of connections between nodes that are connected to the papillary muscle, the endpoints on the leaflet surface, and branching points in the middle. The connection between the nodes of the chordae structure is modeled as a linear elastic beam with a linear Hooke constitutive model based on experimental data [MES⁺11]. The displacement of chordae nodes representing the papillary muscles (shown in yellow in Fig.3.2) are restricted by the pinned boundary condition. The branching points are free to move and rotate depending on the movement of the leaflet and chordae structure. Due to the challenges in MV geometry acquisition, and the complexity of the chordae structure near the leaflet surface, no study was able to accurately extract the chordae structure in the region near the leaflets or find the exact position of the attachment points of the chordae to the leaflets. A common technique used in the literature is to specify the chordae endpoints near the leaflet where the visibility of the chordae structure is acceptable [DKS18, Pan21]. In both image-based and generic valves, a sphere of influence with the chordae endpoint in the center is defined to connect the nodes on the leaflet surface to the chordae structure. Leaflet nodes within this sphere are linked to the endpoint, resulting in coupled displacements between them. An illustration showing the sphere of influence a chordae attachment point exerts on the leaflet nodes is shown in Fig.3.9.

Based on this approach, for each chordae attachment, a gradually decreasing distribution of the chordae forces over a group of leaflet nodes avoids the concentration of forces over a single node and potentially prevents element distortion. This also reduces the degree of freedom of leaflet nodes with respect to the chordae endpoint. The chordae endpoints are attached to the leaflet nodes using a ball joint connection. Connecting only the inner surface of the leaflets to chordae results in shear stress through the leaflet thickness, which causes element distortion. By contrast, involving nodes on both sides of the leaflet thickness eliminates the unnecessary shear tension and reduces the excessive deformation in the elements. Therefore, we used an influence sphere with a size of the leaflet thickness to include leaflet nodes on both sides of the leaflet surface.

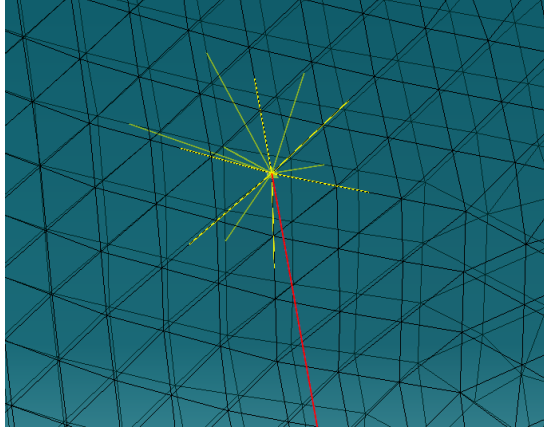


Figure 3.9: Sphere of influence for chordae endpoints: The chordae are depicted in red, while the connections between the chordae endpoint and the leaflet nodes are illustrated in yellow. The dark lines represent a transparent view of the tetrahedral elements.

3.3.5 Blood

In our study, we focused on simulating the MV closure. The simulation starts from the beginning of the systolic phase until the peak systole in the cardiac cycle. Time-dependent transvalvular pressure based on real measurements extracted from [Lev13] is applied on the bottom of the fluid domain, as shown in Fig.3.2, to simulate the pressure difference between the LV and left atrium. The blood is simulated as an incompressible, isothermal, and Newtonian fluid with a dynamic viscosity of $2e^{-3} Pa.s$ and density of $1060 kg/m^3$. No-slip boundary conditions, i.e. a zero blood velocity relative to the surface, are considered on the leaflets as well as the ventricle wall, which is the common way to model the fluid-structure interface.

The tubular LV is presented by linear 3D elements consisting of 8-node reduced integration. A reduced integration element is an element that uses fewer integration points than a fully integrated element. This means that the stiffness matrix is computed using a lower-order approximation of the strain field. The number of integration points used in a reduced integration element depends on the order of the element. A linear element has a single integration point, a quadratic element has two integration points, and so on. The higher the order of the element, the more integration points are needed to accurately integrate the strain field. Reduced integration elements are used to improve the computational efficiency of analysis, but in the case of cubic elements, they are prone to skewness caused by hourglassing.

Hourglassing refers to a numerical instability in which an element displays a non-physical, trapezoid-like deformation. In this case, the overall deformation of the element is zero, but one side of the element contracts while the other stretches. It can lead to false oscillations in the solution [BOLK84]. In our model, the reduced integration element is coupled with hourglass control which eliminates the skewness that might occur in the lagrangian step of the immersed boundary formulation which was explained in the previous chapter. The hourglass control works by adding a penalty term to the stiffness matrix that penalizes the element for being skewed. The penalty term is proportional to the hourglass strain, which is the strain that would be generated if the element were to distort. Using reduced integration coupled with hourglass control lowers

the computational cost. Stiffness added to the fluid elements is regulated by monitoring the amount of energy that is being dissipated due to hourglassing to guarantee a negligible impact on mechanical accuracy.

3.3.6 Assembly of the numerical domains

The overall assembly of the tubular LV, leaflets, and the chordae structure numerical domain for the case of the generic valve are shown in Fig.3.10.a. As discussed in the previous chapter, in the immersed boundary method, first it is necessary to define the presence of blood in the fluid domain by using the volume fraction. Blood initially occupies the entire fluid domain except where the leaflet is located. For each FSI setup, we began by identifying fluid elements whose position coincides with the leaflet elements. Subsequently, a volume fraction equal to one was assigned to these fluid elements, indicating the presence of blood, while a volume fraction of zero was designated to elements occupied by the leaflet. This process results in a volume fraction map similar to the one presented in Fig.1.6 in the previous chapter. For example, the final result after registering the volume fraction on the FSI setup of the generic MV is shown in Fig.3.10.b.

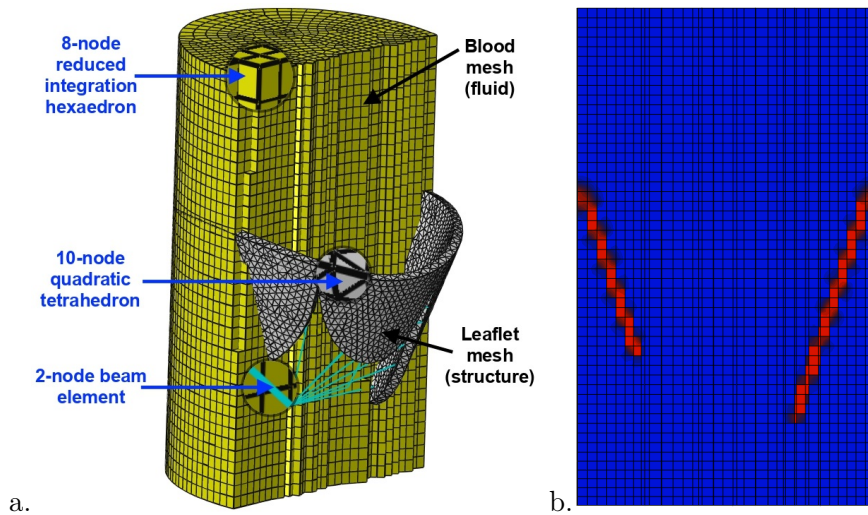


Figure 3.10: (a.) FSI discretized domain in case of generic MV. For better visibility, only the cross-section of the fluid domain is shown. (b.) Cross-section of the blood volume fraction: The blue region shows the presence of blood in fluid elements and the red region is considered as void.

In terms of computation, both fluid and solid domains are simulated simultaneously in one explicit solver. The full cardiac cycle lasts approximately 0.8 seconds. We designated a total simulation time of 0.1 seconds for the dynamic closure of the MV in a single time step. Depending on the residuals, an adaptive time increment is used with the initial time increment of $4e^{-4}$. The stable time increment is the minimum time step that can be used in the analysis without introducing numerical instability. If the time increment is too large, the analysis will be unstable and the results will be inaccurate. It is important to choose a time increment that is small enough to ensure stability, but not so small that it makes the analysis prohibitively expensive. The stable time increment is determined based on the speed of sound in the material and the

smallest element length scale in the mesh. The value of the stable time increment is calculated from the following equation:

$$\Delta t = \frac{l^e}{C_d}. \quad (3.4)$$

The smallest element length scale, l^e , is determined by the cube root of the smallest element in the numerical domain V^e , where V^e represents the volume of that element: $l^e = \sqrt[3]{V^e}$. The speed of sound (or material wave propagation speed), C_d , is the distance that a sound wave travels inside a material in a unit of time. It is determined by the material's elastic modulus (E) and density ρ . For a linear elastic material with Poisson's ratio equal to zero, the speed of sound is given by:

$$C_d = \sqrt{\frac{\rho}{E}}. \quad (3.5)$$

Typically, a smaller element length and a higher speed of sound result in a reduced stable time increment. As simulations progress and elements undergo distortion, resulting in elements with smaller volumes, the computational time increases. Hence, simulations involving large deformation, like MV dynamic closure where elements are highly susceptible to distortion, tend to be more computationally demanding [BO04].

3.4 Conclusion

In this chapter, the implementation of fluid-structure interaction (FSI) case setup for mitral valve (MV) simulation is detailed by exploring different aspects including the numerical domain, the contact model for capturing the self-contact between the MV leaflets, and model configuration. The contact model is already implemented in the Abaqus explicit solver and we discussed the underlying strategies that make it possible to have an efficient and practical contact model able to capture the complex interaction between the leaflet surfaces.

We then outlined the various approaches for the assembly of the numerical domain, particularly focusing on the left ventricle (LV). We also explored the boundary conditions and numerical configurations integral to the FSI setup. In addition, we discuss the computation aspects, including time increment and how the simulation progresses through time. This information collectively offers a basic understanding that is crucial for the experiments and analyses presented in subsequent chapters.

Chapter 4

Capturing Contact in Fluid-Structure Interaction Simulation of Generic Mitral Valve

Fluid-structure interaction (FSI) simulation of the mitral valve (MV) opens a way toward planning for surgical repair. In the literature, blood leakage is identified by measuring the flow rate but detailed information about closure efficiency is missing. We present in this chapter a detailed analysis of the MV dynamic closure and focus on improving the detection of blood leakage by building a map of contact. The details of the FSI model we used which is based on immersed boundary (IB) formulation are discussed in chapter 1. We also explored the contact model we used for our study and gave a perspective on challenges and important features in modeling self-contact between mitral valve leaflets in chapter 3.

We investigated the MV behavior and their closure characteristics in three typical clinical situations: MV with regurgitation that shows blood leakage, MV in case of prolapse in which the leaflets show bulging in the peak systole, and MV in a healthy condition. In addition to the classical ways of evaluating MV closure, such as stress distribution and flow rate, the contact map provides easy detection of leakage with identification of the sources of leakage and a quality assessment of the closure.

The primary contributions of this chapter include the implementation of the healthy and clinically diseased MV using the efficient and practical FSI method outlined in prior chapters, along with an exploration of their dynamic closure. We realize that our self-contact model enhances the simulation quality by allowing for sealed closure and efficient simulation. In addition, we introduce novel techniques to investigate MV behavior. In this chapter, we begin by exploring the process of replicating pathologies and their simulation setup. Following that, we present the simulation outcomes and offer an in-depth discussion of these results.

4.1 Replicating pathologies

By manipulating the chordae structure of the generic MV in the healthy case, we replicated pathological conditions such as prolapse and regurgitation. To have a better understanding

of how these cases are obtained, we need to get more familiar with the different categories of chordae structure. The Chordae structure is a group of fibrous cords that can be categorized based on their attachment points on the leaflet surface. The chordae structure is very complex and varies for each patient. The chordae anatomy is typically classified into primary, secondary, and tertiary chordae. The primary chordae have endpoints attached to the leaflet's free edge. The secondary chordae endpoints connect to the body of the leaflet, while the tertiary chordae endpoints are situated near the left ventricle (LV) wall.

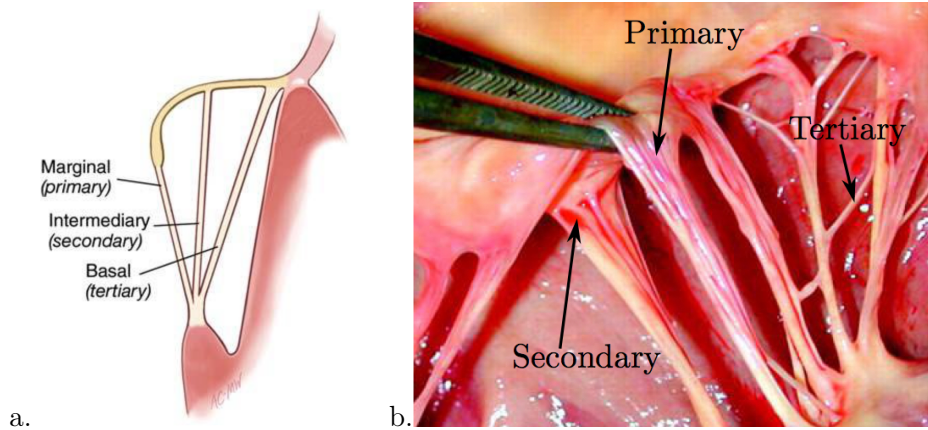


Figure 4.1: (a.) Cross-section view of the MV showing the approximate position of each chordae category [CAF10]. (b.) Different chordae categories are shown on dissected MV [TBP⁺17].

The chordae structure of the generic MV in the healthy case initiates from two fixed nodes representing the papillary muscles, 14 primary chordae attached to the border of the leaflets, and 6 secondary chordae attached to the body of the leaflets. To replicate the regurgitation, three primary chordae attached to a corner of the anterior leaflet are removed. For the case of prolapse, all six secondary chordae have been removed. Fig.4.2 shows the deleted chordae highlighted in red for each pathology.

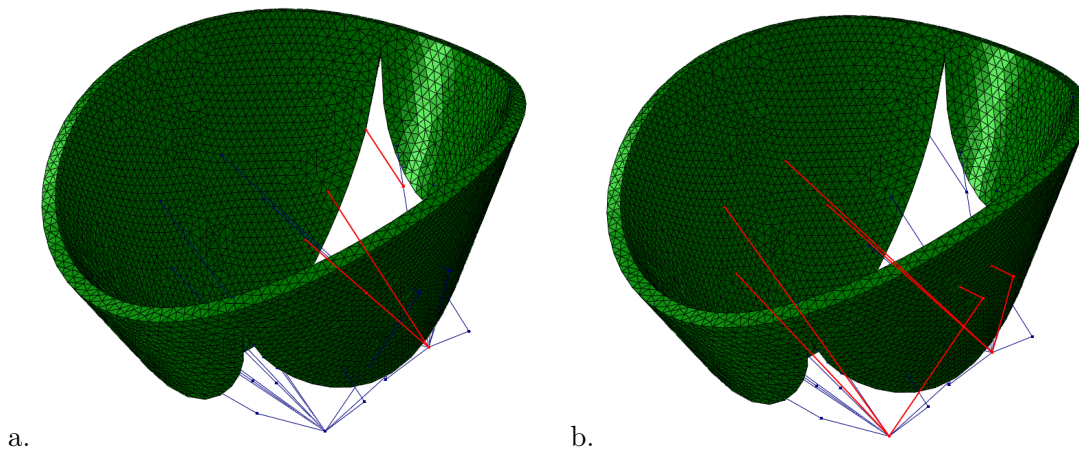


Figure 4.2: Removed chordae highlighted in red in case of (a.) regurgitation, and (b.) prolapse.

4.2 Simulation setup

In this section, we will discuss the technical details tailored for the simulation of generic MV dynamic closure in healthy and pathological cases. This information includes the constitutive model used to model the leaflet behavior, resolution of the numerical domain, and membrane blood leakage in the immersed boundary formulation.

4.2.1 Isotropic constitutive model

Initially, we neglected the anisotropic behavior of the leaflets and considered the leaflet tissue to be isotropic, which is a simplified model frequently used in the literature [MGG⁺13, LAG⁺14, AAAB⁺22, PG20, ETZA⁺21, KFN17, DPDFS05]. The mechanical response of the leaflet is modeled as a homogeneous incompressible 3rd-order Ogden hyperelastic material. The Ogden hyperelastic material is a widely used constitutive model in computational mechanics, which provides a mathematical description of the strain-energy density of a material as a function of its deformation state. The basis of hyperelastic models, in general, is the strain energy function W , which describes the mechanical energy stored in a deformed body. This function depends on the strain measures that show the deformation. The most commonly used strain measure in the Ogden model is the principal stretch ratio which is described as follows:

$$\mathbf{W} = \sum_{i=1}^N \frac{\mu_i}{\alpha_i} (\lambda_1^{\alpha_i} + \lambda_2^{\alpha_i} + \lambda_3^{\alpha_i} - 3). \quad (4.1)$$

λ_1 , λ_2 , and λ_3 , are the principal stretch ratios, μ_i and α_i are material parameters that are determined by fitting experimental data on the strain energy function.

By incorporating $N = 3$, the constitutive model has a higher degree of flexibility in capturing the non-linear stress-strain behavior of materials over a wider range of deformations. To obtain the material parameters, we used the built-in curve fitting capability of Abaqus for extracting material parameters. The parameters are obtained by minimizing the discrepancy between the stress-strain response predicted by the third-order Ogden model and the experimental data reported in [MNY95]. The data reported in this study is widely used in the literature [KMP19, RT23]. The mechanical response of the posterior leaflet is more similar to isotropic than the anterior leaflet, therefore, we selected the mechanical response of the posterior leaflet reported in this study. In Figure 4.3, dots represent the measurement points associated with the mechanical behavior of the posterior leaflet in the circumferential direction. Triangles, on the other hand, denote measurement points related to the mechanical behavior of the posterior leaflet in the radial direction. We used the average of measurements in both directions to extract the material parameters for the Ogden model. The optimization process iteratively adjusts the material coefficients to minimize the error metric, typically a sum of squared residuals. The material parameters extracted from the optimization process are reported in table 4.1. We validated these parameters by incorporating them into the third-order Ogden material model using the Abaqus explicit solver. The mechanical response obtained from these parameters is depicted as a blue line in Figure 4.3 which is in agreement with the experimental measurements.

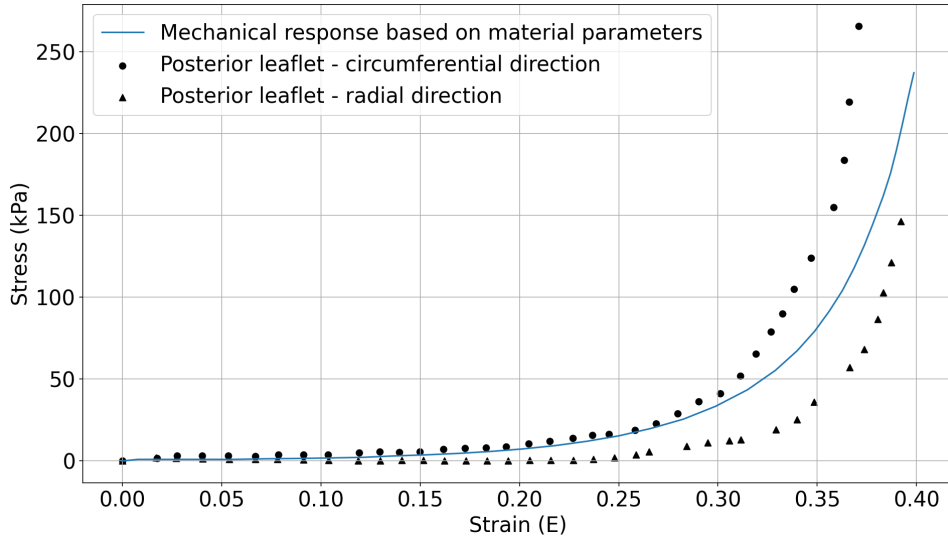


Figure 4.3: Experimental measurements of the MV posterior leaflet from [MNY95] and mechanical response of the third-order Ogden material model with the fitted parameters.

	$i = 1$	$i = 2$	$i = 3$
$\mu :$	0.002	1010.038	1230.418
$\alpha :$	63.659	9.471	22.412

Table 4.1: Material parameters for the 3rd-order Ogden hyperelastic material model, derived from experimental data reported in [MNY95].

Obtaining parameters from the curve-fitting process for isotropic materials, where the material behaves uniformly in all directions, is relatively straightforward. For more complex constitutive models that account for material anisotropy, parameter acquisition is more challenging. Later in the next chapter, we explore the intricacies of incorporating such material models and obtaining their parameters.

4.2.2 Mesh independence study

The size of the elements, which serve as the foundational unit of the mesh representing the physical domain, influences the accuracy of the simulation outcomes. A more refined mesh gives a better approximation of the physical domain, but it also comes with a higher computation cost. To have an accurate representation of the physical domain without spending unnecessary resources on computation, a mesh independence study is needed. A mesh independence study aims to ensure that the solution obtained from the simulation is primarily reflective of the physical scenario rather than the resolution of the mesh size. If results alter significantly with varying mesh sizes, it indicates that the solution is still mesh-dependent. The desired outcome is to reach a stage where further refinement of the mesh does not lead to appreciable changes in the key result parameters. The procedure typically involves performing simulations on progressively refined meshes and comparing the outcomes based on specific criteria. After a certain level

of refinement, if the difference between solutions on successive meshes falls below a predefined threshold, the solution is considered mesh-independent.

We used stress and strain distribution over the MV leaflets for the mesh independence study. We launched the MV dynamic closure simulation with several mesh resolutions. The meshing of the MV structure is done automatically with the Abaqus software by defining an average element size. Table 4.2 shows the average stress and strain for mesh resolutions consisting of $20k$ and $80k$ elements. Using a mesh with less than $20k$ elements yields simulation results that are still sensitive to mesh resolution, and it does not ensure numerical stability or the accuracy of the simulation in all scenarios. In some instances, using mesh resolution less than $20k$ leads to simulation divergence. We notice that using a more refined mesh gives more accuracy, but the difference between the results of the mesh with $20k$ elements and the mesh with $80k$ elements is negligible.

	Average Stress	Average Strain
$20k$ elements	93.5 kPa	0.25147
$80k$ elements	92.6 kPa	0.25266
Difference %	0.9 %	0.4 %

Table 4.2: Comparison of stress and strain between leaflet mesh with $20k$ and $80k$ elements.

4.2.3 Membrane blood leakage

In the FSI simulation of MV based on the immersed boundary formulation, depending on the resolution of the fluid mesh in comparison to the thickness of the leaflet, it is possible for a small amount of fluid to penetrate through the surface of the leaflets without any orifice holes existing on the surface. This amount of penetration also depends on the penalty constraint properties such as pressure-overclosure, stiffness behavior (linear or nonlinear), and stiffness value. In our simulation, for the interaction between the structure and the fluid, these values are automatically specified based on the stability measures of the Abaqus explicit solver [BO04]. To have a better insight, we added a practical comparison of the influence of the LV mesh resolution on the flow rate. The flow rate is a common metric used in the literature to measure the passage of blood through the MV during the cardiac cycle [FQG⁺18, GMQ⁺14, CWG⁺19]. In the case of healthy MV, once the valve is closed, the value of the flow rate should drop to zero. Any leftover residual is attributed to membrane blood leakage due to the small thickness of the valve implemented in the immersed boundary approach.

We measured the flow passing the bottom of the tubular LV (see Fig.3.2) after the valve closes. This process is repeated in three different mesh resolutions and their temporal progression of blood leakage is shown in Fig.4.4. The amount of flow rate averaged over time is also reported in the table below 4.3. Due to the dynamic motion of the valve, the temporal blood leakage oscillates over the averaged values. As expected, the value of blood leakage is smaller for mesh with smaller element sizes. In addition, there is a noticeable difference between the mesh resolution with $71k$ elements and the other three resolutions. Among the $280k$, $100k$, and $80k$, due to the

large oscillation, the difference in blood leakage is negligible. Therefore, we selected the mesh resolution with 80k for our simulation purposes.

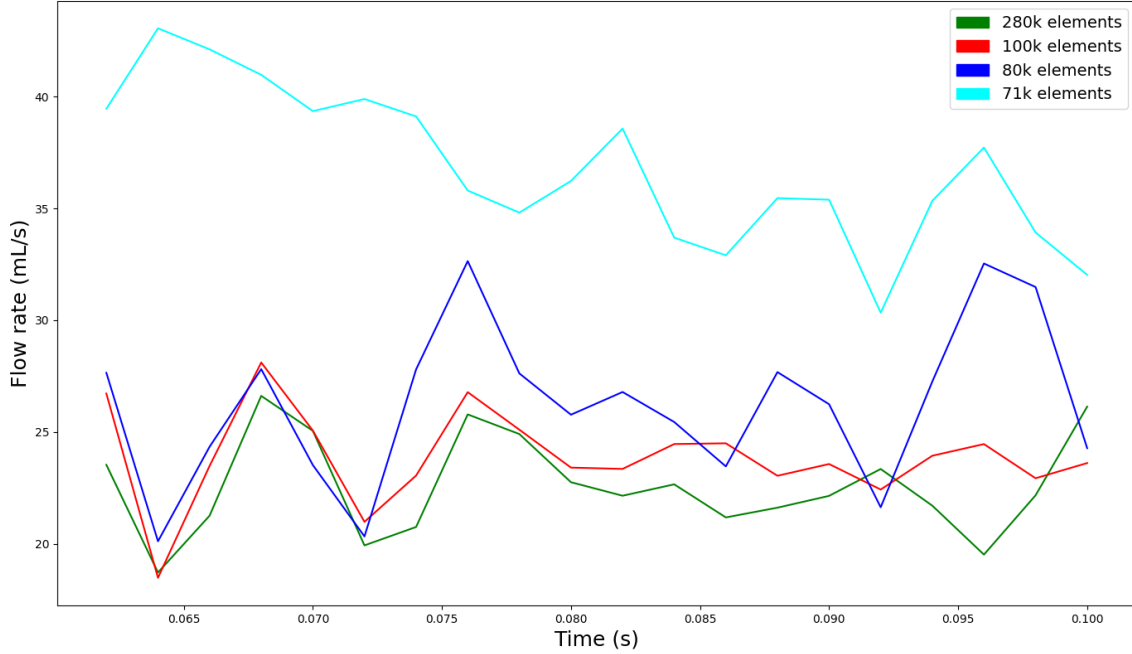


Figure 4.4: Blood leakage after closure in four different mesh resolutions.

Number of elements:	280k	100k	80k	71k
Average blood leakage (mL/s):	22.6	23.9	26.2	36.8

Table 4.3: Average blood leakage in four different fluid mesh sizes.

4.3 Results and discussion

We propose here to quantitatively measure the MV dynamic closure. Simulation results are provided in different typical medical configurations: MV with no chordae, leakage (regurgitation), bulging (prolapse), and healthy MV. These results show the ability of our model to reproduce the expected MV behavior. Both fluid and solid domains are simulated at the same time in Abaqus explicit solver with contact formulation of fluid and solid domain based on an enhanced immersed boundary method [Ben92]. The mesh resolutions for the tubular LV and MV leaflets are set at 80k and 20k elements, respectively. The simulation took 14 hours on an Intel Xeon 3.60 GHz workstation with 12 processors. With respect to the FSI studies of MV in the literature, for example, five days of computation time in [CMM⁺18], and 18 hours of computation time in [LDSB10], the framework we presented in this study is comparably faster. In the following, we discuss the simulation results with various metrics.

4.3.1 Deformed shape

The first step in qualitatively evaluating the outcome of the FSI simulation is observing the deformed geometry at the end of the simulation. The closed state of the MV in the four different scenarios has been studied and the final state of the simulation is shown in Fig.4.5. The contour represents the true strain distribution over the leaflet. Fig.4.5.a shows the results with no chordae holding the leaflets to test the simulation. It checks if the mechanical modeling, particularly the constitutive law, allows the valve to completely open and checks if it is not overly constrained. Closure of MV with leakage is shown in Fig.4.5.b. Notice that the orifice hole where the blood is leaking through is visible in the final state. In Fig.4.5.c, MV with severe bulging is shown. The case of bulging shows the high strain in the inflated area, which is a sign of a diseased valve. The difference between the MV final state in the case of bulging and leakage can be compared with the MV in a healthy state (Fig.4.5.d) where no orifice hole or severe bulging is visible. We have replicated this simulation with a real porcine heart that emerged in a water tank and where pressure was applied through a pump¹. Though the considered geometry in the real and the simulated case are not identical, similar behavior is observed: similar acceleration during closure and a slight back-and-forth lateral motion near the end.

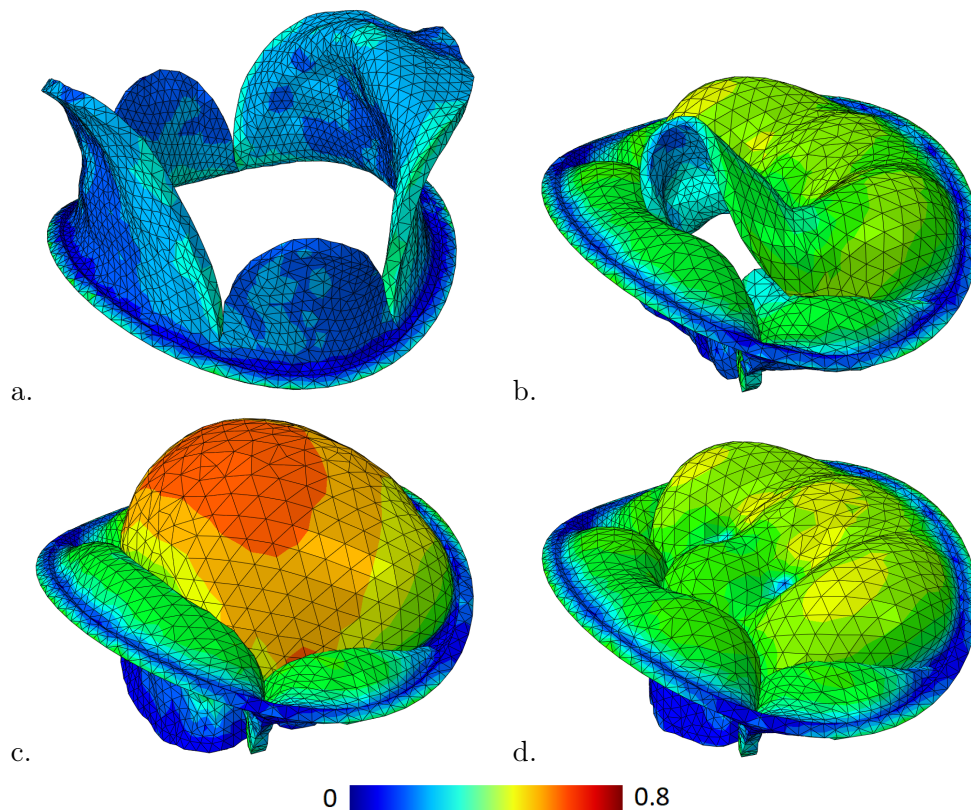


Figure 4.5: Closed state of the generic MV in case of (a.) no chordae attached, (b.) leakage, (c.) bulging, and (d.) healthy.

¹Slow-motion video of MV closure: <https://hal.archives-ouvertes.fr/hal-03419776>

4.3.2 Stress map

Another common way to check qualitatively the validity of the simulation is to analyze the stress over the leaflet in the final state by displaying the Von Mises distribution. Stress distribution in different scenarios is presented in Fig.4.6. In each case analyzed, a high-stress distribution is observed in the annulus ring. This elevated stress is due to the annulus boundary condition being fixed, which results in elements in the annulus being under high stress. On the leaflet surface, a relatively large difference in stress distribution can be observed by comparing the results from healthy MV (Fig.4.6c) and MV with bulging (Fig.4.6b). MV leaflets in the bulging case experience a higher stress range in each cycle. These results are in accordance with clinical observations, in which bulging adds unnecessary force and more fatigue to the MV. Even though variations may exist in the size of the MV geometry and in certain boundary conditions among different studies, the stress distribution across the leaflet surface and the magnitude of the forces in both MV with leakage (Fig.4.6.a) and healthy MV (Fig.4.6.c) are consistent with findings presented in the existing literature [CWG⁺19, FQG⁺18, GMQ⁺14, LDSB10, CMMS20]. The magnitude of the stress distribution of the simulation results is in agreement with the ones shown in the literature [CWG⁺19, CMMS20] (see Fig.4.7.a and Fig.4.7.b). A similar high-stress distribution near the chordae attachment points and low-stress distribution near the coaptation area is observed in [CMMS20], as depicted in Fig.4.7.a. However, distinctions between our simulation results and those presented in [CMMS20] do exist. Specifically, in our model, a high-stress distribution is apparent near the annulus ring. This difference arises from the specific boundary condition employed in our simulation, wherein the annulus is pinned to the tubular LV. This high-stress distribution near the annulus ring is also apparent in the results reported in [CWG⁺19] (see Fig.4.7.b).

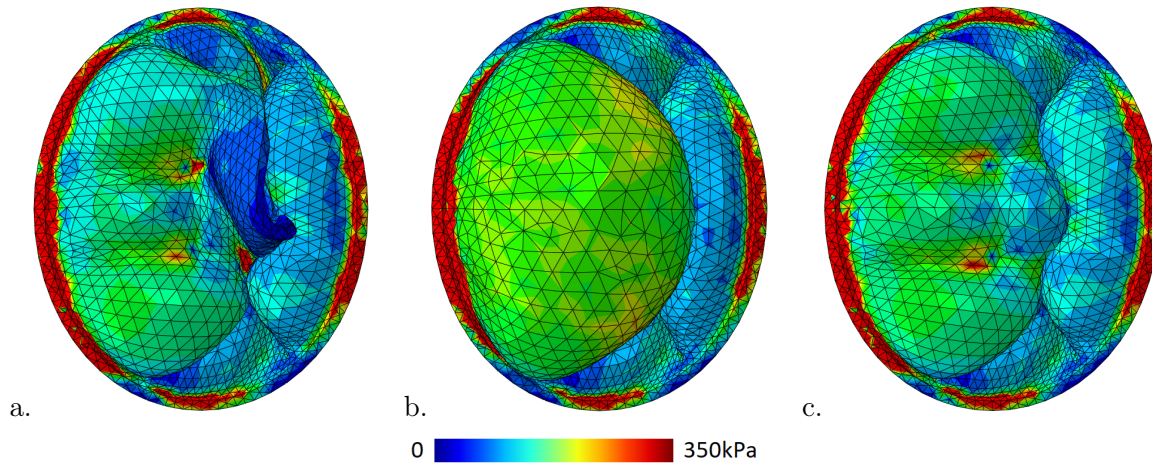


Figure 4.6: Stress distribution of leaflets with (a.) leakage, (b.) bulging, and (c.) perfect closure.

4.3.3 Streamlines

Streamlines are commonly used in the literature to analyze fluid behavior [GMQ⁺14, FQG⁺18]. A streamline represents a path that a massless particle would follow if it were present in the

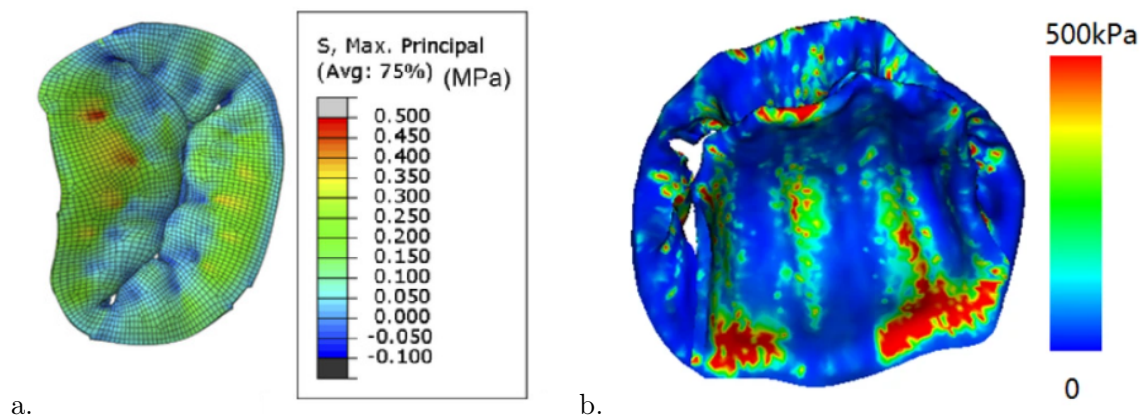


Figure 4.7: Stress pattern and magnitude reported in the literature: [CMMS20] (a.) and [CWG⁺19] (b.).

fluid flow. They help with qualitative and sometimes quantitative visualization of fluid flow patterns. The streamlines effectively depict the direction of flow, help identify circulation zones and vortices, and provide information regarding blood leakage. Additionally, they give insights into the complex interaction blood has with the MV, jet behaviors in case of leakage, and potential simulation issues. In the FSI simulation utilizing the IB method, the fluid domain comprises both fluid and void regions. Fig.4.8.a illustrates a cross-sectional view of the fluid domain at the beginning of the simulation when the MV is open. In this figure, the red area indicates the void region, whereas the blue area denotes the fluid-filled section. Conversely, Fig.4.8.b demonstrates the MV in a closed position. This image shows that when the MV is in the closed state, it obstructs the fluid flow across the leaflet. Once the valve is closed, the blood above the leaflets exits from the top of the tube. The cross-section of the fluid domain during the dynamic closure of the MV is available by following this link¹).

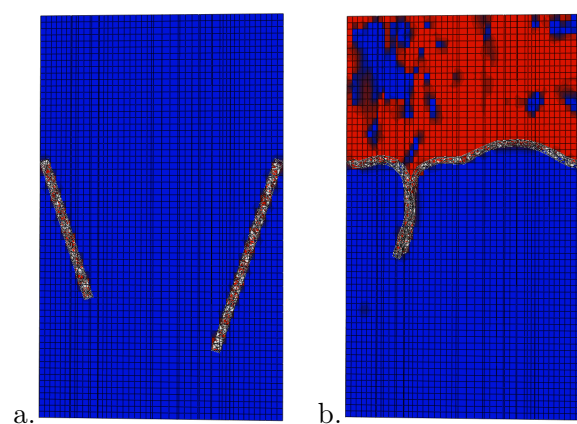


Figure 4.8: (a.) illustrates the volume of fluid in the open state, and (b) depicts the volume of fluid when the MV is closed. Blue regions indicate the areas occupied by fluid, whereas red regions represent areas that are void of fluid.

¹<https://youtube.com/shorts/86nYpwLIHkY?feature=share>

Fig.4.9 shows the flow pattern with streamlines initiating from a segment at the inlet. For better visualization, the tubular LV and the generic MV have been rendered transparent. The streamlines for the MV with no chordae (Fig.4.9a) show the fluid going straight to the outlet as expected. No blood leakage is visible in the case of healthy (Fig.4.9d) and bulging (Fig.4.9c) MV, and in MV with leakage, streamline of blood leakage through the orifice hole is visible in Fig.4.9b. The blood flow through the orifice hole has a higher velocity which creates jet flows penetrating the MV closing area. In the case of MV closure with bulging, different high momentum flow patterns appear in comparison with the healthy MV closure. This difference is due to the cavity region created by the severe deformation of the MV anterior leaflet. The fluid behavior can be described by the Reynolds number, which is a dimensionless quantity used to predict fluid flow patterns by characterizing the ratio of inertial forces to viscous forces within the fluid. The value of the Reynolds number serves as a criterion for predicting the flow regime of a fluid: a low Reynolds number (typically less than 2000) suggests laminar flow, while a high Reynolds number (generally greater than 4000) indicates turbulent flow. Intermediate values often denote transitional flow, where the fluid behavior can shift between laminar and turbulent states. In both MV with bulging and healthy cases, the Reynolds number reaches a value above 2000 (with a maximum of 28000). Due to the pressure boundary condition specified in the inlet, the Reynolds number is not constant throughout the simulation. The fluid passing through the MV starts as a laminar flow. The Reynolds number then increases gradually until flow reversal starts to appear, and in some regions, chaotic breakdown of the vortices occurs. Eventually, the flow becomes stationary soon after the valve closes. High momentum flow appears near the leaflet surface as the blood passes through the complex geometry of the leaflets.

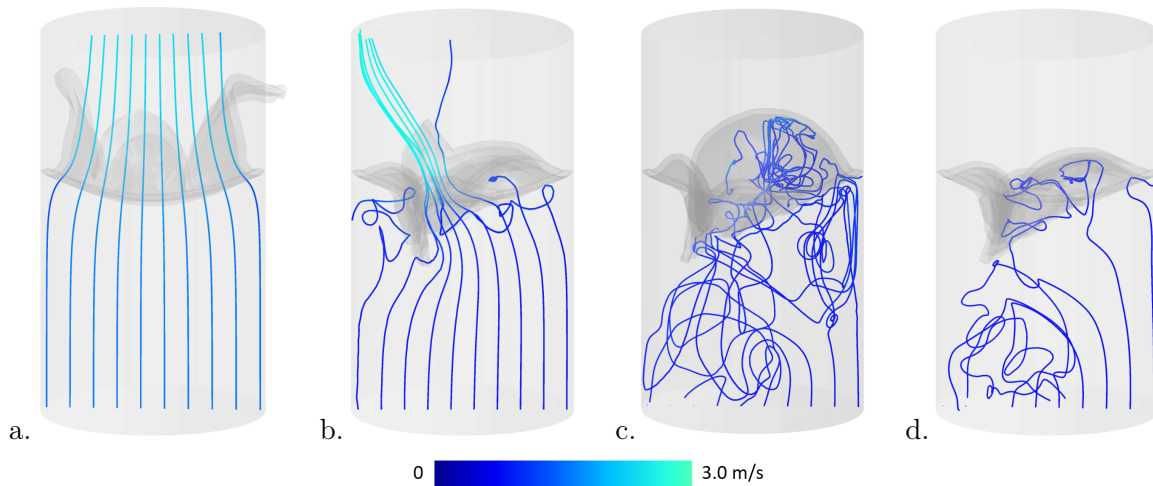


Figure 4.9: Streamlines over MV with (a.) no chordae attached, (b.) leakage, (c.) bulging, and (d.) healthy.

4.3.4 Cross-section

In order to better appreciate the quality of the contact region between both leaflets, cross-sections of leaflets in the three case setups are compared in Fig.4.10. In both healthy and bulging cases, as

expected, contact between leaflets occurs. As highlighted in the introduction chapter, a saddle-shaped final state (refer to Fig.4) is indicative of a healthy MV. The MV shape at the peak systole is determined by the geometry of its leaflets and the chordae structure. Nonetheless, for our generic MV in the case of healthy closure, the cross-section is nearly flat, closely resembling a saddle shape. In the case of bulging, a large balloon-shaped deformation is visible which causes high-stress loading on the leaflets in each cycle. The orifice area in the case of leakage appears as a gap that allows for blood to pass through the MV.

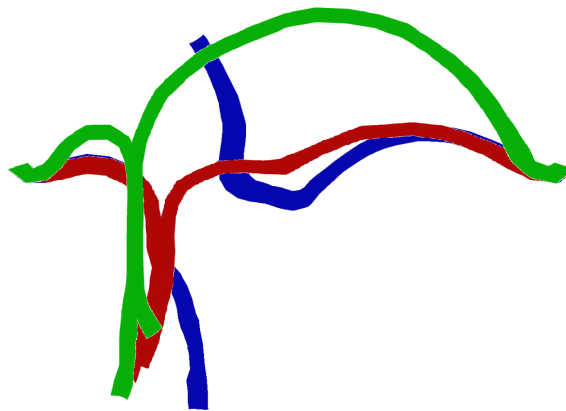


Figure 4.10: Mid-leaflet cross-section of MV in case of leakage (blue), bulging (green), and healthy (red).

4.3.5 Flow rate

The most frequent tool used in the literature to evaluate the closure of the MV and measure the blood leakage is flow rate. Fig.4.11 exhibits flow rate results. As the ventricular pressure builds up from the bottom of the tube, the fluid momentum increases, leading to an exponential rise in flow rate. As the simulation progresses, the valve opening gets smaller, resulting in a decreased flow rate. This continues until the valve is fully closed, at which point the flow rate reaches zero. Based on the results shown in Fig.4.11, flow rates decay to zeros for the healthy and bulging cases. In the case of leakage, the flow rate reaches a certain value depending on the severity of the regurgitation. Unfortunately, this metric is not sufficiently sensitive to accurately measure leaks or identify holes. Indeed the ratio of leaks or holes areas is very small with respect to the leaflet areas, thus leading to near zeros flow rates. For example in [GMQ⁺14], the flow rate for the cardiac cycle reaches zero despite the orifice areas apparent in the simulation. For these reasons, we propose to evaluate the quality of the closure based on a new approach which is discussed in the next section.

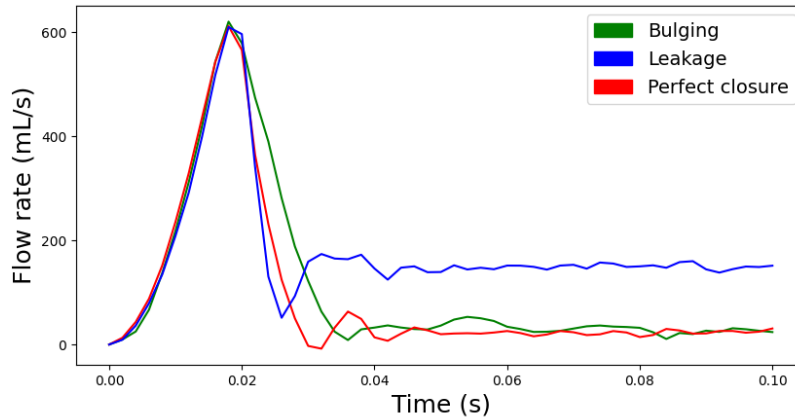


Figure 4.11: Flow rate in case of leakage (blue), bulging (green), and healthy (red).

4.3.6 Contact map

Obtaining the contact map

To accurately detect the leakage in the MV, here we propose the contact map, a new method for evaluating the quality of the MV closure. To obtain the contact map, we first identify the nodes on the leaflet surface that are involved in self-contact. For better visualization, we display the closed state of one leaflet (specifically, the anterior leaflet) in Fig.4.12.a. In this picture, the color-coded region shows the nodes in contact with a contour map representing the magnitude of the contact force. The contact force increases from blue to red and the area in silver shows the region where no contact occurs. We then used the node labels to extract the initial position of each node from the simulation files and create a cloud of nodes from nodes in contact in 3D space as shown in Fig4.12b. Subsequently, this cloud was projected onto a cylinder, as illustrated in Fig4.12c. To transform this into a more accessible view, the cylinder was then unfolded, yielding a 2D representation of these nodes, as seen in Fig4.13a. To ensure comprehensive representation, this procedure was repeated for all nodes on the leaflet surface. Ultimately, by harnessing the node labels and the relative proximity of nodes, we managed to construct the leaflet in a 2D triangular mesh format, as showcased in Fig4.13b. Finally, we integrated the 2D representation of the nodes in contact with the leaflet's triangular mesh and created the contact map as shown in Fig4.13c.

Analyzing the results with contact map

The comparison of coaptation area and contact force in the case of healthy and pathological MV is shown in Fig.4.14. From the contact map, we can extract several important information:

- Assurance of sealed closure by observation of coaptation belt made from nodes with non-zero contact pressure.
- Detection of leakage and pinpointing the location of discontinuity of the coaptation are on the leaflet surface.

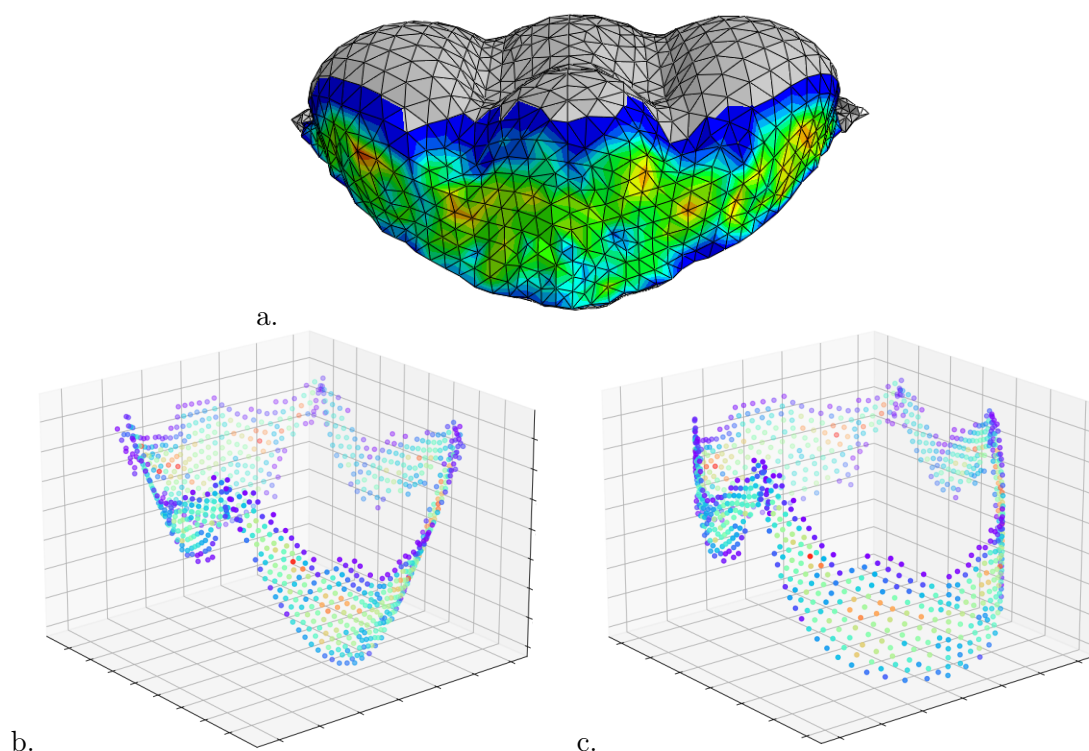


Figure 4.12: Obtaining contact map: (a.) One of the leaflets in contact, (b.) cloud of points in contact, and (c.) projection on a cylinder.

- Assessment of the thickness of the coaptation area and where it is situated on the leaflet surface.
- The magnitude of the contact pressure, identifying the pressure distribution pattern and regions with weak contact pressure.

In terms of clinical application, the contact map provides valuable information that can help the surgeon in their decision-making process. In the following, we discuss the results of simulation with generic MV based on these aspects. In the case of healthy MV (Fig.4.14a), non-zero contact forces in the contact map create a coaptation belt without interruption. While minor discontinuities do occur, mostly near the leaflet edges, these are largely due to the unwrapping process and additional tissue folds. The near-continuous coaptation belt verifies the absence of any large orifice holes in the leaflets, thereby blocking the passage of blood through the MV. This is a confirmation for sealed closure which is expected from the MV in the healthy case. In the case of MV with leakage (Fig.4.14b), a large gap in the coaptation belt shows the presence of orifice holes. The source of leakage can be accurately detected by observing the discontinued regions on the contact map. In the instance of a bulging MV, a nearly continuous coaptation belt is observed (Fig.4.14c), indicative of a sealed closure. A minor discontinuity is evident on the contact map of the MV with bulging, with a negligible size. This discontinuity also arises from a slight fold at the juncture where the two leaflets converge and the contact map metric could not detect. In the case of the healthy MV, the coaptation area is thicker compared to the

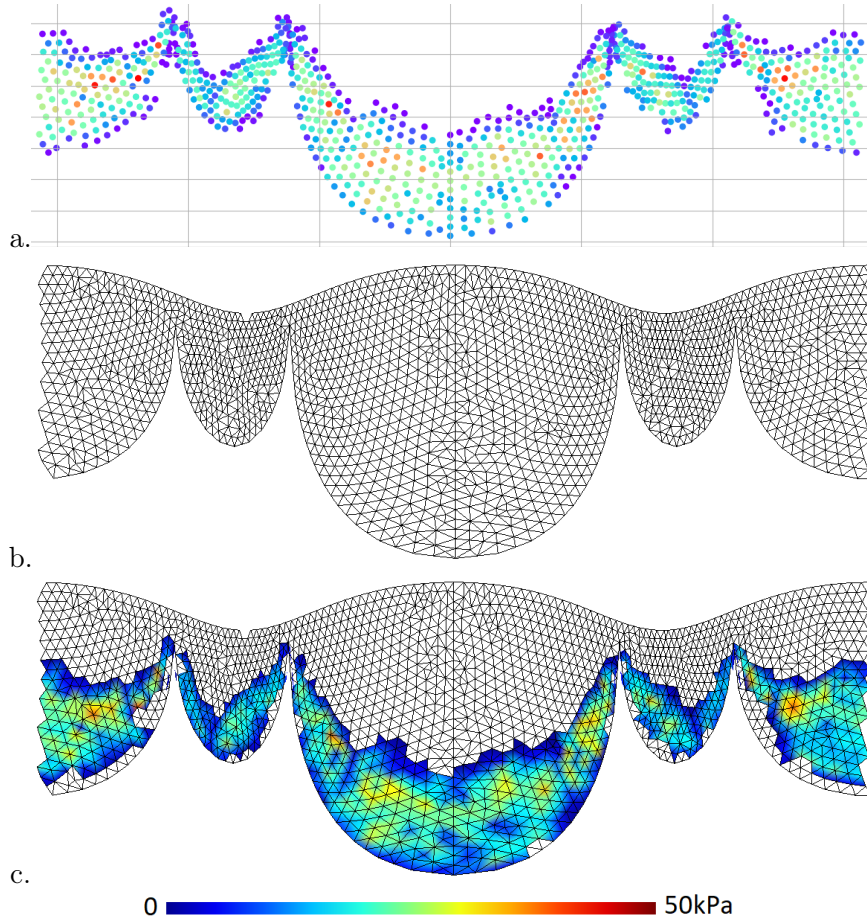


Figure 4.13: Obtaining contact map: (a.) Flat representation of the cloud of points in contact, (b.) flat representation of the leaflets with triangular mesh, and (c.) final result of contact map (for the case of healthy MV).

MV with bulging (see Fig.4.14c). Consequently, in the case of bulging, the contact pressure is localized in a more compact region, leading to a relatively higher magnitude of contact pressure. However, it is important to note that the contact pressure is more uniformly distributed across the leaflet surface in a healthy MV compared to one with bulging.

4.4 Conclusion

In this chapter, we used our fluid-structure interaction (FSI) model based on the immersed boundary (IB) formulation to simulate the mitral valve (MV) behavior by focusing on perfect closure with no orifice hole. A generic MV geometry and isotropic hyperelastic material model were used to simulate the dynamic closure of MV in healthy and pathological cases. The results show that our FSI model enables reliable simulations capable of identifying pathological valves while requiring less computational time than commonly reported in existing literature. We aimed to accurately represent detailed contact in the FSI simulation of MV. Blood leakage can be identified either by monitoring the flow rate or by extracting the coaptation area from the

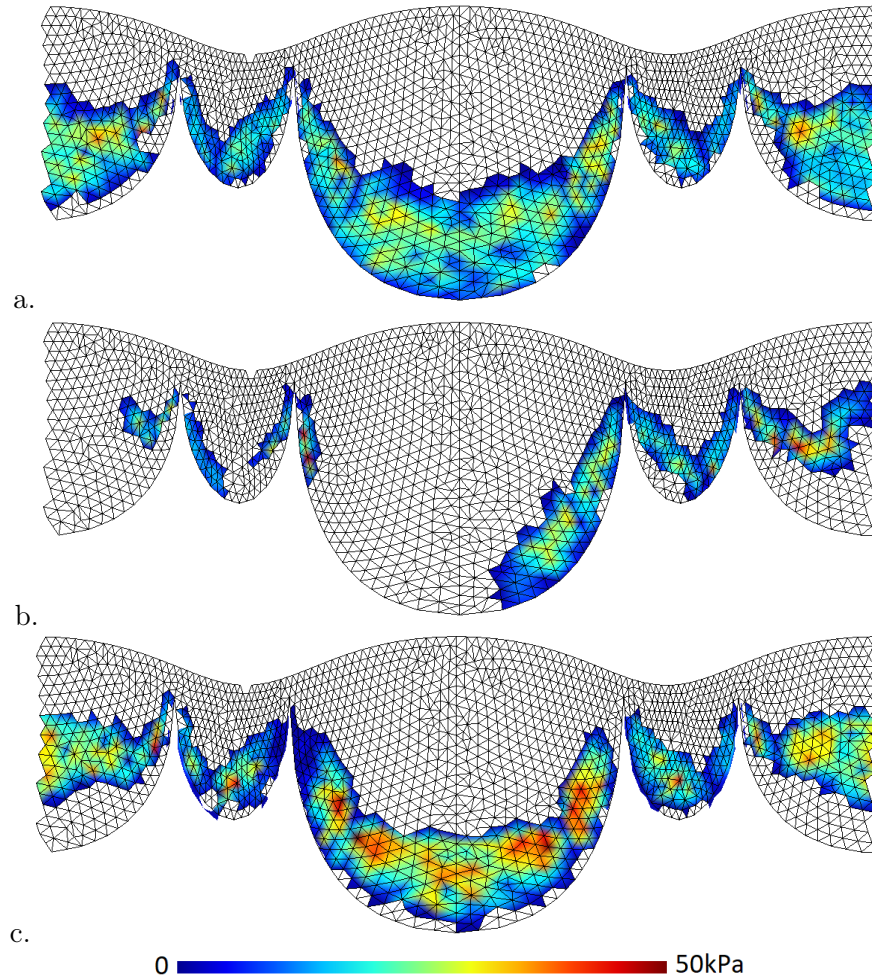


Figure 4.14: Contact map: Healthy (*a.*), leakage (*b.*), and bulging (*c.*).

contact map. These metrics can be obtained during the post-processing phase, following the completion of the simulation. We also conducted simulations without chordae, demonstrating the high numerical stability of our model. A key feature of our model is its ability to faithfully capture contacts while maintaining relatively low computational costs.

There are also some limitations to the presented simulations that should be considered when interpreting the results. We used a generic geometry without a reference ground truth against which to compare the behavior of the MV. The comparison was solely conducted based on the available data from the literature and the anticipated physiological response of the MV. In the contact map, the small discontinuities appear which is caused by the unwrapping of the leaflets and small folds in the leaflets tissue. In addition, the fluid leakage from the MV tissue membrane caused by the inherent limitation of the IB approach is another limitation of our model. Furthermore, we did not consider the annulus deformation which is important in having a realistic simulation.

We evaluated the quality of the dynamic closure of MV with different measurements such as the stress map, cross-section, and flow rate. We also introduced a new method for evaluating the

quality of the dynamic closure of MV. Contact map significantly improves the detection of MV dysfunctions. It can be used to identify regions with poor contact quality to predict pathological diseases. There are also some limitations to this metric. The small discontinuity shown in the contact map in the case of MV with bulging represents a limitation of this metric. Enhancements to the algorithm could be implemented to account for the small folds where contact occurs, but which are not currently reflected in the coaptation area as depicted by the contact map metric.

In the following chapter, we study the use of a more complex material model, that incorporates anisotropy in the leaflet mechanical response, and provide insights into its implementation. Moreover, we investigate the influence of case setup and incorporate image-based MV geometry. This will help us move forward in having a patient-specific model and potentially a clinical use of the simulation.

The use of the balanced master-slave approach and penalty formulation made our model numerically stable and efficient. This allows our model to effectively capture the self-contact between MV leaflets and preserve the physiological realism of the simulation.

Chapter 5

Investigating the Influence of Anisotropy and Geometry

The dynamic behavior of the mitral valve (MV) is highly influenced by the material model used to describe the leaflet tissue. Due to the presence of collagen fibers, MV leaflet tissue shows an anisotropic behavior. In this chapter, we incorporate a more intricate material model that considers the anisotropic nature of the MV leaflets and provides detailed information regarding their implementation. We investigate whether a more complex material model is able to better reflect the valve closure. To investigate the influence of the material model on the simulation results, we used two constitutive models, Holzapfel-Gasser-Ogden (HGO) for the anisotropic, and third-order Ogden for the isotropic.

We move toward having a patient-specific model by implementing MV geometry extracted from medical imaging. Chapter 2 addressed the specifics of image-based geometry and its corresponding case setup is discussed in chapter 3. In this chapter, we studied the influence of anisotropy on both generic and image-based MV. The image-based geometry is extracted from the segmentation of a medical image and it leads to various challenges compared to generic geometry. The leaflets have non-regular contours with some noise. Many folds can occur during the closing process. In this context, we investigated the influence of the smoothness rate of the image-based MV surface extracted from the segmentation process, and how the shape of the tubular left ventricle (LV), influences the dynamic closure of the MV. There are other case setup factors that could affect the simulation outcome however, our focus was solely on the aforementioned aspects.

The FSI simulations are based on the immersed boundary formulation, which is described in chapter 3. To evaluate the quality of the MV closure, we used several metrics including bulging volume, contact map, and flow rate. We also compared the simulation outcome with the chordae force ex-vivo measurements available in the literature [PIMW⁺20]. The ex-vivo measurement of chordae forces is achieved by placing the MV inside a 3D-printed left heart simulator, with a limited annulus motion. This ex-vivo study aimed to validate a chordae repair technique by measuring the chordae forces from the baseline near the chordae attachment to the papillary muscles, both before and after the surgery. We use the distribution of forces measured for the different groups of chordae as a reference in our study.

This chapter consists of two primary sections, followed by a discussion of the results. In the

first section, we describe the material models and implementation challenges. Then, we provide details concerning the geometry and case setup. The chapter concludes with a presentation and discussion of the results.

5.1 Material models

Specifying a material model in MV simulation that fairly represents the actual mechanical response of leaflet tissue poses several challenges. The choice of a proper constitutive model, that formulates the behavior of the material, and the experimental measurements, notably planar biaxial tensile testing, influence the overall behavior of the MV. Obtaining the material parameters by fitting the data from these measurements to the equations of the anisotropic constitutive model is not straightforward. In chapter 4, the Ogden isotropic constitutive model is discussed.

The fact that whether modeling the anisotropic response of the leaflets in the MV simulation is important or not was not clear in the literature. While some studies considered the MV leaflet to be anisotropic [RFS⁺13], some studies such as [LSP⁺23, LRJ⁺19] reported a regional variation in the anisotropy rate in the MV leaflet. In the stress-strain measurements, the gap between the mechanical responses of the tissue in the circumferential direction and the radial direction is referred to as anisotropy rate. This motivated us to compare the dynamic closure of MV with constitutive models that consider the MV leaflets to have an anisotropic and isotropic mechanical response. We first explore the various types of constitutive models that incorporate anisotropy, and then we continue by discussing the challenges in utilizing such models for MV simulation.

5.1.1 Anisotropic constitutive models

In the literature, various constitutive models are used to model the anisotropic behavior of the MV leaflets. Most commonly used anisotropic constitutive models for biological tissues are often described in terms of a strain energy function with exponential term [WMG96, AMDM09, ASMD10, DBB04, GOH06, MNY98, FFP79]. The constitutive models can be categorized based on the variables used in their strain energy function, or based on a sum of terms characterizing either isotropy or anisotropy in the strain energy function (more known as coupled and decoupled). In the following, we will first discuss the categorization based on the variables used, followed by the categorization based on the coupled and decoupled terms.

The strain energy function in the anisotropic constitutive models can be described based on strain, anisotropic invariant, and fiber dispersion. Invariants are scalar quantities derived from the strain tensor that remain unchanged under a coordinate transformation. They provide insight into the material's deformation independent of the coordinate system being used. The first constitutive model based on strain is presented by Fung et al in [FFP79]. In this model, the strain energy function is an exponential term with a direct relation to the strain in different directions. One limitation of such models is not considering the microstructure of the tissue. In anisotropic constitutive models based on anisotropic invariants, for example in [HGO00, MNY98, HSGR05], the strain energy function is defined based on invariants of the strain tensor. In this approach, the microstructure of the tissue is considered, but the fibers are considered to be parallel to each other. In the models based on fiber dispersion [Lan79, Lan83, GOH06] a dispersion factor is

specified which describes how fibers are dispersed in the tissue. An extensive study on the fitting performance of twelve different anisotropic constitutive models is described in [DADH23]. The study concludes that the anisotropic models based on the dispersion of the fibers show better fitting performance compared to the other categories mentioned. In this chapter, we focus on the constitutive model itself, and more in-depth investigation of the leaflet microstructure and their distribution within the tissue is presented in the chapter 6.

Another approach to categorize the anisotropic constitutive models are as coupled [MNY98, FFP79] and decoupled [GOH06]. May-Newman et al [MNY98] proposed an anisotropic constitutive model specific for MV leaflets in which the strain energy function consists of a single term describing the material behavior in all directions. In decoupled models, such as the HGO constitutive model [GOH06], the strain energy function consists of one isotropic and one anisotropic term which in combination describes the desired anisotropic behavior. In [RFS⁺13] performance of both coupled and decoupled anisotropic models is compared to in vivo measurement on ovine data with shell structure simulations. The study indicates that the average nodal displacement error relative to in vivo measurements is lower when utilizing the decoupled HGO model. Therefore, it concludes that the decoupled HGO model serves as a more effective constitutive model for simulating mitral valve behavior.

To incorporate the anisotropy, we investigated the use of the decoupled HGO model and the coupled generalized Fung [FFP79] anisotropic hyperelastic material model. In addition, for the isotropic model, we used the third-order Ogden hyperelastic constitutive model we already presented in the chapter 4. Several constitutive models are available for incorporating anisotropic and isotropic materials. However, the HGO, general Fung, and Ogden constitutive models are frequently utilized in the literature. Therefore, we have selected these existing models for our simulation purposes. In the following, we explore the details of these models.

Generalized Fung model

The generalized Fung anisotropic constitutive model refers to a mathematical representation of anisotropic soft biological tissues proposed by Yuan-Cheng Fung [FFP79]. He was a pioneer in biomechanics and his work has greatly influenced the understanding of soft tissue mechanics, particularly in cardiovascular tissues. The generalized Fung model accounts for the non-linearity and anisotropy of the MV leaflet tissue. Fung proposed an exponential strain-energy function that captures the nonlinear anisotropic behavior of soft biological tissues. The generalized Fung strain energy function is written as:

$$\psi = \frac{c}{2}(\exp Q - 1) + \frac{1}{K} \left[\frac{(J^2 - 1)}{2} - \ln J \right]. \quad (5.1)$$

In this equation, the first term accounts for the mechanical response of the tissue, while the second term addresses the tissue's compressibility. D is a material parameter that is obtained as $D = 2/K$. K is the bulk modulus, a measure of a substance's resistance to uniform compression, and is described as:

$$K = V \frac{dP}{dV}. \quad (5.2)$$

V is the initial volume of the material, dP indicates the change in pressure, and dV denotes the change in volume. Materials with a high bulk modulus are relatively incompressible, meaning that they don't change volume much under pressure. For example, water has a relatively high bulk modulus, which makes it almost fully incompressible. On the other hand, gases typically have a much lower bulk modulus, making them much more compressible. In equation 5.1, J is the total volume ratio, calculated based on how much the volume of the material is changing: $J = V_{deformed}/V_{initial}$. In the case of incompressible material, J is equal to one. It is worth noting that as most of the MV tissue is made of water, the MV leaflet is considered incompressible. Therefore, for MV tissue, the second term in equation 5.1 will be zero. In the first term, c is a material constant, and Q is a quadratic form of the Green-Lagrange strains, which is given by:

$$Q = E_{ij}b_{ijkl}E_{ij}. \quad (5.3)$$

Where E_{ij} are the components of the Green-Lagrange strain tensor, and b_{ijkl} is the symmetric fourth-order tensor of material parameters. Since the generalized Fung constitutive model is considered "coupled", the anisotropy in the model has been introduced through the b_{ijkl} terms. The selection of these constants can represent different anisotropy orientations and degrees of anisotropy. The material parameters in the generalized Fung model, b_{ijkl} and c , are obtained by fitting data from experimental measurements on its strain energy function. Later in section 5.1.3, the process of obtaining these parameters is explained in detail.

Holzapfel-Gasser-Ogden model

The HGO constitutive model was originally used to describe the mechanical behavior of arterial walls [GOH06]. The HGO strain energy function is:

$$\psi = C_{10}(I_1 - 3) + \frac{K_1}{2K_2} \sum_{\alpha=1}^N [\exp(K_2 \langle E_\alpha \rangle^2) - 1] + \frac{1}{K} \left[\frac{(J^2 - 1)}{2} - \ln J \right]. \quad (5.4)$$

Contrary to the generalized Fung model, the strain energy function in the HGO model is "decoupled", consisting of two separate terms defining the mechanical response of the tissue, and one term addressing the compressibility. In this model, the anisotropic behavior is introduced by families of fibers running through a uniform medium. The uniform medium is considered isotropic and the first term of the equation 5.4, is addressing the isotropic part. The second term introduces the anisotropy to the model by defining the specifics of the fibers embedded in the uniform medium. Similar to the generalized Fung model, due to the incompressibility of the MV leaflet tissue, the last term is equal to zero.

The isotropic part is captured using the linear neo-Hookean model. The C_{10} coefficient in the linear part of the equation 5.4 dictates the characteristics of the uniform medium. N denotes the number of fiber families. The distribution of fibers in the MV leaflet is complex, some studies [WS13] consider two families of fibers for the MV leaflet. In our case, we used a simpler representation of the constitutive model by incorporating only one family of fibers, $N = 1$, to dictate the direction of the anisotropy in the leaflet tissue. Both K_1 and K_2 are specifying the characteristics of the fibers. In the stress-strain curve, K_1 , also known as fiber modulus, dictate the slope of the curve at the beginning of the plot, and K_2 (also known as the fiber exponential

coefficient) dictate the nonlinearity of the relationships [HOB20]. The effective stretch of the fibers $\langle E_\alpha \rangle$ is active only when the fibers are stretched. This behavior is enforced by:

$$\langle E_\alpha \rangle = \frac{|E_\alpha| + E_\alpha}{2}. \quad (5.5)$$

According to this equation, during compression, the term $\langle E_\alpha \rangle$ will be equal to zero and the fibers will not contribute to the mechanical response of the tissue. In the case of fiber stretching, this term is defined as:

$$E_\alpha = \kappa(I_1 - 3) + (1 - 3\kappa)(I_{4(\alpha\alpha)} - 1). \quad (5.6)$$

I_1 is the first deviatoric strain invariant, and $I_{4(\alpha\alpha)}$ is the pseudo-invariant related to the fibers. κ is the dispersion factor that determines how dispersed the fiber family is. The value of κ can be between zero, parallel fiber families, to 1/3, randomly distributed fibers.

5.1.2 Planar biaxial tensile test

The stress-strain response of the MV leaflet has been measured in several experimental studies [LRJ⁺19, JLK⁺18b], using a biaxial tensile test. A biaxial tensile test is a mechanical setting that applies stretching forces on a tissue specimen simultaneously in two perpendicular directions. The purpose of this test is to extract the stress-strain response of the specimen, for example, MV leaflet tissue, in two directions. Many studies in the literature, consider the direction of the anisotropy in the MV leaflet to be parallel to the surface plane approximating the annulus (planer annulus surface) [KMP19, SVR09, VCV⁺08]. In Fig.5.1.a, the blue surface is the plane that has the minimum distance to the nodes on the annulus ring (shown as red dots). This means that the MV leaflet tissue has two main directions, circumferential, parallel to the planar annulus surface, and radial, perpendicular to the planar annulus surface. In this chapter, we also consider the MV leaflet fiber family to be parallel to circumferential direction as shown in Fig.5.1.b. But in reality, the microstructure of the leaflet tissue is more complex and we conducted an investigation on this subject which will be discussed in chapter 6.

The procedure in the planar biaxial tensile test includes sample preparation, test setup, strain measurement, and data analysis. For the preparation step, a rectangular piece of a specimen is separated from the dissected MV tissue as shown in Fig.5.2.a. Note that the specimen is removed from the middle of the anterior leaflet near the annulus ring in the circumferential and radial directions. Following that, the rectangular specimen is installed on the tensile test system (Fig.5.2.b), by securing the specimen with multiple hooks. In this system, the arms connected to the hooks will apply stretching forces and the temporal magnitude of the applied force is recorded during the test. In the meantime, small debris of charcoal is sprinkled on the specimen so that the deformation of the specimen can be captured by the camera installed above the specimen to monitor the strain rate. The video from the camera is processed as shown in Fig.5.2.c and combined with the force measurements in both directions to obtain the stress-strain response of the tissue. Images of the biaxial tensile test shown in Fig.5.2 were conducted in Boston Child Hospital as a collaboration carried out by the CURATIVE associated team¹. This experiment was

¹<https://team.inria.fr/curative/team-members/>

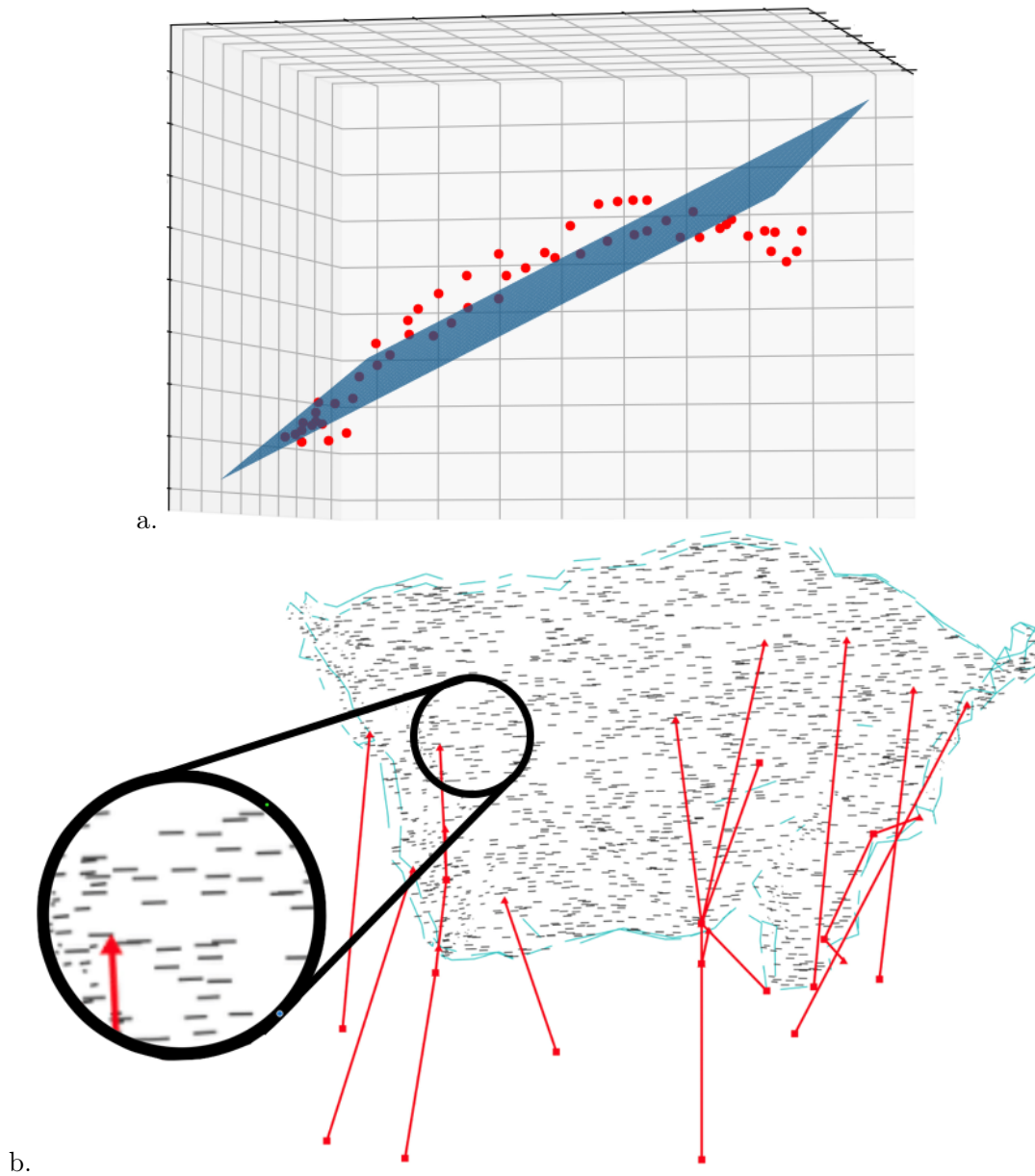


Figure 5.1: Planar annulus surface: a flat plane with a minimum distance to the nodes on the annulus ring (*a.*). Fibers specified parallel to the circumferential direction of the MV leaflet. For better visualization, only the anterior leaflet is shown (*b.*).

conducted to address the inconsistencies observed in the stress-strain data presented in various studies in the literature. For example, studies such as [JLK⁺18b, MNY95, WS13] all reported different stress-strain responses for MV leaflets. However, we found that the measurements from the Boston Child Hospital produced overly elastic simulations, leading to unrealistic leaflet stretching and excessive bulging in which the saddle shape of the leaflet at peak systole was not visible anymore. Therefore, we use the measurements reported in the literature [JLK⁺18b] for our simulation purposes. A video showing the dynamic closure of the MV with the measurements

from the Boston Child Hospital is accessible through this link²

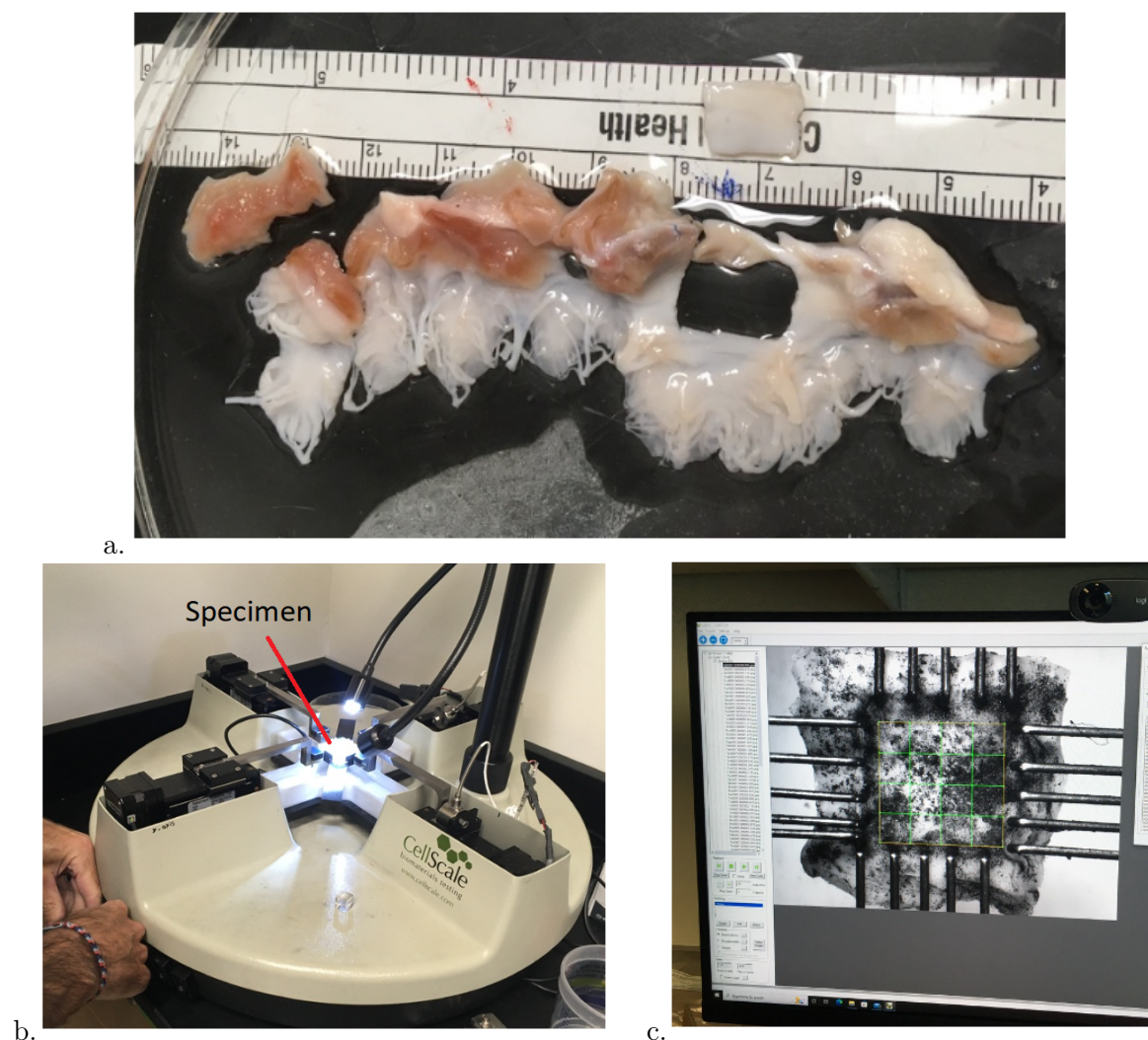


Figure 5.2: Biaxial tensile test: (a.) specimen preparation, (b.) test setup, and (c.) data analysis.

The reported data on the experimental test is mostly represented based on stress-strain (S_{ij} versus E_{ij}), as in [Sac99], or stress-stretch (S_{ij} versus λ_{ij}) plot, as in [JLK⁺18b]. In the following, we will present information regarding fitting experimental data on different constitutive models, as well as discuss the associated challenges.

5.1.3 Fitting experimental data on the generalized Fung constitutive model

The generalized Fung model was previously used for material behavior of heart tissue in [Sac99, Ham11, ABVA16, Pan21], and it was the first anisotropic model we tried to implement for our simulation purposes. In the following, we will explore the fitting process to obtain the generalized Fung parameters in two-dimensional (2D) and three-dimensional (3D).

²<https://youtube.com/shorts/FwJXmVfVd8c>

Obtaining material parameters for two-dimensional generalized Fung model

From the experimental measurements, we have access to the stress-strain data. Therefore, the first step is to relate the stress term to the generalized Fung strain energy function. The relation between the stress predicted by the constitutive model (S_{ij}^p) and the strain energy function is:

$$S_{ij}^p = \frac{\partial \psi}{\partial E_{ij}}. \quad (5.7)$$

In the case of the 2D model, this equation is expanded as:

$$\begin{aligned} S_{11}^p &= \frac{\partial \psi}{\partial E_{11}} = \frac{c}{2} \times \exp(b_{1111}E_{11}^2 + b_{2222}E_{22}^2 + 2b_{1122}E_{11}E_{22} + b_{1212}E_{12}^2) \\ &\quad \times (2b_{1111}E_{11} + 2b_{1122}E_{22}), \\ S_{22}^p &= \frac{\partial \psi}{\partial E_{22}} = \frac{c}{2} \times \exp(b_{1111}E_{11}^2 + b_{2222}E_{22}^2 + 2b_{1122}E_{11}E_{22} + b_{1212}E_{12}^2) \\ &\quad \times (2b_{2222}E_{22} + 2b_{1122}E_{11}), \\ S_{12}^p &= \frac{\partial \psi}{\partial E_{12}} = \frac{c}{2} \times \exp(b_{1111}E_{11}^2 + b_{2222}E_{22}^2 + 2b_{1122}E_{11}E_{22} + b_{1212}E_{12}^2) \\ &\quad \times (2b_{1212}E_{12}). \end{aligned} \quad (5.8)$$

Here, S_{11}^p , S_{22}^p , and S_{12}^p are stress in the first principal direction, second principal direction, and shear tension respectively. This means that in order to obtain the material parameters for the generalized Fung model, in addition to both principal stresses, the measurement data of the shear tension is also needed. Therefore, in equation 5.8, values of stress (S), and strain (E) are known values from the experimental data, and the purpose of the optimization is to obtain the values of b.

In [Sac99], a planar biaxial tensile test is conducted to obtain the mechanical response of the heart myocardium. In this study, an interesting approach is described to indirectly obtain the shear data. This was achieved by executing the biaxial tensile test in several protocols and orienting the specimen away from the principal directions. Later, by data manipulation, they re-calculated the stress-strain data for the two principal directions and extracted the shear tension based on how much the specimen rotated during the testing procedure. The protocols refer to the different loading conditions. For example, in Fig.5.3.a, the stress-strain data in two protocols of 1 : 1 and 1 : 3 is presented. In the first protocol, the strain in the first direction (circumferential), is equal to the strain in the second direction, (radial), $E_{11} = E_{22}$. For the second protocol, the strain in the second direction is three times larger than the strain in the first direction, $E_{22} = 3E_{11}$. In the first measurement protocol (1 : 1), no rotation is observed on the specimen. But, due to the asymmetry of applied forces in the protocol 1 : 3, it was possible to obtain the shear data which is reported in Fig.5.3.b.

To fit the experimental measurements on the generalized Fung model, we need to solve an optimization problem. The objective function we used for this purpose is:

$$R_{Fung} = \sum_{i=1}^n \sum_{j=1}^m (S_{11}^{p(i)} - S_{11}^{exp(i)})_j^2 + (S_{22}^{p(i)} - S_{22}^{exp(i)})_j^2 + (S_{12}^{p(i)} - S_{12}^{exp(i)})_j^2. \quad (5.9)$$

Here, m is the number of measurement points, and n is the number of measurement protocols which in this case is 2. The purpose of the objective function is to reduce the difference between

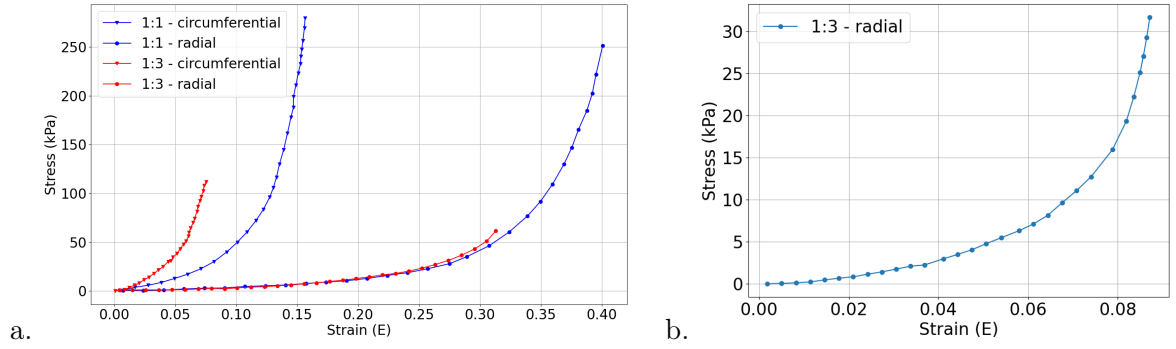


Figure 5.3: Mechanical response of the heart myocardium tissue: (a.) Stress-strain data in 1 : 1 and 1 : 3 measurement protocol, (b.) Shear tension in 1 : 3 measurement protocol [Sac99].

the value of stress reported in the experimental measurements, S_{ij}^{exp} , and the one calculated based on the generalized Fung model, S_{ij}^p . It is beneficial to cross-check the extracted material parameters using third-party finite element solvers to confirm if the expected minimum has been reached. Therefore, once the global minimum for the objective function is reached, the extracted material parameters should be examined by conducting benchmark problems in any available finite element solver.

Obtaining material parameters for three-dimensional generalized Fung model

Extracting the coefficients of the generalized Fung model is challenging. In [Sac99], the material parameters for the 2D generalized Fung are obtained. However, this data is only useful for the simulations representing the MV leaflet with 2D surface elements. In numerical simulations, employing 2D representation of structural elements reduces the computation time compared to 3D configurations. However, in complex deformation, a lack of depth in 2D models can introduce errors. In our FSI simulation, which is based on the IB approach, a 2D representation of the leaflet tissue results in excessive blood leakage and unrealistic MV deformation. Consequently, it is necessary for us to incorporate 3D elements for the accurate depiction of leaflet tissue, necessitating the selection of material parameters specifically tailored for 3D configurations.

For extracting the 3D coefficients of the generalized Fung model, shear data in all three directions is needed. Since MV stress-strain data is obtained from planar biaxial tests, it is not possible to extract the shear data in the direction perpendicular to the specimen surface. In [ABVA16], an inverse finite element study is used to optimize the constitutive model coefficients based on an in vitro experimental study. However, in this approach, they only tracked the displacement of the leaflet in only one single node and obtained the coefficients based on this single measurement. In addition, this approach needs a complex in vitro setting and the material parameters extracted this way are only tailored for that specific setup and valve and cannot be used in other studies. Therefore, it is not possible to extract the material parameters for the 3D generalized Fung model since it requires shear data in all three main directions.

5.1.4 Obtaining the material parameters for the Holzapfel-Gasser-Ogden constitutive model

The fact that the HGO model is based on fibers laying on a uniform medium, simplifies the extraction of material parameters compared to the generalized Fung model. With this method, there is no need for shear data; the stress-strain response in the principal directions alone suffices to determine the material parameters. In our study, we attempted to extract the HGO material parameters in two approaches. One directly fitting the experimental data on the HGO strain energy function, and one based on inverse finite element analysis. In the following, we explore both approaches.

Fitting the experimental data on the strain energy function

From the experimental measurements, [JLK⁺18b], we have access to stress-stretch (S_{ij}^p versus λ_k) data. λ_k represents the tissue stretch in x , y , and z directions. In equation 5.6, the terms I_1 and $I_{4(\alpha\alpha)}$ can be written based on λ_k as:

$$I_1 = \lambda_1^2 + \lambda_2^2 + \lambda_3^2, \quad (5.10)$$

and

$$I_{4(\alpha\alpha)} = \lambda_1^2 \text{Cos}(\gamma^\circ)^2 + \lambda_2^2 \text{Sin}(\gamma^\circ)^2. \quad (5.11)$$

γ° represents the angle between the fiber family and the circumferential direction. In our study, we assume that the fiber families in the MV leaflet align parallel to the circumferential direction, setting γ° to zero. This yields:

$$I_{4(\alpha\alpha)} = \lambda_1^2. \quad (5.12)$$

In the experimental measurements, only the stretch in the circumferential and radial direction is reported, and the stretch in the direction perpendicular to the MV tissue surface (λ_3) is missing. In the case of incompressible materials, we have:

$$\lambda_1 \lambda_2 \lambda_3 = 1. \quad (5.13)$$

Therefore, the term λ_3 can be written as:

$$\lambda_3 = \frac{1}{\lambda_1 \lambda_2}. \quad (5.14)$$

This will allow us to liberate 5.10 from λ_3 and re-write it only based on λ_1 and λ_2 as:

$$I_1 = \lambda_1^2 + \lambda_2^2 + \frac{1}{(\lambda_1 \lambda_2)^2}. \quad (5.15)$$

By inserting equation 5.12 and 5.15 into equation 5.4, the HGO strain energy function, based on stretch, will be represented as:

$$\psi = C_{10}(\lambda_1^2 + \lambda_2^2 + 1/(\lambda_1 \lambda_2)^2 - 3) + K_1/2K_2[\exp(K_2 < E_\alpha >^2) - 1], \quad (5.16)$$

with the term E_α being:

$$E_\alpha = \kappa(\lambda_1^2 + \lambda_2^2 + 1/(\lambda_1\lambda_2)^2 - 3) + (1 - 3\kappa)(\lambda_1^2 - 1). \quad (5.17)$$

To relate the stress data obtained from the experimental measurements to the HGO strain energy function, we need to combine the equation of green strain tensor (E), which is based on the deformation gradient tensor (F) with Eq.5.7. The green strain tensor is expressed as:

$$E = 1/2(F^T \cdot F - I). \quad (5.18)$$

Here, I is the identity matrix. In the case of a biaxial tension test without shear, F is a diagonal tensor, described as:

$$F = \begin{bmatrix} \lambda_1 & 0 & 0 \\ 0 & \lambda_2 & 0 \\ 0 & 0 & 1/\lambda_1\lambda_2 \end{bmatrix}. \quad (5.19)$$

Therefore, the relation between the green strain and stretch is:

$$E_{11} = 1/2(\lambda_1^2 - 1), \quad (5.20)$$

$$E_{22} = 1/2(\lambda_2^2 - 1).$$

Equation 5.20 can be expressed as:

$$\frac{\partial E_{ii}}{\partial \lambda_i} = \lambda_i. \quad (5.21)$$

Utilizing the chain rule, the relation between the HGO strain energy function and stress can be articulated as:

$$\frac{\partial \psi}{\partial \lambda_i} = \frac{\partial \psi}{\partial E_{ii}} \times \frac{\partial E_{ii}}{\partial \lambda_i} = S_{ii}^p \times \lambda_i. \quad (5.22)$$

Therefore, the predicted stress is expressed as:

$$S_{ii}^p = \frac{\partial \psi}{\partial \lambda_i} \times \frac{1}{\lambda_i}. \quad (5.23)$$

In any biaxial experimental measurement protocol, the relation between stress component and stretch is given by equation 5.24 and equation 5.25.

$$S_{11}^p = \frac{C_{10}}{\lambda_1} [2\lambda_1 - \frac{2}{\lambda_2^2\lambda_1^3}] + \frac{K_1}{2K_2\lambda_1} \exp(K_2 < E_\alpha >^2) \times (2K_2 < E_\alpha >) \times [< \kappa[2\lambda_1 - \frac{2}{\lambda_2^2\lambda_1^3}] + (1 - 3\kappa)2\lambda_1 >], \quad (5.24)$$

$$S_{22}^p = C_{10}/\lambda_2 [2\lambda_2 - \frac{2}{\lambda_1^2\lambda_2^3}] + \frac{K_1}{2K_2\lambda_2} \exp(K_2 < E_\alpha >^2) \times (2K_2 < E_\alpha >) \times (< \kappa[2\lambda_2 - \frac{2}{\lambda_1^2\lambda_2^3}] >). \quad (5.25)$$

Objective function: The literature does not provide HGO coefficients (C_{10} , K_1 , K_2 , and κ) specific to MV tissue. Indeed, Such parameters are available in [RFS⁺13], but it is specifically tailored for a single ovine MV. Other reported HGO parameters, as cited in [LPT20], are based on the aortic valve. Therefore, we decided to use stress-strain experimental data from [JLK⁺18b] to extract the proper coefficients for our simulation. In our direct approach, we attempted to extract the coefficients of the strain energy function by performing an optimization to minimize the objective function expressed as:

$$R_{HGO} = \sum_{i=1}^n \sum_{j=1}^m (S_{11}^{p(i)} - S_{11}^{exp(i)})_j^2 + (S_{22}^{p(i)} - S_{22}^{exp(i)})_j^2. \quad (5.26)$$

Here, the R_{HGO} represents the loss function, i is the index identifying different measurement protocols, and m is the number of measurement points in each protocol. In the case of the HGO model, the strain energy function consists of one linear and one exponential term with four different coefficients. This makes it challenging to fit experimental data.

For the optimization process, we experimented with various approaches, utilizing different Python and MATLAB libraries, including "levenberg-marquardt", "lsqcurvefit", and "L-BFGS-B" in "basinhopping" to derive the material parameters. Yet, when we tested the derived coefficients using the Abaqus solver on benchmark cases, we noticed significant errors in the material model's mechanical response. One of the benchmark cases we tested was applying stretching forces on four sides of a square plane with the same thickness as the MV leaflet, replicating the experimental biaxial tensile test in the numerical environment. The discrepancy emerged due to the nonlinearity of the strain energy function and the high degree of freedom in the objective function concerning the material parameters. As mentioned in [SS05], the objective function can have several local minima.

We also tried to escape the local minima by conducting a grid search, which did not help with the problem due to the vast range of upper and lower bounds of the coefficients and the relatively long computation time. We used several initial values with the upper and lower bounds mentioned in table 5.1 which we guessed based on the similar values reported in the literature, for example in [RFS⁺13, LPT20]. The grid search takes more than several days to find multiple local minima but failed to give us the global one.

The root of the problem is that the range of the values each parameter can accept is large, making the gap in the resolution of the grid search too wide, which the global minima can hide inside. For visualization, Fig.5.4 shows the contour of the residuals versus the C_{10} and K_1 , when fixing the K_2 and κ to be 17.5 and 0.05 respectively. We notice that values of both C_{10} and K_1 falling below their lower bound results in higher residual values. Moreover, mid-range values of C_{10} lead to smaller residual. In addition, in some of our attempts to find the global minima with the grid search, the global minima seemed to be outside of the specified range for the parameters, which makes the parameter extraction more challenging.

Material parameter:	C_{10}	K_1	K_2	κ
Lower bound:	1×10^5	1×10^8	1×10^5	0.32
Upper bound:	10	1×10^3	10	0.05

Table 5.1: Upper and lower bounds and an example of initial value for the direct optimization of the strain energy function.

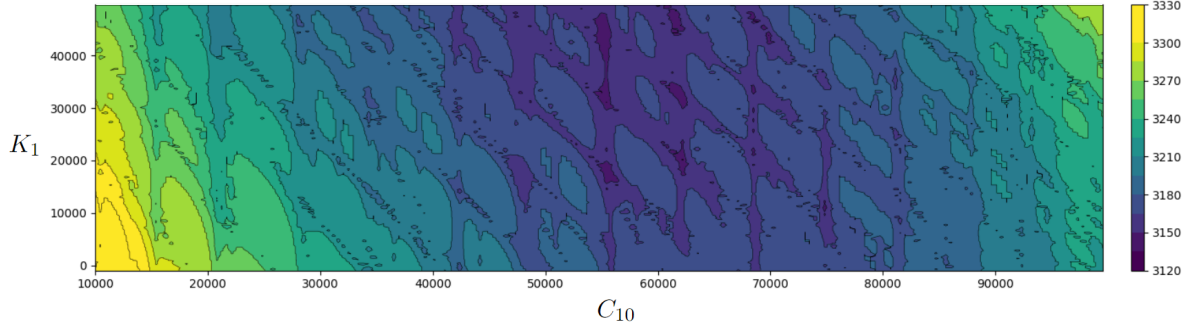


Figure 5.4: Illustration of the grid search, show the isocontour of residuals for C_{10} and K_1 by fixing the K_2 and κ .

Fitting the experimental data by using inverse finite element analysis

As our direct approach to obtain the material parameters was not successful, we decided to employ another approach already used in the literature which is based on inverse finite element analysis [ABVA16]. In this approach, instead of minimizing the prediction error from the strain energy function, the error between the results from a finite element analysis and a set of experimental data is conducted. The finite element analysis is usually a simulation of a tension test on a simple rectangular cube. The material model is already implemented in the inverse finite element analysis and a fitness function is described to minimize the prediction error. The optimization process is done with the MCalibration software¹ which is connected to the Abaqus solver to execute the inverse finite element analysis calculations. The overall flowchart of the process is shown in Fig.5.5.

The solver uses a normalized mean absolute difference (NMAD) fitness function as:

$$NMAD = 100 \times \frac{|S^{exp} - S^p|}{\max(S^{exp}, S^p)} \quad (5.27)$$

This fitness function can be optimized with various optimization techniques already embedded in the MCalibration. Depending on the chosen optimization technique, the results turn out to be unstable and sensitive to the initial estimate. We thus use genetic algorithms for minimization, consider more than a hundred plausible initial values, and keep the one that provides the smallest residual. During the process, MCalibration offers a visual comparison between the stress-strain response from the finite element simulation and the experimental data. This feature simplifies the task of setting initial values for the optimization. The parameters computed with this method are reported in table.5.2. In Fig.5.6, the dashed lines depict the mechanical response of the

¹<https://polymerfem.com/mcalibration/>

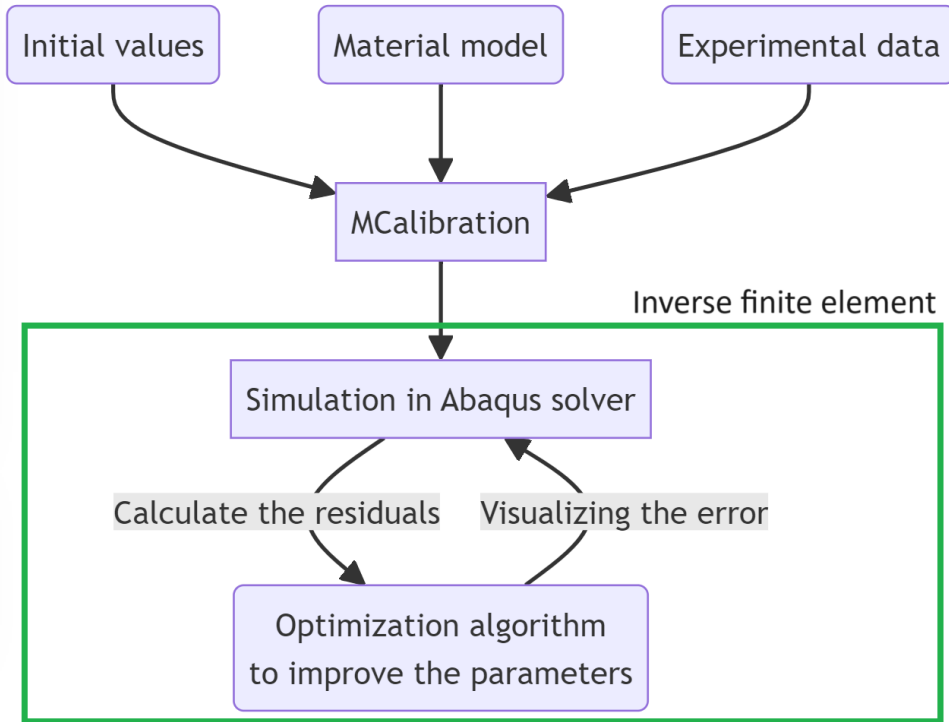


Figure 5.5: Flowchart showing the process of obtaining the material parameters in MCalibration.

HGO model, as simulated in Abaqus using the specified parameters. The solid lines show the input measurement data reported in [JLK⁺18b]. By observing the Fig.5.6, it is evident that the computed mechanical response in the second direction (represented by the red dashed line) is not perfectly aligned with the experimental data, particularly for stress values exceeding $200kPa$. While this discrepancy highlights a limitation in the parameters we have extracted, we deemed them acceptable for this study. This decision was based on the observation that the majority of the stress distribution on the leaflet falls below the $200kPa$ threshold.

Material parameter:	C_{10}	K_1	K_2	κ	D
Optimized value:	2272	4000	150	0.25	0.0

Table 5.2: Material parameters for the HGO model, derived from experimental data reported in [JLK⁺18b].

5.1.5 Isotropic model

This chapter primarily explores how anisotropy affects the dynamic behavior of MV. To accomplish this, we use the anisotropic HGO model described in this section and compare its simulation results with the isotropic third-order Ogden model described in the previous section. To obtain the isotropic material parameters comparable with the anisotropic one, first, we set the dispersion coefficient, κ , in equation 5.4 to the maximum, $1/3$, which makes the HGO constitutive

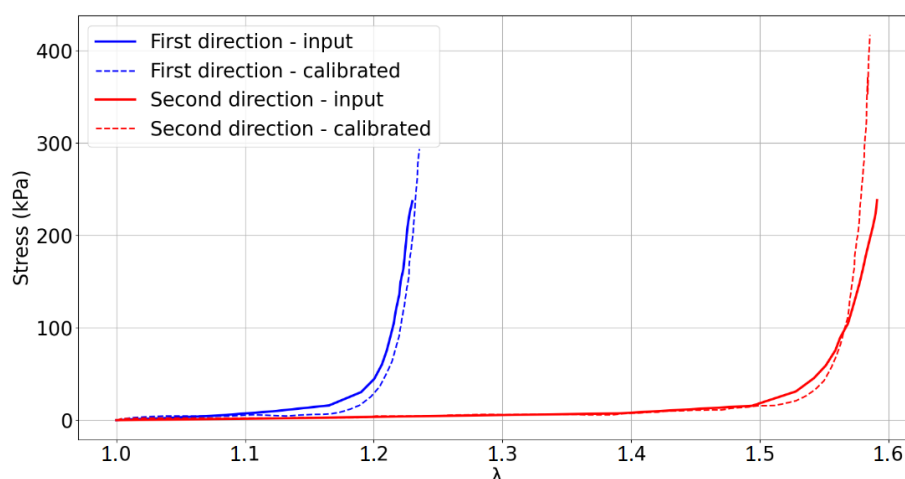


Figure 5.6: The result of the inverse finite element analysis procedure: Showing the mechanical response of the HGO model with the optimized parameters (dashed lines) compared to the input data (solid lines) [JLK⁺18b].

model act as isotropic in the leaflet surface. The dashed line in Fig.5.7 shows the mechanical response of the HGO model if $\kappa = 1/3$. The stress-strain response is then extracted and used as input data to obtain the material parameters in the third-order Ogden hyperelastic constitutive model. The material parameters are reported in table 5.3. We used these parameters to delineate the isotropic response of the MV. This allowed for a comparative analysis of the MV dynamic closure when subjected to both isotropic and anisotropic material models. The findings from this analysis are presented in section 5.3.

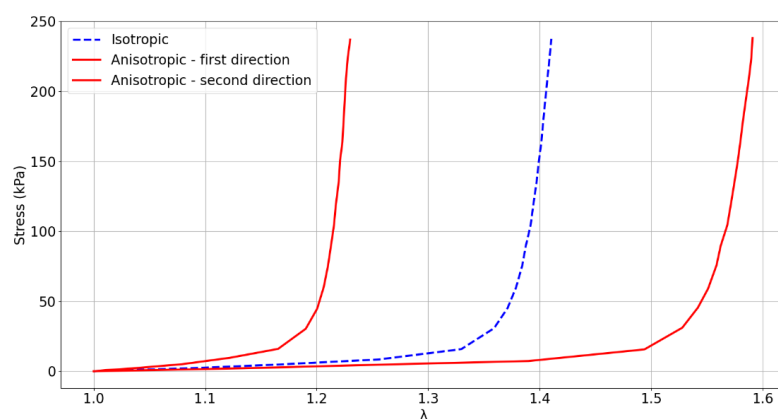


Figure 5.7: Comparison of the HGO mechanical response in case of $\kappa = 1/3$, which results in planar isotropic characteristics, against the stress-strain data (solid lines) reported in [JLK⁺18b].

	$i = 1$	$i = 2$	$i = 3$
$\mu :$	-481836.3	484166.6	742.8
$\alpha :$	-19.4	-19.3	-25

Table 5.3: Material parameters for the 3rd-order Ogden hyperelastic material model, derived from experimental data reported in [JLK⁺18b].

5.2 Image-based geometry and case setup

In patient-specific simulations, the closed state and dynamic behavior of the MV depends on the accuracy of the input data: geometry of MV and chords and the setup which describes how the MV interacts with the neighboring anatomic structures or the fluids. Here, we describe how we can modify the FSI case setup to improve the representation of the MV inside the fluid domain.

With patient-based simulation in view, we first aim to extend the work described in chapter 4 to the case of image-based MV models. The details of incorporating an image-based MV geometry are described in chapter 2. Image-based geometries may be irregular with an annulus shape neither elliptic nor planar. In addition, the use of a fitted tube is often impossible since the MV in the open state may lie outside the cylinder defined by the annulus. We thus propose in this chapter an investigation on how using a large cylinder as a representation of LV can influence the simulation outcome compared to the fitted tube. In the case of large cylinder, housing is used to seal the annulus to the tube walls. This large cylinder can be seen as an intermediate solution between a fitted tube, which is not realistic, and a complete model of the ventricle which is difficult to obtain and implement.

For this purpose, we implemented three image-based geometries, P-1, P-2, and P-4 already shown in Fig.2.5 of chapter 2, to manifest that our model is not tailored only for one set of data, which in the literature, the work of several groups are continuously based on only a single sample set (an example is [TBP⁺17]). We incorporated both valves into the case setup with the large cylinder, as illustrated in Fig.5.8.a, Fig.5.8.b, and Fig.5.8.c. In the following section, we discuss the results of comparing the MV behavior when using a large cylinder versus when a fitted tube represents the LV. For the P-2 and P-4 setup, the MV with the fitted tube performed poorly, resulting in an open valve. Thus, we only present the comparison for P-1 between the large cylinder and fitted tube configurations. The setup for P-1 with the fitted tube can be seen in Fig.5.8.d.

5.3 Results and discussion

Besides closure, which is an important criterion in valve simulation, our study assesses the results of both generic and patient-specific FSI simulations through several key metrics. These metrics encompass various aspects, including the quality of leaflet contact and coaptation area, as visually represented in the contact map, as well as the analysis of cumulative distribution functions (CDF, denoted as $P(\text{Pressure} > s)$), measured flow rates, and the distribution of stress across the leaflet surface. Furthermore, our evaluation takes into account the alignment of our results with physiological behaviors reported in clinical studies. Specifically, we consider factors

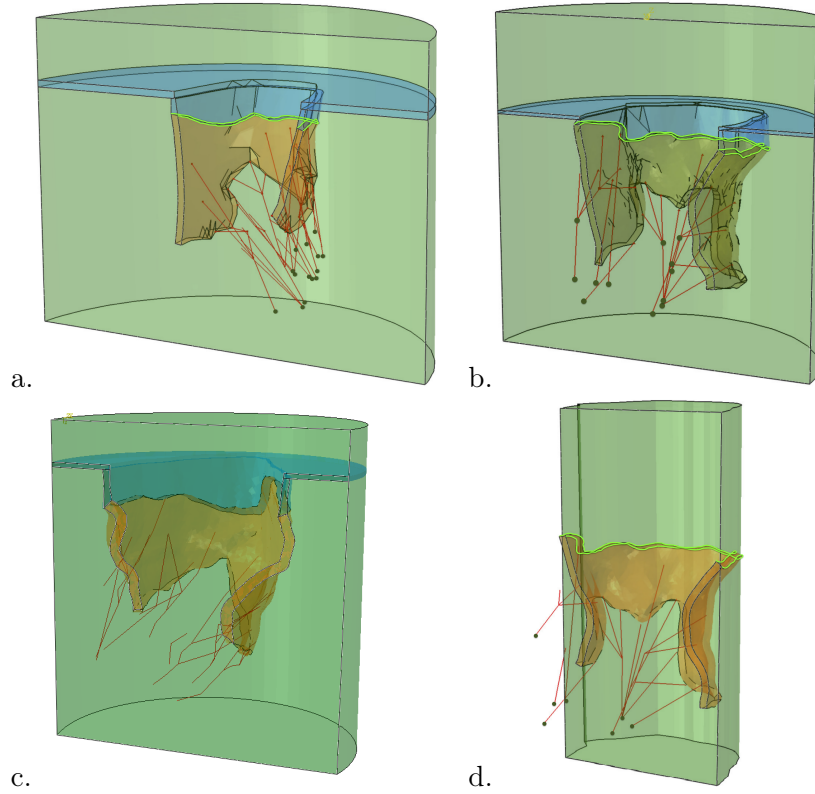


Figure 5.8: P-1 (a.), P-2 (b.), and P-4 (c.) inside a large tube. Orange: valve, red: chordae, blue: additional geometry to obstruct the flow, and light green: pinned annulus region. (d.) shows the P-1 inside a fitted tube.

such as minimal valve bulging, a characteristic of healthy valves, and the balanced distribution of forces between primary and secondary chordae throughout the cardiac cycle, as studied in the literature using ex vivo data [PIMW⁺20]. Both bulging and force distribution over time serve as essential evaluation criteria in our experiments. Our findings are organized into two sections. First, we present the impact of anisotropy on valve behavior, and then we discuss the influence of geometric features and fluid volume on the simulation results.

5.3.1 Influence of anisotropy

We compare in this section the simulations obtained with and without considering anisotropy in the case of a generic and an image-based valve. Our real valve data geometry comes from microCT where the shape of the annulus in the peak systole differs from the state where the geometry was segmented. Our case setup is currently based on a fixed annulus ring inside a cylinder. This however does not fully reflect the heart physiology since the annulus ring may deform noticeably during the cardiac cycle. Comparing our final simulated geometry with microCT data with a different annulus shape is subsequently not straightforward. Therefore, we used a contact map, bulging volume, and measurements from the literature (chordae force), to compare the behavior and patterns emerging in the simulation. All the results from this section are based on MV inside a fitted tube as the LV.

Bulging volume

The bulging volume is a valuable metric introduced in [JHG⁺18]. We used this metric to compare our simulation results. Fig.5.9 presents a comparison of the bulging volume for both the anisotropic and isotropic constitutive models, across image-based and generic valves. To calculate this metric, we initiate the process by delineating a curved surface that intersects with the annulus ring. Subsequently, we measure the shortest distance between every triangular facet on the leaflet’s surface and the curved annulus surface. Multiplying each of these distances by the surface area of its respective triangular facet yields the volume of each facet. The accumulation of all positive values results in the determination of the final bulging volume. In Fig.5.9, the red surface shows where the bulging occurs and the green region is the part of the tissue leaflet that drops below the annulus curved surface.

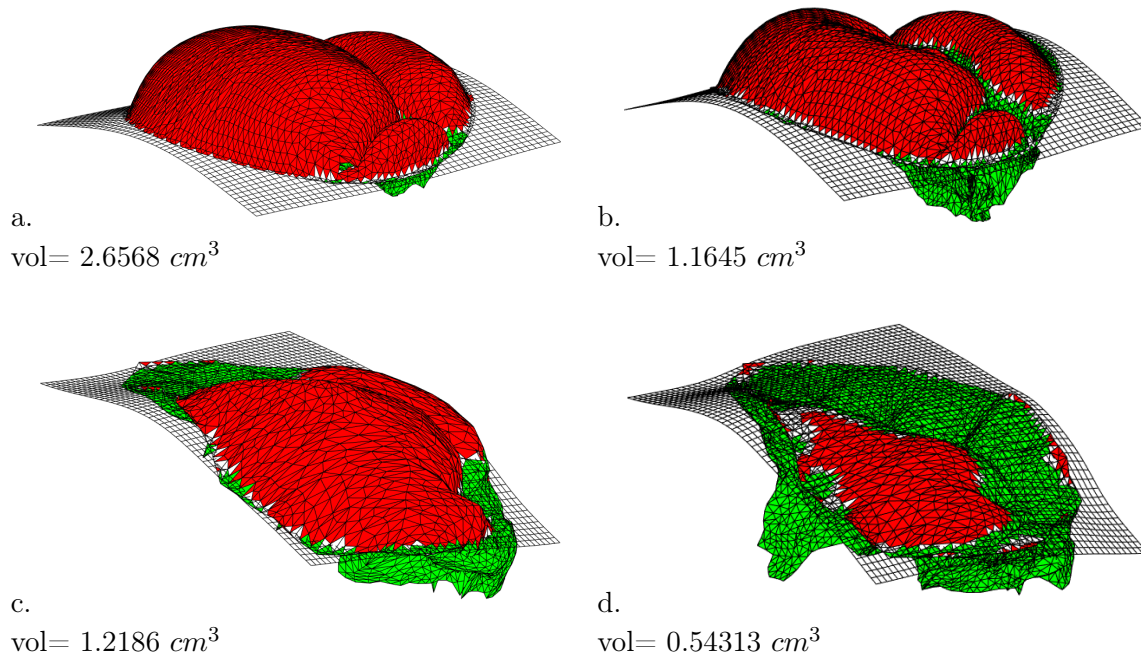


Figure 5.9: Top row: bulging on the generic valve with (a.) isotropic and (b.) anisotropic constitutive model. Bottom row: bulging on the image-based valve with (a.) isotropic and (b.) anisotropic constitutive model

Both for generic and image-based cases, the use of the isotropic constitutive model induces a high bulging of the leaflet (see Fig.5.9.a and Fig.5.9.c), whereas anisotropy shows a decreased bulging. This fact is in good agreement with clinical knowledge which states that “A normal mitral valve has a large surface of coaptation with the free edge positioned low below the plane of the orifice” [CAF10]. In the image-based MV with the anisotropic constitutive model, the bulging is the least, and the saddle-shape curvature of the leaflet in the final state of the simulation is apparent.

Chordae forces

Another interesting observation is the ability of our model to reproduce the imbalanced chordae forces between primary and secondary chordae, a phenomenon previously quantified in an ex vivo study by Paulsen et al in [PIMW⁺20] and visually depicted in Fig.5.10.a. Our simulations during closure have to be compared to this graph in the time interval [0.1 – 0.2] seconds. As indicated by the data in Figure 5.10.b and Figure 5.10.c, the order of chordae forces across different categories is expected to align with the ex-vivo measurements (Figure 5.10.a). During the closure phase, the ex-vivo data shows an increasing trend globally in chordae forces. This trend is replicated in both isotropic (Fig.5.10.b) and anisotropic (Fig.5.10.c) simulations, with two exceptions: the posterior secondary chordae in the isotropic case, and the posterior primary chordae in the anisotropic case. In the isotropic model, we observe that the force magnitudes for the posterior secondary chordae fall below those of the primary chordae. On the contrary, the order of chordae forces in different categories is respected in the simulation with anisotropy. Furthermore, the magnitude of chordae forces in this case is more similar to the values reported in the ex-vivo measurement.

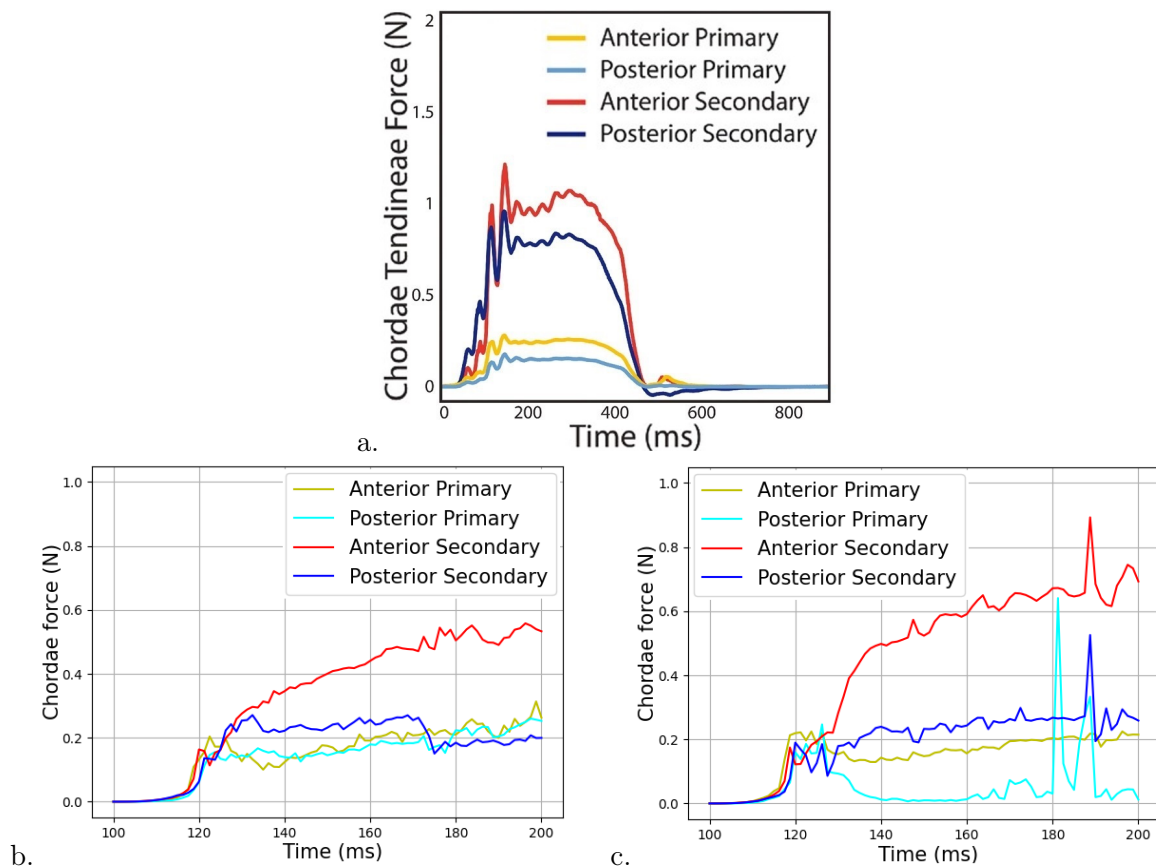


Figure 5.10: Chordae force distribution on ex-vivo data from [PIMW⁺20] (a.), simulation with isotropic (b.), and anisotropic (c.) constitutive model.

Contact

When analyzing the results from the contact map, there is no ground truth in how exactly the contact between the leaflets should occur. However, in our analysis, we favor a more uniform shape of the coaptation area, a larger coaptation area, and stronger contact pressure. These criteria are open to debate and more studies on this subject are needed. In addition, experts in the field seem to have different opinion on how the contact between the leaflets should occur. One of the experts, Dr. Peter E. Hammer, who is a member of the CURATIVE associate team² suggested that as the valve close, the intensity of the contact pressure is not of interest, but only the surface area and the shape of the coaptation are important to evaluate the good quality closure. Another team in Lyon medical school [GBL⁺20] working on using piezoelectric sensors to measure the contact pressure in the peak systole and they believe that the contact pressure is important to evaluate the quality of the closure.

The map of contact obtained with the isotropic and anisotropic constitutive model is presented in Fig.5.11. The coaptation area in the case of the isotropic constitutive model (Fig.5.11.a) is very irregular. The coaptation strap near the annulus in this case is caused by high bulging folding the leaflet in this region and creating a crease near the annulus. In the case of the anisotropic constitutive model, the region in contact is more regular, creating a smooth and uniform coaptation area that is parallel to the annulus.

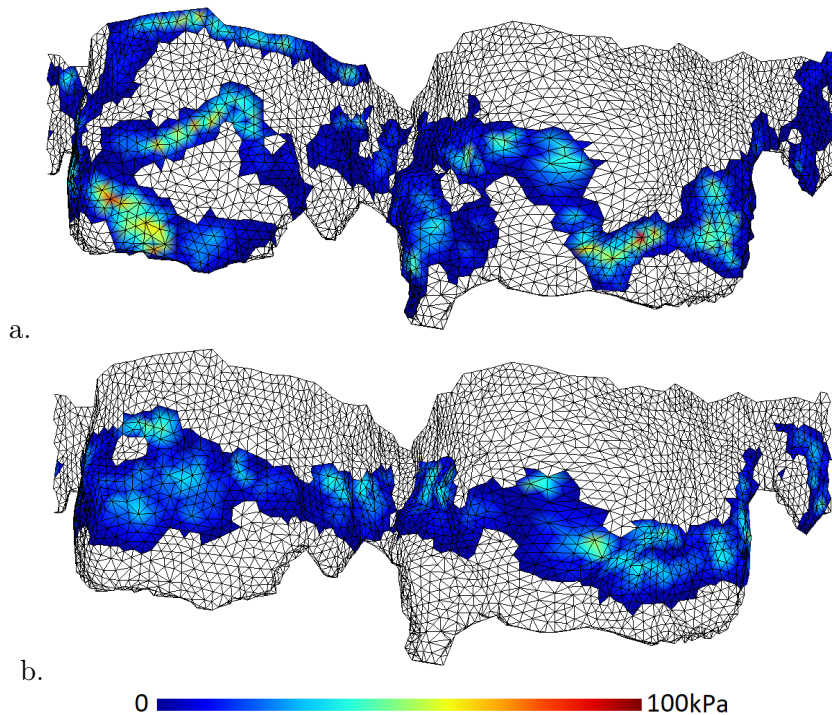


Figure 5.11: Contact map with isotropic (a.) and anisotropic constitutive model (b.).

The contact pressure distribution in both cases appears to be evenly spread across their coaptation areas. Nonetheless, the isotropic case exhibits slightly stronger contact, an observation

²<https://team.inria.fr/curative/team-members/>

that aligns with its larger bulging volume. To have a better understanding of the contact pressure distribution, we studied the probability of contact pressure distribution by using a cumulative map, i.e. $P(|pressure| > t)$, which is presented in Fig.5.12. According to this map, higher contact pressure amplitude is more common in the isotropic case. More specifically, when the amplitude is between 20 to 60 kPa .

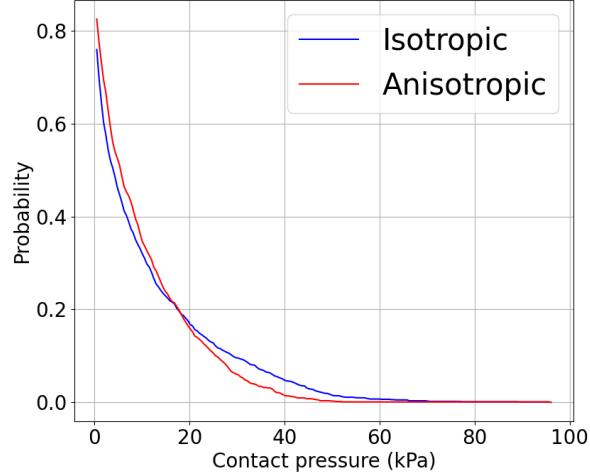


Figure 5.12: Cumulative distribution function (CDF) of the contact pressure in both isotropic and anisotropic constitutive models.

Despite the irregular coaptation area in the isotropic case, the flow rate in both instances exhibits a comparable behavior (see Fig.5.13). As pressure accumulates from the bottom of the tubular LV, the flow rate reaches its maximum at the same time frame, with the anisotropic case showing a slightly lower peak. Following that, the flow rate drops to zero in both cases and starts to oscillate. The coaptation area and flow rate measurements both affirm that the valve is sealed in both the isotropic and anisotropic cases. However, a high bulging volume and irregular coaptation area in the isotropic case underscore its limited capacity to properly simulate the dynamic closure of the MV.

5.3.2 Influence of geometry and fluid volume

In this part, we used the anisotropic constitutive model and the P-1 image-based valve to investigate the influence of smoothing of the segmented geometry and fluid volume in the simulation results. In the case of the P-1 valve, by using an Intel Xeon 3.60 GHz workstation with 4 processors, the simulation was completed in 47 hours with a large cylinder comprising 196k $C3D8$ cubic elements in the fluid domain and 30k $C3D4$ tetrahedron elements for the leaflets. In addition, the simulation for the image-based MV with the fitted tube, which had 80k $C3D8$ cubic elements in the fluid domain and 30k $C3D4$ tetrahedron elements for the leaflets, took 14 hours to compute. (For more information on the different element types, see chapter 2). The resolutions for both the fluid and structural numerical domains were chosen to ensure mesh independence in the simulation. The width of the large cylinder was selected in a way to include all of the MV geometry inside with a small margin to keep the distance from the tubular LV walls. The height

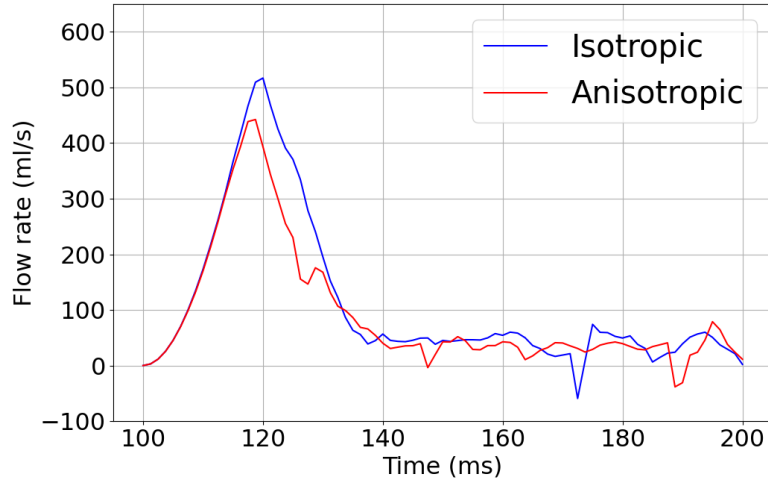


Figure 5.13: Flow rate in both isotropic and anisotropic constitutive models.

of the tube is subjective. We considered 35mm for the length of the lower part (from the inlet to the planar annulus surface) to mimic the LV size. This will give enough clearance between the inlet and the free edge of the leaflet. The length of the upper part, which represents the left atrium, is considered 15mm to have a clearance between the leaflet's top surface and the outlet.

Smoothed leaflet

To investigate the influence of the smoothness of the MV leaflet from the segmentation process, here we compare the simulation results of both the original P-1 and the smoothed valve as described in chapter 2. The purpose of investigating the smoothness of the leaflets was to understand how the roughness of the extracted geometry from the segmentation process influences the simulation outcome. Depending on the quality of the segmentation process and the resolution of the geometry extracted, the roughness of the extracted MV leaflet from the segmentation process can vary [CMB⁺21]. Therefore, we applied smoothing with an average absolute distance of 0.145mm on the leaflet of the P-1 geometry. This approach aimed to reduce surface roughness on the valve leaflets while maintaining the leaflets essential characteristics, such as the size of the opening orifice and the original curvature. The opened state of the P-1 valve in both the original shape and the smoothed version is shown in Fig.2.7 within chapter 2.

Our experiments show that smoothing enhances the contact between the leaflets and slightly improves the bulging volume (see Fig.5.14). In the contact map depicted in Fig.5.15, it is evident that the coaptation area in the smoothed case increased compared to the original P-1 valve. Furthermore, as illustrated in the cumulative distribution function (CDF) plot in Fig.5.16, the contact pressure magnitude is notably higher in the case of the smoothed valve. In general, the roughness of the surface obtained from the segmentation process influences the coaptation and contact pressure, but the overall shape of the MV in the peak systole was not affected. Better contact and coaptation are expected by smoothing of the leaflets, as this process reduces the surface noise on the geometry. However, at some point, increasing the smoothing changes the overall geometry of the leaflet, enlarging the valve opening. Such alterations compromise the

valve's ability to close properly, resulting in closure with orifice holes.

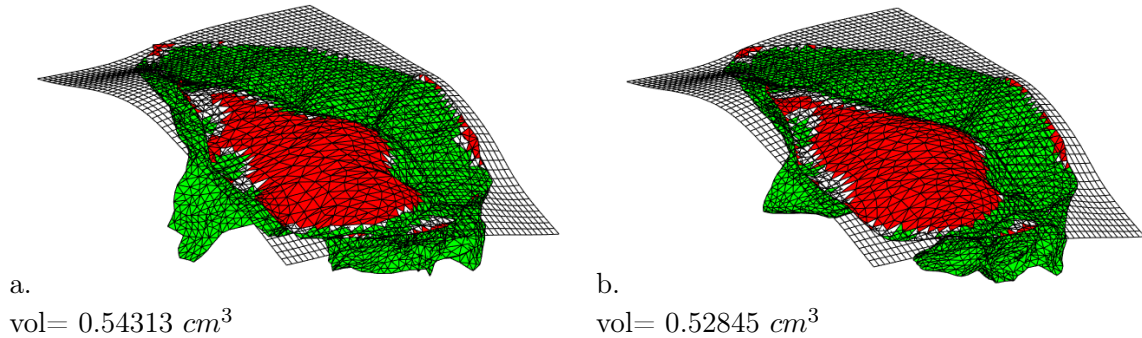


Figure 5.14: Bulging on the (a.) P-1 with fitted tube and anisotropic model and (b.) smoothed P-1 with the fitted tube and anisotropic model.

Using the large cylinder as the tubular left ventricle

For the case of the large cylinder, the presence of the additional part blocking the flow passing over the annulus, caused some instabilities as vibration on the leaflet during the closure. We minimize this numerical instability by refining the resolution of the elements in the large cylinder. The influence of this vibration is visible in the flow rate shown in Fig.5.17. The closure is achieved in all cases. The fluctuation shown in the flow rate is due to the vibration of the valve pushing the flow outward at the bottom of the large cylinder. A video of the smoothed P-1 valve closure in the large cylinder is available through this link¹.

The stress distribution in the closed state for the smoothed P-1 in the case setup with the fitted tube and the large cylinder is illustrated in Fig.5.18. It can be seen that neither the fitted tube (Fig.5.18.a) nor the large cylinder representing the LV (Fig. 5.18.b) exhibited any visible orifice hole. Notably, the stress patterns and their magnitudes were consistent across all three scenarios. However, a minor distinction was observed: the stress magnitudes in the case of the large cylinder were slightly lower than those found in the fitted tube. Furthermore, areas of high stress near the annulus ring and chordae attachment points appear which are shown in red. Regarding the quality of closure, the final state of the smoothed P-1 valve in both cases of fitted tube and large cylinder appears to exhibit a relatively flat profile, as indicated by the bulging volume illustrated in Fig.5.19.

According to the contact map shown in Fig.5.15, the use of a large cylinder increased the size of the coaptation area. In the simulation with the fitted tube, as pressure rises, there is a tendency for the fluid to infiltrate the contact area, leading to a separation of the free edges of the leaflets (as seen in Fig.5.15.a and Fig.5.15.b). In contrast, the simulation involving the larger tube provides a more accurate representation, as the large volume of blood in the ventricle exerts pressure on the leaflets, thereby ensuring that the free edges remain closed as shown in Fig.5.15.c. In addition, the contact pressure in the simulation with a large cylinder is notably stronger compared to the simulation with the fitted tube (see Fig.5.16).

¹https://youtube.com/shorts/61EgS0Y8_ic

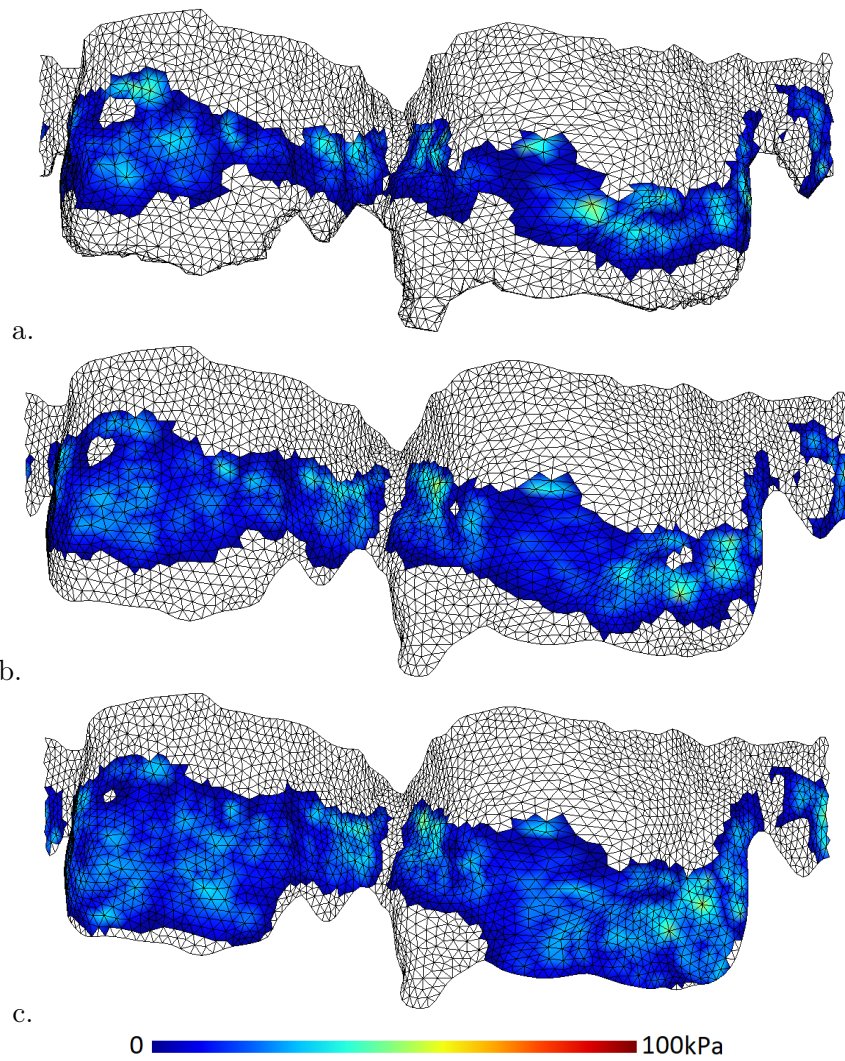


Figure 5.15: Contact maps for the P-1 valve with the fitted tube setup and anisotropic model (*a.*), the smoothed P-1 valve with the fitted tube setup and anisotropic model (*b.*), and the smoothed P-1 valve with the large cylinder setup and anisotropic model (*c.*).

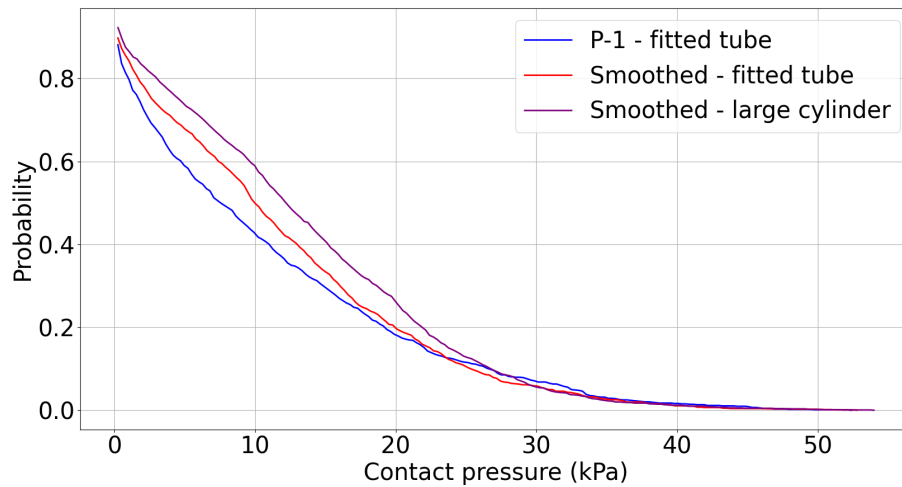


Figure 5.16: Cumulative distribution function (CDF) of the contact pressure with anisotropic model.

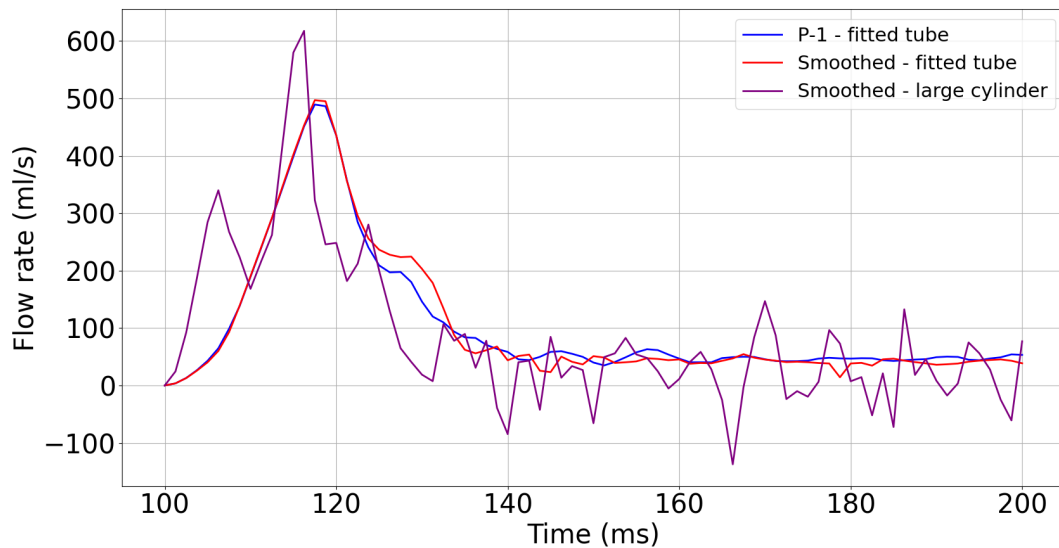


Figure 5.17: Flow rate shown for P-1 in the fitted tube, smoothed P-1 in the fitted tube, smoothed P-1 in the large cylinder. All cases are with the anisotropic model.

To show the versatility of our FSI model, we implemented all the image-based geometries we had, including P-2, P-3, and P-4 valves, already introduced in chapter 2. In the following section, we discuss the closure of the additional image-based valves.

Reusability of the model

In the case of P-2 and P-3, extracted from manual segmentation of the MV in the opened state, and P-4, derived from the automatic segmentation of the MV in the closed state, the simulation with the fitted tube did not close properly. Fig.5.20 shows the results of the P-2, P-3, and P-4 mounted inside the fitted tube in the peak systole. These valves failed to close properly as large

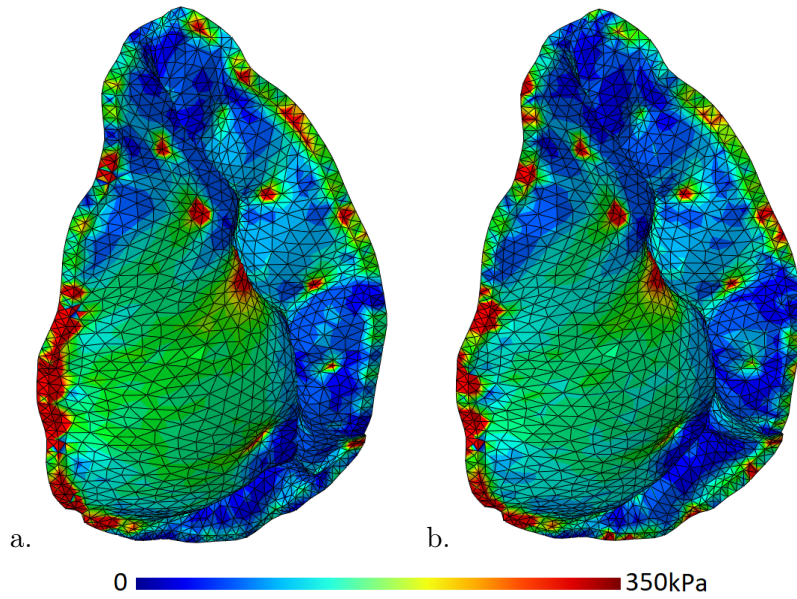


Figure 5.18: Top view of the stress distribution in case of P-1 with fitted-tube and anisotropic model (a.) and P-1 with large cylinder and anisotropic model (b.).

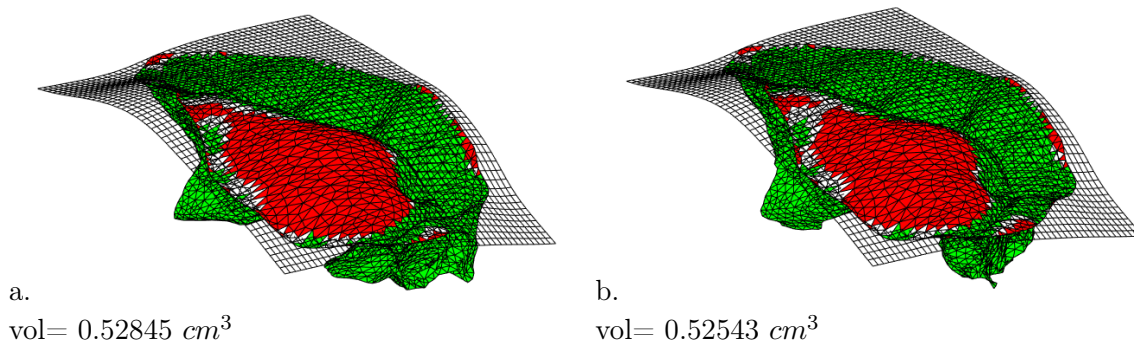


Figure 5.19: Bulging on the (a.) smoothed P-1 with the fitted tube and anisotropic model, (b.) and smoothed P-1 with the large cylinder and anisotropic model.

orifice hole appeared (as in **Fig.5.20.a**), or the leaflet tissue exited the fitted tube and folded over the annulus ring (see Fig.5.20.b and Fig.5.20.c). Moreover, in Fig.5.20.a a large area in red indicates that the leaflet is experiencing high levels of stress which shows that the valve is not properly closed. Conversely, when using a large cylinder setup, proper closure was achieved for the P-2 and P-4 valves. The mesh resolution for the P-2 and P-4 in the large cylinder is reported in table 5.4. The simulation of MV dynamic closure in the case setup with the large cylinder for P-2 and P-4 are accessible through these links^{1,2}.

¹<https://youtube.com/shorts/tDscocfHlco>

²https://youtube.com/shorts/Nf08_JgvS_4

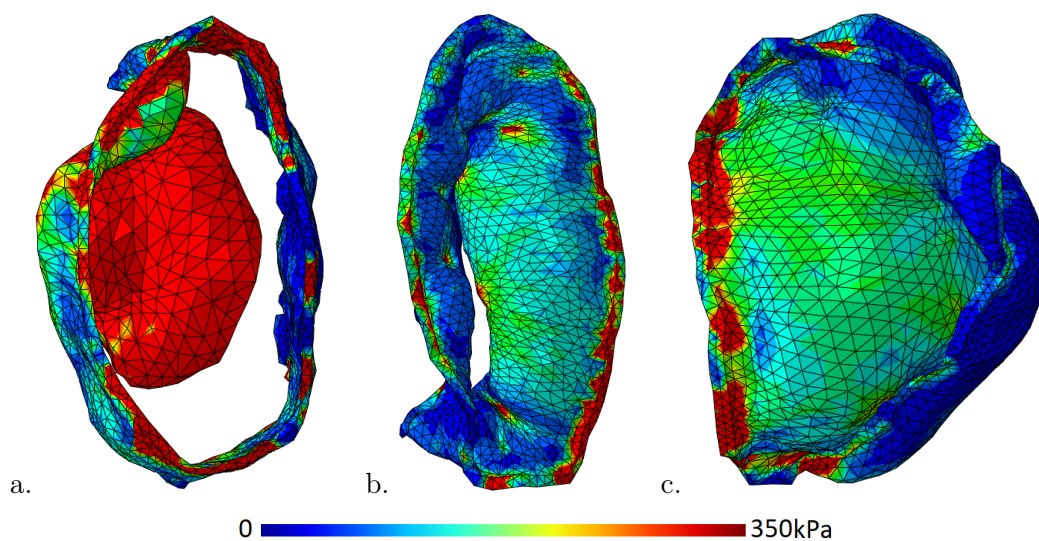


Figure 5.20: Top view of the stress distribution: (a.) in case of P-2 with the fitted tube and anisotropic model, (b.) in case of P-3 with the fitted tube and anisotropic model, and (c.) in case of P-4 with the fitted tube and anisotropic model.

	Fluid volume element number	Leaflets element number
P-2 :	30k	171k
P-4 :	38k	193k

Table 5.4: Number of elements used in the simulation of P-2 and P-4 with the case setup of large cylinder.

Fig.5.21 displays the top view of the stress distribution for P-2 and P-4 valves. It can be seen that the closure in the case of P-4 is properly sealed, while in the case of P-2, the closed state contains a small orifice hole. This imperfection could be attributed to either a missing chordae attachment or the fixed annulus boundary condition during the dynamic closure of the valve. In addition, the stress distribution on these two valves is in agreement with the values reported in the literature [CMMS20, CWG⁺19] (see Fig.4.7 in chapter 4).

Fig.5.22 shows the better visualization of the P-2 and P-4 valves in the closed state. In this figure, the bulging volume and the saddle shape of the MV in the closed state are reported. The simulation reveals a noticeably large bulging volume in the P-4 valve. This can be attributed to the fact that P-4 was segmented in the closed state, in which the leaflets were already stretched, and consequently, the dynamic closure of the P-4 will further stretch the valve.

5.4 Conclusion

In this chapter, we investigated three important features that influence the fluid-structure interaction (FSI) simulation of the mitral valve (MV), namely, the anisotropic mechanical response of the MV leaflet tissue, the smoothness of the segmentation outcome, and the use of a large cylinder compared to a tube fitted on the annulus ring. We studied the influence of anisotropy

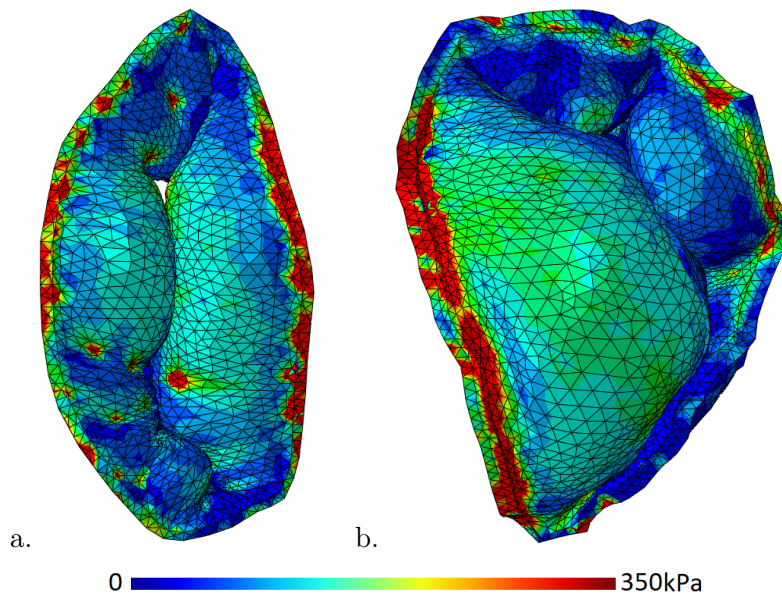


Figure 5.21: Top view of the stress distribution: (a.) in case of P-2 with large cylinder and anisotropic model, and (b.) in case of P-4 with large cylinder and anisotropic model.

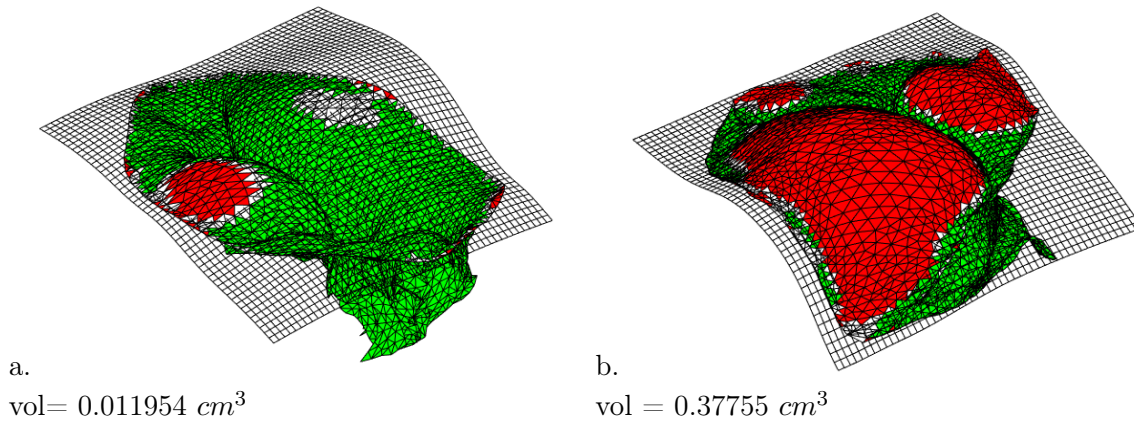


Figure 5.22: Bulging on the (a.) P-2 with the large cylinder and anisotropic model, and (b.) P-4 with large cylinder and anisotropic model.

by studying two constitutive models and the details of their implementation. We explored the challenges in extracting the material parameters in two anisotropic cases. Our study confirms that the success of the optimization relies on the initial values of the coefficients. Moreover, we addressed the challenges associated with implementing patient-specific MV geometries extracted from medical imaging, highlighting the irregularities inherent in such data. We analyzed the influence of geometry and fluid volume by studying how variables like the smoothness of image-based MV surfaces and various tubular left ventricle (LV) shape contribute to the dynamic behavior of the MV.

The impact of the anisotropy has been shown on both a generic and image-based geometry. The simulation results suggest an improvement with the anisotropic model, namely, less bulging

and better contact properties were noticed with the anisotropic model compared to the isotropic one. Additionally, the chordae forces during the closure are compared with ex-vivo data of the literature and the results from the anisotropic model show good similarities with the ex-vivo measurements. From the contact map, we can identify the overall shape of the coaptation, the size of the coaptation, and the strength of the contact forces. We based our conclusion on considering more uniform coaptation, larger coaptation area, and stronger contact force to be favorable. However, it is still not clear ideally, how the coaptation should be in actual MV closure. Despite our efforts, we did not find an agreement between experts on this matter and there is still the need for more sophisticated measurements to evaluate our predictions.

We used the anisotropic constitutive model to simulate the dynamic closure of three image-based geometries. The results suggest that smoothing the leaflet leads to better contact and a slight improvement over the bulging volume. While the closure was achieved in both valves with the large cylinder, there were also some limitations to the simulation setup with the large cylinder. Notably, the leaflet experienced vibrations due to an additional component in the cylinder, leading to a volatile flow rate. Overall, these findings highlight the importance of the constitutive model of the leaflets, representation of the segmented geometry and fluid volume, as well as choosing the appropriate fluid volume, in order to accurately capture the dynamic behavior of the MV.

In our upcoming chapter, we will investigate further the material model, highlighting the various approaches to modeling the microstructure of the leaflets and introducing our innovative methods for this task.

Chapter 6

Microstructure of the Leaflets

The anisotropic behavior of the mitral valve (MV) leaflet is attributed to the presence of collagen fibers within its tissue. The complex distribution of the collagen fibers leads to a notable difference in the stress-strain data reported in the literature on MV leaflet tissue. Obtaining fiber orientation is challenging as it varies for each patient. It requires the valve to be dissected and directly observed for each patient, which is not possible for patient-specific simulation with a clinical application. In this chapter, we are looking for an alternative to the study of specimens for the fiber map. A promising strategy to address this issue involves modeling the fiber directions without going through the complex procedure of experimentally observing the fiber orientation of the leaflet tissue for each patient. This will be beneficial for the process of simulating the MV behavior, potentially eliminating the need for dissecting the valve to observe fiber direction. In pursuit of a proper ruled-based fiber orientation, we used our fluid-structure interaction (FSI) model described in chapter 3 to compare the MV dynamic closure in several different fiber distributions.

In the following, first, we will explore the state-of-the-art solutions addressing this challenge and a detailed exploration of each fiber model and its implementation. Following that, we will compare the simulation outcome from each scenario and provide a discussion of our findings.

6.1 Fiber models

According to the measurements of the MV leaflet tissue reported in the literature [PS14, LRJ⁺19, JLK⁺18b, JLK⁺18a], it is observed that the leaflet tissue shows anisotropic behavior. In some studies, for example in [LRJ⁺19], the measurements show that the anisotropy rate depends on the region where the specimen is extracted for the stress-strain test. They took samples from six different regions of the MV anterior leaflet tissue and measured their stress-stretch response. The results show a noticeable difference in the anisotropy rate in different regions of the leaflet (see Fig.6.1). This can be due to tissue heterogeneity where the material properties differ along the leaflet, or only due to changes in the fiber direction while maintaining the same material characteristics everywhere. There is a consensus in the community that it is due to a variation of anisotropic directions. One explanation is considering leaflet tissue as a composite of fiber families running through an isotropic base material and assuming that fiber orientation dictates the anisotropy rate. The assumption that fiber orientation dictates the anisotropy

rate is mentioned in [PS09]. This idea is in line with the physiological characteristics of the MV leaflet microstructure. The MV leaflet comprises four primary layers, namely Atrialis, Spongiosa, Fibrosa, and Ventricularis [MRR10], with the Fibrosa layer comprising crimped collagen fibers that function as a load-bearing mechanism and strengthen the tissue in its direction. Therefore, in MV simulation, it is important to have a fiber map that defines the fiber direction in each region of the leaflet.

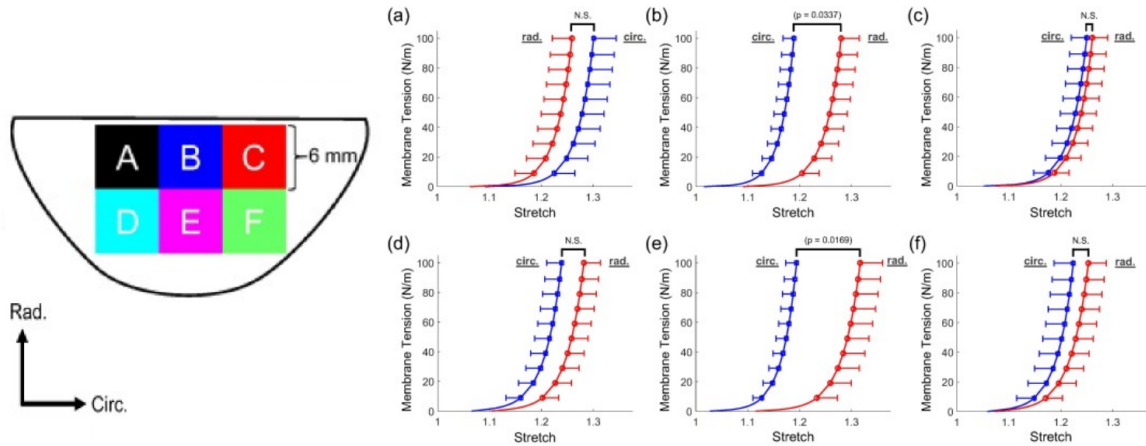


Figure 6.1: The anisotropy rate changes depending on the region where the specimen is obtained. Data reported in [LRJ⁺19].

In this chapter, we will study the extraction of fiber orientation from the state-of-the-art:

- Measurement-based and representation simplification, which includes fiber maps based on:
 - Extracting the fiber map from direct observation of each MV leaflet by using small-angle light scattering (SALS) approach.
 - Measurement of a specific sample of MV and use it as a template fiber map for other samples.
 - Parallel: the fibers follow the direction parallel to the planar surface crossing the annulus ring as a representation simplification.
- Physical computation including:
 - Stress-based: The fiber orientation is specified based on the direction of the maximum principal stress.
 - Affine model: Fiber model which follows the affine kinematic notion, oriented in the direction of the maximum principal strain.

These approaches do not consider the physiological aspects of the MV structure, such as the chordae insertion points. Therefore, after exploring the existing approaches, we will present our contribution, offering alternative solutions that address these overlooked aspects.

6.1.1 Measurement-based and representation simplification

Fiber measurement

In many of the studies in the literature, fibers are modeled by implementing the fiber map extracted from observing the micro-structure of the leaflets as described in [SSHP22, LAG⁺14, CGD⁺12]. Usually, the fiber map is extracted by using small-angle light scattering (SALS) to observe the microstructure of the leaflet [SHB⁺02]. An example of MV anterior leaflet microstructure obtained by SALS data is shown in Fig.6.2. The fiber map is unique for each specimen and obtaining it is time-consuming work and needs resources and expertise in conducting experimental studies.

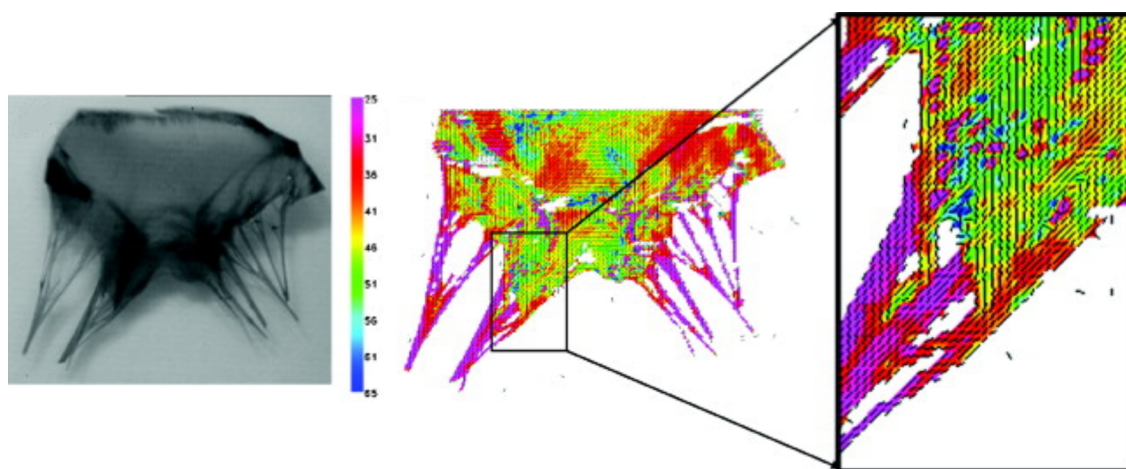


Figure 6.2: Left: MV anterior leaflet. Middle: the small-angle light scattering data. Right: magnified view of the fiber orientations near the chordae insertion point [PSL⁺10].

Fiber map

To have a practical model, that can be used for any patient-specific case, simplification in modeling different aspects of the MV is inevitable. Numerous studies have sought to develop a fiber model by observing the MV leaflet microstructure. In [CKC⁺91], they extracted the fiber orientation in the MV anterior leaflet tissue by using polarized light microscopy (PLD). By observing the fiber map they proposed (see Fig.6.3), we realize that in the middle of the leaflets, the fibers seem to be parallel to the annulus direction, and close to the commissures, which are the regions between the anterior and posterior leaflets, being perpendicular to the free edge. The free edge is referred to as the boundary of the leaflet which is not attached to the annulus. Another example is the experimental study on the *in vivo* data presented in [SHB⁺02], reporting that the fibers in the central region of the leaflet are oriented in the circumferential direction of the leaflet. An interesting observation is that the anisotropy rate presented in [LRJ⁺19] (see Fig.6.1) appears to be in agreement with the fiber map proposed in [CKC⁺91] (see Fig.6.3). For instance, in Fig.6.1, sections B and E exhibit a higher anisotropy rate than regions A, D, C, and F. Furthermore, by considering these regions in the fiber map shown in Fig.6.3, it becomes apparent that in areas of high anisotropy, fibers align more parallel to the circumferential direction, while in other ar-

eas, they are more obliquely oriented. This idea is independently implemented in the literature. For example, in [NKI⁺13], they used a fiber model that in the central region of the leaflets are oriented in the circumferential direction, but they become radial, perpendicular to the annulus ring, near the commissures.

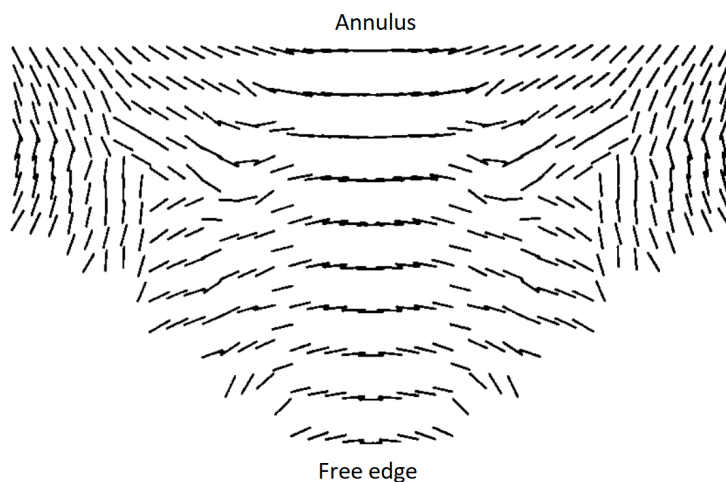


Figure 6.3: Map of fibers for MV anterior leaflet obtained based on PLD data [CKC⁺91].

A prominent effort in obtaining a generalized fiber map was undertaken by Einstein et al in [EKR⁺05b]. They concluded that the anisotropy rate used to describe the mechanical response of the MV leaflet influences the MV function. They used the SALS data reported in [CKC⁺91] to determine the average directions of collagen fibers. They created a standard template for fiber maps (see Fig.4 in [EKR⁺05b]) which has been widely used in the literature [RFS⁺13, EKR⁺04, PHS09, SPN11, PSSH10, EDPJ⁺10].

Parallel fibers

In the majority of the studies, they simply directed the fibers to be parallel to the surface plane approximating the annulus, (see Fig.5.1 in chapter 5), as in [KMP19, SVR09, VCV⁺08]. In the previous chapter, we also used the parallel model which we considered the fibers to be aligned with the annulus surface (see Fig.5.1 in chapter 5).

6.1.2 Fiber map based on physical computation

One major limitation of the models we specified so far is their lack of consideration for the mechanical response of the MV leaflet in the peak systole, when the leaflets are under the maximum tension. This oversight becomes clear when considering that the fibers are load-bearing structures. Their primary role is to bear the additional load of the leaflet. Ideally, their direction should be oriented toward where they are mostly needed, to reduce excess strain. At the cellular level, it has been studied that the heart valve cell stiffness increases in the direction of applied stress [MYL⁺06]. Studies such as [DCBB08, Lau12] have explored the remodeling of heart valve collagen fibers at the macroscopic level. These studies have found that the stress-based approach, which involves re-orienting collagen fibers based on the maximum principal stress at each point

on the leaflet, leads to deformed shapes that are more consistent with experimental observations. In addition, an experimental study in [LZL⁺15] explored the affine kinematic notion, which proposes that crimped collagen fibers in heart valve tissue deform and rotate to align with the macroscopic deformation of the tissue. This study confirmed that, at the homogenized tissue level, fiber orientation does indeed deform in accordance with the affine kinematic model.

To consider these two aspects in our simulations, we used two more fiber models based on the principal stress and principal strain directions. We began by simulating the dynamic closure of the smoothed P-1 image-based MV with the random fiber distribution. From the simulation results, for each leaflet element, we captured the positive principal stress and strain during peak systole. Using 3D vector manipulation, we projected these principal directions from the MV final state back to its initial state when the valve was open. Finally, We implemented these directions in our diffusion algorithm based on the Gaussian smoothing approach to have a slightly more uniform and smoother fiber map. Our observations indicate that the impact of smoothing parameters on simulation results is minimal, provided that excessive smoothing is avoided. Over-smoothing washes out the influence of stress and strain vectors used as initial distributions of the fiber vectors.

The fiber maps based on maximum principal stress and affine model are shown in Fig.6.4.a and Fig.6.4.b. An interesting observation is that the fiber maps in the case of stress-based and affine model are influenced by the chordae attachment points, which suggests that the physiological traits of the MV can be influential in the microstructure of the leaflets. In Fig.6.4.a and Fig.6.4.b, some of the chordae attachment points that influenced the distribution of the fibers are identified with a blue circle.

6.1.3 Expert observation and physiological traits

In this chapter, we also attempted to obtain a fiber model based on direct observation of the fibers in the MV leaflet tissue. In this model, an expert, Dr. Peter E. Hammer, a member of the CURATIVE associate team¹ who is directly working with the heart surgeons, conducted a study within the framework of the CURATIVE associate team. He delineated a set of fiber directions in different regions of the leaflet based on the observation of numerous dissected porcine MV leaflets and human pathology specimens with normal MV.

Fig.6.5 presents an example of an explanted MV leaflet from a porcine heart. In this figure, fibers running through the leaflet are observed to form creases on the surface of the leaflet. These creases trace a noticeable arc that connects the chordae insertion points. For the expert-based fiber map, Dr. Hammer attempted to identify and extract several arcs that mimic the crease pattern occurring on the P-1 image-based MV geometry. These initial arcs are shown in Fig.6.6 as a set of blue lines. We used these directions and implemented in a diffusion algorithm based on the Gaussian smoothing approach to extract the fiber orientation in the rest of the elements. The 2D representation of the fiber orientation, obtained by unfolding the 3D representation, is shown in Fig.6.6. The red lines represent the chordae structure.

While the expert-based fiber model may appear more convenient than dissecting and directly observing each MV leaflet, it has some limitations. The model's robustness can be affected by

¹<https://team.inria.fr/curative/team-members/>

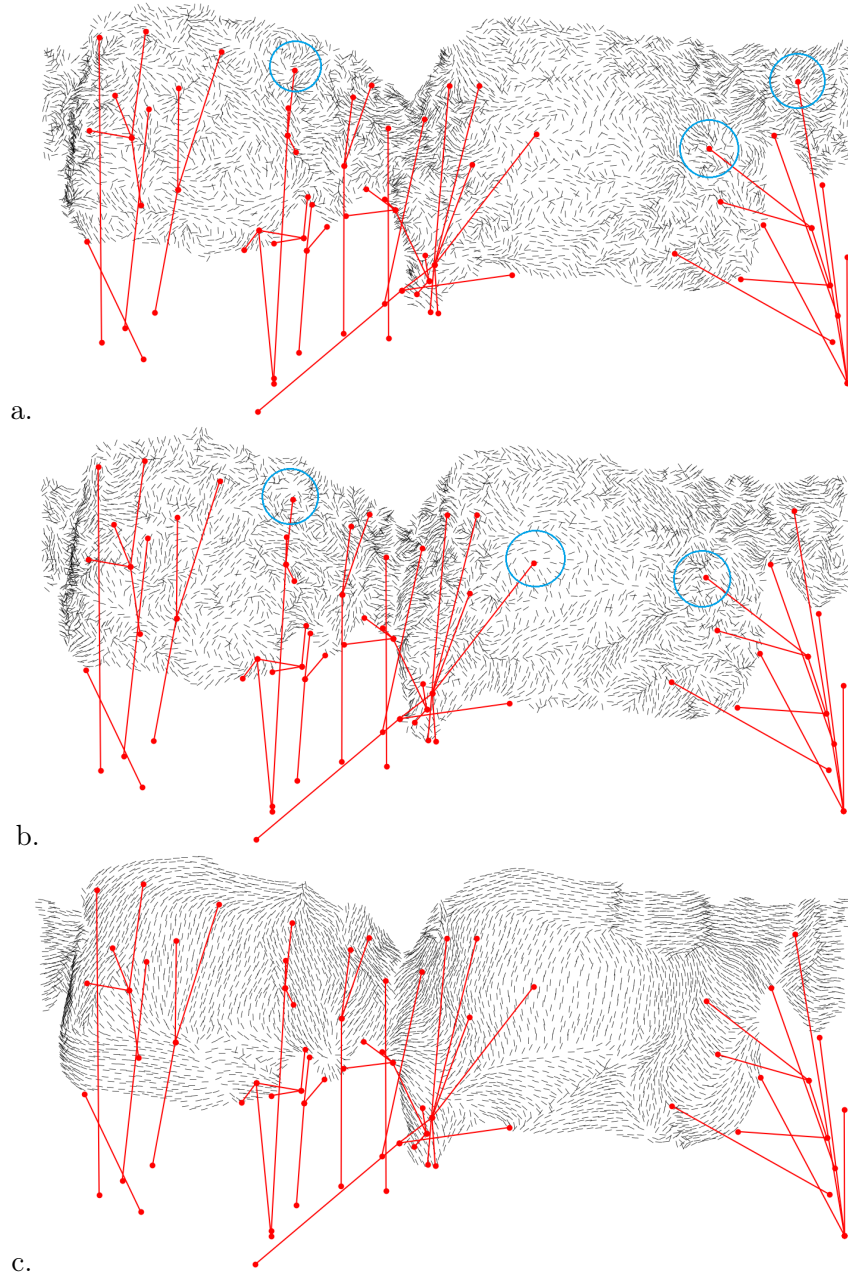


Figure 6.4: Fiber map based on maximum principal stress direction (*a.*), affine model (*b.*), and the chordae structure (*c.*).



Figure 6.5: An example of expert observation of MV leaflet tissue. A hypothesis is that the presence of fibers within the leaflet tissue can be detected through the crease lines that these bundles of fibers leave on the tissue surface.

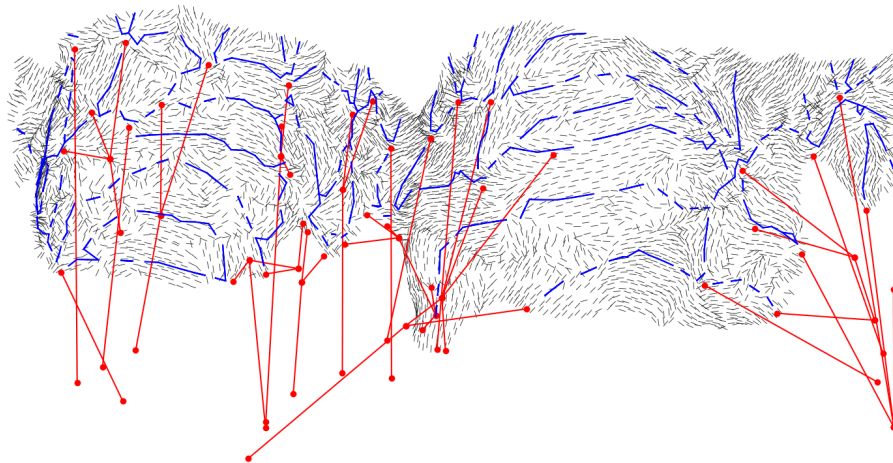


Figure 6.6: Expert-based fibers: Fibers following the trail defined based on numerous observations of MV leaflet microstructure.

various factors. For instance, the delineation of the fiber directions relies on the judgment of the expert, making it subjective. Additionally, the final fiber map is influenced by distribution processes such as smoothing and diffusing the fiber directions and parameters used in these operations.

In our case, the implemented fiber map did not exactly follow the expert's instructions. More specifically, translating expert drawings on the image of MV geometry to the leaflet elements is not straightforward. The process of extracting the blue lines was automatic, and by observing Fig.6.6, we notice that most of the time, the blue lines are not continuous. Consequently, in some regions, the fibers after the diffusion process (shown in dark short lines in Fig.6.6), do not align with the blue lines. This misalignment is a result of the imperfections in the automatic

extraction of the expert delineations.

Pathologies such as prolapse can arise from improper stress and strain distribution on the leaflet, which is highly dependent on the location of chordae attachment points. It is also mentioned in [TBP⁺17], that there is no clear boundary between the leaflet and the chordae structure, which are bundles of collagen fibers that originate from the papillary muscles and branch out within the leaflet surface. The hypothesis of chordae being a bundle of collagen fibers and diffusing inside the leaflet surface is also mentioned in [PSL⁺10]. They used the data obtained from SALS to extract a fiber map as shown in Fig.6.2. In this figure, the region in purple indicates that most of the fibers are aligned in a single predominant direction. On the contrary, the blue shows the region in which the fibers are oriented in various directions (in a more haphazard way). We noticed that the chordae are mostly purple and they transition into red and green in a complex way. This indicates that the chordae insertion points influence the fiber distribution on the leaflet tissue.

This motivated us to define a fiber orientation that considers the chordae attachment point and its direction. We used the vector between each chordae attachment point and its connection point with the papillary muscle and used our diffusion algorithm to obtain the fiber direction in other regions of the leaflet. The final fiber map based on the chordae insertion points is shown in Fig.6.4.c.

In the case of stress-based and affine models, the stress and strain principal directions are used as an initialization vector in the diffusion process to obtain the fiber distribution on each leaflet element. In regions with anisotropy, the fibers tend to be more uniform, and in regions with isotropy, the fibers are more randomly distributed. In the case of stress-based and affine fiber models, the number of initialization vectors is relatively much higher compared to the chordae-based fiber model. With a high number of initialization vectors in the diffusion process, it is possible to keep the diffusion parameters small so that the influence of stress and strain is preserved. However, in the case of the chordae-based and the expert-based fiber models, since the initial directions introduced to the diffusion system are limited to a small number of nodes in the space, the diffusion parameters were stronger. By observing the fiber maps shown in Fig.6.4, we notice that the fiber fibers are more uniform in the chordae-based fiber map compared to the stress-based and affine fiber model, which is the result of using stronger diffusion parameters.

6.1.4 Random fiber model

The complex distribution of fibers on the leaflets has led some recent studies to suggest that the MV leaflet tissue is in fact resembling an isotropic behavior [LRJ⁺19, LSP⁺23]. A highly dispersed fiber orientation results in a material model with a planar isotropic mechanical response. As the fibers lay randomly on the leaflet surface, it prevents the excessive stretch of the leaflet tissue, while preserving the flexibility of the leaflet surface for bending and movement. We take this possibility into account and specify one of our fiber models to be randomly distributed on the surface of the leaflet.

6.2 Results and discussion

In this section, we detail the simulation results for each mentioned fiber model. Since no ground truth data is available for comparison, we compare the fiber models by determining which model's results align most closely with the anticipated physiological traits of the MV dynamic closure. From a physiological standpoint, the optimal microstructure should provide maximum flexibility, enabling the leaflet to move seamlessly throughout the cardiac cycle. It should also ensure effective coaptation and contact pressure while minimizing tissue bulging and stretching [CAF10]. Consequently, in our simulation, we aim to identify the fiber model that best exhibits these mechanical characteristics.

We employed the FSI model outlined in chapter 3 and the HGO constitutive model from chapter 5 for these simulations. All the simulations presented in this chapter are based on the smoothed P-1 image-based valve mounted in the large cylinder as the tubular left ventricle. In the figures presented in this section, a through f respectively depict the results for fiber models based on the following criteria: parallel to the annulus, expert-based, random distribution, stress-based, affine model, and chordae insertion points.

6.2.1 Closed state

Fig.6.7 shows the strain distribution on the leaflet tissue at peak systole for all the fiber models. We notice that in the case of parallel and chordae-based fiber models, a significant stretch is appearing. It is also apparent that the stretching in the parallel model is more uniformly distributed compared to the one in the chordae-based model. Conversely, other fiber models exhibit more moderate tissue stretching, with the random fiber model revealing the least stretch.

This observation correlates with the bulging volume illustrated in Fig.6.8. Both parallel and chordae-based fiber models exhibit extensive bulging, while the random fiber model presents the least bulging volume among all the fiber models. Excessive strain leading to pronounced leaflet bulging can be symptomatic of a compromised valve. We assume that the strain distribution should be small across the leaflet [CAF10], minimizing unnecessary stretching throughout the cardiac cycle. Therefore, according to these two metrics, both parallel and chordae-based fiber models performed poorly compared to the expert-based, random, stress-based, and affine fiber models.

6.2.2 Contact

Figure 6.9 presents the contact map across all the fiber models. Notably, the parallel model exhibits the largest coaptation area, while the random model shows the smallest. Although there are minor variations in the shape and size of the coaptation area among most models, these differences are relatively subtle. The exception to this pattern is the parallel model, which deviates significantly in both the shape and size of the coaptation area compared to the others. The surface size of the coaptation area in all cases is uniformly distributed close to the free edge of the leaflets, with no significant discontinuity, which shows sealed closure.

The contact pressure in the stress-based model is weaker compared to other models (see Fig.6.10). Both parallel and chordae-based fiber models manifest notably strong contact pressures. This observation is consistent with the fact that both models demonstrated a comparably

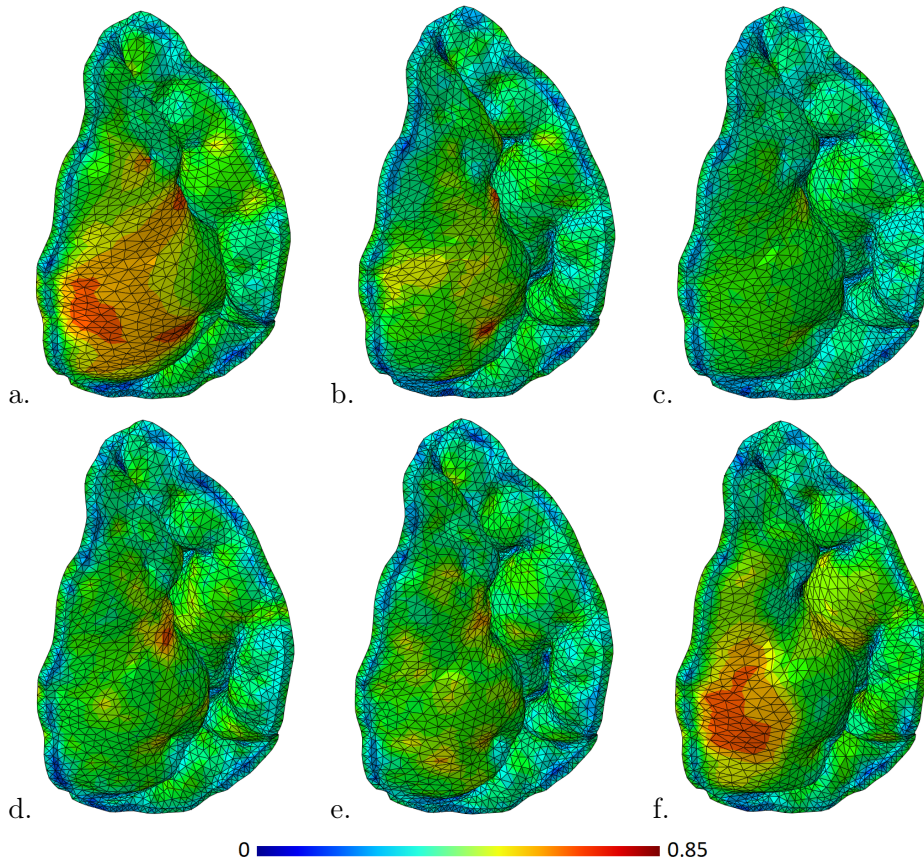


Figure 6.7: Distribution of the logarithmic strain over the leaflet tissue at the peak systole in case of fiber models based on: Parallel to the annulus (*a*), expert-based (*b*), random distribution (*c*), stress-based (*d*), affine model (*e*), and chordae-based (*f*).

larger bulging volume. Typically, an increased bulging volume results in higher compression of the leaflets against each other. According to the cumulative distribution shown in Fig.6.10 and the coaptation area reported in Fig.6.9, the contact pressure and coaptation area in expert-based, random, and affine models fall within a similar range. The weak contact pressure in the stress-based model suggests that the MV tissue is relatively rigid when configured with this fiber model.

6.2.3 Chordae forces

By observing the distribution of the chordae forces during the MV dynamic closure, we realized that in parallel, random, stress-based, and affine fiber models, the sequence of each chordae category aligns with the order observed in the ex vivo measurement data reported in [PIMW⁺20] (see Fig.6.11). However, in the expert-based and chordae-based fiber models, the forces exerted by the posterior secondary and anterior primary chordae appear to overlap. This contrasts with the ex-vivo measurement data, where a noticeable gap between these two categories is evident. Notably, the magnitude of forces and the separating gap between the primary and secondary chordae are more pronounced in the random, stress-based, and affine fiber models.

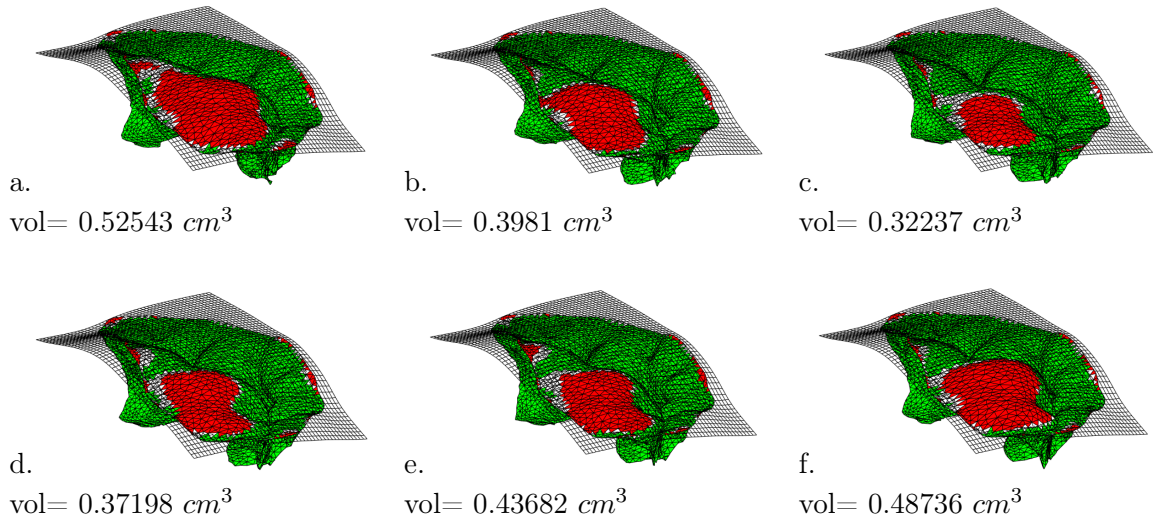


Figure 6.8: Bulging volume at the peak systole in case of fiber models based on: Parallel to the annulus (a), expert-based (b), random distribution (c), stress-based (d), affine model (e), and chordae-based (f). The red region shows the bulging volume where the valve stretches over the annulus surface.

6.3 Conclusion

In this chapter, we simulated the dynamic closure of the mitral valve (MV) using various rule-based leaflet microstructures. By evaluating the performance of fiber models based on the physiological characteristics of the MV leaflet—factors such as reduced stretching, minimized bulging, large coaptation area, robust contact, and alignment with ex vivo chordae force measurements—we realized that each model presented its unique strengths and shortcomings in various metrics when we compared the simulation results, which are described in the following.

By analyzing the results of the simulation, we observed that the proper valve closure is achieved in all fiber models. Although some models showed favorable results in certain categories, these were counterbalanced by their outcomes in other areas, yielding an overall balanced performance in all fiber models. Take the parallel fiber model, commonly used in the literature, as an example: despite its pronounced bulging, it shows a large coaptation area and robust contact pressure. Furthermore, all the models were consistent in replicating the chordae force observed in ex vivo literature measurements. One instance worth mentioning is the stress-based fiber model. In this approach, even though it achieves a sealed closure with small bulging volume, the leaflet tissue appears rigid—a characteristic not ideal for leaflet tissue. Regarding other fiber models, no particular model emerged as the superior choice across all evaluation criteria.

The fiber models mentioned are easy to implement in a clinical workflow. It is thus a good alternative to methods that resort to lab-based imaging techniques to produce fiber maps. It is important to mention that while rule-based fiber models are a promising alternative, we were not able to definitively identify the best fiber model according to our available metrics. Work needs to be done to define explicit guidelines for such rule-based models and compare the valve behavior in different fiber models with the ground truth. With ground truth available, future

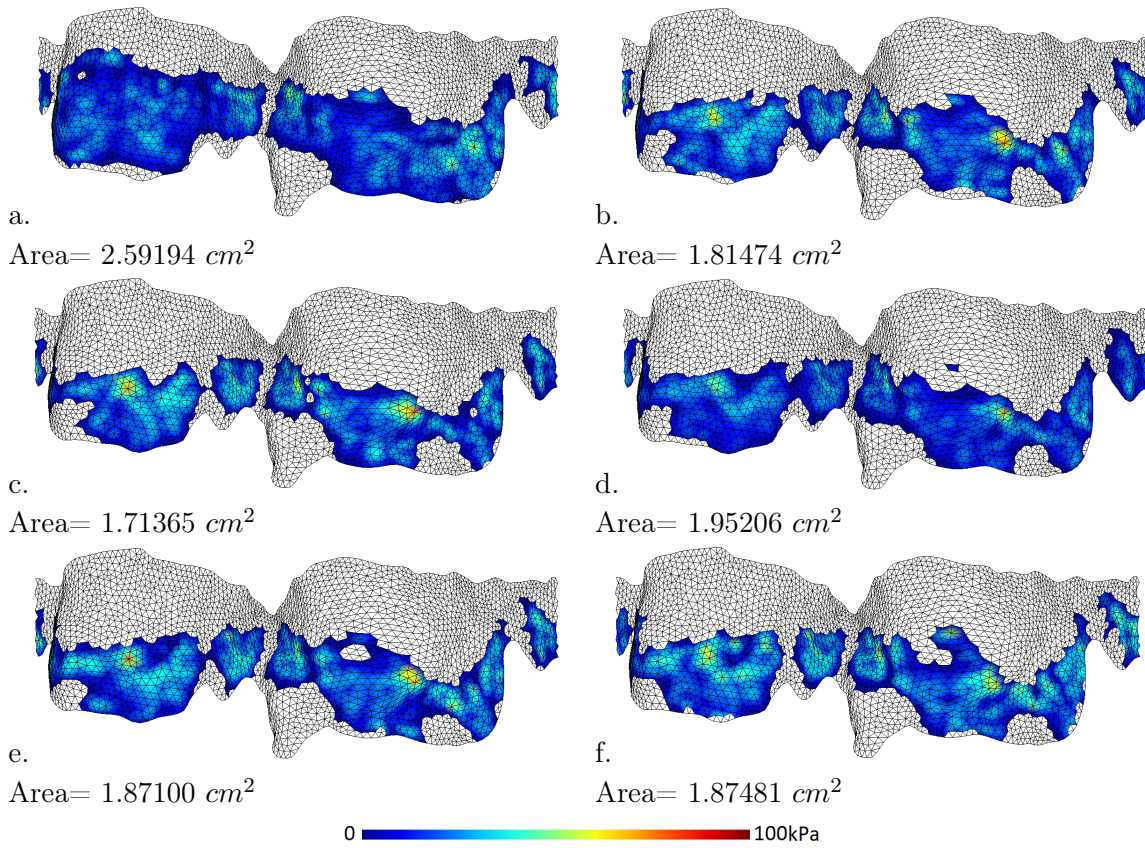


Figure 6.9: Contact map showing the coaptation area and the contact pressure in case of fiber models based on: Parallel to the annulus (*a*), expert-based (*b*), random distribution (*c*), stress-based (*d*), affine model (*e*), and chordae-based (*f*).

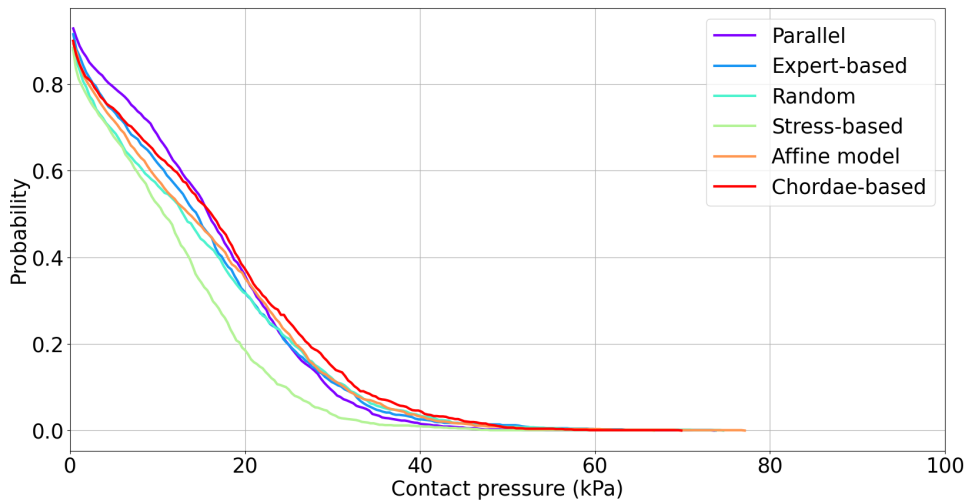


Figure 6.10: Cumulative distribution function (CDF) of the contact pressure in various fiber models.

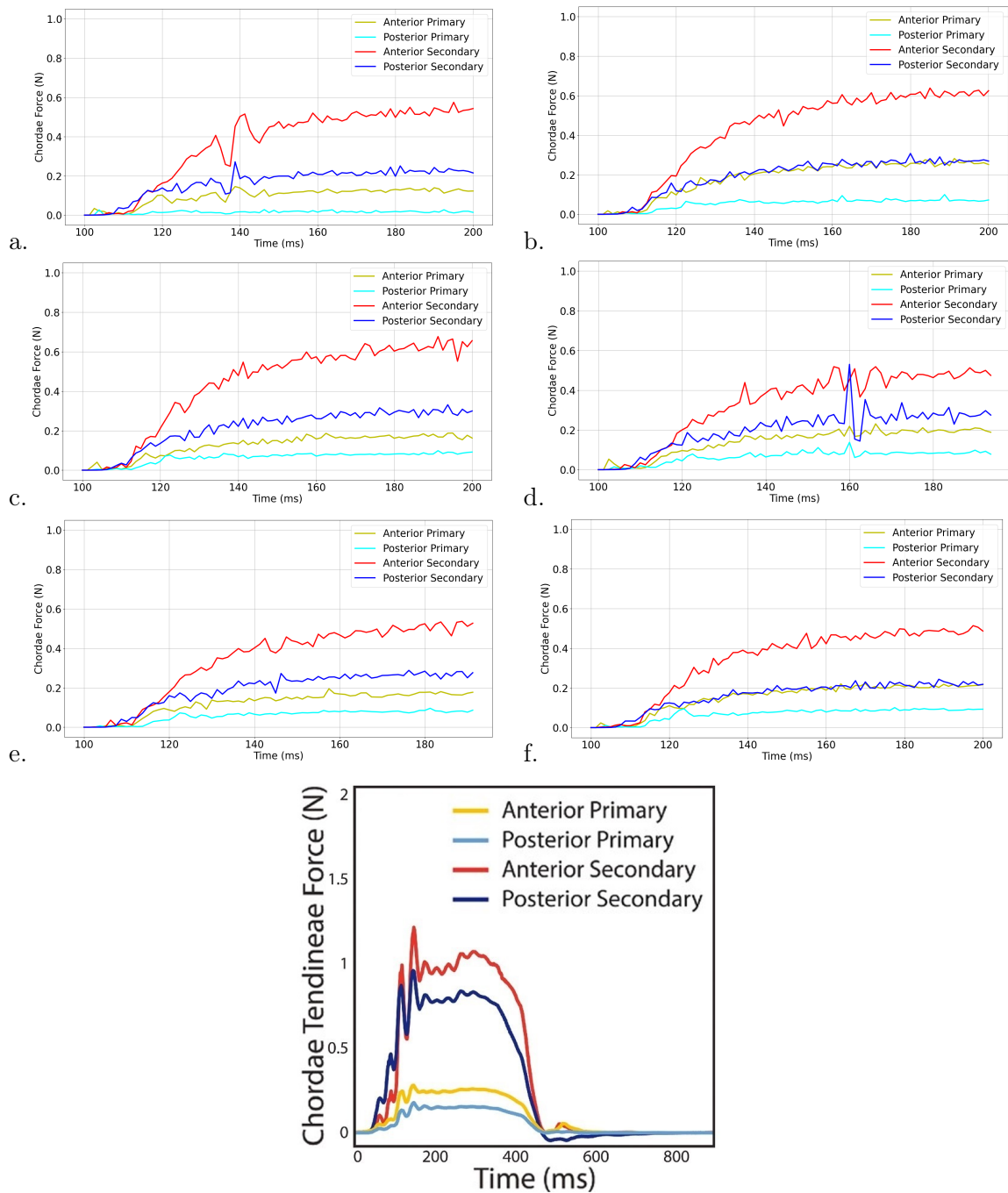


Figure 6.11: The chordae force during the dynamic closure of the MV in case of fiber models based on: Parallel to the annulus (*a*), expert-based (*b*), random distribution (*c*), stress-based (*d*), affine model (*e*), and chordae-based (*f*). The figure at the bottom shows the ex vivo measurement of the chordae force during the cardiac cycle reported in [PIMW⁺20].

research can employ a more comprehensive comparison of the rule-based fiber models mentioned in this chapter. This enables conclusive determination of the most effective model for simulating mitral valve behavior. Another limitation to our study is that we analyzed the influence of rule-

based fiber maps on one image-based MV. Future works can more extensively investigate the influence of rule-based fiber models by incorporating more patient data, considering the influence of diffusion parameters, and defining better criteria by experts for drawing the rule-based fiber models. In addition, by conducting experimental work on measuring the coaptation area in the leaflet can help with defining better criteria for evaluating the performance of the rule-based fiber models.

Studies similar to the one presented in this chapter also hold significant potential for the development of prosthetic heart valves. By emphasizing specific criteria—whether it is minimizing bulging or maximizing the coaptation area—and aligning the fiber placement with the corresponding fiber model, one can craft a valve tailored for specific performance.

Conclusion

In this thesis, we employed a fluid-structure interaction (FSI) simulation, based on the immersed boundary formulation, to simulate the dynamic closure of the mitral valve (MV), taking into account both the blood flow and the MV physical response. We focus on having a model able to capture detailed contact between the MV leaflets and incorporate any image-based MV geometry. In this section, we will outline the main contributions of this thesis and subsequently explore the potential routes for future research that will be in continuation of our work.

1 Contributions

1.1 Exploring various numerical frameworks for fluid-structure interaction simulation of mitral valve dynamic closure

In the literature on numerical simulation of MV behavior, several FSI approaches are implemented which are mostly based on arbitrary Lagrangian-Eulerian (ALE), smoothed-particle hydrodynamics (SPH), and the immersed boundary formulation. Each approach has its unique capabilities. We prioritized an FSI model that is robust, computationally efficient, adaptable to any geometry, and can accurately replicate MV dynamic closure. We tackled challenges associated with MV simulations and identified issues leading to numerical instabilities. After a detailed examination of the three formulations, we found that the FSI simulation using the immersed boundary method is the most suitable to capture the sealed closure of MV while maintaining a low computation cost. This approach bypasses some of the challenging intricacies regarding the interaction of fluid and solid numerical domains. Additionally, it offers stable simulations with consistent convergence quality, independent of the input data. We coupled the robust FSI simulation based on the immersed boundary with an efficient contact model based on a balanced master-slave formulation that handles self-contact between the leaflets which further reduces the computation cost and able to gives us detailed information regarding the normal and frictional contact between the leaflets.

1.2 Replicating mitral valve behavior in healthy and pathological cases

Using our FSI model, we replicated the behavior of the MV in both healthy and pathological states with a generic MV geometry and a simplified material model. We used the Abaqus explicit solver which is capable of simulation based on the immersed boundary. We managed to have a proper closure with no orifice holes in the case of the healthy MV. In addition, we provided detailed information on the coaptation area and contact pressure after the valve closure. We

introduced a new method for evaluating the quality of the dynamic closure of MV, the contact map, which significantly improves the detection of MV dysfunctions.

1.3 Investigating the influence of material model and case setup on both generic and image-based mitral valve geometries

In the next step, we moved toward having a patient-specific model by incorporating image-based geometry of MV obtained from medical imaging techniques. We further investigated the influence of anisotropy on the dynamic behavior of the MV, and the impact of the smoothness of the segmentation outcome on the simulation results. We also explored the effect of using different shapes for representing the tubular left ventricle on the simulation outcome. We showcased the results for four image-based geometry and one generic MV. The simulation outcome stated that the results from the anisotropic constitutive model reflect more the physiological characteristics of the actual MV behavior compared to the isotropic one. In addition, the smoothed geometry improved the coaptation area and resulted in better contact, while giving a similar bulging volume compared to the original geometry extracted from the segmentation process. In addition, by comparing the results of using a fitted tube and a large cylinder representing the tubular left ventricle, the second one also improved the coaptation area and closure quality.

1.4 Microstructure of the leaflet tissue

We finished the thesis by a comparison study on various approaches to model the microstructure of the leaflet tissue. We explored several rule-based fiber models to describe the microstructure of the leaflet tissue. Rule-based fiber models can potentially facilitate the biomechanical simulation of heart function. The performance of each fiber model is compared based on the quality of closure and ex vivo measurements of the chordae forces available in the literature. Due to lack of ground truth data, our study was not conclusive. Our results show that each model excels in certain criteria while falling short in others. Similar studies are potentially beneficial in having a simulation tool easy to implement in clinical workflow or in designing prosthetic valves, particularly when aiming for specific qualities like flexibility or good coaptation and contact.

2 Future works

2.1 Evaluating the simulation results

One of the major bottlenecks of our work in this thesis was the ability to compare the simulation outcome with the experimental measurements. While simulations provide invaluable insights, evaluating them compared to the ground truth data is important. Future research could benefit by comparing simulation outcomes against ground truth data, ensuring that the simulations are both accurate and reflective of real-world conditions. A potential strategy involves scanning a phantom MV geometry and then integrating this segmented geometry into the numerical model. Subsequently, this MV can be placed within a pulse duplicator system and its closure is observed using stereoscopic cameras. The results from the experimental setup can then be used as a ground truth to compare with the results from the FSI simulation. We had planned to

undertake a similar project at Boston Children’s Hospital in collaboration with the CURATIVE team. However, due to visa issues, it was not realized.

2.2 Real-time simulation with application to the surgery room

The simulations detailed in this thesis take hours to compute, making them unsuitable for real-time use in surgical settings. However, they encompass both fluid and structural effects, offering a better representation of actual MV behavior. This provides an opportunity to refine real-time simulations using the FSI findings, aiming for a precise representation of MV dynamic closure applicable in clinical scenarios. To better integrate this research into surgical environments, one approach could be leveraging the force distribution data from the FSI simulation as input for structural analysis. Practically, structural analyses are quicker, with the computation time on the scale of minutes. This method could yield a more complex distribution of forces across the leaflets while being computed close to real-time, opening the possibility of being used in surgery rooms.

2.3 Work toward more accurate material model

In this thesis, we explored several rule-based fiber models. For future work, one promising path of study is the exploration of alternative rule-based fiber models to delineate the microstructure of the leaflets. This is important as the leaflet microstructure influences the mechanical response and functionality of the valve. By investigating and comparing various fiber models, researchers can gain a more precise understanding of the underlying physiological processes, potentially leading to more accurate and practical MV simulations. This might also be beneficial for better prosthetic valve manufacturing.

Furthermore, an equally important topic is studying the influence of various MV leaflet stress-strain responses reported in the literature. In each measurement, there is always some variation which can be explained by the complex microstructure of leaflets, or the accuracy of the experimental test. However, this variance significantly influences the simulation outcome. Therefore, understanding its influence and the roots of such variation is beneficial. By systematically reviewing and comparing these diverse measurements, researchers can not only refine simulation accuracy but also further our understanding of the biomechanics of MV leaflets, potentially leading to more accurate models for surgical and clinical applications.

List of publications

Publications

- Khaledian, N., Villard, P. F., Berger, M. O. (2022). Capturing contact in mitral valve dynamic closure with fluid-structure interaction simulation. *International Journal of Computer Assisted Radiology and Surgery*, 17(8), 1391-1398.
- Khaledian, N., Villard, P. F., Hammer, P. E., Perrin, D. P., Berger, M. O. (2023, June). Influence of Anisotropy on Fluid-Structure Interaction Simulations of Image-Based and Generic Mitral Valves. In *International Conference on Functional Imaging and Modeling of the Heart* (pp. 455-464). Cham: Springer Nature Switzerland.

Awards

- **Best paper award:** Issued by IPCAI - International Conference on Information Processing in Computer-Assisted Interventions, Jun 2022, Tokyo, Jpan.
- **1st prize for the oral presentation session:** Issued by FIMH - International Conference on Functional Imaging and Modeling of the Heart, Jun 2023, Lyon, France.

Appendix A

Résumé Étendu en Français

La valve mitrale (VM) est l'une des quatre valves du cœur, située entre l'oreillette gauche et le ventricule gauche (VG). Elle comprend deux feuillets principaux, les feuillets antérieur et postérieur, qui sont entourés par l'anneau annulaire. De plus, la surface du tissu des feuillets et leur bord libre sont reliés au muscle papillaire à la base du ventricule gauche (VG) par un ensemble de structures chordales. Ces cordages tendineux agissent comme une attache, maintenant les feuillets de la VM en place pendant le cycle cardiaque et les empêchant de s'inverser dans l'oreillette gauche. Le principal objectif de la VM est de fournir un passage unidirectionnel pour le sang de manière efficace.

À l'instar d'autres tissus et organes biologiques du corps, la valve mitrale (VM) est également sujette à des pathologies. L'intervention chirurgicale offre une solution viable pour traiter les pathologies de la VM. La restauration de la fonction correcte de la valve peut inclure la suppression ou la suture de certaines parties des feuillets pour obtenir la géométrie souhaitée, ainsi que le remodelage de la structure des cordages et de l'anneau annulaire en incorporant des composants supplémentaires [CAF10].

Les décisions concernant les modifications de la structure de la valve mitrale (VM) reposent sur l'expertise des professionnels de la santé, tandis que le succès global de la procédure est fortement influencé par leur expérience. Une approche pour améliorer les résultats chirurgicaux globaux consiste à utiliser des outils informatiques pour simuler le comportement de la VM. L'objectif principal de la simulation de la VM est de développer un outil pratique pouvant être appliqué dans un cadre clinique. Sur la base des données d'imagerie médicale et des tests expérimentaux sur les tissus biologiques, ces outils informatiques peuvent anticiper le résultat attendu de la procédure et fournir des informations précieuses qui peuvent être utilisées de différentes manières pour soutenir les professionnels de la santé et augmenter les chances de succès.

Les simulations d'interaction fluide-structure (IFS) de la valve mitrale (VM) sont l'un de ces outils de calcul qui incluent la modélisation de plusieurs domaines physiques. Le mouvement dynamique de la VM implique deux états physiques distincts : la phase fluide représentée par l'écoulement sanguin et la phase solide représentée par les cordages et les feuillets. Les principes de la dynamique des fluides sont appliqués pour modéliser le mouvement dynamique de l'écoulement sanguin, tandis que des techniques d'analyse structurelle sont utilisées pour modéliser le mouvement de la VM elle-même. Dans cette thèse, nous avons utilisé la simulation

IFS pour simuler la fermeture dynamique de la VM, en tenant compte à la fois de l'écoulement sanguin et de la réponse physique de la VM. Nous nous concentrons sur la résolution de ses défis techniques et l'incorporation de diverses capacités afin de rendre le modèle adapté à une utilisation en planification chirurgicale. Certains de ces défis impliquent des problèmes de convergence et le temps de calcul de la simulation. Nous avons également mis en évidence et utilisé des approches essentielles pour capturer le contact détaillé entre les feuillets de la VM afin de mieux comprendre le fonctionnement correct de la valve et sa fermeture étanche. De plus, nous avons étudié l'impact des aspects fondamentaux de la simulation de la VM, y compris les modèles de matériaux, la configuration des cas et la géométrie. Dans ce qui suit, les contributions de cette thèse sont brièvement mentionnées.

A.1 Exploration de divers cadres numériques pour la simulation d'interaction fluide-structure de la fermeture dynamique de la valve mitrale

Dans la littérature sur la simulation numérique du comportement de la valve mitrale, plusieurs approches d'interaction fluide-structure (IFS) sont mises en œuvre, principalement basées sur la formulation Lagrangienne-Eulérienne arbitraire (ALE), la dynamique des particules lissées (SPH) et la méthode de la frontière immergée. Dans le chapitre 1, une exploration approfondie de ces approches et des représentations de maillage est présentée. Chaque approche possède des capacités uniques. Nous avons privilégié un modèle IFS qui est robuste, efficace sur le plan computationnel, adaptable à toute géométrie, et capable de reproduire avec précision la fermeture dynamique de la valve mitrale. Nous avons abordé les défis associés aux simulations de la valve mitrale et identifié les problèmes conduisant à des instabilités numériques. Après un examen détaillé des trois formulations, nous avons constaté que la simulation IFS utilisant la méthode de la frontière immergée, introduite dans [Pes72], est la plus adaptée pour capturer la fermeture étanche de la valve mitrale tout en maintenant un coût computationnel faible. La frontière immergée est un cadre mathématique et computationnel pour la simulation des problèmes IFS où une structure élastique est immergée dans un fluide visqueux et incompressible, permettant une interaction bidirectionnelle entre le fluide et la structure.

L'incorporation d'une telle représentation de maillage dans notre modèle améliore les propriétés de convergence de la simulation de la valve mitrale en réduisant les complexités associées à la déformation du maillage dans la simulation IFS. Dans notre modèle, le maillage fluide reste intact malgré la déformation significative du feuillet, minimisant ainsi le besoin de techniques de remaillage et éliminant les facteurs qui entravent la convergence de la simulation. Les facteurs supplémentaires qui impactent la convergence incluent le contrôle du maillage et les conditions aux limites, en particulier la définition des conditions aux limites de l'attache des cordages et de l'anneau. Cette approche contourne certaines des complexités difficiles liées à l'interaction des domaines numériques fluides et solides. De plus, elle offre des simulations stables avec une qualité de convergence constante, indépendamment des données d'entrée.

Le contact entre les feuillets lors de la fermeture implique une interaction arbitraire entre un grand nombre de nœuds, et un modèle de contact efficace pour gérer cette interaction complexe

influence la convergence de la simulation. Nous avons couplé la simulation IFS robuste basée sur la frontière immergée avec un modèle de contact efficace basé sur une formulation maître-esclave équilibrée qui gère le contact entre les feuillets, ce qui réduit encore le coût de calcul.

Cette thèse présente précisément comment le contact a été modélisé pour un calcul robuste et rapide. En utilisant notre modèle IFS, nous avons reproduit le comportement de la valve mitrale dans des états sains et pathologiques avec une géométrie générique de la valve mitrale et un modèle de matériau simplifié. Nous avons utilisé le solveur explicite Abaqus, capable de simuler basé sur la frontière immergée. Nous avons réussi à obtenir une fermeture correcte sans trous d'orifice dans le cas de la valve mitrale saine. Nos résultats sont publiés dans le IJCARS (International Journal of Computer Assisted Radiology and Surgery) sous forme d'article de journal [KVB22].

A.2 Mesure du contact

L'une de nos contributions est la description détaillée de la modélisation du contact entre les feuillets lors de la fermeture dynamique de la valve mitrale de manière efficace (voir chapitre 4). Un avantage de notre modèle IFS basé sur la représentation de maillage de la frontière immergée est sa compatibilité avec la capture du contact réel. Nous avons inclus à la fois le contact normal et le contact frictionnel entre les feuillets dans notre modèle, permettant l'analyse détaillée de la fermeture étanche de la valve mitrale, de la carte de contact et de la zone de coaptation. Dans la littérature, aucune étude sur la simulation IFS de la valve mitrale n'a fourni d'informations détaillées concernant la zone de coaptation, la force de contact et la fermeture étanche. Auparavant, des travaux expérimentaux mesuraient la zone de coaptation [GDD⁺10, YWK⁺09] ou la force de contact [GBL⁺20, GBC⁺20] lors de la fermeture de la valve mitrale, et notre carte de contact est le premier outil numérique capable de prédire si la valve se ferme correctement avec des informations relatives à la zone de coaptation. Des informations détaillées sur la manière dont nous avons obtenu la carte de contact sont présentées au chapitre 4.

A.3 Vers un modèle spécifique au patient

Un modèle spécifique au patient se réfère à une simulation numérique basée sur les données individuelles d'un patient et capable de capturer de manière réaliste le comportement de la valve mitrale. Un tel modèle vise à reproduire les caractéristiques et les mécaniques uniques de la valve mitrale pour un patient spécifique. Un modèle spécifique au patient doit être pratique, c'est-à-dire capable de gérer diverses données d'entrée avec des défis inhérents tels que le bruit et les erreurs de segmentation, tout en ayant la capacité de simuler un comportement réaliste.

Dans l'étape suivante, nous avons progressé vers un modèle spécifique au patient en incorporant la géométrie de la valve mitrale basée sur des images obtenues par des techniques d'imagerie médicale et en explorant des modèles de matériaux plus complexes. Nous avons fourni des informations détaillées sur les défis liés à la mise en œuvre de géométries de la valve mitrale basées sur des images. Initialement, nous avons mis en œuvre une géométrie générique et un modèle de matériau simplifié décrit au chapitre 4, qui considère la réponse contrainte-déformation des feuil-

lets de la valve mitrale comme homogène. Ensuite, nous avons évolué vers un modèle spécifique au patient en mettant en œuvre une géométrie basée sur des images et un modèle de matériau plus complexe, comme décrit au chapitre 5. La majorité des études dans la littérature utilisent une géométrie simplifiée de la valve mitrale [BGG⁺19, MGG⁺13, GFQ⁺17]. La première étape consistait à mettre en œuvre des géométries avec une structure de cordages précise et des feuillets segmentés à partir d’images micro-CT dans notre modèle IFS.

Un aspect essentiel d’un modèle spécifique au patient est sa polyvalence, garantissant qu’il n’est pas exclusivement conçu pour un ensemble particulier de données d’entrée. Le modèle doit posséder la capacité de converger et de simuler avec précision les données de patients comprenant des géométries diverses. La plupart des études dans la littérature sont basées sur une seule géométrie de valve mitrale. Malgré les difficultés posées par l’utilisation de géométries complexes et non lisses avec des irrégularités dans la topologie de la géométrie, notre modèle est capable d’accepter des géométries basées sur des images et de simuler la fermeture dynamique de la valve mitrale avec des géométries spécifiques aux patients. Pour nos études, nous disposons de cinq géométries de valve mitrale et, avec la même configuration de cas, nous avons réussi à exécuter la simulation sur quatre géométries basées sur des images et une valve générique, ce qui démontre la flexibilité de notre modèle. Nous avons présenté les résultats de simulation de deux de ces géométries basées sur des images au chapitre 5.

A.4 Influence de la géométrie et du volume de fluide

Dans la littérature sur la simulation IFS de la valve mitrale, un ventricule gauche simplifié est souvent représenté par un tube ajusté dans les simulations numériques [DYS⁺19, TBP⁺17, OÖB⁺21]. Nous avons approfondi cette approche en étudiant comment la taille de ce tube et le placement de la valve mitrale à l’intérieur de ce volume influencent le résultat de la simulation. Une telle exploration nous permet de discerner l’effet que la variation de la représentation du volume sanguin a sur les résultats. De plus, la géométrie segmentée de la valve mitrale est souvent caractérisée par des irrégularités à sa surface. Ces irrégularités, y compris les inexactitudes mineures introduites lors du processus de segmentation, peuvent potentiellement affecter le résultat de la simulation. Pour comprendre cela, nous avons utilisé le filtrage Laplacien pour réduire la rugosité du feuillet segmenté. Cette approche nous a permis de préserver la géométrie globale tout en minimisant les irrégularités de surface.

Nous avons également étudié l’influence de la régularité du résultat de la segmentation sur les résultats de la simulation. Nous avons exploré l’effet de l’utilisation de différentes formes pour représenter le ventricule gauche tubulaire sur le résultat de la simulation. Nous avons présenté les résultats pour quatre géométries basées sur des images et une valve mitrale générique. Les résultats de la simulation ont indiqué que la géométrie lissée améliorait la zone de coaptation et aboutissait à un meilleur contact tout en offrant un volume de saillie similaire par rapport à la géométrie originale extraite du processus de segmentation. De plus, en comparant les résultats de l’utilisation d’un tube ajusté et d’un grand cylindre représentant le ventricule gauche tubulaire, le second a également amélioré la zone de coaptation et la qualité de la fermeture. Au chapitre 5, nous discutons de l’influence de la géométrie de la valve mitrale et du volume de fluide sur les résultats de la simulation. Nous pensons que cette approche contribue à générer une simulation

plus fiable de la valve mitrale.

A.5 Investigation de différents modèles de matériaux

En ce qui concerne le modèle de matériau, les mesures expérimentales indiquent que les feuillets de la valve mitrale présentent un comportement anisotrope, affichant des réponses contrainte-déformation variables selon les différentes directions [JLK⁺18b]. Afin de capturer avec précision les caractéristiques du matériau, nous avons incorporé un modèle constitutif anisotrope dans notre représentation du matériau, ce qui reflète mieux les propriétés matérielles réelles.

Les feuillets de la valve mitrale sont constitués d'une structure tissulaire complexe renforcée par un réseau complexe de fibres de collagène, avec de multiples points d'insertion des cordages répartis sur leur surface. Ainsi, chaque spécimen possède ses propres caractéristiques matérielles uniques. L'une des limitations de la simulation de la valve mitrale est d'obtenir les données matérielles appropriées, d'interpréter ces données et de les mettre en œuvre dans le modèle numérique. Un autre défi consiste à obtenir les paramètres matériels en ajustant les données expérimentales aux équations du modèle constitutif. Nous avons mis en lumière les difficultés et les défis de cette tâche et avons réussi à obtenir les coefficients nécessaires grâce à un processus d'optimisation. Nous avons publié nos résultats sur l'influence du modèle de matériau sur les valves mitrales basées sur des images et génériques dans le cadre de la conférence internationale FIMH (Functional Imaging and Modeling of the Heart) sous forme d'article de conférence [KVH⁺23].

Un autre facteur influençant la simulation de la valve mitrale est la distribution des fibres de collagène des feuillets. Chaque feuillet de la valve mitrale possède sa propre microstructure, dont l'obtention constitue une tâche difficile. Nous avons approfondi le modèle de matériau en menant une étude comparative sur diverses approches de modélisation de la microstructure du tissu des feuillets. Nous avons exploré plusieurs modèles de fibres basés sur des règles pour décrire la microstructure du tissu des feuillets. Ces modèles de fibres basés sur des règles peuvent potentiellement faciliter la simulation biomécanique de la fonction cardiaque. La performance de chaque modèle de fibres est comparée en fonction de la qualité de la fermeture et des mesures ex vivo des forces des cordages disponibles dans la littérature. En raison du manque de données de référence, notre étude n'a pas été concluante. Nos résultats montrent que chaque modèle excelle dans certains critères tout en étant insuffisant dans d'autres. Des études similaires peuvent être bénéfiques pour rendre un outil de simulation facile à mettre en œuvre dans le flux de travail clinique ou pour concevoir des valves prothétiques, en particulier lorsqu'il s'agit de viser des qualités spécifiques telles que la flexibilité ou une bonne coaptation et contact.

A.6 Travaux futurs

A.6.1 Évaluation des résultats de la simulation

L'un des principaux obstacles de notre travail dans cette thèse a été la capacité de comparer les résultats de la simulation avec les mesures expérimentales. Bien que les simulations fournissent des informations précieuses, il est important de les évaluer par rapport aux données de référence. Les recherches futures pourraient bénéficier de la comparaison des résultats de la simulation avec

les données de référence, en veillant à ce que les simulations soient à la fois précises et reflètent les conditions réelles. Une stratégie potentielle consiste à scanner une géométrie de valve mitrale fantôme et à intégrer cette géométrie segmentée dans le modèle numérique. Ensuite, cette valve mitrale peut être placée dans un système duplicateur de pulsations et sa fermeture observée à l'aide de caméras stéréoscopiques. Les résultats de l'installation expérimentale peuvent ensuite être utilisés comme référence pour comparer avec les résultats de la simulation IFS. Nous avons prévu de réaliser un projet similaire à l'hôpital pour enfants de Boston en collaboration avec l'équipe CURATIVE. Cependant, en raison de problèmes de visa, cela n'a pas été réalisé.

A.6.2 Simulation en temps réel avec application à la salle d'opération

Les simulations détaillées dans cette thèse nécessitent des heures de calcul, les rendant inadaptées à une utilisation en temps réel dans les environnements chirurgicaux. Cependant, elles intègrent à la fois les effets fluides et structurels, offrant une meilleure représentation du comportement réel de la valve mitrale. Cela offre une opportunité de perfectionner les simulations en temps réel en utilisant les résultats des simulations IFS, dans le but d'obtenir une représentation précise de la fermeture dynamique de la valve mitrale applicable aux scénarios cliniques. Pour mieux intégrer cette recherche dans les environnements chirurgicaux, une approche pourrait consister à utiliser les données de distribution des forces issues de la simulation IFS comme entrée pour l'analyse structurelle. En pratique, les analyses structurelles sont plus rapides, avec un temps de calcul de l'ordre de quelques minutes. Cette méthode pourrait fournir une distribution plus complexe des forces sur les feuillets tout en étant calculée presque en temps réel, ouvrant ainsi la possibilité d'une utilisation dans les salles d'opération.

A.6.3 Vers un modèle de matériau plus précis

Dans cette thèse, nous avons exploré plusieurs modèles de fibres basés sur des règles. Pour les travaux futurs, une voie d'étude prometteuse est l'exploration de modèles de fibres alternatifs basés sur des règles pour décrire la microstructure des feuillets. Cela est important car la microstructure des feuillets influence la réponse mécanique et la fonctionnalité de la valve. En investiguant et en comparant divers modèles de fibres, les chercheurs peuvent obtenir une compréhension plus précise des processus physiologiques sous-jacents, ce qui pourrait conduire à des simulations de la valve mitrale plus précises et pratiques. Cela pourrait également être bénéfique pour une meilleure fabrication de valves prothétiques.

De plus, un sujet tout aussi important est l'étude de l'influence des différentes réponses contrainte-déformation des feuillets de la valve mitrale rapportées dans la littérature. Dans chaque mesure, il y a toujours une certaine variation qui peut être expliquée par la microstructure complexe des feuillets ou par la précision du test expérimental. Cependant, cette variance influence de manière significative le résultat de la simulation. Par conséquent, comprendre son influence et les causes de cette variation est bénéfique. En examinant et en comparant systématiquement ces différentes mesures, les chercheurs peuvent non seulement améliorer la précision des simulations, mais aussi approfondir notre compréhension de la biomécanique des feuillets de la valve mitrale, ce qui pourrait conduire à des modèles plus précis pour les applications chirurgicales et cliniques.

A.7 Structure de la thèse

Cette thèse est divisée en plusieurs chapitres, chacun explorant un aspect différent de la simulation de la valve mitrale (VM). Dans le chapitre 1, intitulé "Techniques d'interaction fluide-structure pour la modélisation du comportement de la valve mitrale", nous explorons l'état de l'art dans la simulation de la VM avec l'interaction fluide-structure (IFS) et comment le contact entre les feuillets est modélisé dans ces études. Nous présentons ensuite les détails des données géométriques que nous avons utilisées pour représenter la VM dans nos simulations au chapitre 2, intitulé "Données". Dans ce chapitre, nous discutons de la manière dont la géométrie des VM générique et basée sur des images est obtenue.

Dans le chapitre 3, intitulé "Proposition du modèle d'interaction fluide-structure", nous explorons la compréhension de base de la méthode de la frontière immergée (IB) ainsi que la mise en œuvre des conditions aux limites et la configuration du modèle nécessaires pour simuler la fermeture dynamique de la valve mitrale. Nous détaillons également le modèle de contact que nous avons utilisé pour capturer le contact entre les feuillets. Par la suite, nous mettons en lumière les informations relatives aux défis, aux modifications nécessaires et aux diverses configurations de cas dans la simulation IFS de la valve mitrale.

Ensuite, nous discutons d'abord des résultats initiaux obtenus à partir du modèle générique dans le chapitre 4, intitulé "Capture du contact dans la simulation d'interaction fluide-structure de la valve mitrale générique", en reproduisant la fermeture dynamique de la valve mitrale dans des cas sains et pathologiques. Dans le chapitre 5, intitulé "Investigation de l'influence de l'anisotropie et de la géométrie", nous nous efforçons de mettre en œuvre une géométrie spécifique au patient et d'explorer des modèles constitutifs plus complexes dans nos simulations. Dans ce chapitre, nous explorons les effets de l'incorporation de l'anisotropie dans la réponse mécanique des feuillets, en explorant différents modèles constitutifs, ainsi que le processus d'optimisation et l'obtention des coefficients. Nous comparons également les résultats de simulation en fonction de différents volumes de fluide et de la régularité de la géométrie basée sur les images. Ce chapitre se terminera par une discussion des résultats.

Le chapitre 6, intitulé "Microstructure des feuillets", fournira une brève introduction à la microstructure des feuillets, un aperçu des différents modèles de fibres, et conduira vers des modèles plus avancés basés sur des règles. Le chapitre se termine par une discussion des résultats.

Enfin, la thèse se conclut en résumant toutes les découvertes et en exposant les pistes potentielles pour les recherches futures.

Bibliography

- [AAAB⁺22] Yousef Alharbi, Amr Al Abed, Azam Ahmad Bakir, Nigel H Lovell, David WM Muller, James Otton, and Socrates Dokos. Fluid structure computational model of simulating mitral valve motion in a contracting left ventricle. *Computers in Biology and Medicine*, 148:105834, 2022.
- [AABS21] Mohammad Ali Ansari, Reza Abdi Behnagh, and Alberto Salvadori. Numerical analysis of high-speed water jet spot welding using the arbitrary lagrangian-eulerian (ale) method. *The International Journal of Advanced Manufacturing Technology*, 112:491–504, 2021.
- [ABVA16] Mostafa Abbasi, Mohammed S Barakat, Koohyar Vahidkhah, and Ali N Azadani. Characterization of three-dimensional anisotropic heart valve tissue mechanical properties using inverse finite element analysis. *Journal of the mechanical behavior of biomedical materials*, 62:33–44, 2016.
- [AEHE19] Saeed Adham Esfahani, Kamran Hassani, and Daniel M Espino. Fluid-structure interaction assessment of blood flow hemodynamics and leaflet stress during mitral regurgitation. *Computer methods in biomechanics and biomedical engineering*, 22(3):288–303, 2019.
- [AGPT09] Matteo Astorino, Jean-Frédéric Gerbeau, Olivier Pantz, and Karim-Frédéric Traoré. Fluid–structure interaction and multi-body contact: application to aortic valves. *Computer Methods in Applied Mechanics and Engineering*, 198(45-46):3603–3612, 2009.
- [AGS07] Carla Antoci, Mario Gallati, and Stefano Sibilla. Numerical simulation of fluid–structure interaction by sph. *Computers & structures*, 85(11-14):879–890, 2007.
- [AMDM09] V Alastrué, MA Martinez, M Doblaré, and Andreas Menzel. Anisotropic micro-sphere-based finite elasticity applied to blood vessel modelling. *Journal of the Mechanics and Physics of Solids*, 57(1):178–203, 2009.
- [AMP17] Eirini Apostolidou, Andrew D Maslow, and Athena Poppas. Primary mitral valve regurgitation: Update and review. *Global cardiology science & practice*, 2017(1), 2017.

- [ANAW22] Syed Samar Abbas, Mohammad Shakir Nasif, and Rafat Al-Waked. State-of-the-art numerical fluid–structure interaction methods for aortic and mitral heart valves simulations: a review. *Simulation*, 98(1):3–34, 2022.
- [ASFB14] M Ahmadzadeh, B Saranjam, A Hoseini Fard, and AR Binesh. Numerical simulation of sphere water entry problem using eulerian–lagrangian method. *Applied Mathematical Modelling*, 38(5-6):1673–1684, 2014.
- [ASMD10] V Alastrué, P Sáez, MA Martínez, and Manuel Doblaré. On the use of the bingham statistical distribution in microsphere-based constitutive models for arterial tissue. *Mechanics Research Communications*, 37(8):700–706, 2010.
- [BCL⁺15] Brian Baillargeon, Ivan Costa, Joseph R Leach, Lik Chuan Lee, Martin Genet, Arnaud Toutain, Jonathan F Wenk, Manuel K Rausch, Nuno Rebelo, Gabriel Acevedo-Bolton, et al. Human cardiac function simulator for the optimal design of a novel annuloplasty ring with a sub-valvular element for correction of ischemic mitral regurgitation. *Cardiovascular engineering and technology*, 6:105–116, 2015.
- [Ben92] David J Benson. Computational methods in lagrangian and eulerian hydrocodes. *Computer methods in Applied mechanics and Engineering*, 99(2-3):235–394, 1992.
- [BGG⁺19] Benedetta Biffi, Maurizio Gritti, Agata Grasso, Elena G Milano, Marianna Fontana, Hamad Alkareef, Joseph Davar, Paramijit Jeetley, Carol Whelan, Sarah Anderson, et al. A workflow for patient-specific fluid–structure interaction analysis of the mitral valve: A proof of concept on a mitral regurgitation case. *Medical Engineering & Physics*, 74:153–161, 2019.
- [BLZ⁺21] George C Bourantas, DS Lampropoulos, Benjamin F Zwick, VC Loukopoulos, Adam Wittek, and Karol Miller. Immersed boundary finite element method for blood flow simulation. *Computers & Fluids*, 230:105162, 2021.
- [BO04] David J Benson and Shigenobu Okazawa. Contact in a multi-material eulerian finite element formulation. *Computer methods in applied mechanics and engineering*, 193(39-41):4277–4298, 2004.
- [BOLK84] Ted Belytschko, Jame Shau-Jen Ong, Wing Kam Liu, and James M Kennedy. Hourglass control in linear and nonlinear problems. *Computer Methods in Applied Mechanics and Engineering*, 43(3):251–276, 1984.
- [Bor13] Iman Borazjani. Fluid–structure interaction, immersed boundary-finite element method simulations of bio-prosthetic heart valves. *Computer Methods in Applied Mechanics and Engineering*, 257:103–116, 2013.
- [BRI⁺16] Alessandra M Bavo, Giorgia Rocatello, Francesco Iannaccone, Joris Degroote, Jan Vierendeels, and Patrick Segers. FSI simulation of prosthetic aortic valves: comparison between immersed boundary and arbitrary lagrangian-eulerian techniques for the mesh representation. *PloS one*, 11(4):e0154517, 2016.

-
- [BVG⁺23] Lorenzo Bennati, Christian Vergara, Vincenzo Giambruno, Ivan Fumagalli, Antonio Francesco Corno, Alfio Quarteroni, Giovanni Puppini, and Giovanni Battista Luciani. An image-based computational fluid dynamics study of mitral regurgitation in presence of prolapse. *Cardiovascular Engineering and Technology*, pages 1–19, 2023.
- [CAF10] Alain Carpentier, David H Adams, and Farzan Filsoufi. *Carpentier’s reconstructive valve surgery*. Elsevier Health Sciences, 2010.
- [CGD⁺12] Christopher A Carruthers, Bryan Good, Antonio D’Amore, Jun Liao, Rouzbeh Amini, Simon C Watkins, and Michael S Sacks. Alterations in the microstructure of the anterior mitral valve leaflet under physiological stress. In *Summer Bioengineering Conference*, volume 44809, pages 227–228. American Society of Mechanical Engineers, 2012.
- [CKC⁺91] RP Cochran, KS Kunzelman, CJ Chuong, MS Sacks, and RC Eberhart. Nondestructive analysis of mitral valve collagen fiber orientation. *ASAIO transactions*, 37(3):M447–8, 1991.
- [CMB⁺21] Patrick Carnahan, John Moore, Daniel Bainbridge, Mehdi Eskandari, Elvis CS Chen, and Terry M Peters. Deepmitral: Fully automatic 3d echocardiography segmentation for patient specific mitral valve modelling. In *Medical Image Computing and Computer Assisted Intervention–MICCAI 2021: 24th International Conference, Strasbourg, France, September 27–October 1, 2021, Proceedings, Part V 24*, pages 459–468. Springer, 2021.
- [CMM⁺18] Andrés Caballero, Wenbin Mao, Raymond McKay, Charles Primiano, Sabet Hashim, and Wei Sun. New insights into mitral heart valve prolapse after chordae rupture through FSI computational modeling. *Scientific reports*, 8(1):1–14, 2018.
- [CMMS20] Andrés Caballero, Wenbin Mao, Raymond McKay, and Wei Sun. Transapical mitral valve repair with neochordae implantation: Fsi analysis of neochordae number and complexity of leaflet prolapse. *International Journal for Numerical Methods in Biomedical Engineering*, 36(3):e3297, 2020.
- [CVM⁺19] Dario Collia, Marija Vukicevic, Valentina Meschini, Luigino Zovatto, and Gianni Pedrizzetti. Simplified mitral valve modeling for prospective clinical application of left ventricular fluid dynamics. *Journal of Computational Physics*, 398:108895, 2019.
- [CWG⁺19] Li Cai, Ying Wang, Hao Gao, Xingshuang Ma, Guangyu Zhu, Ruihang Zhang, Xiaoqin Shen, and Xiaoyu Luo. Some effects of different constitutive laws on fsi simulation for the mitral valve. *Scientific Reports*, 9(1):12753, 2019.
- [CZCP19] Chiara Celotto, Luigino Zovatto, Dario Collia, and Gianni Pedrizzetti. Influence of mitral valve elasticity on flow development in the left ventricle. *European Journal of Mechanics-B/Fluids*, 75:110–118, 2019.

- [CZW⁺23] Li Cai, Tong Zhao, Yongheng Wang, Xiaoyu Luo, and Hao Gao. Fluid–structure interaction simulation of pathological mitral valve dynamics in a coupled mitral valve-left ventricle model. *Intelligent Medicine*, 3(2):104–114, 2023.
- [DADH23] Hüsnü Dal, Alp Kağan Açıkan, Ciara Durcan, and Mokarram Hossain. An in silico-based investigation on anisotropic hyperelastic constitutive models for soft biological tissues. *Archives of Computational Methods in Engineering*, pages 1–32, 2023.
- [DBB04] Niels J. B. Driessen, Carlijn V. C. Bouten, and Frank P. T. Baaijens. A Structural Constitutive Model For Collagenous Cardiovascular Tissues Incorporating the Angular Fiber Distribution. *Journal of Biomechanical Engineering*, 127(3):494–503, 12 2004.
- [DCBB08] Niels JB Driessen, Martijn AJ Cox, Carlijn VC Bouten, and Frank PT Baaijens. Remodelling of the angular collagen fiber distribution in cardiovascular tissues. *Biomechanics and modeling in mechanobiology*, 7:93–103, 2008.
- [Dev92] LS-DYNA Dev. Ls-dyna®. 1992.
- [DGH82] Jean Donea, S Giuliani, and Jean-Pierre Halleux. An arbitrary lagrangian-eulerian finite element method for transient dynamic fluid-structure interactions. *Computer methods in applied mechanics and engineering*, 33(1-3):689–723, 1982.
- [DKS18] Andrew Drach, Amir H Khalighi, and Michael S Sacks. A comprehensive pipeline for multi-resolution modeling of the mitral valve: Validation, computational efficiency, and predictive capability. *International journal for numerical methods in biomedical engineering*, 34(2):e2921, 2018.
- [DP15] Federico Domenichini and Gianni Pedrizzetti. Asymptotic model of fluid–tissue interaction for mitral valve dynamics. *Cardiovascular engineering and technology*, 6:95–104, 2015.
- [DPDFS05] F Dal Pan, G Donzella, C Fucci, and M Schreiber. Structural effects of an innovative surgical technique to repair heart valve defects. *Journal of biomechanics*, 38(12):2460–2471, 2005.
- [DVD⁺12] Sigrid Kaarstad Dahl, Jan Vierendeels, Joris Degroote, Sebastiaan Annerel, Leif Rune Hellevik, and Bjorn Skallerud. Fsi simulation of asymmetric mitral valve dynamics during diastolic filling. *Computer methods in biomechanics and biomedical engineering*, 15(2):121–130, 2012.
- [DYM⁺21] Yaghoub Dabiri, Jiang Yao, Vaikom S Mahadevan, Daniel Gruber, Rima Arnaout, Wolfgang Gentzsch, Julius M Guccione, and Ghassan S Kassab. Mitral valve atlas for artificial intelligence predictions of mitralclip intervention outcomes. *Frontiers in Cardiovascular Medicine*, 8:759675, 2021.
- [DYS⁺19] Yaghoub Dabiri, Jiang Yao, Kevin L Sack, Ghassan S Kassab, and Julius M Guccione. Tricuspid valve regurgitation decreases after mitralclip implantation: Fluid

-
- structure interaction simulation. *Mechanics research communications*, 97:96–100, 2019.
- [EDPJ⁺10] Daniel R Einstein, Facundo Del Pin, Xiangmin Jiao, Andrew P Kuprat, James P Carson, Karyn S Kunzelman, Richard P Cochran, Julius M Guccione, and Mark B Ratcliffe. Fluid–structure interactions of the mitral valve and left heart: comprehensive strategies, past, present and future. *International Journal for Numerical Methods in Biomedical Engineering*, 26(3-4):348–380, 2010.
- [EKR⁺04] Daniel R Einstein, KS Kunzelman, PG Reinhall, MA Nicosia, and RP Cochran. Haemodynamic determinants of the mitral valve closure sound: a finite element study. *Medical and Biological Engineering and Computing*, 42(6):832–846, 2004.
- [EKR⁺05a] Daniel R Einstein, Karyn S Kunzelman, Per G Reinhall, Mark A Nicosia, and Richard P Cochran. Non-linear fluid-coupled computational model of the mitral valve. *J Heart Valve Dis*, 14(3):376–385, 2005.
- [EKR⁺05b] Daniel R Einstein, Karyn S Kunzelman, Per G Reinhall, Mark A Nicosia, and Richard P Cochran. The relationship of normal and abnormal microstructural proliferation to the mitral valve closure sound. *J. Biomech. Eng.*, 127(1):134–147, 2005.
- [ESH14] Daniel M Espino, Duncan ET Shepherd, and David WL Hukins. Evaluation of a transient, simultaneous, arbitrary lagrange–euler based multi-physics method for simulating the mitral heart valve. *Computer methods in biomechanics and biomedical engineering*, 17(4):450–458, 2014.
- [ETZA⁺21] K Carlos El-Tallawi, Peng Zhang, Robert Azencott, Jiwen He, Elizabeth L Herrera, Jiaqiong Xu, Mohammed Chamsi-Pasha, Jessen Jacob, Gerald M Lawrie, and William A Zoghbi. Valve strain quantitation in normal mitral valves and mitral prolapse with variable degrees of regurgitation. *Cardiovascular Imaging*, 14(6):1099–1109, 2021.
- [FFP79] YC Fung, K Fronek, and P Patitucci. Pseudoelasticity of arteries and the choice of its mathematical expression. *American Journal of Physiology-Heart and Circulatory Physiology*, 237(5):H620–H631, 1979.
- [FGG⁺19] Liuyang Feng, Hao Gao, Boyce Griffith, Steven Niederer, and Xiaoyu Luo. Analysis of a coupled fluid–structure interaction model of the left atrium and mitral valve. *International journal for numerical methods in biomedical engineering*, 35(11):e3254, 2019.
- [FGQ⁺21] Liuyang Feng, Hao Gao, Nan Qi, Mark Danton, Nicholas A Hill, and Xiaoyu Luo. Fluid–structure interaction in a fully coupled three-dimensional mitral–atrium–pulmonary model. *Biomechanics and Modeling in Mechanobiology*, 20:1267–1295, 2021.

- [FMB08] Paul WM Fedak, Patrick M McCarthy, and Robert O Bonow. Evolving concepts and technologies in mitral valve repair. *Circulation*, 117(7):963–974, 2008.
- [FQG⁺18] Liuyang Feng, Nan Qi, Hao Gao, Wei Sun, Mariano Vazquez, Boyce E Griffith, and Xiaoyu Luo. On the chordae structure and dynamic behaviour of the mitral valve. *IMA journal of applied mathematics*, 83(6):1066–1091, 2018.
- [GBC⁺20] Daniel Grinberg, Alexis Bruhat, Pierre-Jean Cottinet, Minh Quyen Le, David H Adams, and Anthony Costa. Mitral valve repair based on physical characterization of coaptation forces. *The Journal of Thoracic and Cardiovascular Surgery*, 159(3):e181–e183, 2020.
- [GBL⁺20] Daniel Grinberg, Alexis Bruhat, Minh Quyen Le, David H Adams, Jean François Obadia, Anthony Costa, and P-J Cottinet. Outils innovants pour guider la réparation mitrale: méthodes et perspectives. *Bulletin de l’Académie Nationale de Médecine*, 204(5):500–507, 2020.
- [GDD⁺10] George Gogoladze, Sophia L Dellis, Robert Donnino, Greg Ribakove, David G Greenhouse, Aubrey Galloway, and Eugene Grossi. Analysis of the mitral coaptation zone in normal and functional regurgitant valves. *The Annals of thoracic surgery*, 89(4):1158–1161, 2010.
- [GFQ⁺17] Hao Gao, Liuyang Feng, Nan Qi, Colin Berry, Boyce E Griffith, and Xiaoyu Luo. A coupled mitral valve—left ventricle model with fluid–structure interaction. *Medical engineering & physics*, 47:128–136, 2017.
- [GMQ⁺14] Hao Gao, Xingshuang Ma, Nan Qi, Colin Berry, Boyce E Griffith, and Xiaoyu Luo. A finite strain nonlinear human mitral valve model with fluid-structure interaction. *International journal for numerical methods in biomedical engineering*, 30(12):1597–1613, 2014.
- [GOH06] T Christian Gasser, Ray W Ogden, and Gerhard A Holzapfel. Hyperelastic modelling of arterial layers with distributed collagen fibre orientations. *Journal of the royal society interface*, 3(6):15–35, 2006.
- [GQF⁺17] Hao Gao, Nan Qi, Liuyang Feng, Xingshuang Ma, Mark Danton, Colin Berry, and Xiaoyu Luo. Modelling mitral valvular dynamics—current trend and future directions. *International Journal for Numerical Methods in Biomedical Engineering*, 33(10):e2858, 2017.
- [Ham11] Peter E Hammer. *Simulating heart valve mechanical behavior for planning surgical repair*. PhD thesis, Tufts University, 2011.
- [Heu12] Olivier Heuzé. General form of the mie–grüneisen equation of state. *Comptes Rendus Mécanique*, 340(10):679–687, 2012.
- [HGB85] JO Hallquist, GL Goudreau, and DJ822741 Benson. Sliding interfaces with contact-impact in large-scale lagrangian computations. *Computer methods in applied mechanics and engineering*, 51(1-3):107–137, 1985.

-
- [HGG05] Emil Hayek, Christian N Gring, and Brian P Griffin. Mitral valve prolapse. *The Lancet*, 365(9458):507–518, 2005.
- [HGO00] Gerhard A Holzapfel, Thomas C Gasser, and Ray W Ogden. A new constitutive framework for arterial wall mechanics and a comparative study of material models. *Journal of elasticity and the physical science of solids*, 61:1–48, 2000.
- [HOB20] Zuoxian Hou, Ruth J Okamoto, and Philip V Bayly. Shear wave propagation and estimation of material parameters in a nonlinear, fibrous material. *Journal of biomechanical engineering*, 142(5):051010, 2020.
- [HPH11] Peter E Hammer, J Pedro, and Robert D Howe. Anisotropic mass-spring method accurately simulates mitral valve closure from image-based models. In *International Conference on Functional Imaging and Modeling of the Heart*, pages 233–240. Springer, 2011.
- [HSGR05] Gerhard A Holzapfel, Gerhard Sommer, Christian T Gasser, and Peter Regitnig. Determination of layer-specific mechanical properties of human coronary arteries with nonatherosclerotic intimal thickening and related constitutive modeling. *American Journal of Physiology-Heart and Circulatory Physiology*, 289(5):H2048–H2058, 2005.
- [JHG⁺18] Matthew A Jolley, Peter E Hammer, Sunil J Ghelani, Adi Adar, Lynn A Sleeper, Ronald V Lacro, Gerald R Marx, Meena Nathan, and David M Harrild. Three-dimensional mitral valve morphology in children and young adults with marfan syndrome. *Journal of the American Society of Echocardiography*, 31(11):1168–1177, 2018.
- [JLK⁺18a] Samuel Jett, Devin Laurence, Robert Kunkel, Anju R Babu, Katherine Kramer, Ryan Baumwart, Rheal Towner, Yi Wu, and Chung-Hao Lee. Biaxial mechanical data of porcine atrioventricular valve leaflets. *Data in brief*, 21:358–363, 2018.
- [JLK⁺18b] Samuel Jett, Devin Laurence, Robert Kunkel, Anju R Babu, Katherine Kramer, Ryan Baumwart, Rheal Towner, Yi Wu, and Chung-Hao Lee. An investigation of the anisotropic mechanical properties and anatomical structure of porcine atrioventricular heart valves. *Journal of the mechanical behavior of biomedical materials*, 87:155–171, 2018.
- [JSH⁺03] Jorge Hernan Jimenez, Dennis Dam Soerensen, Zhaoming He, Shengqiu He, and Ajit P Yoganathan. Effects of a saddle shaped annulus on mitral valve function and chordal force distribution: an in vitro study. *Annals of biomedical engineering*, 31:1171–1181, 2003.
- [KEC07] KS Kunzelman, Daniel R Einstein, and RP Cochran. Fluid–structure interaction models of the mitral valve: function in normal and pathological states. *Philosophical Transactions of the Royal Society B: Biological Sciences*, 362(1484):1393–1406, 2007.

- [KFN17] Seyedvahid Khodaei, Nasser Fatourae, and Malikeh Nabaei. Numerical simulation of mitral valve prolapse considering the effect of left ventricle. *Mathematical biosciences*, 285:75–80, 2017.
- [KMP19] Alexander D Kaiser, David M McQueen, and Charles S Peskin. Modeling the mitral valve. *International Journal for Numerical Methods in Biomedical Engineering*, 35(11):e3240, 2019.
- [KSE⁺23] Alexander D Kaiser, Nicole K Schiavone, Christopher J Elkins, Doff B McElhinney, John K Eaton, and Alison L Marsden. Comparison of immersed boundary simulations of heart valve hemodynamics against in vitro 4d flow mri data. *Annals of Biomedical Engineering*, pages 1–22, 2023.
- [KVB22] Nariman Khaledian, Pierre-Frédéric Villard, and Marie-Odile Berger. Capturing contact in mitral valve dynamic closure with fluid-structure interaction simulation. *International Journal of Computer Assisted Radiology and Surgery*, 17(8):1391–1398, 2022.
- [KVH⁺23] Nariman Khaledian, Pierre-Frédéric Villard, Peter E Hammer, Douglas P Perrin, and Marie-Odile Berger. Influence of anisotropy on fluid-structure interaction simulations of image-based and generic mitral valves. In *International Conference on Functional Imaging and Modeling of the Heart*, pages 455–464. Springer, 2023.
- [LAG⁺14] Chung-Hao Lee, Rouzbeh Amini, Robert C Gorman, Joseph H Gorman III, and Michael S Sacks. An inverse modeling approach for stress estimation in mitral valve anterior leaflet valvuloplasty for in-vivo valvular biomaterial assessment. *Journal of biomechanics*, 47(9):2055–2063, 2014.
- [Lan79] Y Lanir. A structural theory for the homogeneous biaxial stress-strain relationships in flat collagenous tissues. *Journal of biomechanics*, 12(6):423–436, 1979.
- [Lan83] Yan Lanir. Constitutive equations for fibrous connective tissues. *Journal of biomechanics*, 16(1):1–12, 1983.
- [Lau12] Kevin Daniel Lau. *Numerical simulation of mitral valve function*. PhD thesis, University College London (University of London), 2012.
- [LDSB10] K.D. Lau, V. Diaz, P. Scambler, and G. Burriesci. Mitral valve dynamics in structural and fluid–structure interaction models. *Medical Engineering & Physics*, 32(9):1057–1064, 2010.
- [LDZSB11] KD Lau, V Díaz-Zuccarini, P Scambler, and G Burriesci. Fluid–structure interaction study of the edge-to-edge repair technique on the mitral valve. *Journal of biomechanics*, 44(13):2409–2417, 2011.
- [Lev13] J Rodney Levick. *An introduction to cardiovascular physiology*. Butterworth-Heinemann, Oxford, 2013.

-
- [LJ18] Kwangwoo Lee and Sangseom Jeong. Large deformation fe analysis of a debris flow with entrainment of the soil layer. *Computers and Geotechnics*, 96:258–268, 2018.
- [LPT20] Colin Laville, Christophe Pradille, and Yannick Tillier. Mechanical characterization and identification of material parameters of porcine aortic valve leaflets. *Journal of the mechanical behavior of biomedical materials*, 112:104036, 2020.
- [LRJ⁺19] Devin Laurence, Colton Ross, Samuel Jett, Cortland Johns, Allyson Echols, Ryan Baumwart, Rheal Towner, Jun Liao, Pietro Bajona, Yi Wu, et al. An investigation of regional variations in the biaxial mechanical properties and stress relaxation behaviors of porcine atrioventricular heart valve leaflets. *Journal of biomechanics*, 83:16–27, 2019.
- [LSP⁺23] Hao Liu, Natalie T Simonian, Alison M Pouch, Joseph H Gorman, III, Robert C Gorman, and Michael S Sacks. A computational pipeline for patient-specific prediction of the post-operative mitral valve functional state. In *International Conference on Functional Imaging and Modeling of the Heart*, pages 636–647. Springer, 2023.
- [LZL⁺15] Chung-Hao Lee, Will Zhang, Jun Liao, Christopher A Carruthers, Jacob I Sacks, and Michael S Sacks. On the presence of affine fibril and fiber kinematics in the mitral valve anterior leaflet. *Biophysical journal*, 108(8):2074–2087, 2015.
- [Man12] Abaqus Scripting User’s Manual. Abaqus 6.11. <http://130.149>, 89(2080):v6, 2012.
- [Mat22] John E Matsson. *An introduction to ANSYS fluent 2022*. Sdc Publications, 2022.
- [MCM⁺17] Wenbin Mao, Andrés Caballero, Raymond McKay, Charles Primiano, and Wei Sun. Fully-coupled fluid-structure interaction simulation of the aortic and mitral valves in a realistic 3d left ventricle model. *PloS one*, 12(9):e0184729, 2017.
- [MES⁺11] Laura Millard, Daniel M Espino, Duncan ET Shepherd, David WL Hukins, and Keith G Buchan. Mechanical properties of chordae tendineae of the mitral heart valve: Young’s modulus, structural stiffness, and effects of aging. *Journal of mechanics in medicine and biology*, 11(01):221–230, 2011.
- [MGG⁺13] Xingshuang Ma, Hao Gao, Boyce E Griffith, Colin Berry, and Xiaoyu Luo. Image-based fluid–structure interaction model of the human mitral valve. *Computers & Fluids*, 71:417–425, 2013.
- [MNY95] Karen May-Newman and FC Yin. Biaxial mechanical behavior of excised porcine mitral valve leaflets. *American Journal of Physiology-Heart and Circulatory Physiology*, 269(4):H1319–H1327, 1995.
- [MNY98] K. May-Newman and F. C. P. Yin. A Constitutive Law for Mitral Valve Tissue. *Journal of Biomechanical Engineering*, 120(1):38–47, 1998.
- [MRR10] Karen P McCarthy, Liam Ring, and Bushra S Rana. Anatomy of the mitral valve: understanding the mitral valve complex in mitral regurgitation. *European Journal of echocardiography*, 11(10):i3–i9, 2010.

- [MVV19] Valentina Meschini, Francesco Viola, and Roberto Verzicco. Modeling mitral valve stenosis: A parametric study on the stenosis severity level. *Journal of biomechanics*, 84:218–226, 2019.
- [MYL⁺06] W David Merryman, Inchan Youn, Howard D Lukoff, Paula M Krueger, Farshid Guilak, Richard A Hopkins, and Michael S Sacks. Correlation between heart valve interstitial cell stiffness and transvalvular pressure: implications for collagen biosynthesis. *American Journal of Physiology-Heart and Circulatory Physiology*, 290(1):H224–H231, 2006.
- [NKI⁺13] Thilo Noack, Philipp Kiefer, Razvan Ionasec, Ingmar Voigt, Tammaso Mansi, Marcel Vollroth, Michael Hoebartner, Martin Misfeld, Friedrich-Wilhelm Mohr, and Joerg Seeburger. New concepts for mitral valve imaging. *Annals of cardiothoracic surgery*, 2(6):787, 2013.
- [NRRS19] AMA Nasar, Benedict D Rogers, Alistair Revell, and PK Stansby. Flexible slender body fluid interaction: Vector-based discrete element method with eulerian smoothed particle hydrodynamics. *Computers & Fluids*, 179:563–578, 2019.
- [OÖB⁺21] Robert Ott, Alper Ö Öner, Paul Hermann Bellé, Finja Borowski, Klaus-Peter Schmitz, and Michael Stiehm. Validation of a fluid-structure interaction model for the characterization of transcatheter mitral valve repair devices. *Current Directions in Biomedical Engineering*, 7(2):605–608, 2021.
- [Pan21] Daryna Panicheva. *Image-based mitral valve modeling for biomechanical applications*. PhD thesis, Université de Lorraine, 2021.
- [Pes72] Charles S Peskin. Flow patterns around heart valves: a numerical method. *Journal of computational physics*, 10(2):252–271, 1972.
- [Pes02] Charles S Peskin. The immersed boundary method. *Acta numerica*, 11:479–517, 2002.
- [PG20] Salvatore Pasta and Caterina Gandolfo. Pre-operative modeling of transcatheter mitral valve replacement in a surgical heart valve bioprosthesis. *Prosthesis*, 2(1):4, 2020.
- [PHS09] V Prot, R Haaverstad, and B Skallerud. Finite element analysis of the mitral apparatus: annulus shape effect and chordal force distribution. *Biomechanics and modeling in mechanobiology*, 8:43–55, 2009.
- [PIMW⁺20] Michael J Paulsen, Annabel M Imbrie-Moore, Hanjay Wang, Jung Hwa Bae, Camille E Hironaka, Justin M Farry, Haley J Lucian, Akshara D Thakore, John W MacArthur Jr, Mark R Cutkosky, et al. Mitral chordae tendineae force profile characterization using a posterior ventricular anchoring neochordal repair model for mitral regurgitation in a three-dimensional-printed ex vivo left heart simulator. *European Journal of Cardio-Thoracic Surgery*, 57(3):535–544, 2020.

-
- [PMFC01] Elisabeth Pichelin, Katia Mocellin, Lionel Fourment, and Jean-Loup Chenot. An application of a master-slave algorithm for solving 3d contact problems between deformable bodies in forming processes. *Revue Européenne des Eléments*, 10(8):857–880, 2001.
- [PS09] V Prot and B Skallerud. Nonlinear solid finite element analysis of mitral valves with heterogeneous leaflet layers. *Computational Mechanics*, 43(3):353–368, 2009.
- [PS14] Thuy Pham and Wei Sun. Material properties of aged human mitral valve leaflets. *Journal of Biomedical Materials Research Part A*, 102(8):2692–2703, 2014.
- [PSL⁺10] Muralidhar Padala, Michael S Sacks, Shasan W Liou, Kartik Balachandran, Zhaoming He, and Ajit P Yoganathan. Mechanics of the mitral valve strut chordae insertion region. 2010.
- [PSSH10] Viktorien Prot, Bjorn Skallerud, Gerhard Sommer, and Gerhard A Holzapfel. On modelling and analysis of healthy and pathological human mitral valves: two case studies. *Journal of the mechanical behavior of biomedical materials*, 3(2):167–177, 2010.
- [PVH⁺21a] Daryna Panicheva, Pierre-Frédéric Villard, Peter E Hammer, Douglas Perrin, and Marie-Odile Berger. Automatic extraction of the mitral valve chordae geometry for biomechanical simulation. *International Journal of Computer Assisted Radiology and Surgery*, 16(5):709–720, 2021.
- [PVH⁺21b] Daryna Panicheva, Pierre-Frédéric Villard, Peter E Hammer, Douglas Perrin, and Marie-Odile Berger. Automatic extraction of the mitral valve chordae geometry for biomechanical simulation. *International Journal of Computer Assisted Radiology and Surgery*, pages 709–720, 2021.
- [PVHB19] Daryna Panicheva, Pierre-Frederic Villard, Peter E Hammer, and Marie-Odile Berger. Physically-coherent extraction of mitral valve chordae. In *2019 Computing in Cardiology (CinC)*, pages Page–1. IEEE, 2019.
- [QHG11] Gang Qiu, Sascha Henke, and Jürgen Grabe. Application of a coupled eulerian–lagrangian approach on geomechanical problems involving large deformations. *Computers and Geotechnics*, 38(1):30–39, 2011.
- [RFS⁺13] Manuel K Rausch, Nele Famaey, Tyler O’Brien Shultz, Wolfgang Bothe, D Craig Miller, and Ellen Kuhl. Mechanics of the mitral valve: a critical review, an in vivo parameter identification, and the effect of prestrain. *Biomechanics and modeling in mechanobiology*, 12:1053–1071, 2013.
- [RMK14] Yonghoon Rim, David D McPherson, and Hyunggun Kim. Effect of leaflet-to-chordae contact interaction on computational mitral valve evaluation. *Biomedical engineering online*, 13:1–11, 2014.
- [RT23] Seyed Esmail Razavi and Amin Talebi. Comparative modeling of the mitral valve in normal and prolapse conditions. *BioImpacts*, 13(4), 2023.

- [RZG⁺17] Manuel K Rausch, Alexander M Zöllner, Martin Genet, Brian Baillargeon, Wolfgang Bothe, and Ellen Kuhl. A virtual sizing tool for mitral valve annuloplasty. *International journal for numerical methods in biomedical engineering*, 33(2):e02788, 2017.
- [Sac99] MS Sacks. A method for planar biaxial mechanical testing that includes in-plane shear. 1999.
- [SB09] Fotis Sotiropoulos and Iman Borazjani. A review of state-of-the-art numerical methods for simulating flow through mechanical heart valves. *Medical & biological engineering & computing*, 47:245–256, 2009.
- [SDKT23] Shiyin Sha, Ashley P Dyson, Gholamreza Kefayati, and Ali Tolooiyan. Simulation of debris flow-barrier interaction using the smoothed particle hydrodynamics and coupled eulerian lagrangian methods. *Finite Elements in Analysis and Design*, 214:103864, 2023.
- [SHB⁺02] Michael S Sacks, Zheng He, Lotte Baijens, S Wanant, P Shah, H Sugimoto, and AP Yoganathan. Surface strains in the anterior leaflet of the functioning mitral valve. *Annals of biomedical engineering*, 30:1281–1290, 2002.
- [Skr12] Andrzej Skrzat. Application of coupled eulerian-lagrangian approach in metal forming simulations. *Zeszyty Naukowe Politechniki Rzeszowskiej. Mechanika*, (84 [284], nr 4):25–35, 2012.
- [SMB11] Andrei-Ionut Stefanu, Silviu-Cristian Melenciuc, and Mihai Budescu. Penalty based algorithms for frictional contact problems. *Buletinul Institutului Politehnic din Iasi. Sectia Constructii, Arhitectura*, 57(3):119, 2011.
- [SMC⁺11] Marco Stevanella, Francesco Maffessanti, Carlo A Conti, Emiliano Votta, Alice Arnoldi, Massimo Lombardi, Oberdan Parodi, Enrico G Caiani, and Alberto Redaelli. Mitral valve patient-specific finite element modeling from cardiac mri: application to an annuloplasty procedure. *Cardiovascular Engineering and Technology*, 2:66–76, 2011.
- [SOLT16] M Safdari Shadloo, G Oger, and David Le Touzé. Smoothed particle hydrodynamics method for fluid flows, towards industrial applications: Motivations, current state, and challenges. *Computers & Fluids*, 136:11–34, 2016.
- [Sor05] Olga Sorkine. Laplacian Mesh Processing. In Yiorgos Chrysanthou and Marcus Magnor, editors, *Eurographics 2005 - State of the Art Reports*. The Eurographics Association, 2005.
- [SOV⁺15] Francesco Sturla, Francesco Onorati, Emiliano Votta, Marco Stevanella, Aldo D Milano, Konstantinos Pechlivanidis, Giovanni Puppini, Alberto Redaelli, and Giuseppe Faggian. Repair of mitral valve prolapse through eptfe neochordae: a finite element approach from cmr. *Biomedical Technology*, pages 117–128, 2015.

-
- [SPN11] B Skallerud, V Prot, and IS Nordrum. Modeling active muscle contraction in mitral valve leaflets during systole: a first approach. *Biomechanics and modeling in mechanobiology*, 10(1):11–26, 2011.
- [SS05] Wei Sun and Michael S Sacks. Finite element implementation of a generalized fung-elastic constitutive model for planar soft tissues. *Biomechanics and modeling in mechanobiology*, 4:190–199, 2005.
- [SSHP22] Mohammad Javad Sadeghinia, Bjørn Skallerud, Gerhard A Holzapfel, and Victorien Prot. Biomechanics of mitral valve leaflets: Second harmonic generation microscopy, biaxial mechanical tests and tissue modeling. *Acta biomaterialia*, 141:244–254, 2022.
- [SVR09] Marco Stevanella, Emiliano Votta, and Alberto Redaelli. Mitral valve finite element modeling: implications of tissues’ nonlinear response and annular motion. *Journal of biomechanical engineering*, 131(12), 2009.
- [TBE⁺16] Milan Toma, Charles Bloodworth, Daniel Einstein, Eric Pierce, Richard Cochran, Ajit Yoganathan, and Karyn Kunzelman. High resolution subject-specific mitral valve imaging and modeling: Experimental and computational methods. *Biomechanics and Modeling in Mechanobiology*, 15, 12 2016.
- [TBP⁺17] Milan Toma, Charles H Bloodworth, Eric L Pierce, Daniel R Einstein, Richard P Cochran, Ajit P Yoganathan, and Karyn S Kunzelman. Fluid-structure interaction analysis of ruptured mitral chordae tendineae. *Annals of biomedical engineering*, 45:619–631, 2017.
- [TCAA⁺21] Milan Toma, Rosalyn Chan-Akeley, Jonathan Arias, Gregory D Kurgansky, and Wenbin Mao. Fluid–structure interaction analyses of biological systems using smoothed-particle hydrodynamics. *Biology*, 10(3):185, 2021.
- [TEBI⁺20] Milan Toma, Daniel R Einstein, Charles H Bloodworth IV, Keshav Kohli, Richard P Cochran, Karyn S Kunzelman, and Ajit P Yoganathan. Fluid-structure interaction analysis of subject-specific mitral valve regurgitation treatment with an intra-valvular spacer. *Prosthesis*, 2(2):65–75, 2020.
- [TJE⁺16] Milan Toma, Morten Ø Jensen, Daniel R Einstein, Ajit P Yoganathan, Richard P Cochran, and Karyn S Kunzelman. Fluid–structure interaction analysis of papillary muscle forces using a comprehensive mitral valve model with 3d chordal structure. *Annals of biomedical engineering*, 44:942–953, 2016.
- [VCV⁺08] Emiliano Votta, Enrico Caiani, Federico Veronesi, Monica Soncini, Franco Maria Montevicchi, and Alberto Redaelli. Mitral valve finite-element modelling from ultrasound data: a pilot study for a new approach to understand mitral function and clinical scenarios. *Philosophical Transactions of the Royal Society A: Mathematical, Physical and Engineering Sciences*, 366(1879):3411–3434, 2008.
- [VHP⁺18] Pierre-Frederic Villard, Peter E Hammer, Douglas P Perrin, Pedro J Del Nido, and Robert D Howe. Fast image-based mitral valve simulation from individualized

- geometry. *The International Journal of Medical Robotics and Computer Assisted Surgery*, 14(2):e1880, 2018.
- [WHF94] Bruce F Waller, Jane Howard, and Stephen Fess. Pathology of mitral valve stenosis and pure mitral regurgitation—part i. *Clinical cardiology*, 17(6):330–336, 1994.
- [WMG96] Jeffrey A Weiss, Bradley N Maker, and Sanjay Govindjee. Finite element implementation of incompressible, transversely isotropic hyperelasticity. *Computer methods in applied mechanics and engineering*, 135(1-2):107–128, 1996.
- [WS13] Qian Wang and Wei Sun. Finite element modeling of mitral valve dynamic deformation using patient-specific multi-slices computed tomography scans. *Annals of biomedical engineering*, 41:142–153, 2013.
- [XJN⁺12] Chun Xu, Arminder S Jassar, Derek P Nathan, Thomas J Eperjesi, Clayton J Brinster, Melissa M Levack, Mathieu Vergnat, Robert C Gorman, Joseph H Gorman III, and Benjamin M Jackson. Augmented mitral valve leaflet area decreases leaflet stress: a finite element simulation. *The Annals of thoracic surgery*, 93(4):1141–1145, 2012.
- [XJW⁺21] Fei Xu, Emily L Johnson, Chenglong Wang, Arian Jafari, Cheng-Hau Yang, Michael S Sacks, Adarsh Krishnamurthy, and Ming-Chen Hsu. Computational investigation of left ventricular hemodynamics following bioprosthetic aortic and mitral valve replacement. *Mechanics Research Communications*, 112:103604, 2021.
- [YWK⁺09] Ryotaro Yamada, Nozomi Watanabe, Teruyoshi Kume, Miwako Tsukiji, Takahiro Kawamoto, Yoji Neishi, Akihiro Hayashida, Eiji Toyota, Hiroyuki Okura, and Kiyoshi Yoshida. Quantitative measurement of mitral valve coaptation in functional mitral regurgitation: in vivo experimental study by real-time three-dimensional echocardiography. *Journal of cardiology*, 53(1):94–101, 2009.

Résumé

La valve mitrale est l'une des quatre valves du cœur qui régule le passage du flux sanguin de l'atrium gauche au ventricule gauche. Des pathologies peuvent entraîner des dysfonctionnements de la valve tel que des fuites de sang et des prolapsus. La simulation numérique ouvre la voie à une meilleure compréhension du comportement de la valve dans de tels scénarios. Nous étudions dans cette thèse les techniques de simulation de l'interaction fluide-structure (FSI) sur données synthétiques et sur données réelles. Nous espérons que ces travaux seront une aide pour les cliniciens pour la réparation ou le remplacement de la valve mitrale.

Dans cette thèse, nous avons utilisé une approche FSI basée sur la méthode des frontières immergées pour simuler la fermeture dynamique de la valve. L'utilisation de ces méthodes permet de capturer des informations détaillées sur l'efficacité de la fermeture. Au début, nous avons utilisé une géométrie générique et un modèle de matériau isotrope pour reproduire la fermeture dynamique de la valve dans des cas sains et pathologiques. Notre approche a amélioré la capacité à mesurer la qualité de la fermeture grâce à une meilleure représentation de la zone de coaptation et du contact automatique entre les feuillets.

Nous avons ensuite considéré des données réelles en utilisant la géométrie extraite de la segmentation des cœurs de porcs et en incorporant des modèles de matériau qui tiennent compte de l'anisotropie du tissu des feuillets de la valve. Nos résultats permettent de conclure qu'utiliser un modèle anisotrope reflète mieux l'état physiologique de la valve, en donnant un feuillet moins extensible. De plus, la comparaison des forces des cordages pendant la fermeture avec des données ex-vivo valide notre approche.

Nous avons utilisé notre modèle pour étudier l'influence de facteurs supplémentaires affectant la fermeture dynamique de la valve, y compris la nécessité d'un lissage des feuillets et le rôle du volume de fluide simulant le ventricule. Nous avons utilisé plusieurs géométries de valve extraites de l'image pour nos simulations. Nous avons observé qu'employer un tube ajusté, représentant un ventricule gauche simplifié, ne permet pas la fermeture chez certains patients. Par contre, l'utilisation d'un grand cylindre a entraîné une fermeture efficace de la valve. De plus, l'utilisation d'un grand cylindre a fourni une meilleure zone de coaptation par rapport au tube ajusté.

Enfin, nous avons étudié des approches alternatives pour obtenir expérimentalement la microstructure du tissu des feuillets. Ces approches, qui ne nécessitent pas d'imagerie microscopique spécifique, tiennent compte de la réponse mécanique du tissu en état fermé, et des traits physiologiques, tels que les points d'insertion des cordages. Ces approches devront être approfondies dans l'avenir.

Mots-clés: valve mitrale, interactions fluide-structure, anisotropie, simulation biomécanique.

Abstract

The mitral valve (MV) is one of the four valves of the heart that regulates the passage of blood flow from the left atrium to the left ventricle. Pathologies can cause the MV to dysfunction, such as blood leakage and bulging. Using numerical simulations open the way toward understanding how MV behaves in such scenarios. We study in this thesis how patient-based fluid-structure interaction (FSI) simulation of mitral valve (MV) closure could help clinicians for MV repair or replacement surgery.

In this thesis, we used an FSI approach based on the immersed boundary method to simulate the MV dynamic closure. Using the immersed boundary method allows for capturing detailed information about closure efficiency. At first, we used a generic geometry and isotropic material model to replicate the dynamic closure of MV in healthy and pathological cases. Our approach improved the ability to measure the quality of the closure by better representation of the coaptation area and self-contact between the leaflets.

We went further toward the patient-based model by utilizing image-based geometry extracted from the segmentation of porcine hearts and incorporating more accurate material models that consider the anisotropy of the MV leaflet tissue. Our results conclude that using an anisotropic constitutive model better reflects the physiological state of the MV by giving a less extensible leaflet, which results in less bulging. Furthermore, the comparison of chordae forces during closure with ex-vivo data supports the physiological validity of our approach.

We used our patient-specific model to investigate the influence of additional factors impacting MV dynamic closure, including leaflet smoothness and fluid volume. We realized that applying a smoothing filter on the surface of the leaflet geometry extracted from the segmentation process improves the coaptation area without affecting the bulging volume. We used several image-based MV geometries for our simulations. We observed that employing a fitted tube, representing a simplified left ventricle, did not yield proper closure in some patients, but using a large cylinder resulted in effective valve closure. In addition, using a large cylinder provided a better coaptation area compared to the fitted tube.

Finally, we investigated alternative approaches to experimentally obtaining the microstructure of the leaflet tissue. These approaches, which do not require any specific microscopic imagery, take into account the mechanical response of the tissue in the closed state, and physiological traits, such as chordae insertion points. These approaches will be more investigated in the future.

Keywords: mitral valve, fluid-structure interactions, anisotropy, biomechanical simulation.